TOWARDS A BETTER UNDERSTANDING OF THE MECHANISMS CONTROLLING THE DURABILITY OF FRP COMPOSITES IN CONCRETE

by

Abu Sayed Md. Kamal

A thesis submitted in partial fulfillment of the requirements for the degree of
Doctor of Philosophy

University of Saskatchewan
Division of Environmental Engineering
Saskatoon, Saskatchewan, Canada
August 2011

PERMISSION TO USE

In presenting this thesis in partial fulfillment of the requirements for a degree of doctor of Philosophy from the University of Saskatchewan, I agree that the Libraries of this University may make it freely available for inspections. I further agree that permission for copying of this thesis in any manner, in whole or in part, for scholarly purposes may be granted by the professor or professors who supervised my thesis work, Professor Moh. Boulfiza or in his absence, by the Head of the Division or the Dean of the College in which my thesis work was done. It is understood that any copying or publication or use of this thesis or parts thereof for financial gain shall not be allowed without my written permission. It is also understood that due recognition shall be given to me and to the University of Saskatchewan in any scholarly use which may be made of any material in my thesis.

Requests for permission to copy or to make other use of material in this thesis in whole or on part should be addressed to:

Head of the Division of Environmental Engineering
University of Saskatchewan
57 Campus Drive
Saskatoon, Saskatchewan
Canada S7N 5A9

ABSTRACT

Wide adoption by the construction industry of Fibre Reinforced Polymer (FRP) rebars - a relatively recent construction material that offers numerous advantages of corrosion resistance, higher strength, lighter weight, etc. over conventional reinforcing materials for concrete, such as steel - is at least partially impeded due to a lack of an effective long term in-service performance prediction model and relatively high initial costs. A reliable service life prediction model for FRP composites in concrete depends on a clear understanding of the transport mechanisms of potentially harmful chemical species into the FRP composites and their subsequent contribution to any potentially active degradation mechanism(s).

To identify which mechanisms control the degradation of Glass Fibre Reinforced Polymers (GFRP) in alkaline environments, GFRP rebars were immersed into simulated concrete pore solutions and subjected to accelerated ageing tests (Phase 1). The conditioned samples were analyzed by various electron microscopy (SEM, EDS) and spectroscopic methods (FTIR). Analyses of these tests revealed that fibre-matrix debonding took place in few samples exposed to 75 °C (the highest temperature considered in this study), and tested after one year, despite the fact that the glass fibres and polymer matrix remained essentially intact and that no penetration of alkalis into the GFRP rebars was observed. Hence, this study shows that the Vinyl Ester (VE) polymer matrix used acts as an effective semi-permeable membrane by allowing the penetration of water while blocking alkali ions. The findings showing that most of the damage seems to be confined to the fibre-matrix interphase (or interface), under the considered test conditions, stimulated an investigation on the effects of sizing on the strength retention and water up-take of GFRP rebars in Phase 2 of the testing program.

In order to study the effects of sizing on the properties of GFRP rebars, GFRP custom plane sheets with sized and desized glass fibers were produced and exposed to deionized water at 4 °C, 23 °C, and 50 °C. Irrespective of sample types, the tensile strength decreased with temperature while the mass gain and moisture diffusivity increased with temperature. However, the sized samples showed a similar mass gain behavior as the desized ones, at the same exposure environment. This study confirms that sizing in GFRP custom plane sheets contributes not only

to the initial strength of the composite by enhancing the adhesion between the glass fibre and a matrix, but also to the strength retention (i.e., durability) when exposed to harsh environments.

The experiments of Phase 2 were carried out at 100% relative humidity (RH). However, field service conditions vary with respect to RH and temperature for GFRP composites in concrete. Therefore, a further study was conducted to investigate the effects of RH and temperature on the properties of GFRP rebars in Phase 3.

The effects of RH were investigated by exposing GFRP rebars to nine RH environments (9%-100%) while monitoring mass changes during drying and wetting. Moreover, the thermal effects of GFRP rebars on water uptake in deionized water at 4 °C, 23 °C, and 50 °C were studied and compared with those for GFRP custom plane sheets. The effects of RH on drying and wetting for GFRP rebars exhibited a hysteretic behavior. The percent of mass gain at 100% RH showed a significant difference from that in other RH environments. Mass gain and moisture diffusivity were found to increase for both rebars and custom sheets with increasing temperature. A typical Fickian behaviour of water absorption was observed for both types of samples at all exposure conditions, except the GFRP rebars at higher temperatures (starting at 50 °C) which showed non-Fickian behaviour for water absorption. The dependence of the diffusion coefficient on temperature was found to follow the Arrhenius equation.

Literature reports severe matrix cracking and fibre dissolution of GFRP in accelerated ageing tests. The results of this investigation confirmed that no matrix or fibre degradation was found in any sample up to 75 °C. However, the interface of samples exposed to 75 °C started to show signs of debonding at the fibre-matrix interface. Hence, any likely candidate mechanism must be related to some degradation at the interface/interphase of the GFRP composite. It was proposed here to assess whether preexisting microdefect locations could serve as sites for potential formation and growth of a microblister (local osmotic cells).

Based on the thermodynamics of microblister formation and growth, a rational model has been proposed to address the mechanisms of microblister formation at the interphase of FRP composites. Results of the analyses, show that the critical pressure that needs to be overcome by the osmotic pressure before a microblister can grow is much higher than this latter one for both GFRP rebar and GFRP sheet samples until 75 °C for the temperatures considered in this study. Therefore, one can conclude that no microblister is formed at the given experimental conditions of samples immersed at a pH 7 with the temperatures of 4 °C, 23 °C, 50 °C, and 75 °C. The

same model also predicted that if temperature is spiked to very high values (around 95 °C), a preexisting microblister would be able to grow, which could eventually lead to matrix volume changes and/or cracking, even if the temperature remains below the glass transition temperature (T_g) of the matrix.

ACKNOWLEDGEMENT

First of all, I would like to express my sincere thanks to Almighty Allah for His kind blessings to complete this thesis successfully.

I would like to place my deepest respect and profound gratitude to my supervisor Professor Mohamed Boulfiza for his valuable guidance, inspiration, assistance, advice, and cordial dealings throughout the study period. Special thanks and respect for Professor Richard Evitts, Professor Leon Wegner, Professor Ikechukwuka Oguocha, Professor Yen-Han Lin, and Professor Mehdi Nemati for their valuable suggestions during my Ph.D. study and actively guidign my research as advisory committee members (ACM). Also, thanks to Dr. Satya Panigrahi for serving as an ACM for a certain period of time during my study.

A hearty thanks to all lab technicians including Brennan Pokoyoway and Dale Pavier of Civil engineering, Doug Fisher of Environmental engineering, Louis Roth, Randy and Bill of Ag & Bio-resource Engineering, and Rob Peace of Mechanical engineering for helping me to prepare samples, making mould, and setting experiments. Special thanks to Tom Bonli of Geological Sciences and Ken Thoms of Saskatchewan Structural Sciences Centre for assisting me to analyze samples.

Thanks to Jan Compain, the secretary of Environmental and Biomedical Engineering, and Cynthia Hanke, the secretary of Civil Engineering for being very nice and helpful in my time of need and making my work easier.

I express my gratitude and thanks to Intelligent Sensing for Innovative Structures (ISIS), Canada, for providing financial support in pursuing my study at the University of Saskatchewan.

Sincere thanks to my parents and all family members for their all sorts of supports. Thanks to my all well-wishers, whose encouragements were always with me during my study.

DEDICATION

Dedicated to my beloved wife Mony

TABLE OF CONTENTS

LIST OF TABLES

LIST OF FIGURES

LIST OF ABBREVIATIONS

AFRP	Aramid fibre reinforced polymer
APDES	Aminopropyl-methyldiethoxysilane
APMES	Aminopropyl-dimethylethoxysilane
APTES	Aminopropyl-triethoxysilane
ASP	Alumino silicate phosphate
ASTM	American society for testing and materials
BE	Backscattered electron
BEI	Backscattered electron images
CFRP	Carbon fibre reinforced polymer
DSC	Differential scanning calorimetry
DMTA	Dynamic mechanical thermal analysis
EDS	Energy dispersive spectroscopy
FRP	Fibre reinforced polymers
FTIR	Fourier transform infrared
GFRP	Glass fibre reinforced polymer
HDPE	High density poly ethylene
NMR	Nuclear magnetic resonance
PE	Poly ester
RH	Relative humidity
SE	Secondary electron
SEM	Scanning electron microscopy
SMC	Sheet moulding compound
TS	Tensile strength
VARTM	Vacuum assisted resin transfer moulding
VE	Vinylester
VIP	Vacuum infusion process

LIST OF SYMBOLS

λ	Wavelength, *cm*
$\bar{v}$	Vibrational frequency, cm^{-1}
A and *B*	Chemical species in a binary diffusion
A	Blister surface area, um^2
a	Radius of the sample, *m*
*A**	Chemical species in a self diffusion
c	Velocity of light, *cm/s*
C	Concentration of diffusing species, kg/m^3
D	Diffusion coefficient, m^2/s
D_0	Pre-exponential constant, m^2/s
dC/dx	Concentration gradient
E	Young's modulus, *GPa*
E_a	Activation energy, *J/mol*
$E_{elastic}$	Elastic energy, *J/mol*
E_o	Accelerating voltage, *J/mol*
h	Distance between two charged plates, *um*
h	Outer layer thickness of a GFRP composite, *um*
J	Flux, kg/m^2-*s*
m_1	Mass of first atom, *g*
m_2	Mass of second atom, *g*
M_∞	Quantity of diffusing substance after an infinite time, *wt%*
M_t	Quantity of diffusing substance after t time, *wt%*
P	Pressure of a blister, *Pa*
P_{os}	Osmotic pressure, *Pa*
r	Blister radius, *um*
R	Ideal gas constant, *J/mol-K*
r_i	Radius of a blister, *um*
r_{max}	Maximum radius of a blister, *um*

T	Temperature, $°C/K$
T_g	Glass transition temperature, $°C$
U_w	Molar volume of water, m^3/mol
V	Molar volume of water in a blister, m^3/mol
W_A	Energy of adhesion, J/m^2
W_b	Baseline specimen mass, g
W_i	Current specimen mass, g
x	Depth of electron penetration, um
Xi	Mole fraction of water, %
α, β, γ	Chemical species in a multi-component diffusion
α_n	Roots of Equation
δ	Surface charge density, $coulomb/m^2$
ε	Dielectric constant
ρ	Density of the sample materials, g/cm^3
υ	Poisson's ratio
$\omega(r)$	Deflection of a blister, um

CHAPTER ONE

INTRODUCTION

1.1 Overview

One significant challenge facing the world today is the decay of infrastructure. The cost of protecting and restoring concrete structures worldwide is a large and growing problem. The annual costs of metallic corrosion in USA have recently been estimated to be about $276 billion per year, which is about 3.1 percent of the national gross domestic product (Koch et al. 2005). A major component of infrastructure decay is the degradation of bridges and highways due to the corrosion of the embedded reinforcing steel. The direct cost of corrosion for highway bridges is estimated to be $8.3 billion per year in USA where $3.8 billion would be used for replacing structurally deficient bridges over the next ten years, $2.0 billion for maintenance and cost of capital for concrete bridge decks, $2.0 billion for maintenance and cost of capital for concrete substructures (minus decks), and $0.5 billion for maintenance painting of steel bridges (Koch et al., 2005). The main long-term deterioration mechanism involves moisture movement and the transport of dissolved harmful chemical species within concrete, which lead to steel reinforcement corrosion.

Glass Fibre Reinforced Polymer (GFRP) materials have not been used in large-scale construction applications despite their numerous advantages over traditional materials such as steel. Economic and technical barriers hinder industry's widespread adoption of this new technology. The primary economic barrier preventing their use is often their high initial cost, whereas the primary technical hurdle remains the relative uncertainty about the long-term performance of Fibre Reinforced Polymer (FRP) reinforced structures in their service environment. The widespread adoption of FRP composites by the construction industry has been impeded, at least partly, due to the absence of satisfactory service life prediction models. However, unless the transport mechanisms of potentially harmful chemical species into FRP composites and the subsequent degradation mechanisms, if any, are clearly understood, it would be very difficult to make reliable predictions regarding the lifetime performance of FRP

composites in concrete. Obviously, the performance of FRP in concrete depends upon the interaction of bars embedded in concrete with their surrounding environment, especially the highly alkaline pore solution, as well as on the presence of applied stresses.

The performance of a concrete structure depends on its field conditions. Monitoring the real life of a field structure might take 100 years or more. However, it is not practical to wait such a long period of time before one can assess the service life and performance of new construction materials, such as FRP bars. Therefore, accelerated ageing techniques have been practiced to study the durability of FRP bars (Kim et al. 2009; Chen et al. 2007; Mukherjee and Arwikar 2005; Karbhari and Zhang 2003; Chin et al. 2001; Zhang and Karbhari 1999; Pritchard 1999; Porter and Barnes 1998; GangaRao and Vijay 1997; Sonawala and Spontak 1996; Katsuki and Uomoto 1995; Bank et al. 1995; Schutte 1994; Zheng and Morgan 1993; Pritchard and Speake 1987; Apicella et al. 1983; Marom and Broutman 1981). A comprehensive review on the durability of FRP bars has been performed (Nkurunziza et al. 2005; Karbhari et al. 2003) to identify the gaps of knowledge that need to be filled in this field.

The performance of FRP bars under accelerated ageing conditions has mostly been studied by assessing the loss of strength or some other relevant material property of rebars (Chen et al. 2006; Dejke and Tepfers 2001; Murphy et al. 1999; Porter et al. 1997; Katsuki and Uomoto 1995). The strength loss of FRP rebars has also been shown to be larger in alkali solutions than in water (Chin et al. 1999; Chin et al. 1997). These findings are, however, in sharp contrast with a recent field study (Mufti et al. 2007; Benmokrane and Cousin 2005), carried out by three different research laboratories, where the glass fibres, the polymer matrix, and the GFRP/concrete interface have been shown to remain intact after 6-8 years of service inside concrete. These findings confirmed that the results of accelerated laboratory ageing studies in alkaline solutions cannot easily be extrapolated to field performance evaluation. Based on this latter study, the use of GFRP as a primary reinforcement, as well as prestressing tendons, in concrete is now allowed by the Canadian highway bridge design code CSA S6-06. However, there is still a lack of rational explanation for the discrepancy between the durability of GFRP under accelerated ageing conditions and in the field. Hence, there is a need for a better understanding of the mechanisms governing the performance of GFRP under accelerated or field conditions, and what leads to the marked difference in performance between the two. As a first step towards that goal, an attempt is made in this study to understand the penetration of water

and alkali ions into GFRP bars and how they affect the potential degradation of fibre, matrix, and their interphase.

It has been observed that the presence of load or strain is likely to increase the degradation process of GFRP rebars, as has been reported by several researchers (Chen et al. 2006; Wang 2005; Greenwood 2002; Dejke and Tepfers 2001; Porter et al. 1997; Murphy et al. 1999; Devalapura et al. 1998; Katsuki and Uomoto 1995), and hence, must be addressed in light of the new findings in the future in order to come up with more realistic service life prediction models. However, the primary objective of this study is mostly restricted to investigating whether the outer layer of the GFRP composite does act as a semi-permeable membrane or not and to propose a simple mechanistic model that can explain the behavior exhibited by GFRP composites under accelerated ageing conditions as well as field conditions.

1.2 Objective

The overall objective was to clarify the interaction mechanisms of concrete pore solution with FRP composites, including an assessment of the permeability of the outer layer and the subsequent deterioration to the FRP ingredients. The experiment was set to study the interactions of GFRP rebars with a simulated concrete solution under accelerated ageing conditions by observing the

- Diffusion of any harmful species into GFRP rebars
- Deterioration at fibre-matrix interphase
- Deterioration of matrix
- Deterioration of fibres.

The second major objective was to identify the main mechanism governing the degradations of GFRP composites and use it as the basis for a mechanistic model for assessing whether GFRP rods will degrade or not when exposed to concrete pore solutions.

1.3. Scope

- Though many FRP composite materials are used in real life, only FRP composites used in civil engineering constructions were considered in this research.

- Among three FRP composites (CFRP, AFRP, and GFRP) used in construction applications, only GFRP composites were used for this research.
- The aim of this research was not to predict the service life of FRP composites directly rather, it was intended essentially to help in developing the mechanistic model to predict the service life of GFRP composites in concrete.

1.4. Methodology

The overall objective of this study was to clarify the interaction mechanisms of FRP composite in concrete environment. The research project was divided into three sequential phases where the programme of each phase was guided by the findings of the previous stage. The purpose of phase 1 was to investigate and determine which component of the composite material (vinyl ester matrix, E-glass fibre, their interface) would show signs of degradation under the accelerated ageing conditions considered. An overview of the activities, techniques or methods utilized, together with the expected outcomes in phase 1 are summarised in Figure 1.1. GFRP rebars were immersed in five types of simulated concrete pore solutions at 23 °C, 50 °C, and 75 °C, and tested for 1 month, 3 months, and 12 months. Penetration of alkali ions was assessed using X-ray mapping of Backscattered Electron Images (BEI) and crosschecked by line and point energy dispersive spectroscopy (EDS) techniques. The degradation of the polymer matrix was assessed by Fourier transform infrared (FTIR) Spectroscopy, while the degradation of the fibre was investigated by observing highly-magnified scanning electron microscopy (SEM) images at the interphase, and point EDS on fibre and matrix close to the fibre-matrix interface. The effects of harmful chemical species on the fibre-matrix interphase were evaluated by investigating the potential degradation at the fibre-matrix interphase using high resolution SEM pictures.

Analysis of phase 1 tests revealed that fibre-matrix debonding took place in a few samples despite the fact that the glass fibres and polymer matrix remained essentially intact and that no penetration of alkali ions into the GFRP rebars was observed. This debonding, which occurred only for samples exposed to 75 °C, seems to be caused by the dissolution of fibre sizing by water at high temperatures since the E-glass fibre and vinyl ester (VE) resin looked like they were simply separated from each other without any sign of chemical attack on either the fibre or

the matrix. Clear signs of E-glass fibre degradation would have been detected had the alkali ions in solution reached the fibre. Hence, this study showed that the VE polymer matrix used acted as an effective semi-permeable membrane by allowing the penetration of water while blocking alkali ions.

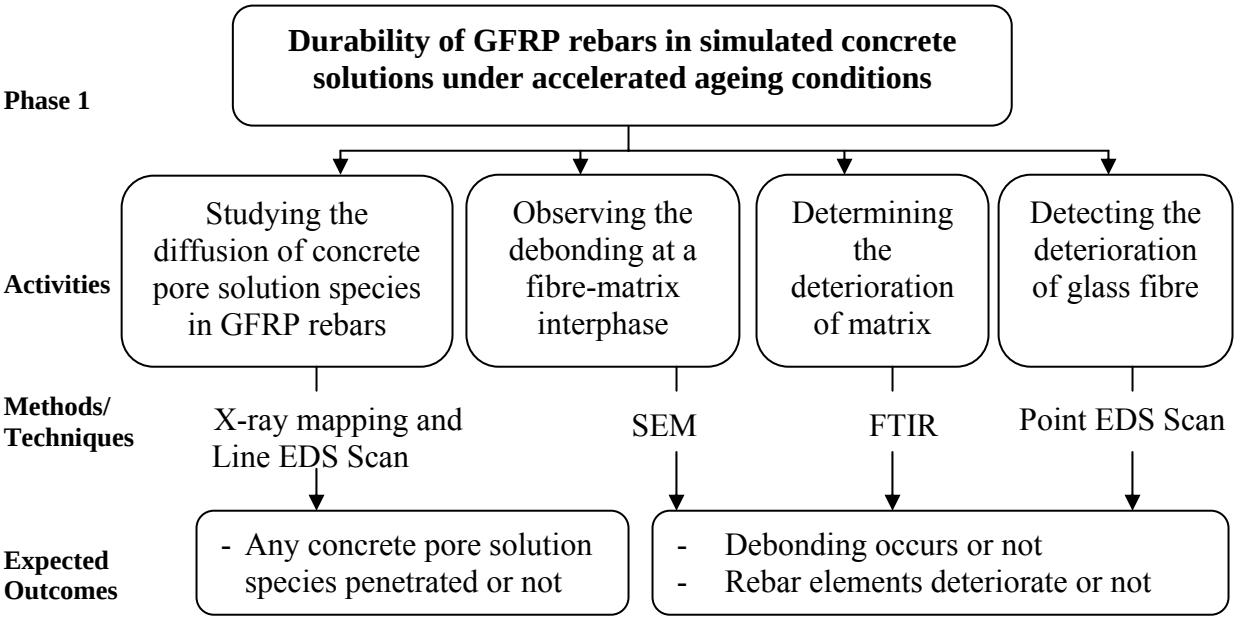

Figure 1.1. An overview of the research in Phase 1.

The findings of Phase 1 showing that most of the damage seemed to be confined to the fibre-matrix interphase (or interface) under the considered test conditions, stimulated an investigation on the effects of sizing. The sizing effects on the composite's properties with respect to the tensile strength and moisture gain were addressed using GFRP custom plane sheets (Phase 2). An overview of the activities, techniques or methods utilized, and expected outcomes in phase 2 are summarised in Figure 1.2. In order to study the effects of sizing on the properties of GFRP rebars, the GFRP custom plane sheet was-produced by a vacuum infusion process (VIP). Usage of the GFRP sheets in place of rebars would allowed one to study, understand, and interpret the behaviour of GFRP composites at an intermediate level between the microscopic level, as represented by a single fibre surrounded by a matrix (too simplistic), and the macroscopic level, as represented by GFRP rebars (too complicated). Two series of experiments were carried out by immersing sheet specimens (sized and de-sized) in deionized water at 4 °C,

23 °C, and 50 °C. The desizing process of the fibreglass mat and the manufacturing process were original techniques specifically developed for this project and performed at a lab-scale.

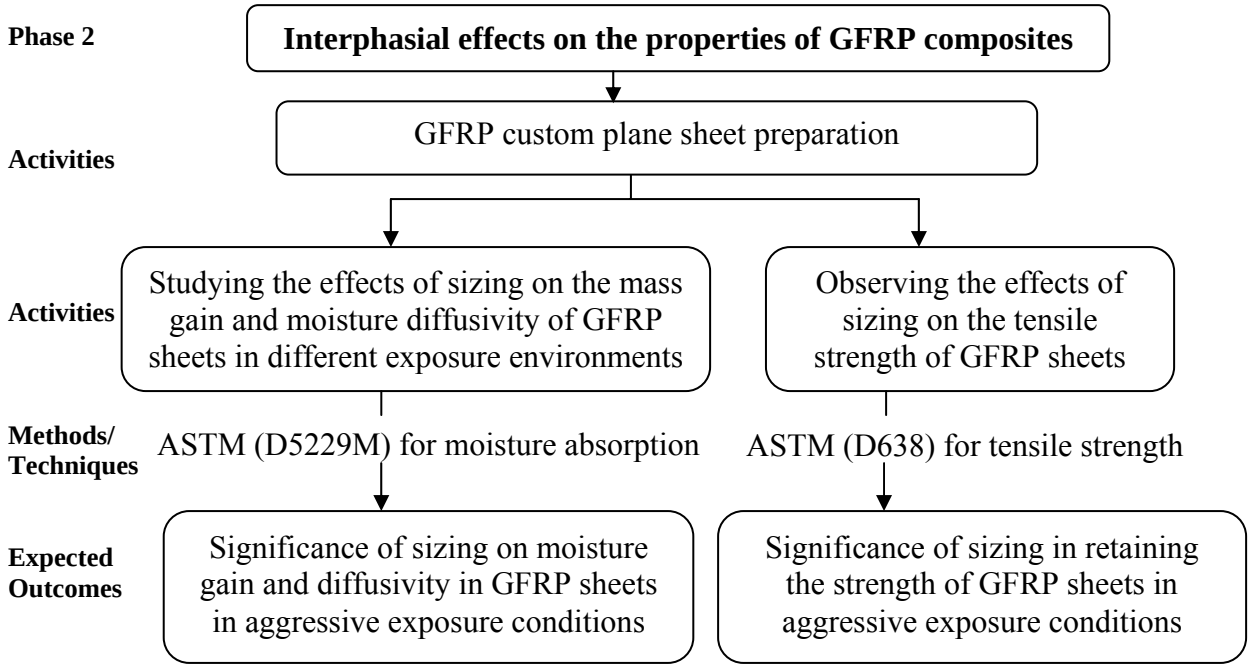

Figure 1.2. An overview of the research in Phase 2.

Experimental results of Phase 2 showed that the tensile strengths of sized specimens, in all exposure conditions, were always higher than those of the corresponding de-sized ones. Adhesion theories explain the fibre-matrix bonds at the interphase, which ultimately contribute the overall strength in both dry and wet conditions. Moreover, the mass gain tests showed that the exposure temperature could lead to a significant increase in moisture gain and moisture diffusivity. However, the sized samples showed a similar mass gain behavior as the de-sized ones at the same exposure environment. This study confirms that sizing in GFRP custom plane sheets contributes not only to the initial strength of the composite by enhancing the adhesion between the glass fibre and a matrix, but also to the strength retention (i.e., durability) when exposed to harsh environments.

The effects of sizing on the mass gain and strength retention of GFRP composites were investigated at 100% relative humidity (RH) in Phase 2. However, field service conditions, with respect to RH and temperature, for GFRP composites in concrete are expected to vary with time. Therefore, a further study was conducted to investigate the effects of RH and temperature on the

properties of GFRP rebars in Phase 3. An overview of the activities, techniques or methods utilized, and expected outcomes in phase 3 are summarised in Figure 1.3. The effects of RH were investigated by exposing GFRP rebars to nine RH environments (9%-100%) and taking mass changes during drying and wetting. Moreover, the thermal effects of GFRP rebars on water uptake in deionized water at 4 °C, 23 °C, and 50 °C were studied and compared with those for GFRP custom plane sheets.

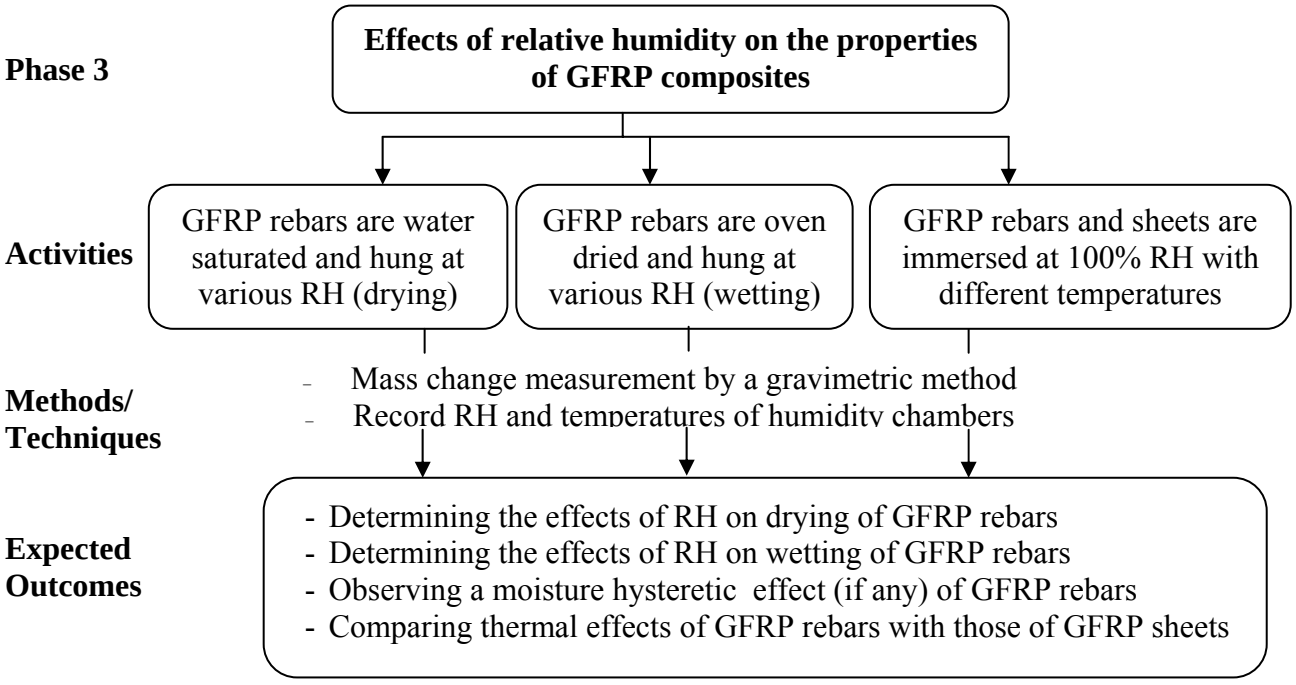

Figure 1.3. An overview of the research in Phase 3.

The effects of RH on drying and wetting for GFRP rebars exhibited a hysteretic behavior. The mass gain vs RH curves were different for drying and for wetting. The percent of mass gain at 100% RH showed a significant difference from that in other RH environments. Mass gain and moisture diffusivity were found to increase for both rebars and custom sheets with increasing temperature. A typical Fickian behaviour of water absorption was observed for GFRP sheets and GFRP samples at all exposure conditions, except the GFRP rebars at higher temperature (starting at 50 °C) showed a non-Fickian behaviour for water absorption. The dependence of the diffusion coefficient on temperature was found to follow the Arrhenius Equation.

A reasonable amount of published data in the technical literature (although usually under harsher conditions of temperature and/or presence of stress than those considered in this study) reports severe matrix cracking and fibre dissolution following exposure to alkali ions. This severe degradation is also accompanied by significant losses in the tensile strength of GFRP, as one would logically expect. The results of this investigation confirmed that no matrix or fibre degradation was found in any sample up to 75 °C. However, the samples exposed to 75 °C started to show signs of debonding at the fibre-matrix interface. Hence, any likely candidate mechanism that can potentially explain this transition in behaviour must be related to some degradation at the interface/interphase of the GFRP composite. Knowing that decomposition of a water soluble part of sizing at the fibre-matrix interphase has been reported elsewhere in the literature, and that microdefects always exist at the interface (due for instance to imperfect wetting of the E-glass by sizing), it was proposed here to assess whether those microdefect locations could serve as sites for potential formation and growth of a microblister (local osmotic cells). A rational model based on the findings of the experimental part of this study has been proposed to address the mechanisms of microblister formation at the interphase of FRP composites.

1.5. Thesis organization

This thesis consists of eight Chapters and three appendices. After Chapter 8, there is a reference section. Chapter 1 presents background, objectives, scope, methodology/overview of research, and thesis organization. Chapter 2 provides a detailed description of the ingredients of FRP composites, deterioration mechanisms of FRP composites, bonding mechanisms at the fibre-matrix interphase, effects of exposure environments on the durability of FRP composites, and principle and operation of material characterization techniques. Chapter 3 describes the experimental programmes conducted in three phases. It includes sample preparation, design and setting of experiments, running of experiments, and test procedures for all phases. Chapter 4 contains the outcomes of experimental results of accelerated ageing tests for GFRP rebars in Phase 1. This experiment confirmed that vinylester (VE) resin around GFRP bars prevent harmful chemical species except water from penetrating into bars. Moreover, the fibre-matrix interphase was found to be intact even at moderately elevated temperatures. Chapter 5 expresses the findings of interphasial effects on the properties of GFRP composites in Phase 2. How the

properties of GFRP composites are controlled by the minor ingredients (sizing) at the interphase is also discussed in this Chapter. Chapter 6 presents the effects of RH on drying and wetting of GFRP rebars in Phase 3. The thermal effects on moisture diffusion in composites were also studied and compared in this Chapter. Chapter 7 discusses the performance of GFRP composites in terms of moisture gain and diffusivity by using a Fickian model of moisture absorption. It also includes the Arrhenius theory of temperature dependence with diffusivity for GFRP composites. Moreover, it explains a rational approach of deteriorating of fibre-matrix interphase by proposing a blister formation concept and verifying the concept with experimental and aggressive conditions. Finally, Chapter 8 presents the key findings of all experiments and theoretical analysis, and recommendations for future research. In addition to Chapters, there are two appendices. Appendix A contains the raw data and Appendix B describes the manufacturing techniques of composite materials.

CHAPTER TWO
LITERATURE REVIEW

2.1. Composite materials

A composite material can be defined as the combination of two or more materials to obtain a desired dimension with specific structural, electrical, and thermal properties. Generally, the combination of participating materials in composites exhibit better characteristics than their individual properties. For instance, a GFRP composite consists of two major ingredients glass fibre and polymer matrix. Glass fibres are strong, stiff and brittle, whereas a polymer matrix is ductile, weak and flexible. Hence, the individual ingredients contribute to better overall properties, such as strength, stiffness, flexibility, and low density in FRP composites (Callister 2010).

2.2. Ingredients of FRP composites

FRP is a specific type of two-component material consisting of high strength fibres embedded in a polymer matrix (ISIS 2003). Several published works are available about the basic components of FRP. A few notable of them are Campbell (2004), ISIS (2003), Jones (2001), Rebenfeld (2000), Massingill and Bauer (2000), Goodman (1998), Kim (1995), and Seymour (1987). The most widely used FRP for Civil Engineering application is Glass Fibre Reinforced Polymer (GFRP), a cost effective and durable composite, developed by impregnating E-glass fibres into a vinylester (VE) resin along with other required minor elements. The basic ingredients of GFRP composites – VE and E-glass - are shown in Figure 2.1.

Even though the synthesis methods of epoxy, polyester, and vinylester resins are discussed in the following sections, the preference of using vinylesters over other esters are mentioned, as VE is one of the basic ingredients of GFRP composites. E-glass fibre is also discussed with a greater importance over other fibres as it is the other basic ingredient of GFRP composites.

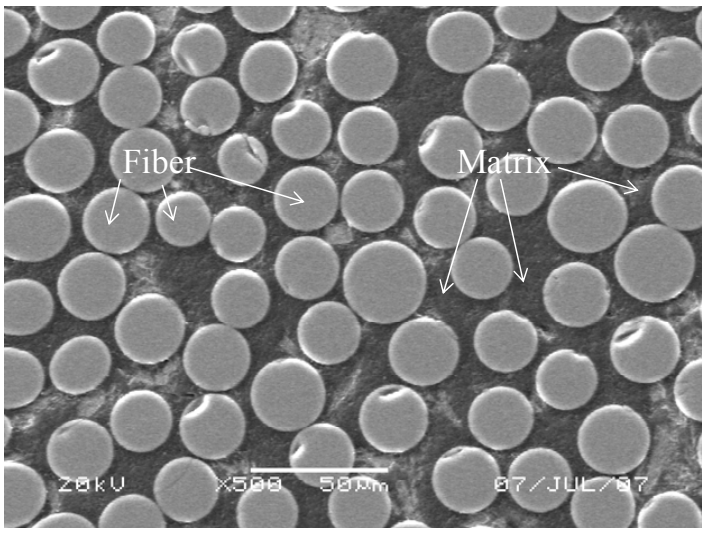

Figure 2.1. An SEM (x500) image on a GFRP rebar cross-section showing the two basic ingredients fibre and matrix.

2.2.1. Matrix

A matrix is a polymeric compound with a long-chain molecules developed from repeating units called monomers. The matrix works as a binder for FRP and plays many important roles. A few essential functions that the matrix performs include (a) binding fibres together, (b) protecting fibres from abrasion and environmental degradation, (c) separating and dispersing fibres within the composite, (d) transferring force to surrounding fibres, and (e) being chemically and thermally compatible with the fibres (ISIS 2003).

The syntheses of various polymer matrices are different. Basically, three types of polymer matrices (epoxy, polyester, and vinylester resins) have been used in FRP production.

Epoxy resin is diglycidyl ether of bisphenol A is produced by the reaction of two moles of epichlorohydrin with one mole of bisphenol A (Figure 2.2). Epichlorohydrin is produced by chlorination of propylene, the resulting allyl chloride being reacted with hypochlorous acid to produce dichlorohydrin, with this being exposed to sodium hydroxide at elevated temperatures to strip off one hydrogen and one chlorine atom. Because of the availability of phenol and acetone and the ease of manufacture, bisphenol A has been the chief dihydric phenol used in epoxy-resin manufacturing. The syntheses of the component for epoxy resin are extensively discussed by Lee and Neville (1957).

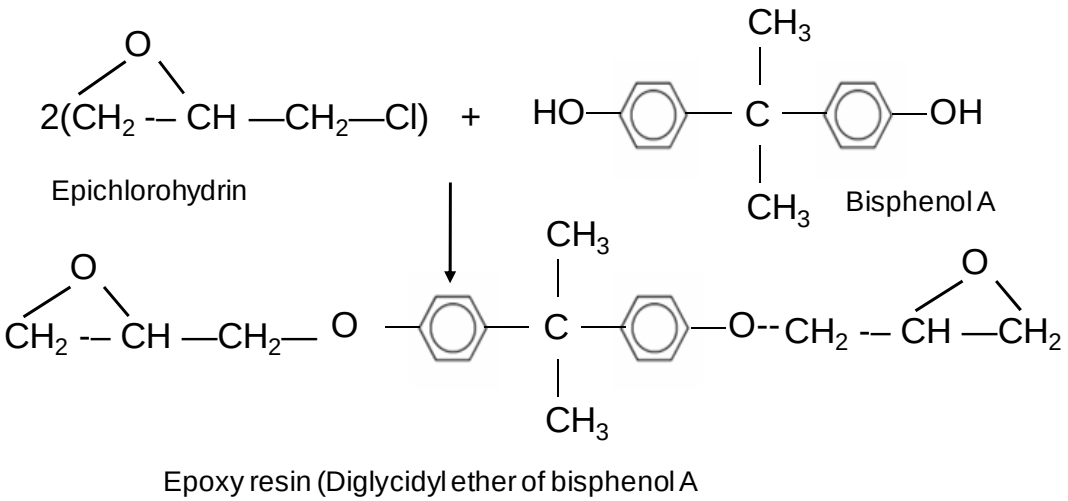

Epoxy resin (Diglycidyl ether of bisphenol A

Figure 2.2. Formation of epoxy resin.

The reaction of maleic anhydride with diethylene glycol is an example of a typical preparation of **unsaturated polyesters** as shown in Figure 2.3 (Irfan 1998). The product is viscous oil with a molecular weight (*g/mol*) in the range 2000-4000.

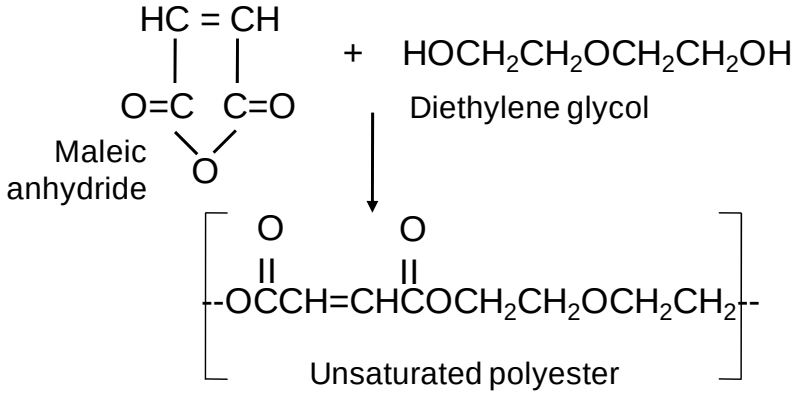

Figure 2.3. Formation of unsaturated polyester.

Basic **vinylester** is produced from diglycidyl ether of bisphenol A (epoxy resin) and methacrylic acid, which can be represented by the Equation shown in Figure 2.4 (Zeske and Goodman 1998).

The carbon-carbon double bonds in the resulting VE ester molecule act as cross-linking sites at the time of curing. Unlike polyester molecules, the carbon-carbon double bonds in vinylester molecules occur only at their ends (Figure 2.4) Thus, in vinylesters, cross-linking can

take place only at the terminal double bonds. Because there are fewer cross-links, a cured vinylester matrix tends to be more flexible and resistant to microcrack formation than a cured polyester matrix (Mallick and Newman 1990). An ingredient essential for the cross-linking of either polyester or vinylester resin is a reactive monomer, such as styrene, which also contains carbon- carbon double bonds in its molecules. This reactive monomer acts as a diluent for the un-reacted resin to co-react with other resin molecules by developing cross-links (Mallick and Newman 1990).

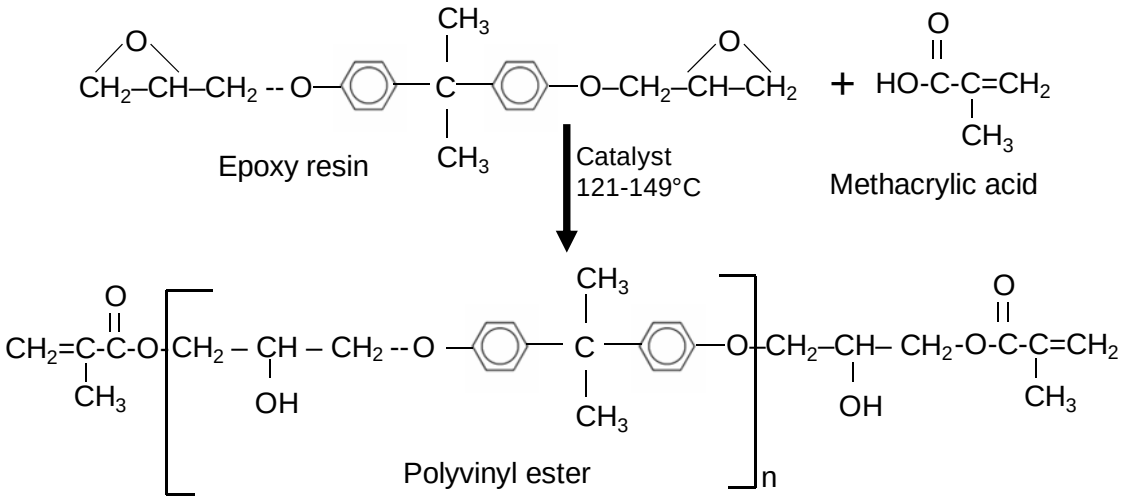

Figure 2.4. Formation of vinylester.

Vinylester offers unique benefits over polyesters. The benefits include (i) excellent reactivity due to terminal vinyl unsaturation, (ii) increased hydrolysis resistance, (iii) fewer (35 to 50%) hydrolysis prone ester linkages, (iv) better wetting and bonding to glass reinforcements, and (v) improved elongation and toughness conferred by the epoxy resin backbone (Zeske and Goodman 1998).

2.2.2. Fibres

Fibres in FRP composites provide the strength and stiffness. The composites are much stronger and stiffer in the fibre direction. Fibres generally contribute high stiffness and high ultimate strength to the FRP composites.

Among three fibres - glass, carbon, and aramid – used in FRP manufacturing, glass fibre is the most inexpensive, and consequently the most widely used fibre in structural applications. E-glass, S-2 glass, and quartz are the three most common glass fibres used. Each kind of glass fibre possesses special characteristics, which lead them to use in specific applications. For example, E-glass shows a good combination of tensile strength (3447 MPa) and modulus (75.84 GPa); S-2 glass retains a greater percentage of its strength at elevated temperatures; and Quartz is a low dielectric fibre used primarily in electrical applications (Campbell 2004). The physical and chemical properties of some of the important fibres are given in Table 2.1.

Table 2.1. Physical and chemical properties of some fibres.

Type of fibre	Tensile strength (MPa)	Tensile modulus (GPa)	Elongation at failure (%)	Density (g/cm^3)	Coefficient of thermal expansion (10^{-6} °C)	Fibre diameter (μm)
E-glass	3447	75.84	4.7	2.58	4.9-6.0	5-20
S-glass	4482	86.87	5.6	2.48	2.9	5-10
Quartz	3378	68.95	5.0	2.15	0.5	9

Source: Campbell 2004

The most common and least expensive glass fibre is E-glass, which is widely used in structural applications. The composition of various E-glasses is shown in Table 2.2. Multiple oxides (Al_2O_3, B_2O_3) are added in order to improve the chemical resistance as well as mechanical, thermal, and optical properties. E-glass has an excellent resistance to acids, whereas it is vulnerable to basic media (pH > 9.0) (Barkatt 2001).

Table 2.2. Chemical composition of various E-glasses (Wallenberger et al. 2001)

Fibre	SiO_2	B_2O_3	Al_2O_3	CaO	MgO	ZnO	TiO_2	Zr_2O_3	Na_2O	Fe_2O_3
Boron-containing E-glass	52-56	4-6	12-15	21-23	0.2-4	-	0.2-0.5	-	0-1	0.2-0.5
Boron-free E-glass	59.0	-	12.1	22.6	3.4	-	1.5	0.9	-	0.2

The composition of FRP bars depends on their applications. Although the strength of FRP bars is controlled by the quality and quantity of fibres, the fibre volume fraction (V_f) is to be optimized to achieve the best strength properties and to maintain reasonable production costs. In order to improve the quality of FRP bars the required ingredients are added by the manufactures. The compositions of a few FRP composites are shown in Table 2.3.

Table 2.3. Composition of FRP bars.

Items	Fibre	Resin	Fillers	Other ingredients	Manufacturing process	References
Rods (Aligned fibre composites Inc., Chatfield, Minnesota)	62% 113 yield roving of fibre	Vinylester and styrene	Filler-6% ASP 400	Catalyst Trigonox 121-BB75 TBP	Pultrusion	Bank et al. 1998
FRP rods	55%	Vinyl resin	-	-	-	Katsuki and Uomoto 1995
Glass fibre rebars	45% E-glass fibre	53% Epoxy/ polyester resin	Crushed rubber	Gel coat, honey wax, and mould releasing agent	Hand lay-up	Kamal et al. 2006
Series E-bar	70% E-glass	30% lsophthalic resin	Calcium carbonate	Catalyst	Pultrusion	Tillco 2006
Series C Rebar	70% 113 Yield fibreglass roving	30% vinylester resin	Calcium carbonate	Catalyst	Pultrusion	Tillco 2006

Besides, the two basic ingredients in FRP composites, minor elements also contribute to their properties. Therefore, the minor elements used in manufacturing composite and their effects on improving the desired qualities are discussed in the following section.

2.2.3. Minor ingredients of composites

Even though the basic components of FRPs are polymer matrix and fibres, which are responsible for the structural properties of FRP rebars in concrete construction, there are several minor ingredients, which are also important to maintain the appropriate quality in the field applications. For example, antioxidants can be used to prevent degradation, exposure to high temperature and UV light. The following section will discuss the minor ingredients and their functions to improve the required properties of FRP composites.

Antioxidants: Antioxidants interfere with the oxidative cycles to inhibit or retard the oxidative degradation in matrix. They are often added to prevent degradation during processing, exposure to high temperatures, exposure to UV light, and to deactivate or retard the metal catalyzed oxidation of polymers.

Coupling agents: Chemicals that improve the adhesion between two phases and are often used in composites are coupling agents. Organosilanes are perhaps the most important coupling agents, often used to improve the strength of interphases (Grossman 2001).

Diluents: It is used to lower the viscosity of the resin, increase pot life (working life), reduce surface tension, and improve wetting. They are often used in epoxy resins. Epoxy resins can contain reactive diluents which are incorporated into the matrix and can decrease mechanical properties. Non-reactive diluents contain no reactive groups and function primarily as viscosity modifiers and plasticizers. The first requirement of such modifiers is that they must be miscible in the resin. Pine oil, dibutyl phthalate and glycol ethers have been used carefully as diluents because of their adverse effects on the cured resin properties.

Fillers: Advantages of fillers are many-fold. Besides reducing cost of epoxy resin, they offer better mechanical properties, fire and smoke reduction, dimensional stability, water and weather resistance and surface smoothness. The types, functions, composition and processability of fillers are well described in Mathur and Venderheid (2001) and ACMA (2004). A few examples of inorganic fillers are calcium carbonate, kaolin, alumina trihydrate, calcium sulphate, mica, feldspar, wollastonite, silica, talc, etc.

Internal release agents: These are often used in moulding compounds. Mould release agents are substances that help separate the cured part from tools. Examples of internal release agents include zinc and aluminum stearate, which are used in low temperature moulding (Murphy 1998).

Flame retardants: Flame retardants are additives impede the combustion process of composites. Organohalides scavenge the free radicals, which are responsible for the combustion of polymer. Antimony trioxide is often added to increase the efficiency of the organohalide additives (Green 2001; ACMA 2004).

2.3. Sizing in composites

2.3.1. Introduction

Sizing of glass fibres is the most important factor in maintaining properties in both fibre and composites. Although only a small amount of sizing is added during fibre manufacturing, it contributes significantly to the overall performance of an FRP composite. Sizing is proprietary to individual manufacturers, so its composition, functions, and mechanisms are hardly known. This section discusses the significance of sizing on composite properties, the composition of sizing, the functions of sizing components, and the factors related to choosing a sizing.

2.3.2. What is sizing

Size(s): Materials used on the surface of the fibres during fabrication to control fibre characteristics are called sizes. Sizes include starch, gelatine, oil, wax or other suitable ingredients applied to fibres. Generally, size is not a single material, rather a complex mixture of several chemicals. Each chemical performs very specific tasks. Composition of sizes and their specific function is discussed in sections 2.3.4.

Sizing: "A process of applying a material on a surface in order to fill pores and thus reduce the absorption of the subsequently applied adhesive or coating or to otherwise modify the surface properties of the substrate to improve the adhesion, and also the material used for this purpose" (ASM 1995).

Sizing is a process of applying sizes on fibres. In various studies, these two terms are used interchangeably. In this thesis, sizing is used for both the material and the process.

2.3.3. Significance of sizing in composites

Sizing in glass fibres is an essential factor in the composite industry as it enhances composite properties by protecting fibres during processing. During fibre manufacturing, it passes through complex and hostile environments, such as corrosive environment, temperature change, mechanical frictions, which might have severe damage on fibres if sizing is not used. As a result, without sizing fibres cannot be produced. In composite properties, sizing plays a significant role. Mechanical properties, such as tensile and flexural strength, are greatly improved by adding specific sizing on fibres. The effect of coupling agent, the active ingredient of sizing, on the flexural strength of glass fibre-resin composites are shown in Figure 2.5 (Marsden 1990).

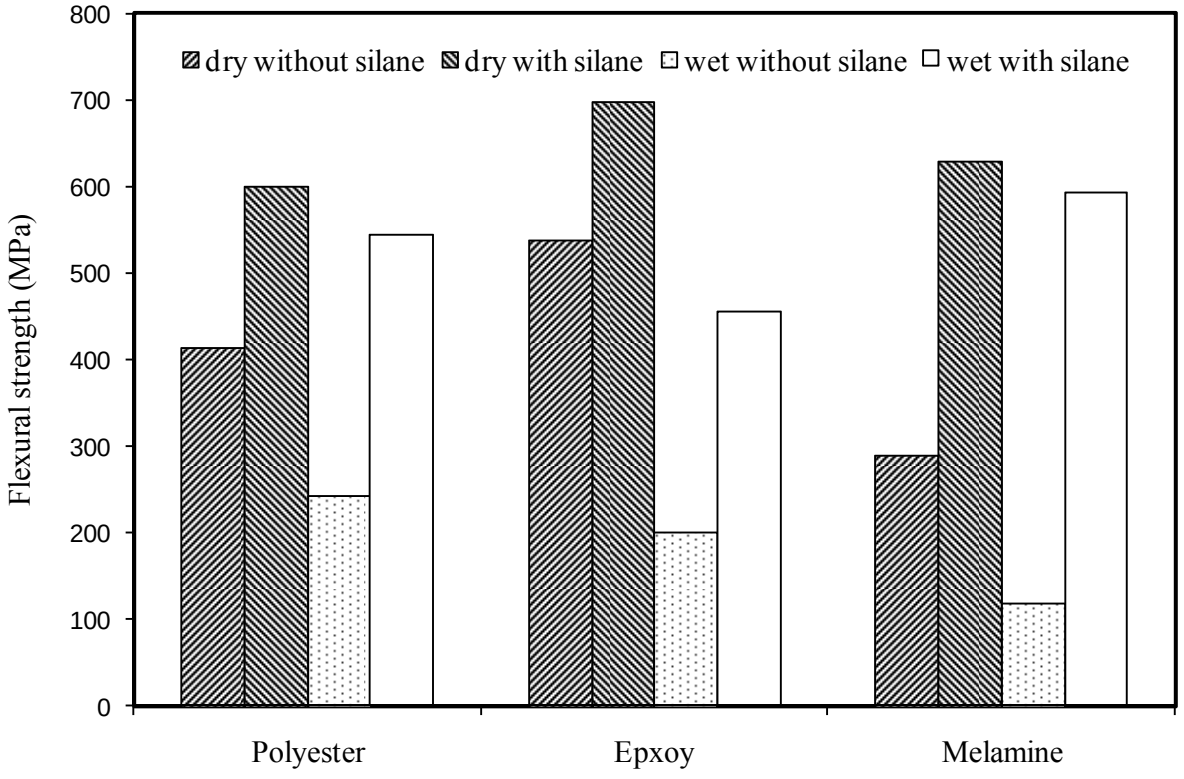

Figure 2.5. Effect of coupling agents on the flexural strength of glass fibre-resin composites.

2.3.4. Composition of sizing and function of components

The overall strength of FRP rebars depends on the effective adhesion of fibres with the matrix. Several minor components called sizing, about 2% by volume of rebar, do this task. Sizing composition is proprietary to glass fibre manufacturers. It is so mysterious even the manufacturers only use numeric (no trade name) for a specific sizing, as shown in Table 2.4.

Sizing varies with manufacturers. However, researchers (Strong 2008; Juska and Puckett 1997; Bascom, 1998) have taken initiative to describe the composition of sizing and the function of sizing components as shown in Table 2.5.

Table 2.4. Sizing of glass fibres and their manufacturers in US.

Sizing	Application/product	Resin compatibility	Manufacturers
2011	Direct draw	Polyester and Vinylester	PPG industries roving and strand sizes
555	Pultrusion	Polyester and Vinylester	Schuler International Glass fibre sizes
591	Pultrusion and Filament winding	Polyester, Vinylester, and Anhydride cure epoxy	Schuler International Glass fibre sizes
700	Filament winding, Weaving, Knitting	Polyester, Vinylester, and Epoxy	Fibreglass industries Glass fibre sizes
317	Filament winding, Weaving and Knitting	Polyester, Vinylester, and Epoxy	Fibreglass industries Glass fibre sizes
366 and 424	Roving	-	Owens corning fibreglass roving and strand sizes

Source: Juska and Puckett 1997

Table 2.5. Composition of a typical sizing and component functions.

Component	Percent	Function
Film former	10	Holds filaments together and protect fibres
Lubricant	0.75	Prevent mechanical damage during fibre production
Coupling agent	0.75	Develops matrix-reinforcement bond
Wetting agent	0.30	Improves adhesion between reinforcement and matrix
Antistatic agent	0.10	Dissipates static charge produce during fibre fabrication
Solvent/Materials carrier	88	Facilitates size application

Source: Juska and Puckett 1997

Film former/Binder: Film former forms films on fibres. It works in two ways (i) it maintains fibre integrity by protecting single filaments from corrosive environments, and (ii) it binds individual filaments in a bundle. Film formers should be compatible with resin, i.e. chemically similar to the matrix. Together with the lubricant, the film former protects the fibre from mechanical damage during processing and storing. There are both natural and anthropogenic source of film formers. Starch materials are the natural sources of film formers. Nowadays, anthropogenic sources of film formers, such as acrylics, epoxies, polyesters, polystyrene, vinyl acetate, and urethanes are widely used.

Lubricant: During fabrication, glass fibres pass through various polls, dies and rollers, which might create mechanical damage on fibres through surface cracks and abrasion. This damage lowers the tensile strength and promulgates corrosion. Lubricants facilitate the passage of fibres in the processing equipment. The most common lubricants used in sizing are modified fatty acids, polymers (low molecular weight polyethylene and polyethylene glycol), mineral oils, and cationic amines.

Coupling agent: The main purpose of using a coupling agent is to bind two highly dissimilar materials – the glass fibres (highly hydrophilic) and matrix resin (highly hydrophobic). An alkoxy silane compound is widely used as a coupling agent in sizing, because of its difuctional groups. Silane coupling agent has a silicon end that bonds well to glass fibre and an opposing organic end that bonds well to resins. Because of its importance in interphase bonding, coupling agents are elaborately discussed in Section 2.3.5.

Wetting agent: It helps the matrix to properly wet the surface of glass fibres. Common wetting agents include soaps, detergents, and surfactants.

Antistatic agent: Static charge is built up over the non-conducting glass fibre during its manufacturing where fibers are typically processed at high speeds around 100 mph. Fibre processing undergoes with a high speed of 100 mph. In order to dissipate that charge, an antistatic agent is used. Inorganic salts (LiCl or $MgCl_2$) and quaternary ammonium salts are used as antistatic agents.

Solvent/Materials carrier: Water is a Ideal solvent used as a carrier for a sizing. Generally, a sizing does not dissolve in water. Therefore, water is used in sizing as the component carrier. Water provides several advantages over organic solvents as the carrier. Water produces a layer over fibres due its low viscosity ($2x10^{-3}$ Pa.s) even after mixing with sizing components. Moreover, it is environmentally friendly and user safe.

2.3.5. Coupling agents in fibre sizing

Coupling agent (adhesion promoter) is a chemical substance capable of reacting with both reinforcement and matrix in composite materials. Its role as an adhesion promoter is versatile including

- Develop strong interphasial bonds between fibre and resin
- Remove adsorbed water from the surface of glass fibres
- Create a hydrophobic surface for effective wetting of matrix

Types Many coupling agents are available for diverse applications. However, coupling agents used for glass fibre reinforcement are basically organo-silanes. Table 2.6 shows the examples of coupling agents and their chemical formulas.

Table 2.6. Coupling agents for glass fibre-resin adhesion.

Coupling agent	Chemical formula
Vinyl	$CH_2=CHSi(OCH_3)_3$
Epoxy	$CH_2\underset{\backslash\ /}{\overset{O}{}}CHCH_2OCH_2CH_2CH_2Si(OCH_3)_3$
Methacrylate	$CH_2=\overset{\overset{CH_3}{\vert}}{C}-COOCH_2CH_2CH_2Si(OCH_3)_3$
Primary amine	$H_2NCH_2CH_2CH_2Si(OCH_3)_3$
Diamine	$H_2NCH_2CH_2\,NHCH_2CH_2CH_2Si(OCH_3)_3$
Mercapto	$HSCH_2CH_2CH_2Si(OCH_3)_3$
Titanate	$[CH_2=C(CH_3)\text{-}COO)_3]TiOCH(CH_3)_2$

Source: Jones 1994

Manufactures generally do not disclose the names coupling agents they use as sizing for glass fibres. The following three coupling agents generally used in sizing. Their trade name, chemical name and manufacturer are listed here

Trade name	**Chemical name**	**Manufacturer**
Z6030	3-methacryloxypropyltrimethoxysilane	Dow Corning
Z6040	3-methacryloxypropyltrimethoxysilane	Dow Corning
A1100	γ-aminopropyltriethoxysilane	Union Carbide

Silanes are generally expressed by the following structures, where $R^{/}$ is the organic part of silane which must be compatible (bonds) to resin, and R is either a methyl or ethyl group.

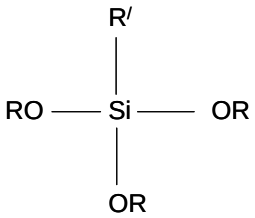

General structure of silanes

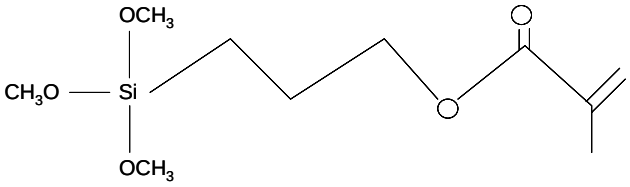

Z-6030 (3-methacryloxypropyltrimethoxysilane)

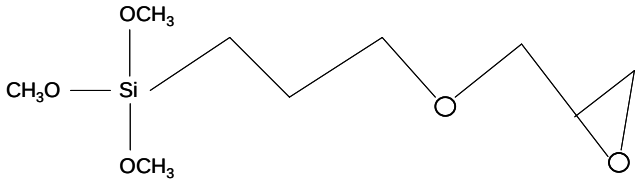

Z6040 (3-methacryloxypropyltrimethoxysilane)

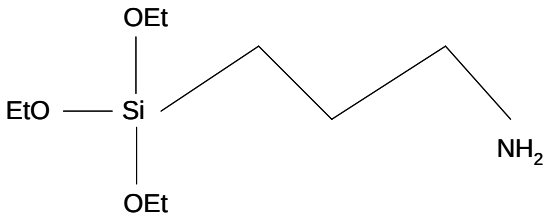

A1100 (γ-aminopropyltriethoxysilane)

The general concept of adhesion at the interphase is that the coupling agent, with a higher degree of cross-linking, will have stronger fibre-matrix bonding. However, this concept was proved invalid for a composite of E-glass fibre-epoxy systems by Iglesias et al. (2002). They concluded that a linear chained coupling agent showed higher mechanical strength than the branched one. Silane coupling agents used included 3-aminopropyl-dimethylethoxysilane (APMES), 3-aminopropyl-methyldiethoxysilane (APDES) and 3-aminopropyl-triethoxysilane (APTES). A schematic representation of the structures with the three salines is shown in Figure 2.6 (Iglesias et al. 2002).

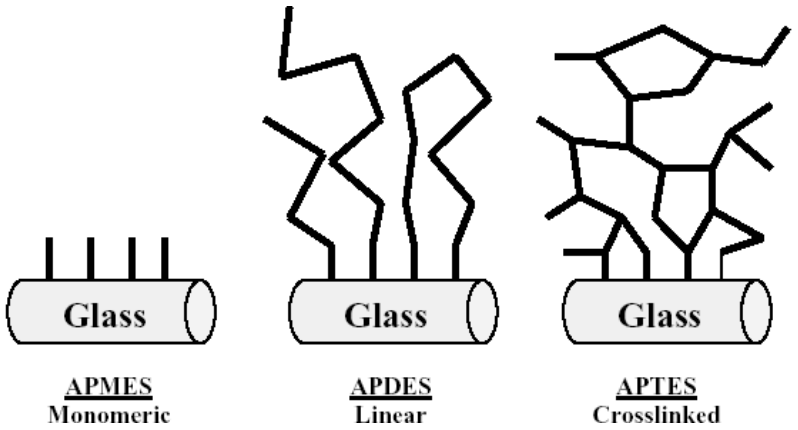

Figure 2.6. A schematic structure of silanes with glass-fibres.

APMES showed higher Young's modulus (5 times) than APTES. This is due to the hydrolytic impact (damage occurs due to the effects of water) on silanes at the fibre-matrix interphase. The higher degree of cross-linking of silanes at the interphase leads to a greater hydrolytic damage.

2.3.6. Factors of choosing a sizing

Choosing a glass fibre sizing for a particular fibre-matrix system depends on several factors, such as resin compatibility, process compatibility, environmental resistance, and reinforcement length. Any sizing that satisfies one factor but not others is not an effective sizing for that particular fibre-matrix system. Therefore, a perfect sizing for glass fibres should satisfy all factors discussed below

Resin Compatibility Generally, sizing has to be chemically compatible with the resin. The coupling agent in sizing reacts with both fibre and resin to promote adhesion between the two of them. For example, the organic end of the organo alkoxy silane is chosen for reacting with a particular resin and the silicon end to react with fibre. If the organic end is not compatible with the resin, it adversely impacts the mechanical properties of the composite. A sizing can be formulated for a particular resin system or several resin systems. For the former case, the greatest fibre resin performance is obtainable, while for the latter case the lower performance is achieved. For example, a sizing designed specifically for a polypropylene matrix might produce 200 percent better mechanical properties than a fibre sized for nylon (Mason 2006).

Process Compatibility The fabrication process is the second most important factor for choosing a sizing for glass fibres. Chemical reactions occur during fabrication among sizing, glass fibres and resin. They are time and temperature dependent. However, all fabrication processes are not favored by similar reaction environments. For example, the reactions in pultrusion require relatively high temperature and rapid processing rate; while the reactions in vacuum-assisted resin transfer moulding (VARTM) need relatively low temperature and a slow processing rate.

Environmental resistance Environmental resistance is another important factor in choosing a sizing. Composites might be applied/used in harsh environmental conditions. For example, FRP rods in concrete constructionsrequire alkali resistant sizing because the concrete environment is highly alkaline.

Length of Reinforcement Based on the length of reinforcement in composites, sizing formulation would be different. Sizing for strand fibres used as continuous reinforcement in FRP rods would be different from sizing for chopped fibres used as dispersed reinforcement in a sheet moulding compound (SMC). For the former case a softer sizing is formulated so that a fibre can maintain its integrity before resin application, whereas for the later case a stiffer sizing is formulated to disperse rapidly.

2.4. Interphase/interface bonds in FRP composites

The properties of composites depend on the effectiveness of an interface/interphase between fibres and a matrix. Applied stress in a FRP bar is transferred from fibres to matrix through the interface/interphase. A better interfacial/interphasial (fibre-matrix) bond provides better inter laminar shear strength, and higher resistance against debonding, fatigue, and corrosion. Therefore, a thorough understanding of the interphase and interface, and theories of adhesion at the interface/interphase, is required to explain the bonding mechanisms of fibre-matrix interface/interphase in FRP composites.

2.4.1. Interface vs. interphase

"An interface is a two dimensional border separating distinct phases, e.g., fibre, matrix, interphase, coating, etc." (Swain et al. 1990). An interphase is the region where fibre and matrix

are either chemically or mechanically bonded. Several phenomena, such as diffusion, nucleation, and chemical reactions, occur at the interphase (Jang 1994). The difference between an interphase and an interface is schematically shown in Figure 2.7 (Jang 1994; Swain et al. 1990).

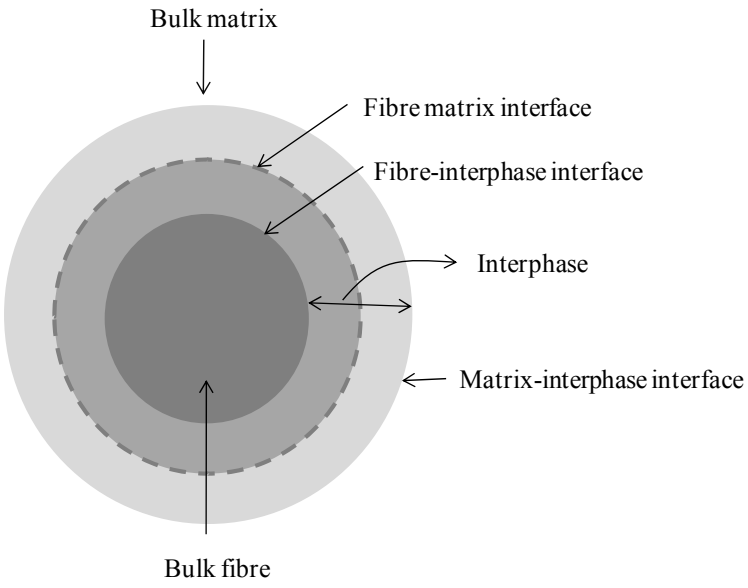

Figure 2.7. A schematic presentation of interface and interphase in a fibre-matrix composite (Jang 1994; Swain et al. 1990).

2.4.2. Adhesion theories in composites

Several theories have been proposed in order to describe the phenomena of adhesion. No single theory describes the complete scenario of adhesion. Some theories are applicable to certain substances and applications, while others are more appropriate to other circumstances. Petrie (2007) includes the following theories to describe the adhesion phenomena

Adsorption and Wetting This theory states adhesion results from molecular contact between two materials. Due to the molecular level interaction between adhesive and substrate in a composite, a bond will be developed due to the van der Waals force. Wetting is the close contact between a fluid and a rigid surface resulting from intermolecular interactions. Better wetting allows sizing to adhere on substrate surface properly. The higher the bubble contact angle, the

weaker the wetting (Figure 2.8). If the sizing develops a bubble on substrate surface like A, it produces a poor wetting, i.e. poor adhesion. Conversely, if the sizing produces a bubble like C, it produces a stronger wetting, i.e., a good adhesion.

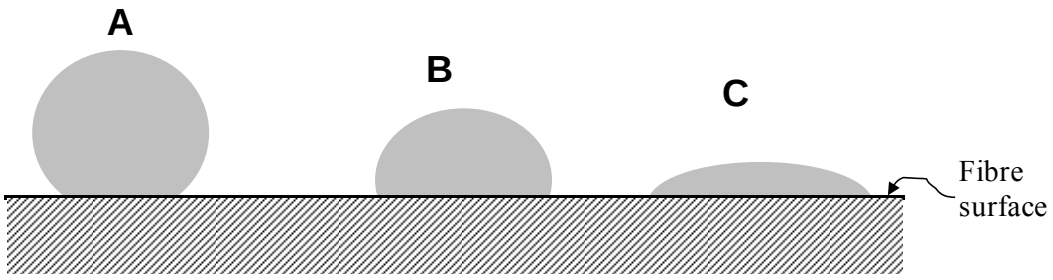

Figure 2.8. Wetting of sizing on the surface of fibres. 'A' shows a sizing with very little wetting but a high contact angle, while 'C' shows a sizing with some wetting but small contact angle.

Adsorption and wetting of sizing on he glass fibre surface of an FRP rebar is a critical phenomenon to describe adhesion. The better the wetting of sizing on the fibre surface, the stronger will be the bond strength.

Mechanical interlocking theory This theory simply results from the mechanical interlocking between two surfaces of adhesive and substrate. Voids and pores on rough surfaces allow stronger mechanical interlocking than plane surfaces. For example, because of its small molecular size, polyurethane can easily penetrate through the voids of polymer, leather and wood surfaces and strongly adhere on their surfaces by mechanical interlocking.

Electrostatic theory An electrical double layer is formed at the interphase of adhesive and substrate. That layer developed from permanent dipoles. Such interactions are operational over less than a 5 *nm* distance. The electrostatic contribution is very little in adhesion in comparison to van der Waals forces. In this theory, the interphase is considered as a capacitor plate, where the energy of adhesion is equal to the energy of separation of both plates. The energy of adhesion/separation in an electrostatic theory is expressed by Equation 2.1. A schematic of an electrical double layer is shown in Figure 2.9 (Petrie 2007). The evidence of this theory arises when an adhesive bond is destroyed and observed in biological cell adhesion.

$$W_A = \delta^2 h / \varepsilon \quad (2.1)$$

where,

W_A : energy of adhesion, J/m^2

δ : surface charge density, $coulomb/m^2$

h : distance between two charged plates (μm), and

ε :dielectric constant.

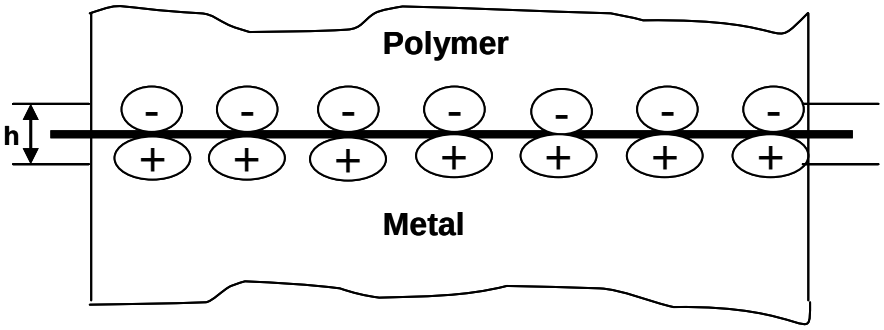

Figure 2.9. A schematic diagram of an electrical double layer.

Diffusion theory The concept of this theory is that the adhesion arises through the inter diffusion of molecules from one material to another. To diffuse, the adhesive and adherent must be chemically compatible in terms of miscibility, i.e. both materials have to be polymeric. Dissimilar polymers are usually incompatible because of their long chain nature and low diffusion coefficient. The chance of smaller size adhesive molecules to diffuse into the substrate is higher and, therefore, the probability of creating interlocking is larger. A schematic of diffusion theory is shown in Figure 2.10.

Chemical bonding theory When two chemical materials containing reactive functional group come close at an interphase of two different surfaces, chemical bonds will be formed. The bonds can be any one of ionic, covalent or hydrogen bonding, depends on the attached functional groups at the interphase. For example, the coupling agent in sizing is compatible to both fibre and matrix. The widely accepted coupling agent is organosilane that has two reactive ends a

silicon end and a long chain polymeric end. The chemically reactive silicon end develops acovalent bonding network with the silanol functional group of glass fibre surface.

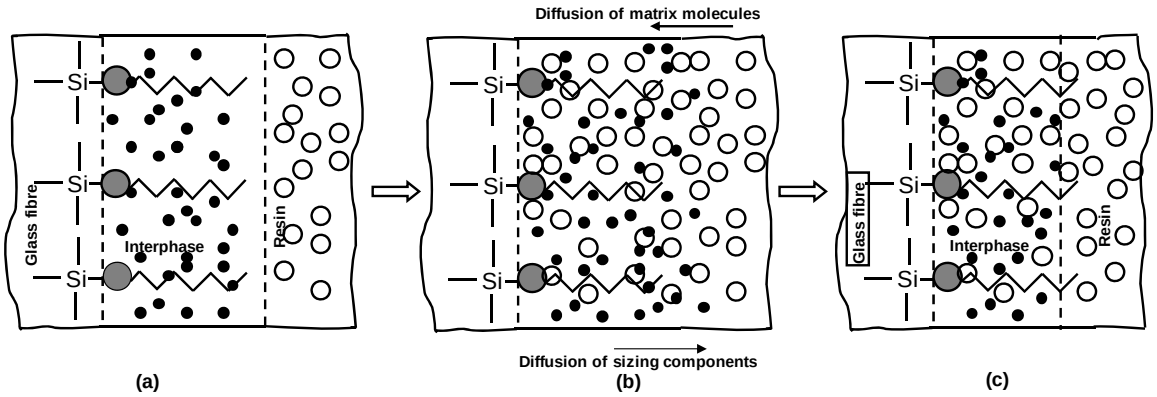

Silane coupling agent, O resin, and ● elements of sizing, such as film former, antistatic agent, lubricant, etc.

Figure 2.10. A schematic presentation of diffusion at a fibre matrix interphase (a) initial stage of diffusion at the fibre-resin interphase, (b) during curing diffusion of both resin and sizing molecules observed, and (c) diffusion completed.

Weak boundary layer theory Generally, an adhesion failure is due to the plasticization of ductile materials at the interphase or the cohesive failure of a weak boundary layer. This layer can be originated from the adhesive, the adherent, and the environment or combination of any of the three. The weak boundary layer can develop any time during adhesive application, curing and service life. Causes of developing this layer are many, such as (i) a low molecular weight polymer (polyethylene) develops a weak boundary layer under stress while it is used either as an adhesive or as a substrate, (ii) weakly bonded oxides, such as, copper oxide at interphase impairs joint strength, (iii) reaction by-products or corrosion products can be developed during ageing and produce this kind of layer, and (iv) diffusion of environmental moisture either by adhesive or adherent. The theories of adhesion, their mechanisms, bond types, and applications are summarized in Table 2.7.

Table 2.7. A comparison of adhesion theories, their mechanisms, bond types and applications

Adhesion theories	How it works	Force/bond type	Applications
Adsorption and Wetting	• The molecular level contact between adhesive and substrate develops van der Waals force, which is the driving force for this type of adhesion. • The higher the contact angle of adhesive over substrate, the poorer will be the adhesion. • Absence of air bubble and gap between adhesive and substrate creates better wetting.	• van der Waals force	• Epoxy resin develops better adhesion with steel than polyethylene or Polytetrafluoro-ethylene (Teflon).
Mechanical	• Works better on rough surfaces with pits and cavities • Surface roughness increases mechanical bonding	• Mechanical interlocking	• Polyurethane adhesive on leather wood on other substrates
Electrostatic	• Electrical double layer with opposite charge at the interphase of two surfaces developed bonds.	• Electrostatic/ dispersive force	• Biological cell adhesion • Adhesion to filler media
Diffusion	• Inter diffusion of molecules from one material to another.	• Concentration gradient	• Usually in thermoplastics
Chemical bonding	• Chemical bonding developed between adhesive and substrate.	• Chemical interaction	• Adhesion of glass fibre and silane
Weak boundary layer	• Develops during application and curing of adhesive on substrate	• Untreated substrate surface, corrosion/ reaction products, and ageing affect accelerate debonding at the interphase.	• Adhesive on titanium surface. It may contain contaminate (e.g., water) which may create weak bonding.

2.5. Diffusion of species

2.5.1. Overview

Diffusion is a process of moving chemical species due to its concentration gradient in a system. Based on the involvement of species, diffusion is classified as multi-component, binary, and self diffusion.

Multi-component diffusion involves more than two different chemical species in a diffusion process, while binary diffusion involves two different chemical species. The chemical species in multi-component diffusion are designated as lower-case Greek letters *α, β, γ...*whereas, the chemical species for a binary diffusion are designated as capital italic letters *A* and *B*. The diffusion of identical chemical species is termed as self diffusion, denoted as *A**, which is different from *A*.

Diffusivity of particular chemical species in one system is different from other systems. For example, the diffusivity of H_2 in a H_2-N_2 (0.674×10^{-4} m^2/s) system is much higher than that in H_2-SiO_2 ($0.6\text{-}2.1 \times 10^{-12}$ m^2/s) system. Chemical species diffuse faster in a gas system than a solid system. Typical orders of magnitudes of diffusivity or diffusion coefficient of gases, liquids, and solids are as follows Gas>Liquid>Solid. The diffusion coefficients of different systems are approximately10^{-5} m^2/s for gasses, 10^{-9} m^2/s for liquids, and 10^{-10} to 10^{-14} m^2/s for solids (Tosun 2007; Bird et al. 2007).

2.5.2. Fick's Laws

Diffusion has two fundamental properties it is random in nature and transport occurs from high to low concentrations. If a system is in equilibrium (steady state), the diffusive flux is proportional to the concentration gradient according to Fick's First Law, expressed in Equation 2.2.

$$J = -D\frac{dC}{dx} \tag{2.2}$$

where,

J flux, $kg/m^2\text{-}s$

D diffusion coefficient, m^2/s

C concentration of diffusing species, kg/m^3

dC/dx concentration gradient,

'-' indicates diffusion direction from high to low concentration.

If a system is not in equilibrium (non-steady state) the rate of change of concentration depends on both time and position according to Fick's Second Law, expressed in Equation 2.3.

$$\frac{\partial C}{\partial t} = D\frac{d^2C}{dx^2} \tag{2.3}$$

where,

C concentration of diffusing species, kg/m^3

D diffusion coefficient, m^2/s

$\frac{\partial C}{\partial x}$ concentration gradient

$\frac{\partial}{\partial t}, \frac{\partial^2}{\partial x^2}$ the rate of change of concentration in terms of both position and time

Fick's laws are used for modeling transport phenomena.

2.6. Degradation of FRP

Degradation of FRP depends on exposing them in harsh environmental conditions, such as highly alkaline solutions, elevated temperature, mechanical stresses, etc. Degradation mechanisms of FRP are not yet clear to researchers due to the complex nature of polymer composites and their interactions with surrounding environments. However, several researchers (Bayrs et al. 2003; Barkatt 2001) reviewed the degradation mechanisms of FRP. From their study, it is evident that the degradation starts at the fibre matrix interphase. To address the deterioration mechanism at the fibre-matrix interphase of FRP composites, the degradation mechanisms of polymer matrix, fibre and interphase are discussed in this context.

2.6.1 Degradation of polymer matrix

Durability of FRP materials essentially depends on the polymer quality (Katsuki and Uomoto 1995); therefore, a study of resin systems is indispensable for the durability the FRP. The polymer matrix is responsible for both the load transfer from one fibre to another and protecting

the fibres from environmental effects. In FRP, either polyester or vinylester is used as polymer matrix. Therefore, the general reactions of ester group are discussed in the following sections.

Most esters do not react with water under neutral conditions, but they hydrolyze under acidic and basic conditions (Wade 2003). In acidic conditions, the hydrolysis reaction is reversible (Equation 2.4), whereas in alkaline aqueous solution ester hydrolysis is essentially irreversible (Equation 2.5) (Carey and Sundberg 1990). Wade (2003) has summarized the chemistry of esters.

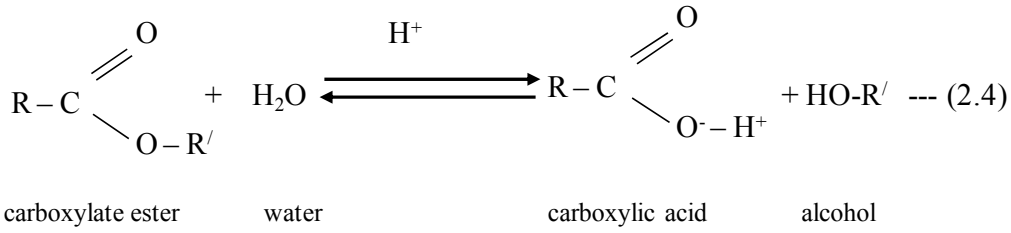

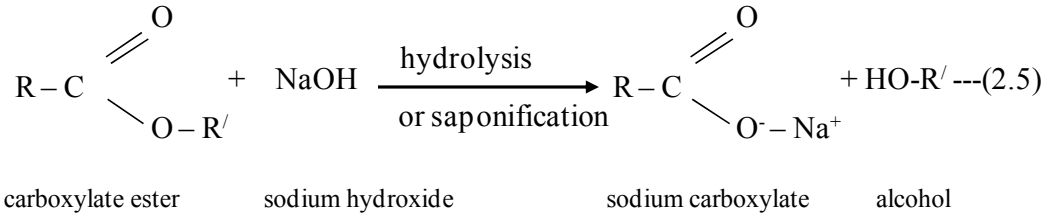

Acid catalyzed hydrolysis of an ester is simply the reverse of the Fischer esterification equilibrium. Addition of excess water drives the equilibrium toward the acid and the alcohol. The mechanisms of ester hydrolysis and saponification are described by Wade (2003) and Carey and Sundberg (1990).

2.6.2. Degradation of fibres

Because of their unique properties, fibres used in FRP are very specific to their applications. A specific fibre possesses special characteristics over others. The glass fibres in GFRP undergo a variety of complex changes, such as physico-chemical processes (leaching and dissolution) and formation of secondary phases. Dissolution of glass fibres in the concrete environment is based on the following types of reactions (Onofrei 2005).

Network dissolution occurs by water [(H_2O, H_3O^+ or OH^-] which diffuses into glass and reacts with Si-O-Si or Si-O-M bonds to form silanol groups. The long-term durability and the mechanisms of fibre-glass degradation are fundamentally controlled (Onofrei 2005) by (i) the composition of the glass and of the leachate solution, (ii) the pH of the leachate, (iii) the temperature, (iv) the flow rate, and (v) the surface-to-volume ratio.

i) Ion-Exchange $n(Si - O^-) - X^n + nH_3O^+ \rightarrow n(Si - OH) + X^n + nH_2O$ (2.6)

ii) Hydrolysis $2Si - O - Na + H_2O \rightarrow 2Si - OH + Na_2O$ (2.7a)

$Si - O - Na + H_2O \rightarrow 2Si - OH + Na^+ + OH^-$ (2.7b)

iii) Network hydrolysis $\equiv Si\text{-}O\text{-}Si \equiv + OH^- \rightarrow \equiv Si\,OH + \equiv Si - O^-$ (2.8a)

$\equiv Si\text{-}O\text{-}Si\equiv + H_2O \rightarrow \equiv Si\text{-}OH + \equiv Si - OH$ (2.8b)

iv) Network dissolution

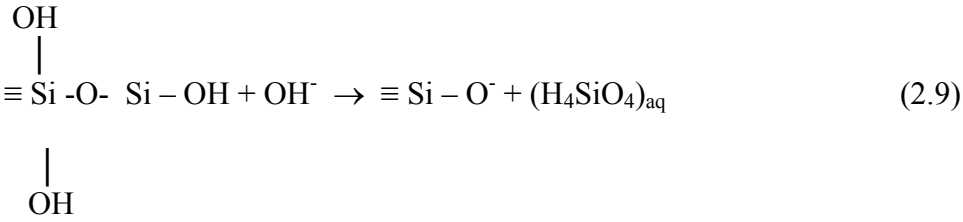

(2.9)

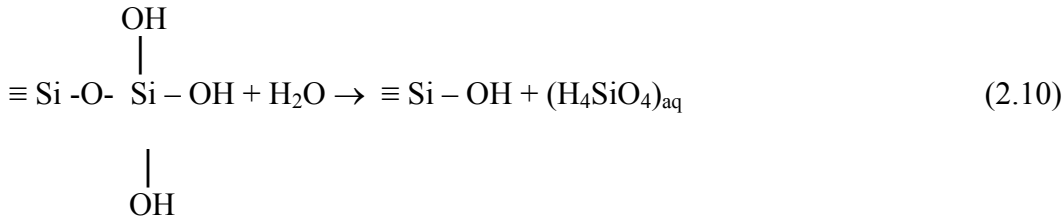

(2.10)

Carbon and aramid fibres have also been used for reinforcement in FRP, but their degradation mechanisms are not cited here, because this research addresses FRP with glass fibres. However, the stepwise degradation mechanisms of glass, carbon, and aramid fibres is explained in the literature (Onofrei 2005; Andrady 2003; Brakatt 2001).

2.6.3 Degradation of an interphase

Fibre-matrix interphase is the most susceptible part in FRP composites in terms of degradation (Barkatt 2001). The degradation propagates in the presence of surface roughness on fibres and insufficient mechanical interlocking between fibres and matrix. Additionally, wetting traps air and gas bubbles at the interphase during composite manufacturing. This accelerates the deterioration mechanisms. Finally, the debonding at the fibre-matrix results in a complete loss of the adhesion. Fibre-matrix bonding is achieved using sizing materials at the fibre-matrix interphase that develops various kinds of bonding from strong covalent bonds to weak van der Waals forces.

Barkatt (2001) explained reasons for debonding at the fibre-matrix interphase. In adverse conditions, initially the secondary bonds (hydrozen bond, Si-OH-O-Si) are broken, then with the severity of exposure environments the covalent bonds are affected. Furthermore, corrosion of fibres is observed at the interphase which results in smoothing of sharp and jagged edges. Moreover, hydrolytic attacks in the presence of stress could to a faster loss in the mechanical properties of composites.

2.7. Effects of exposure environments on the durability of FRP composites

Nowadays, structural designers are no longer concerned with only mechanical properties of the materials they are using but also with the durability of structures and environmental conditions. The durability of structures can significantly change with the exposure environments, such as moisture, alkali, temperature, fire, etc. The durability of FRP in adverse environments is explained by Springer (1988), ISIS (2003), and Searle (2003).

Effects of moisture FRP composites absorb moisture from exposure environments. Usually, the polymer matrix soaks water through diffusion. A fibre-matrix interphase allows the ingress water due to capillary actions. Hence, the ingress of water damages the properties of matrix and fibres (ISIS 2003). The tensile strength of unidirectional composites is unlikely to be affected by water ingress, whereas the compressive and shear strengths, the matrix dominated properties, are likely to be damaged. The general reaction of a polymer matrix with water is described in Section

2.6.1. A comprehensive study of moisture effects on the properties of composites are available in the literature (Kim et al. 2009; Chen et al. 2007; Chu et al. 2005; Mukherjee 2005; Chin et al. 2001; Zhang and Karbhari 1999; Pritchard 1999; Porter and Barnes 1998; GangaRao and Vijay 1997; Sonawala and Spontak 1996; Schutte 1994; Zheng and Morgan 1993; Pritchard and Speake 1987; Apicella et al. 1983; Marom and Broutman 1981).

Effects of alkali The main concern of replacing steel bars by FRP bars is the corrosion resistance. However, the main strength retaining ingredient of FRP bar is glass fibre, which is not free from corrosion unless protected. Concrete environment is highly alkaline (pH 12-13.5) which might have effects on the toughness and strength of FRP bars (ISIS 2003). However, the corrosion kinetics of bare glass fibres are different from protected glass fibres. A recent study has confirmed that the protective layer of the VE matrix around an FRP bar can inhibit the penetration of alkali ions into FRP bars immersed in alkali solutions (Kamal and Boulfiza 2011). The general reactions of glass fibre with alkali solutions are described in Section 2.6.2. The deterioration mechanisms of glass fibres in alkaline environments and subsequent effects on the properties of FRP composites have been discussed in the literature (Chen et al. 2006; Dejke and Tepfers 2001; Murphy et al. 1999; Porter et al. 1997; Katsuki and Uomoto 1995).

Effects of temperature Thermal effects on FRP bars are evident in both high and low temperatures. With the change of FRP exposure temperature, the thermal expansion of FRP components – fibre and matrix - will be different, which will adversely affect the bonding characteristics of fibre-matrix interphase. On the one hand, the service temperature of FRP bars over *Tg* and curing temperature have also negative impact on the mechanical properties. On the other hand, at the cryogenic service temperature, the embrittlement in polymer matrix also reduces the mechanical properties in FRP bars. Moreover, the solution temperatures also aggravate the deterioration mechanisms discussed in the preceding paragraphs. Therefore, the service temperature of FRP bar is still a main concern for the durability of FRP in concrete. A further detail of thermal effects on FRP bars is discussed in the literature (Davalos et al. 2008; El-Badry et al. 2000; Green 2001; Miyano et al. 1999; Gomez and Casto 1996; Karbhari and Engineer 1996; Lord and Dutta 1988; Dutta 1988).

Effects of fire Fire is another important factor to consider for FRP in its service life. The polymer matrix in FRP is more susceptible to fire than fibres due its combustion and softening natures with rising temperature. The matrix creates large amounts of dense, black, and toxic smokes. Therefore, an indoor fire incident is much more severe than an outdoor one. When the temperature exceeds the *Tg* of the polymer matrix, FRP starts losing its Young's modulus. Below *Tg*, the modulus loss is reversible, but becomes irreversible above it. The glass transition temperature is around 130 °C for a VE matrix. Nowadays, FRP can be protected by using fire insulation, matrix additives, ceramic paints, etc. (ISIS 2003; Green 2001). A decent body of knowledge exists today about the performance of various fire protection systems for FRP composites (NRC-CNRC 2010; William et al. 2008; NRC-CNRC 2008).

Effects of Ultraviolet (UV) radiations UV radiation can degrade FRP materials. The energy of UV radiations (300-12,000 kJ/mol) is capable of breaking the covalent bonds of the polymer matrix as most organic compounds have covalent bond energies of 150-950 kJ/mol. Though only the top few microns of FRP bar is affected by UV radiation (photo degradation), the mechanical strength has been found to be reduced. Other factors, such as temperature, moisture, freeze-thaw cycles, and environmental factors also accelerate the effects of UV radiation on FRP composites. A UV resistant paint is recommended to use for FRP composites (ISIS 2003).

CHAPTER THREE
EXPERIMENTAL PROGRAMME

3.1. Overview

An experimental programme was initially set to observe the interaction of GFRP rebars in simulated concrete solutions (Phase 1). The outcome of Phase 1 stimulated the study of the effects of sizing on the properties of GFRP composites (Phase 2). Finally, the results of Phase 2 guided the research to consider the effects of RH on GFRP rebars in Phase 3. Components of the experimental programme included the sample design, experimental setting, image analysis, data recording and analysis. A detailed description of the sample preparation, experimental settings, and analytical methods of each phase is presented in this Chapter.

3.2. GFRP rebars used for this study

GFRP rebars with various nominal diameters (6, 8, 9, 10, 13, 14, 16, 19, 22, 29, 32 mm) are available in the market. The manufacturers of the rebars used for the current study are not disclosed here for reasons of confidentiality. In this study, GFRP rebars with three nominal diameters, as shown in Figure 3.1 were used for practical reasons described below.

A medium sized GFRP rebar with the diameter of 10 mm (Fig. 3.1b) was used for the accelerated ageing test in Phase 1 to assess the potential penetration of any harmful chemical species into the rebars and subsequent deteriorating effects on the constituents of the rebar. A smaller diameter rebar would have been affected faster than a larger diameter rebar which would have taken a longer period of time to show any signs of distress induced by the accelerated ageing conditions.

GFRP rebars with the smallest nominal diameter (8 mm) were used to observe the effects of relative humidity (RH) on mass gain in Phase 3. Prior to hanging the rebars into the different RH chambers, they were immersed in water until their mass became constant. The water saturated samples were used to determine mass loss at different RH values. The GFRP rebars

with 8 mm diameter, as shown in (Figure 3.1a), were selected to shorten the water saturation/ equilibration time. Although, there is no guarantee that this state is the actual saturation level, it is referred to as saturated state in this study.

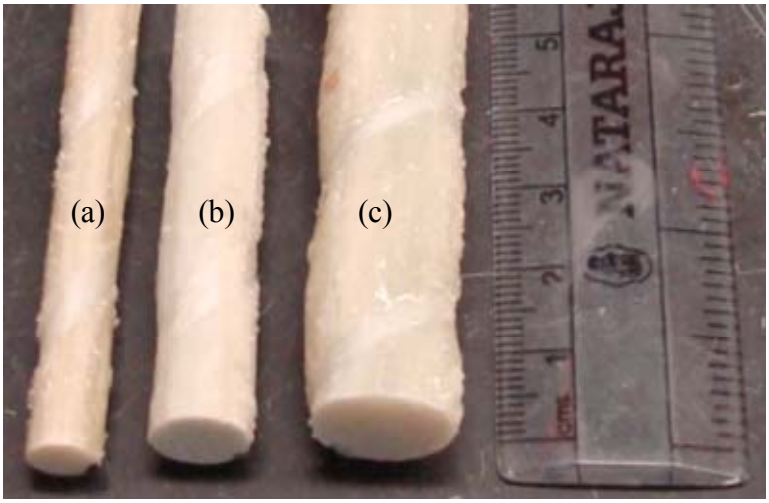

Figure 3.1. GFRP rebars with different nominal diameters (mm) used for the current study (a) 8, (b) 10, and (c) 13.

GFRP rebars with 13 mm nominal diameter were intended for determining in-situ moisture content by a time domain reflectometry (TDR) technique, as shown in Figure 3.1c. A TDR technique can be used to measure the propagation velocity of a voltage step to determine the dielectric constant (K_d), which in turn is related to the moisture content of a porous material. Initially, a calibration curve is produced by plotting the dielectric constant of GFRP rebars as a function of moisture content. The constants obtained from the fitted equation are used to measure the in-situ moisture content directly by the TDR machine as described in Topp and Devis (1982).

The experimental setting for the TDR technique required placing conductive sensors into the GFRP rebars. A copper wire of less than 1 mm diameter was used. Three pairs of holes, each with 1 mm diameter, were made to insert Cu wires to connect to the TDR machine. The GFRP rebars with 13 mm nominal diameter allowed to prepare the TDR samples with the layout shown in Figure 3.2. The rebars were hung in different RH chambers to determine the in-situ moisture content at the considered RH values using the TDR technique. Unfortunately, this experiment was not as effective as anticipated because of the inconsistent data produced by the TDR machine due to the very low porosity of GFRP composites compared to the sensitivity of the

technique. Consequently, the mass loss of GFRP rebars with 13 mm in the different RH chambers were determined using a gravimetric method. The obtained mass loss (kg/m^3) data was useful to compare with the mass gain (kg/m^3) data for GFPR rebars exposed to different RH levels as discussed in Section 3.4.2.

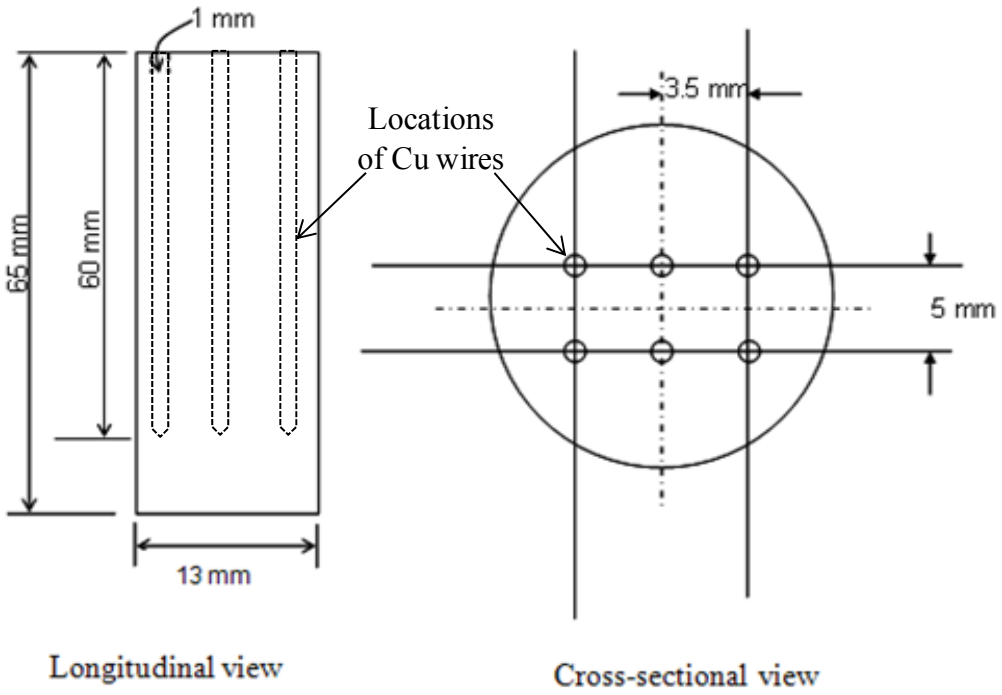

Figure 3.2. A layout of a TDR sample's longitudinal and cross-sectional views.

3.3. GFRP rebars in accelerated ageing conditions (Phase 1)

3.3.1. Overview

GFRP rebars embedded in concrete structures are prone to chemical attack due to the highly alkaline nature of concrete and the susceptibility of E-glass fibres to degradation when exposed directly to such environments. To better understand the interaction mechanisms of GFRP rebars with the simulated concrete pore solutions, GFRP rebars were immersed in both water and alkaline environments at various elevated temperatures. A detailed description of the experimental programme including the preparation of simulated concrete solutions, samples, exposure environments, and analytical techniques is discussed in the following sections.

3.3.2. Simulated concrete solutions

Concrete pore solution is highly alkaline with a pH higher than 13. Reardon (1992) studied the composition of pore solution of various hydrated cement paste systems as determined by the extraction methods and summarized results are shown in Table 3.1.

Several researchers used single alkali solutions, while others used multi-alkali solutions in order to create and maintain a high pH environment. For instance, Dejki (2001) used NaOH (2.0 g/L), KOH (19.6 g/L) and $Ca(OH)_2$ (3.6 g/L), Bank et al. (1998a) used NH_4OH (0.3, 3 and 30%) and Katsuki and Uomoto (1995) used NaOH (1 and 2 mol/L) solutions to simulate concrete pore solutions. The simulated concrete solutions were prepared by dissolving salts in deionized water following the procedure described by Marchand et al. (2001). The components, strength, and pH of exposure solutions used for the current study are shown in Table 3.2.

Table 3.1. Typical composition of the pore solution of various hydrated cement paste systems as determined by the extraction methods.

Items	Longuet 1974	Diamond 1981	Page 1983	Marchand et al. 2001
pH	13.63	13.64	13.7	-
OH^{-1}	592	614	712	2
Ca^{2+}	0.89	0.88	0.8	-
Mg^{2+}	$1x10^{-5}$	$1x10^{-5}$	$1x10^{-5}$	-
Na^{+}	124	262	251	192
K^{+}	547	436	603	592
Al^{3+}	0.12	0.12	0.15	-
SO_4^{2-}	40	42	71	44
Si^{4+}	0.94	1	1.8	-

Notes Results taken from the summary given by Reardon 1992. All solutes concentrations are in millimolalities

Table 3.2. Components, strength and pH of simulated concrete pore solutions.

Exposure environments	Component	Strength of solution (mmol/L)	pH
Single alkali solution	NaOH	192	13.2
	KOH	592	13.8
	$Ca(OH)_2$	21	12.5
Mixed alkali solution	Mixture of NaOH, KOH, and $Ca(OH)_2$	192 592 2	13.7
Deionized water	-	-	7

3.3.3. Sample preparation for the exposure environments

GFRP rebars with 10 mm diameter were cut into 50 mm lengths and were immersed in simulated concrete pore solutions. Prior to immersing, both edges of the rebar samples were epoxy-coated and air-dried to prevent axial (longitudinal) penetration of solutions into the samples (Figure 3.3).

Figure 3.3. Epoxy coating on the edge of a GFRP rebar sample.

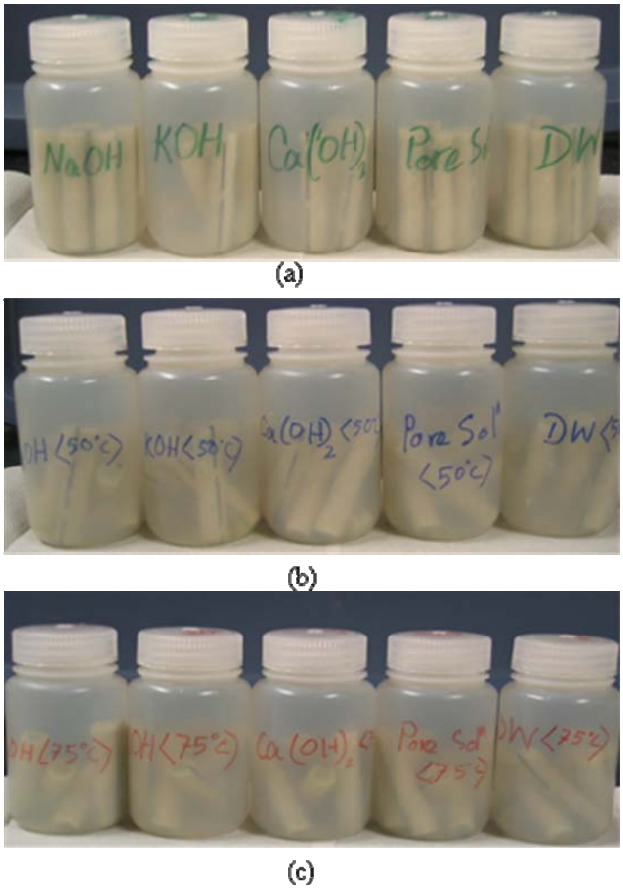

Figure 3.4. Epoxy coated GFRP rebars are immersed in various alkali solutions and deionzed water (a) 23 °C, (b) 50 °C, and (c) 75 °C.

High-density polyethylene bottles with a wide cover and 125 ml capacity were used to contain the samples and solutions (Figure 3.2). The coated samples were immersed in exposure solutions at 23 °C, 50 °C, and 75 °C. They were taken out at 1 month, 3 months, and 12 months; then air dried and stored in a desiccator for microscopic analyses.

3.3.4. Sample preparation for the Electron microscopes

The Standard guide for the Preparation of Metallographic Specimens (ASTM E3-01) was used for mounting and polishing of samples for electron microscopy analyses (SEM and EDS). Stored samples were cut into 5 mm thick disks with a diamond blade and mounted into plastic moulds with a mixed slurry prepared by mixing two parts of mecaprex with five parts by volume of acrylic resin. After being pressurized for 15 minutes by a leco pressure (Figure 3.5), samples were de-moulded and polished by 150, 200, 400, and 600 grit sand papers with a mechanical polisher (Figure 3.5b) at the Mechanical Engineering Lab. Finally, they were polished by 6 and 1 micron diamond pastes as suggested by the same standard method for composite materials. After that, they were dried overnight at 50 °C and coated with an SC7640 sputter coater. Finally, they were analysed with a JEOL 840A scanning electron microscope and a Genesis 7000 EDS machine. A photograph of the sample coater and SEM/EDS machine is shown in Figure 3.6. The sample preparation procedure for an electron microscope is described in Figure 3.7.

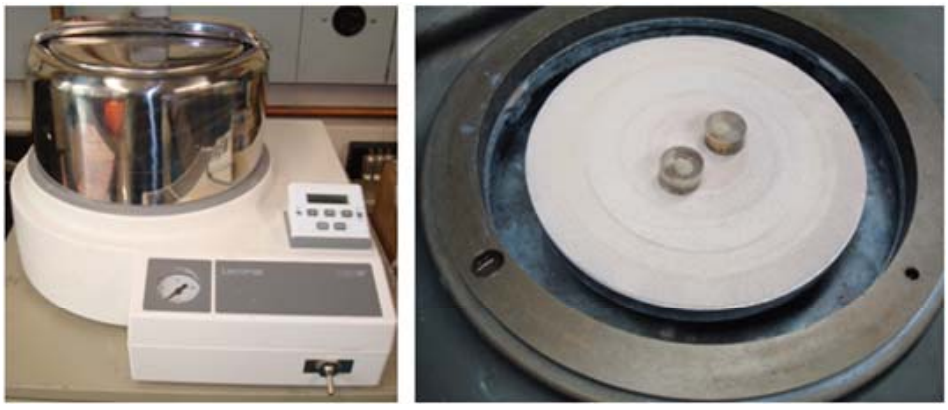

(a) (b)

Figure 3.5. SEM/EDS ample preparation (a) moulding sample in Leco pressure and (b) polishing sample.

(a) (b)

Figure 3.6. Components of SEM/EDS machine (a) coater, and (b) SEM/EDS machines.

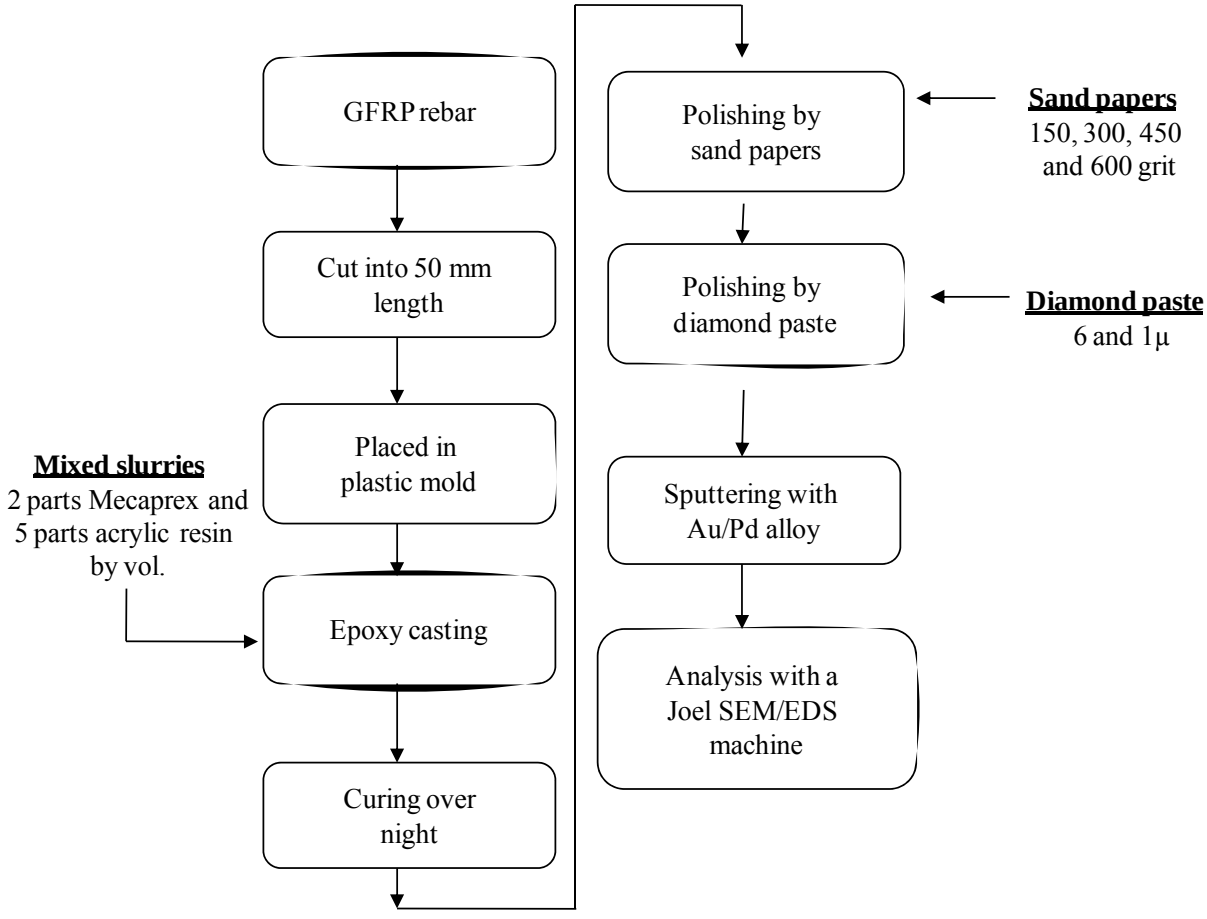

Figure 3.7. GFRP sample preparation for an SEM/EDS analysis.

3.3.5. Sample preparation for Fourier transform infrared (FTIR) spectroscopy

FTIR samples were prepared by crushing GFRP rebars (unconditioned and conditioned samples) into small pieces, segregating the polymer matrix from fibres, and grinding the coarse polymer matrix into a fine powder. The crusher used for this purpose is shown in Figure 3.8. The fine powder was oven dried at 50 °C overnight to remove any trace amount of water. Then, a small amount of dried powder was intimately mixed with potassium bromide (KBr) (powder sample: KBr = 1:4, by weight.) and milled into a very fine powder as reported in WCAS (2009) and Benmokrane and Cousin (2005). This mixed powder was used for the FTIR analysis for both unconditioned and conditioned samples. The prepared FTIR samples were analysed with a BIO-RAD Digilab Division, FTS-40 (mid IR) by using diffuse reflectance cells. The FTIR machines and sample holders are shown in Figure 3.9. The sample preparation procedure for an FTIR analysis is schematically presented in Figure 3.10.

Figure 3.8. A crusher used to crush the GFRP rebars for separating matrix from fibre.

(a)

(b)

Figure 3.9. Components of a FTIR machines (a) a FTS machine with sample injector and (b) sample holders.

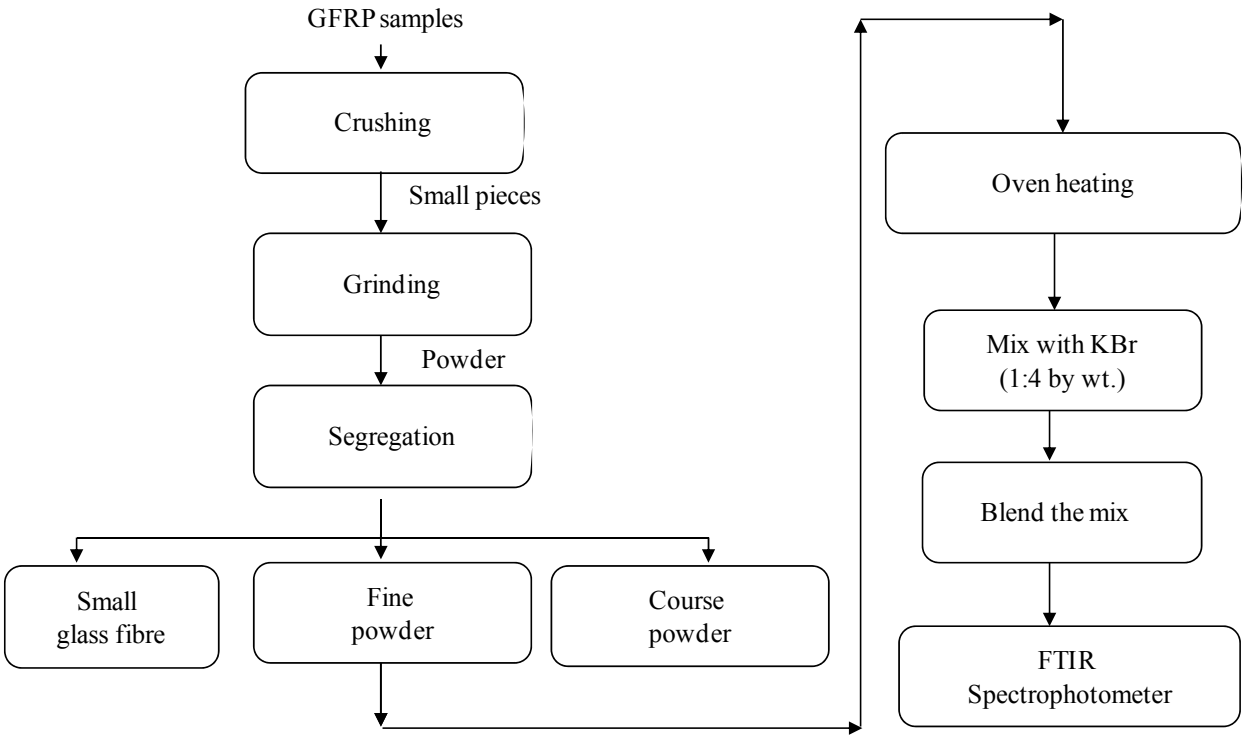

Figure 3.10. GFRP sample preparation for an FTIR analysis.

3.3.6. Methods

In phase 1, samples were tested for two purposes: (1) To observe the deterioration of GFRP components where material characterization techniques, such as SEM and EDS, were used and (2) To assess the degradation of the polymer matrix using FTIR spectroscopy. Therefore, the principles and operations of these three techniques (SEM, EDS, and FTIR) are explained here.

Materials characterization techniques

The Materials Characterization Handbook of The American Society for Materials (ASM International) has defined materials characterization as "Characterization describes those features of composition and structure (including defects) of a material that are significant for a particular preparation, study of properties, or use, and suffice for reproduction of the material"(ASM 1986). It means that the characterization provides the composition, structure, and defects of the materials to be examined.

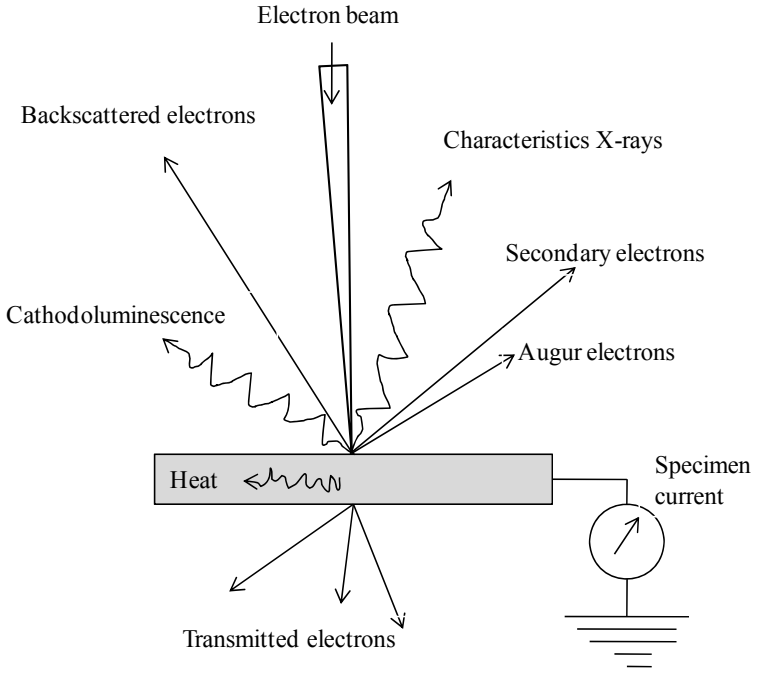

Figure 3.11. A schematic of the principal results of the interaction of an electron beam with a specimen.

An electron beam and sample interaction is the heart of any kind of material characterization technique. While a finely focused electron beam bombards the surface of a specimen, it generates several signals, as shown in Figure 3.11 (Watt 1997; Oguocha 2007).These signals are analyzed for specific purposes to characterize materials. For example, secondary electrons are used in a scanning electron microscopy (SEM) machine for a topography analysis, whereas characteristic X-rays are used in an energy dispersive X-ray spectrometry (EDS) machine for an elemental analysis of a specimen surface. The use of signals for material characterization and the techniques used for analyzing those signals are shown in Table 3.3.

Table 3.3. Signals produced by a beam-sample interaction and their uses with techniques (Watt 1997).

Signals	Uses (techniques)
Secondary electrons	- Topography and morphology information (SEM)
Backscattered electrons	- Topological and atomic number information - Crystallographic information on surfaces (EBSD)
Transmitted electrons	- Internal structure information bright and dark field imageing (TEM) - Elemental analysis and distribution (EELS)
X-rays	- Microanalysis and distribution of elements and elemental mapping (EDS and WDS)
Auger electrons	- Elemental and chemical information on surface layers(AES)
Cathodoluminescenec	- Distribution of energy levels in photon in some minerals and rocks
Absorbed current	- Internal structure of semiconductors (EBIC)

EBSD Electron Backscattered Diffraction, TEM Transmission Electron Microscopy, EELS Electron Energy Loss Spectroscopy, WDS Wavelength Dispersive X-ray Spectroscopy, AES Auger Electron Spectroscopy, and EBIC Electron Beam Induced Current.

Principles and operations of SEM

When an incident electron hits an atom, it is excited. Two types of collisions may occur during the excitement as shown in Figure 3.12 (Flegler et al. 1993). The elastic collisions produce backscattered electrons, while the inelastic collisions produce the secondary electrons. Each incident electron can produce several secondary electrons from the surface depth of 5-150 *nm* with energies of 50 *eV*. These electrons are collected by an Everhart-Thornley detector in an SEM, then amplified and displayed as an image on a cathode ray tube (CRU). A brief description of SEM components and their functions will help understanding the principles of SEM properly. A schematic diagram of an SEM is shown in Figure 3.13 (Flegler et al. 1993).

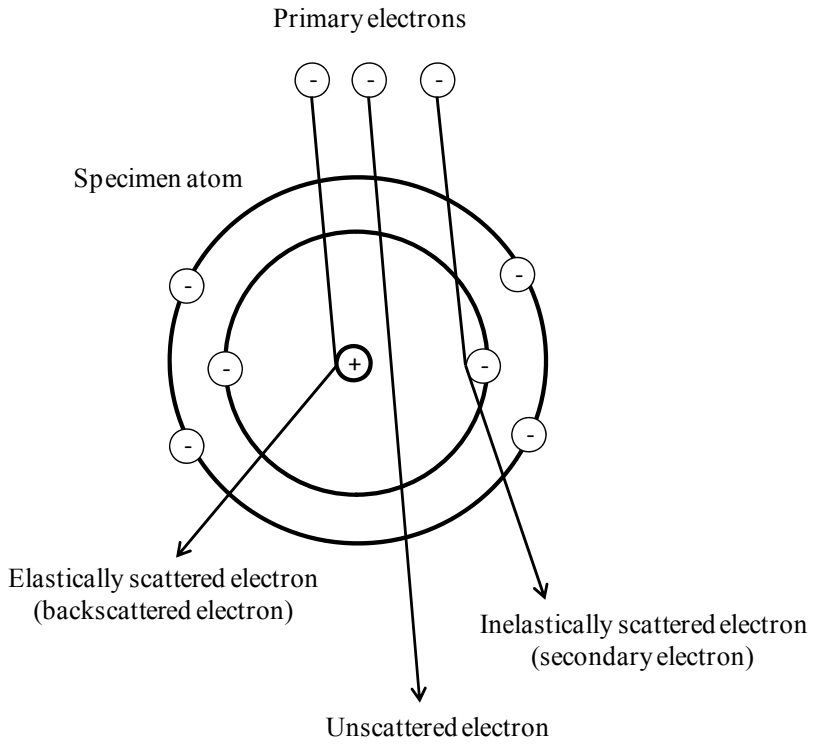

Figure 3.12. Specimen beam interactions.

Beam generation: The first stage of an electron microscope in the process of creating an image is the electron beam production, which is emitted from an electron gun. Three major types of electron gun are used in an SEM. They are tungsten hairpin, lanthanum hexaboride (LaB6) and field emissions. Each gun has advantages over others.

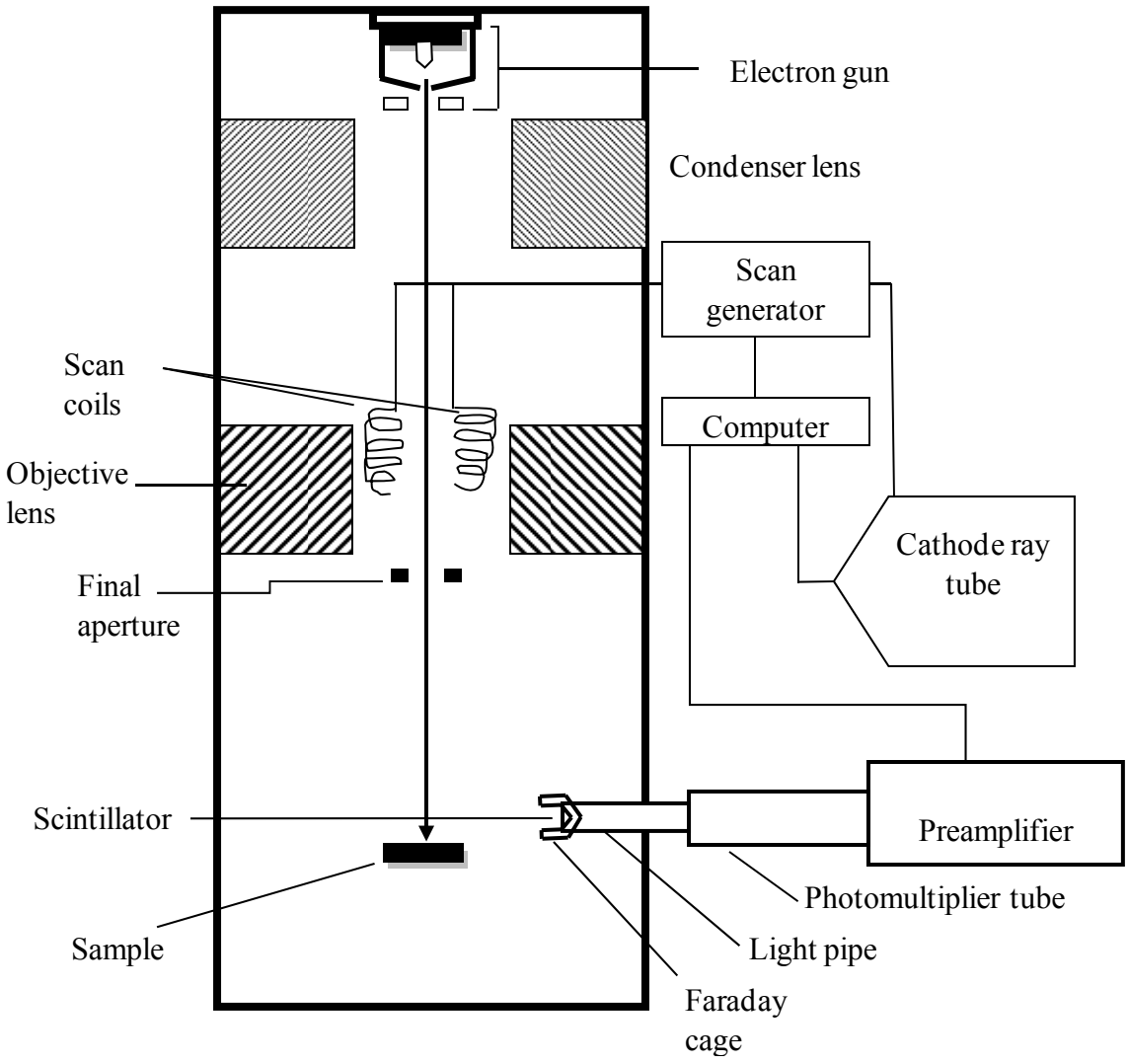

Figure 3.13. A schematic of a scanning electron microscope showing different components.

Beam condensation: The produced electron beam has energies of few hundred *eV* to 40 *keV*, and is passed through 1 or 2 condenser lens. Nowadays, double condenser lens systems are used, which are able to produce 10^4 to10^5 demagnified image (Watt 1997). The condensed beam focuses on the fine point of a sample by the objective lens. A set of scan coils deflects the electron beam back and forth to scan the sample in a raster pattern which is very similar to the raster of a TV receiver.

Beam sample interactions: When the electron beam strikes a sample, it produces a hemispherical or teardrop-shaped volume known as interaction volume with a depth of 100 *nm* to 5 μm into a sample surface. The size and shape of interaction volume depends on the angle of beam incidence, the magnitude of its current, the accelerating voltage and the average atomic number of the materials of the sample. Among those factors, accelerating voltage and density play the largest role in determining the depth of electron interaction. These factors are involved in determining the penetration depth by Equation 3.1.

$$x = \frac{0.1E_0^{1.5}}{\rho}\mu m \tag{3.1}$$

where,

x : depth of electron penetration, μm

E_o : accelerating voltage, *k*eV

ρ : density of the sample materials, g/cm^3

The energy exchange between the beam and sample results in producing high energy electrons, such as secondary electrons, backscattered electrons, X-rays, auger electrons, etc as shown in Figure 3.11. Each response is collected by individual detectors.

Image generation: A single detector in an SEM does not capture all kinds of electrons. A certain type of electron is collected by a specific detector to produce special image. For example, an Everhart-Thornley detector is used for an SEM image generation, while a Li(Si) detector being is used for an EDS analysis.

To produce an SEM image, secondary electrons are collected by an Everhart –Thornley detector, converted into a voltage, and amplified. The amplified signals are displayed as a variation of lightness on a CRT. Therefore, a larger number of secondary electrons will results in a brighter image on the surface of CRT, and vice versa. The image on the CRT is directly captured and displayed on a computer monitor. Thus, the SEM image developed consists of thousand of spots of varying intensity on the face of a CRT that corresponds to the topography of the sample.

Sample preparation is a prerequisite for a conventional SEM. Almost all samples need some type of sample preparation. Samples must be dried, firmly mounted and electrically

conductive. However, the sample preparation stage can be stepped down with the development of an environmental SEM.

Principles and operations of EDS

When an electron beam hits a specimen, the characteristic X-rays are produced with other signals as shown in Figure 3.11. Characteristic X-rays are produced from the surface depth of 0.1-5 μm with the energy higher than secondary electrons. A beam electron can interact with an inner shell electron of a specimen atom. This results in ejecting an electron from the shell by exciting the atom (excited state) as shown in Figure 3.14 (Goldstein et al. 2003). If the excited electron is from K shell, the energy lost should be E_K, binding energy of the ejecting electron in a K shell.

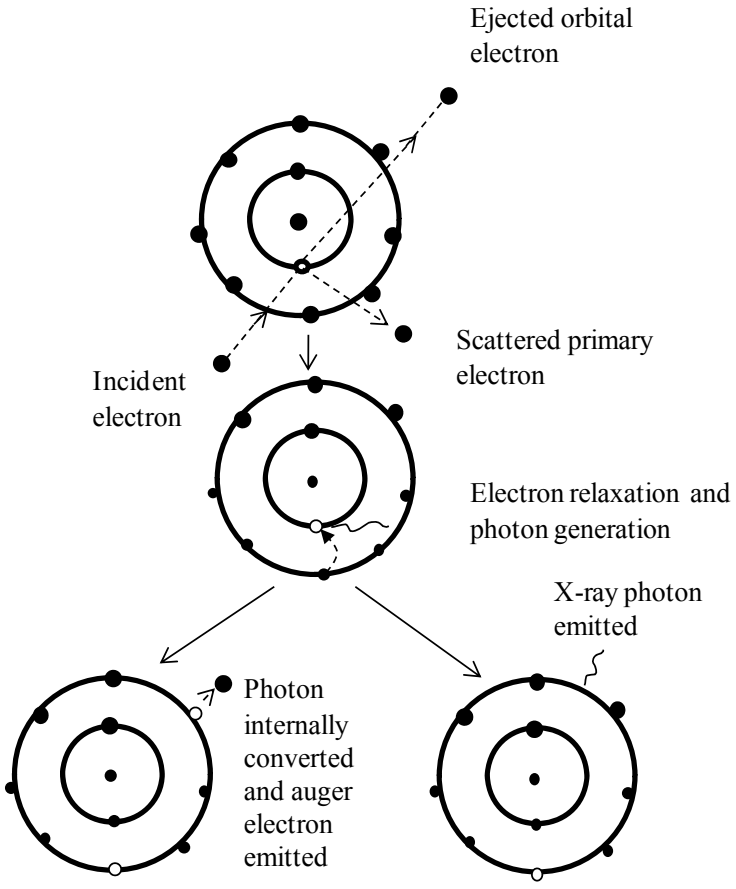

Figure 3.14. Inner shell electron ionization in an atom and subsequent de-excitation by electron transition.

The excited atom relaxes to its ground state (lowest energy) within 1ps by allowing transitions. During relaxation, the excess energy can relax following either way of two options auger process or characteristic X-rays. In the Auger process, the difference in shell energies is transmitted to another outer shell electron by ejecting the electron from the outer shell with a specific kinetic energy. In the characteristics X-ray process, the difference in energy is expressed as a photon of an electromagnetic radiation which has a sharply defined energy. It is customary to show the energy transition by a specific notation, $K_{\alpha 1}$ (for example), where, *K* is the destination shell, α is the location of source shell (α 1 shell up from the destination shell, β 2 shell up from the destination shell) and 1 is the source of subshell. The energy transfer from the subshells of *L* to *K* is shown in Figure 3.15 (Goldstein et al. 2003).

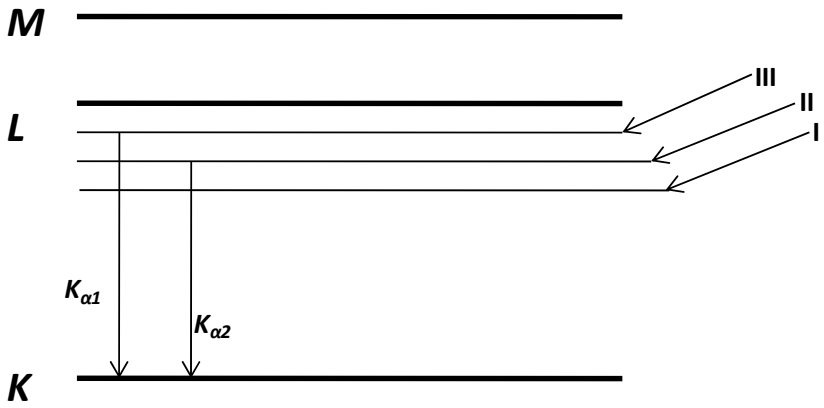

Figure 3.15. A schematic showing energy levels of different shells and sub-shells in an atom.

EDS machine can be either separated or attached. The components of a free standing EDS is shown in Figure 3.16 (Oguocha 2007). An EDS coming with an SEM has four major components beam source, X-ray detector, pulse processor and analyzer.

Beam source: The first stage of an electron microscope is the electron beam production, which is emitted from an electron gun. The condensed beam focuses on the fine point of a sample by the objective lens. The energy exchange between the beam and sample results in producing high energy electrons, such as secondary electrons, backscattered electrons, X-rays, auger electrons, etc., as shown in Figure 3.11. Each response is collected by individual detectors.

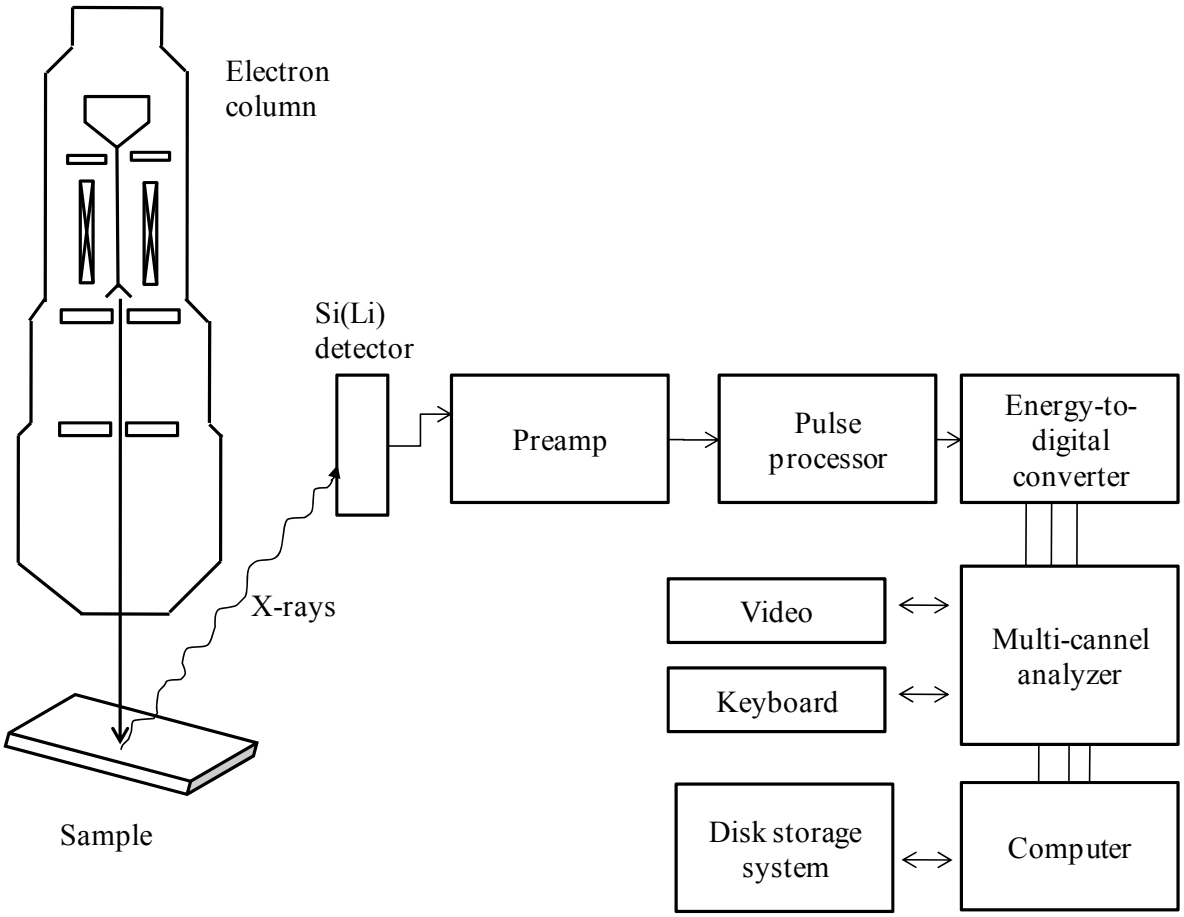

Figure 3.16. Components of a typical EDS system.

X-ray detector: The X-ray detector is typically a lithium-drifted silicon, solid-state device. When an incident X-ray strikes the detector, it creates a charge pulse that is proportional to the energy of the X-ray.

Pulse processor: The charge pulse is converted to a voltage pulse (which remains proportional to the X-ray energy) by a charge-sensitive preamplifier.

Analyzer: Signal is then sent to a multichannel analyzer where the pulses are sorted by voltage. The energy, as determined from the voltage measurement, for each incident X-ray is sent to a computer for display and further data evaluation. The spectrum of X-ray energy versus counts is

evaluated to determine the elemental composition of the sample. A typical EDS micrograph is shown in Figure 3.17 (Boulfiza and Banthia 2005).

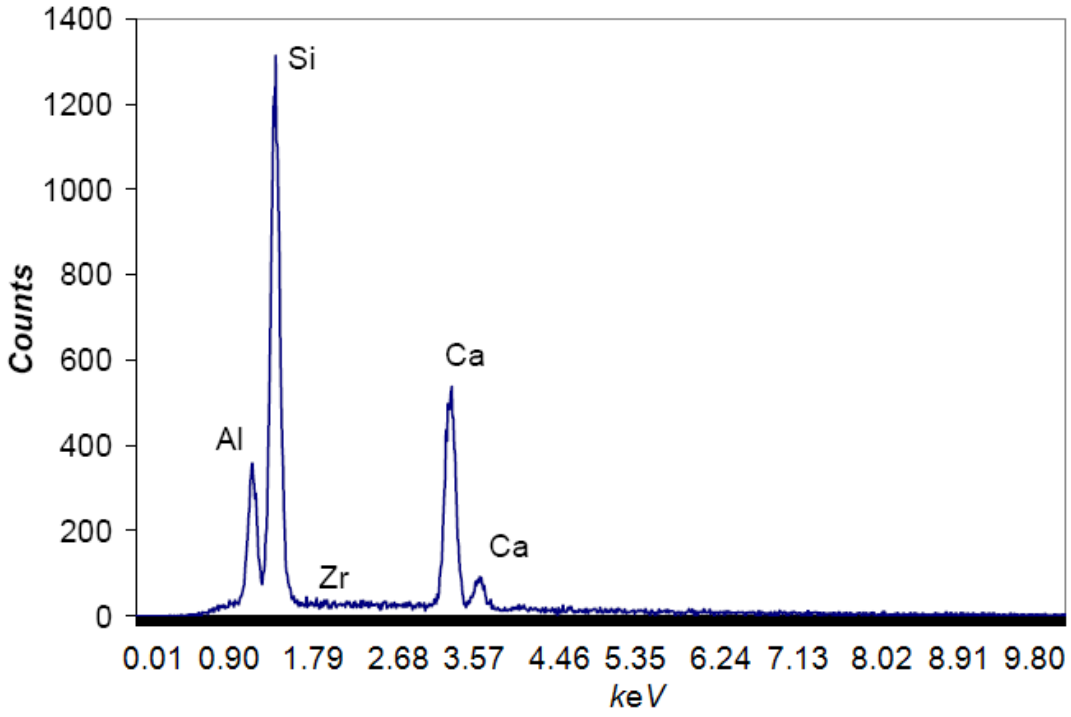

Figure 3.17. A typical EDS micrograph showing a chemical analysis of glass fibres.

Fourier Transform Infrared (FTIR) spectroscopy

FTIR is a useful tool for identifying chemical bonds (functional groups) in organic molecules. The basic principle of FTIR is based on IR spectroscopy whose principle is described in this section. A detailed description of this technique can be found in the large body of published literature on the subject (Wade 2003; Hsu 2011).

Molecules are always vibrating. For a molecule to be IR active, the vibration should give rise to a net change in dipole moment; i.e. molecules first absorb IR energies before they start vibrating. This is the basis of IR spectroscopy. Molecular vibrations are mainly of two types: bending (bond angle changing) and stretching (bond length changing). A vibrational frequency in a molecule having two atoms linked by a spring can be defined by the Hooke's Law shown in Equation 3.2 (DCB 2002). An IR spectrum is usually measured as wavenumber (cm^{-1}), which is simply the inverse of a wavelength, and is proportional to frequency.

$$\bar{v} = \frac{1}{\lambda} = \frac{1}{2\pi c}\sqrt{\frac{f(m_1 + m_2)}{m_1 m_2}} \tag{3.2}$$

where

$\bar{v}$: vibrational frequency, cm^{-1}

λ : wavelength, cm

m_1 : mass of first atom, g

m_2 : mass of second atom, g

c : velocity of light, cm/s

The basic components of both IR and FTIR spectrometers are similar. They typically include a light source, a monochromator/interferometer, and a detector (Figure 3.18). An IR spectrometer uses a monochromator to disperse IR waves through a slit, whereas an FTIR is based on the interferometer technique. The fact that an interferometer in an FITR allows the passing of all IR radiation simultaneously makes the FTIR a faster scanning process than an IR machine. The interferometer is set with both fixed and moving mirrors. The moving mirror allows the creation of the constructive interferogram. After interacting with the samples, the IR radiation beam is finally passed through a detector. In the FTIR machine, the final beam is calculated and transformed to a spectrum by a Fourier Transform technique – a mathematical algorithm for converting raw data into a frequency spectrum.

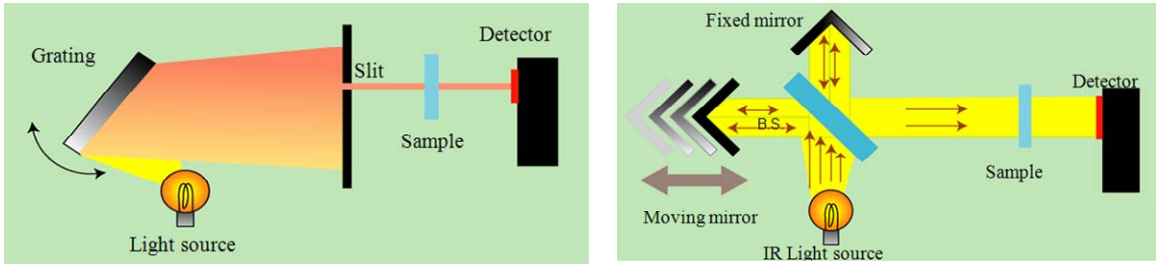

(a) (b)

Figure 3.18. A schematic of the basic components of spectrometer (a) IR and (b) FTIR (adapted from JASCO 2011).

In the FTIR machine, raw data is collected from both sample and background. The final sample spectrum is produced after removal of the background spectrum. A typical spectrum of an organic molecule is shown in Figure 3.19. The spectrum is represented in terms of percent transmittance of light as a function of wavenumbers. However, it is also possible to use absorbance (A) in place of transmittance (T) for an FTIR spectrum. Absorbance can be calculated from transmittance using the relationship, $A = -\log_{10}(T/100)$.

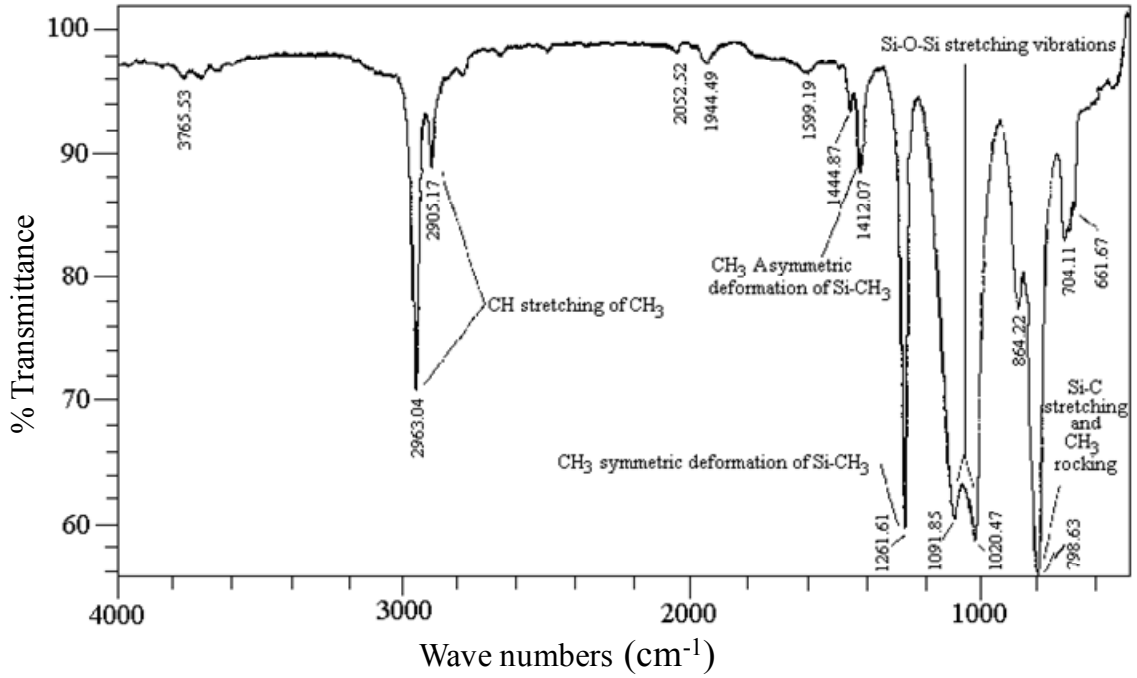

Figure 3.19. An FTIR spectrum showing bonds and functional groups in polydimethylxyloxane (adapted from WCAS 2011).

3.3.7. Method of detecting alkali ions in GFRP rebars

Detection of potential penetration of alkali ions into the GFRP samples was carried out in a two step process. First, an X-ray mapping for the elements of interest (Na, K, and Ca) was conducted over a Backscattered Electron Image (BEI). This covers a relatively large area of the GFRP sample close to the boundary and allows a systematic way for identifying areas for further analysis with more precise techniques, such as line EDS, and possibly point EDS, if needed. The three techniques are briefly described in this section.

To generate an X-ray mapping, a BEI is initially developed by detecting and analysing the backscattered electrons generated by hitting a specimen surface at 150-1000 *nm* depth with an energy higher than 50 eV (Goldstein et al. 2003; Flegler et al. 1993). An X-ray mapping for Ca of a BEI for an unconditioned sample is shown in Figure 3.20a. Ca is a constituent of E-glass fibres as CaO but should not be present in the VE matrix. Therefore, Ca was detected only in fibres and not in the matrix of unconditioned samples.

It has been a standard practice in materials science and engineering to observe the elemental composition at any point on the surface of a sample used for EDS analysis. However, with the technological advancement, it is now possible using Line EDS to detect the concentration of elements along a given line on the surface of the sample more precisely, and hence, provide information on elemental variation along that line. In an SEM-EDS machine, while an electron beam strikes a specimen, several electronic signals, such as auger electrons, secondary electrons (SE), backscattered electrons (BE), X-rays and specimen current, etc. are emitted (Goldstein et al. 2003; Watt 1997). These signals are monitored and detected to analyse the specimen. Both SE and BE are used to get topographical information, such as elemental composition and surface texture. To generate a line EDS, an SEM image is first produced by hitting the sample surface at 5-150 nm depth with a beam energy less than 50 eV (Goldstein et al. 2003; Flegler et al. 1993). After that, a line EDS scan for a particular element is carried out on the SEM image. A line EDS scan for Ca is shown in Figure 3.20b, where the intensity of Ca is effectively zero on the matrix and highest on the fibres. This is expected, as calcium is part of the composition of the glass fibre itself.

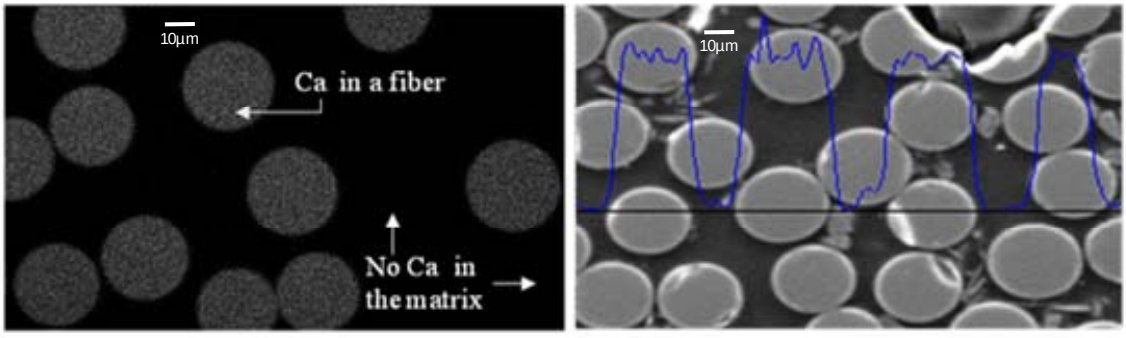

(a) (b)

Figure 3.20. Detection of the presence of Ca for an unconditioned GFRP sample (a) an X-ray mapping for Ca of a BEI and (b) a Line EDS scan for Ca.

3.4. Interphasial effects on the properties of GFRP composites (Phase 2)

3.4.1. Overview

Sizing at an interphase controls the properties of composites. The composition and effects of sizing have been discussed in Section 2.3, while the bonding mechanisms at an interphase have been discussed in Chapter 2.4. The current section deals with a special type of composite – GFRP custom plane sheet. The following subsections discuss (i) the reasons of choosing GFRP custom plane sheets over GFRP rebars, (ii) the ingredients and manufacturing method of GFRP custom plane sheets, and (iii) de-sizing method of fiberglass mat.

3.4.2. Why GFRP custom plane sheets in place of GFRP rebars?

In order to study the sizing effects at an interphase of a GFRP rebar, GFRP custom plane sheets were produced due to the following reasons. Firstly, it is hardly possible to fabricate de-sized glass fibres as sizing is applied during fabrication to protect the fibre and enhance the composite's properties. Because of the non-availability of de-sized glass fibres, it was not possible to get a GFRP rebar with de-sized glass fibres. Secondly, although hypothetically it is possible to fabricate GFRP rebars with de-sized glass fibres, the presence of inhomogeneous layers in GFRP rebars will make the study much more difficult, because the microstructural analyses of a GFRP rebars shows that the outer layer (edge) consists of polymer matrix, sands, and helical wrapping, whereas the inner layer (bulk) consists of only fibres and polymer matrix (Figure 3.21). Thirdly, a single fibre embedded in a polymer matrix is theoretically simpler to study than a GFRP rebar, but difficult to deal with due to its tiny diameter. Researchers have encountered erroneous results in detecting the interphasial shear strength by pulling out a single fibre embedded into a polymer matrix, as the fibre breaks before successful pull-out occurs (Pigot et al. 1985; Eagles et al. 1976). Finally, a single fibre embedded in a polymer matrix does not represent a GFRP rebar that contains large volume fraction of fibres. The design of the GFRP custom plane sheet sample is shown in Figure 3.22.

The ΔY and ΔZ dimensions of the specimens were chosen so that capillary uptake from the sides of the sample was excluded. The thickness of the sample, ΔX, was chosen such that only diffusion and possible chemical reactions in the X direction can take place. Under such conditions, the time lag for the Y and Z direction relative to the glass fibres will be at least 100

times larger than in the X direction. This simple configuration of a GFRP composite allows one to study, understand, and ultimately model the behaviour of GFRP composites at an intermediate level between a microscopic level, as represented by a single fibre surrounded by a matrix (too simplistic), and the macroscopic level, as represented by GFRP rods (too complicated).

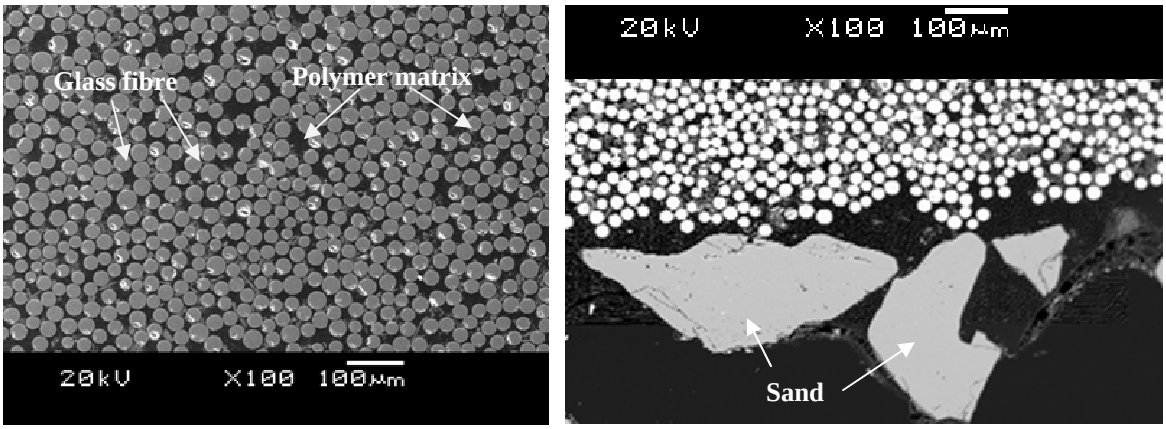

(a) (b)

Figure 3.21. SEM images of a GFRP rebar cross-section (a) a bulk image and (b) an edge image.

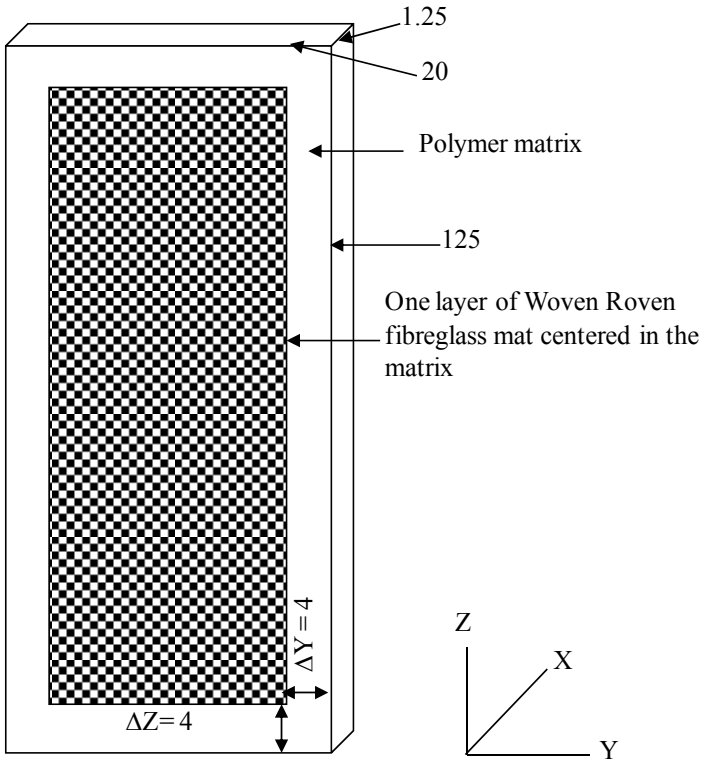

Figure 3.22. A design of a GFRP custom plane sheet (dimensions are in mm and not scaled).

3.4.3. De-sizing of fibreglass mat

The desizing of fibreglass mat is the process of removing sizing from the mat surface. By boiling a fibreglass mat, only sizing from the mat is removed as the other ingredients (sand, kaolin, limestone and colemanite) of glass fibres require higher temperature to melt (Murhpy 1998). The desizing process of a fibreglass mat was developed in the lab by evaluating the mass loss due to boiling. A total of 12 fibreglass mats (450x300 mm) were boiled in deionized water. The boiled water was carefully drained each hour, so that no sizing precipitated on fibres. After each hour, one piece of mat was taken off from boiled water. Thus, the last piece of fibreglass mat was boiled for 12 hours. Finally, all mats were oven dried at 105 °C overnight, desiccated for three hours in a desiccator and weighed. The mass loss of fibreglass mat as a function of boiling time is shown in Figure 3.23. It shows that nine hours of boiling was enough to get a constant mass loss of fibreglass mats. Therefore, the fibreglass mats were boiled nine consecutive hours to desize them for the real experiment.

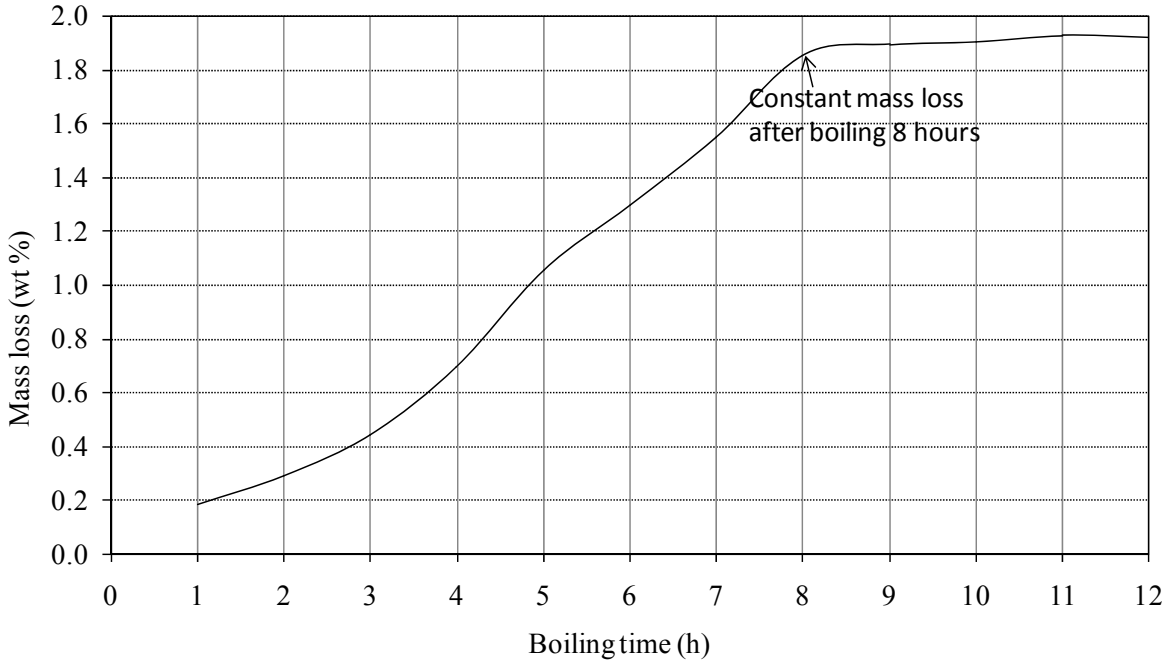

Figure 3.23. Mass loss of glass fibre mat as a function of boiling time.

3.4.4. GFRP custom plane sheets ingredients

E-glass fibre and VE are two major ingredients in GFRP rebars as discussed in Section 2.2. Similar basic ingredients were used for the GFRP custom plane sheet preparation. Hence, GFRP custom plane sheets were composed of a fibreglass mat (E-glass), a polymer matrix, and few

minor ingredients. The woven roving fibreglass mat (E-glass) with a thickness of 0.35 mm and mass of 319.55 g/m^2 was used. The polymer matrix applied was Derakane 411-350 (VE resin) containing 45% styrene with the density of 1.046 g/ml at 25 °C. As minor ingredients, methyl ethyl ketone peroxide (MEKP) and acetylacetone were added in Derakane during the sheet preparation. A few ingredients of the GFRP custom plane sheets are shown in Figure 3.24. A dry GFRP custom plane sheet contains 13% fibre, 86% VE resin, and 1% catalyst by volume.

(a) E-glass fibre

(b) Resin and hardener

Figure 3.24. Ingredients of a GFRP custom plane sheet.

3.4.5. Mould preparation

The configuration and dimensions of the mould used, together with a picture of the actual mould, are shown in Figure 3.25. It was a stainless steel mould with two identical plates. Each plate was prepared by excavating the depth of 0.45 mm. Hence, the final sample thickness would be about 1.25 mm including the mat thickness of 0.35 mm. Each plate had resin input and output holes with a diameter of 6 mm.

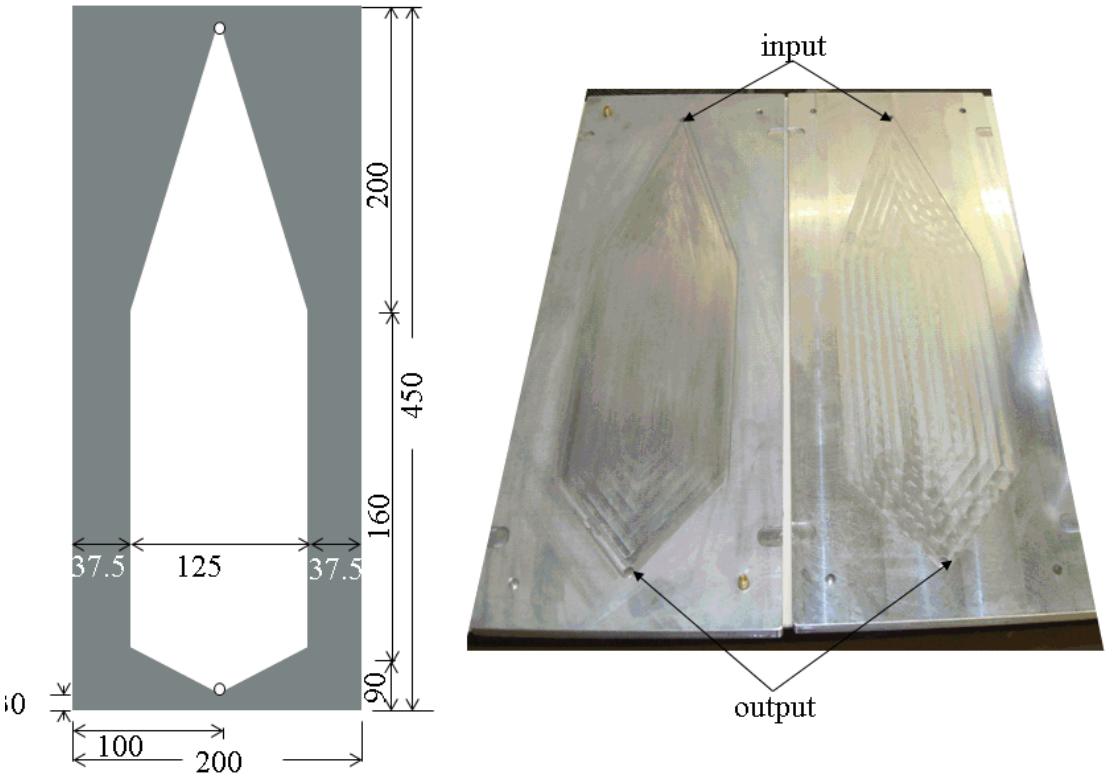

Figure 3.25. Mould for preparing GFRP custom plane sheets (a) the design of a single mould with dimensions, and (b) two identical plates of the mould.

3.4.6. GFRP custom plane sheet preparations

The sheet was designed in such a way that the fibreglass mat with a thickness of 0.35 mm was suspended in VE resin producing a total sheet thickness of 1.25 mm. The sheet preparation consisted of several steps, shown in Figure 3.26. Initially, the mould plates were anodized to reduce surface roughness. Then, mould releasing agents were applied on both plates and air-dried. After that, the fibreglass mat with the dimensions of 450 mm x 300 mm was placed on an anodized plate. Next, the mat was stretched down from both sides, plates were clamped together and the mat beyond the plates was trimmed off. Finally, both plates were sealed with yellow strips and ready for the vacuum infusion.

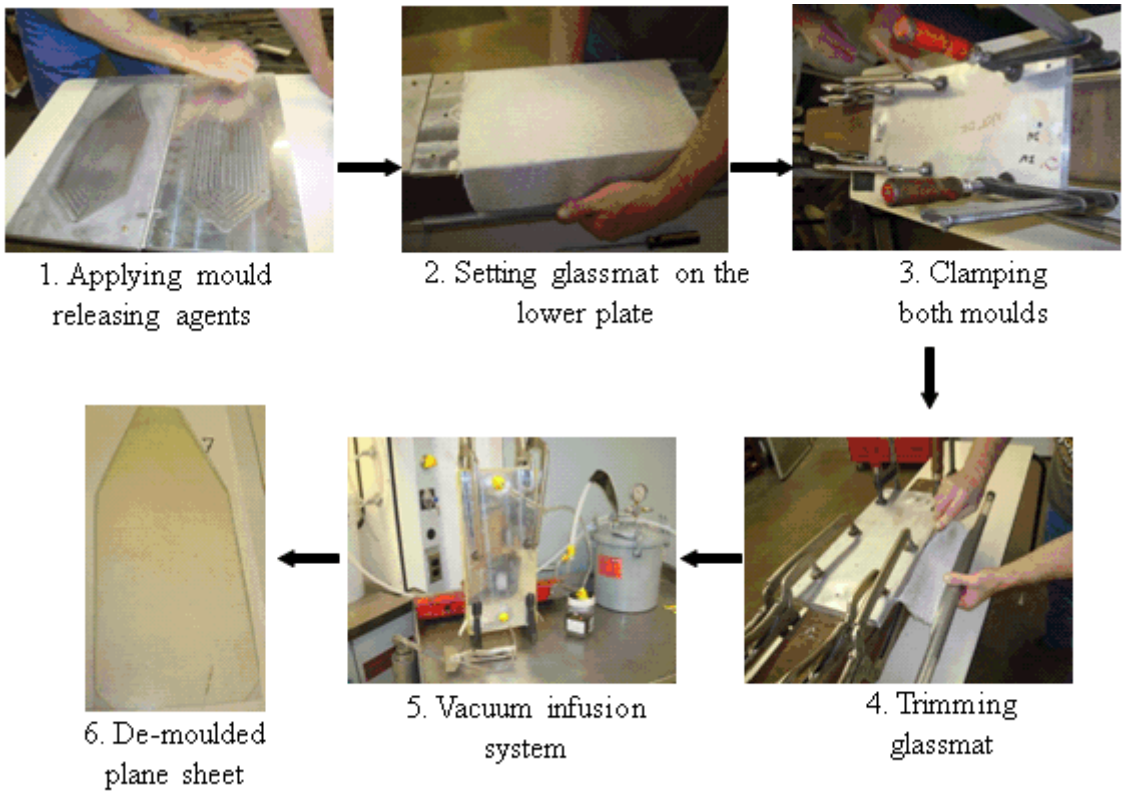

Figure 3.26. The steps of GFRP custom plane sheet preparation.

Prior to vacuum infusion, the VE resin was mixed with minor ingredients and the infusing system had to be sealed. The Derakane was mingled with 0.5 parts per hundred (phr) MEKP-925H and 0.06 phr 2, 4-Pentanedione (acetyl acetone) at 23 °C. The gel time information of Derakane (VE resin) is explained in the Derakane datasheet (Ashland 2004).

The vacuum infusion process operated at five kPa (1-inch) pressure of Hg for 20 minutes. An optimum five kPa vacuum was selected after a series of trial and error methods. A higher vacuum extracted the polymer matrix faster into the system and resulted in imperfect sheet surfaces, whereas a lower vacuum was unable to draw the VE resin into the system. The resin was infused into the mould through the lower part and forced out through the upper part of the mould (Figure 3.27). After that, the vacuum was released and the sheet was cured over night at 23 °C (±0.5). A detailed description of composite manufacturing processes is included in Appendix B.

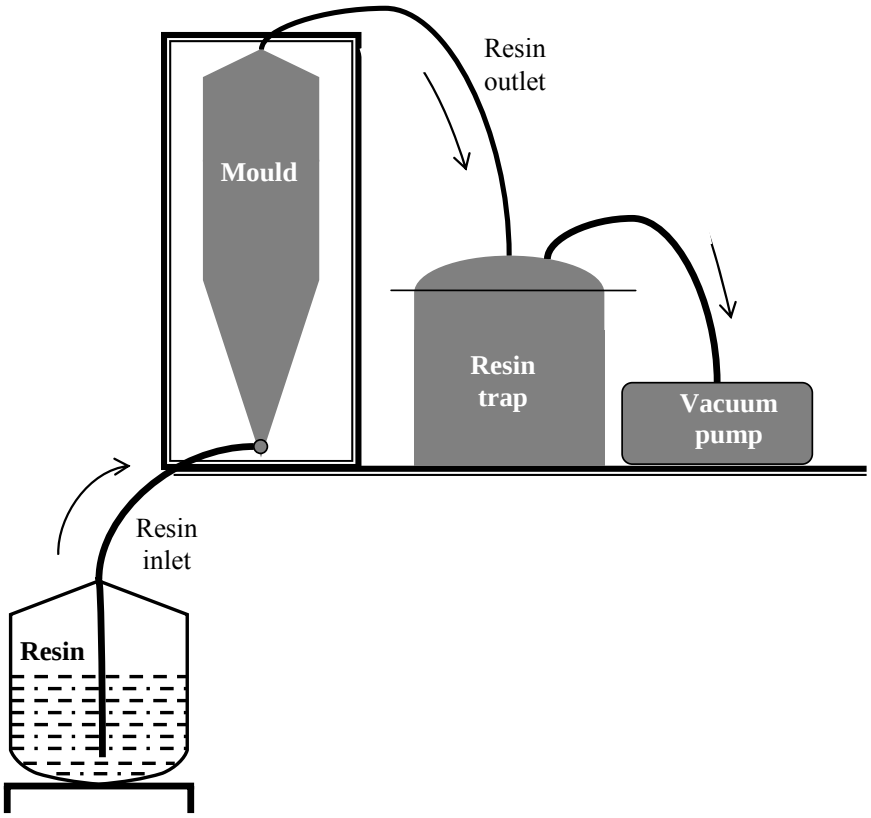

Figure 3.27. A schematic diagram of a vacuum infusion process.

Once the plane sheets with both sized and de-sized fibreglass mats were produced (step 6 in Figure 3.26), they were ready for the second stage. Initially, a demoulded sheet was cut into dimensions of 117 mm x 12 mm x 1.25 mm and placed into the mould again for another run of vacuum infusion. After demoulding, samples were cut again, keeping 4 mm border around them, as shown in Figure 3.28. Thus, the final dimensions of the GFRP custom plane sheet were 125 mm x 20 mm x 1.25 mm as designed.

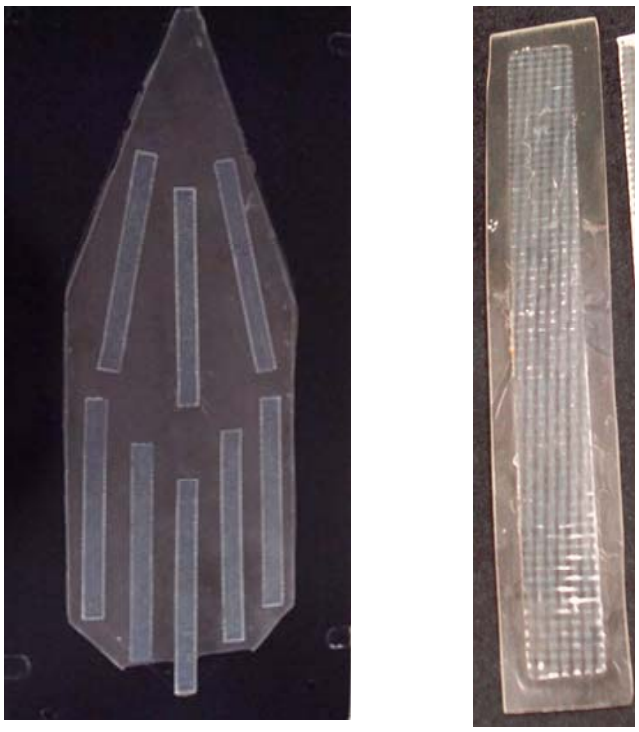

(a) (b)

Figure 3.28. GFRP custom plane sheet preparation (a) a demoulded sheet from the second run of a vacuum infusion, and (b) a final GFRP custom plane sheet sample after cutting 4 mm border around each sample of image a.

3.4.7. Methods

In phase 2, the GFRP custom plane sheets were tested for two purposes:

1) To study the moisture gain characteristics of both sized and desized GFRP sheet specimens, and
2) To determine the relation of tensile strength following potential hydrolytic attacks.

To observe the moisture gain characteristics both sized and de-sized GFRP sheet specimens were immersed in deionized water at temperatures 4 °C, 23 °C, and 50 °C. Sheet specimens were also tested to determine tensile strength before and after exposure.

Specimens were initially dried at 50 °C to obtain the baseline mass (W_b). The instantaneous mass (W_i) of each sample was taken to the nearest 0.001 g by weighing machine. Prior to weighing, samples were wiped out with a lint free towel. None of the samples was kept

outside more than five minutes during weighing, as suggested by ASTM D5229M. The mass gain and moisture diffusion coefficient of both types of samples were calculated by Equations 3.3 and 3.4, respectively (ASTM D5229M).

$$\text{Mass change, \%} = \left| \frac{W_i - W_b}{W_b} \right| x100 \tag{3.1}$$

where,

W_i : the current specimen mass, and

W_b : the baseline specimen mass.

$$\text{Moisture diffusivity } D = \pi \left(\frac{h}{4M_m} \right)^2 \left(\frac{M_2 - M_1}{\sqrt{t_2} - \sqrt{t_1}} \right)^2 \tag{3.2}$$

where,

D : the diffusion coefficient or diffusivity, mm^2/s

h : the average specimen thickness, mm

M_m : the effective moisture equilibrium content,%; and

$(M_2 - M_1)/(\sqrt{t_2} - \sqrt{t_1})$: the slope of moisture absorption plot in the initial linear portion of the curve, $\sqrt{seconds}^{-1}$

Materials are subjected to all kinds of stresses in real life. Therefore, it is essential to know the behaviour of materials in the pressure of applied stress or force. One of the most common tests used for determining the properties of materials is the tension test. By running this test one would understand how a given material behaves with the applied force. This experiment provides basic material properties, such as strength, stiffness, hardness, ductility and toughness.

Standard methods describe the sample preparation and experimental setting steps (ASTM E8 and ASTM D638). However, the sample preparation of a metallic material is different than that of a plastic material as indicated in those standard methods. Both sides of prepared samples are adjusted with the base and cross-head of tensile machine (Figure 3.2a). After that, a gradual load is applied until the sample breaks. The data generated by the tensile machine stress, strain,

Young's modulus, yield strength and tensile strength of the sample is collected by an attached computer.

Tensile specimens were prepared according to the standard described for plastic materials in ASTM D638. An Instron 5500R materials testing machine aided with Bluehill®2 software was used to determine the tensile strength of GFRP sheet specimens before and after exposures. Few important features followed while the samples were tested in the tensile machines are in Table 3.4. A GFRP sheet sample griped by the cross head and base is shown Figure 3.29.

Table 3.4. Important features used for running test in the tensile machine.

Features	Values
Cross head speed	5 mm/s
Speed	100 data/millisecond
Method	TPSedited.im.tens
Source for tensile strength	Extension

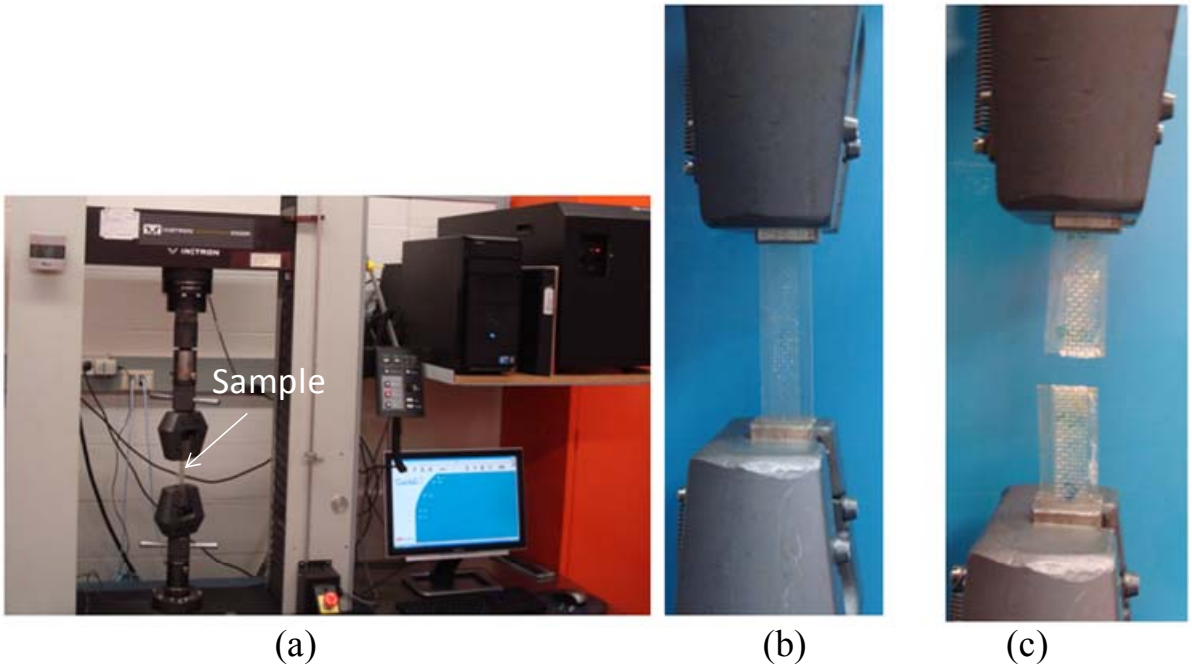

Figure 3.29. Tension test for a GFRP sheet (a) Setting of a tensile machine, (b) before breaking the sheet sample, and (c) after breaking the sheet sample.

3.5. Effects of relative humidity (RH) on GFRP composites (Phase 3)

3.5.1. Overview

Penetration of water into GFRP composites causes strength loss. The extent of strength loss depends on the RH of the exposure environment. Therefore, an attempt was made to identify the effect of RH on the changes of mass (gain and loss) over a wide range of RH. Two sets of samples were prepared. One set was immersed in deionized water until they were saturated. After saturation they were hung in different humidity chambers to identify mass loss. The other set was dried in an oven and also hung in similar humidity chambers to identify mass gain. Detailed descriptions of sample preparation, RH chamber installation, and RH solution preparation are included in the following sections.

3.5.2. Sample preparation

GFRP rebars with 8-mm diameter were cut into 2.54 cm (1 inch) lengths. Any stain/grease was removed from cross-sectional surface according to the method described in ASTM D5229. During sample preparation, grease or stains can develop which can interrupt moisture movement from outside into rebars and vice versa. One set of samples was weighed (baseline mass, W_b) and immersed into deionized water chambers with standard lab conditions. Soaked samples were taken out, wiped by lint free towels, and weighed (current mass, W_i). The percent of water uptake was calculated using Equation 3.1. The mass gain plot as a function of time is shown in Figure 3.30, where one can easily see that samples were saturated in about 50 days. After 3 months, these saturated samples were hung in different RH chambers to identify the effect of RH on mass loss while drying. The other set of samples was oven dried at 50 °C for 24 hours, desiccated, and weighed. The dried samples were hung in similar RH chambers to identify the mass gain while wetting.

3.5.3. Humidity chamber installation

High density poly ethylene (HDPE) bottles with wide openings were used to create humidity chambers. Two holes were made on HDPE stoppers. One hole was used for measuring the humidity and temperature, and the other hole for hanging samples. Three GFRP rebar samples were tied by a copper wire and hung into the chamber by the rubber stopper. The configuration

of RH chambers and probing device of a Traceable® Hygrometer are shown in Figure 3.31. Before hanging samples, the RH chambers were allowed to reach their equilibrium RH values.

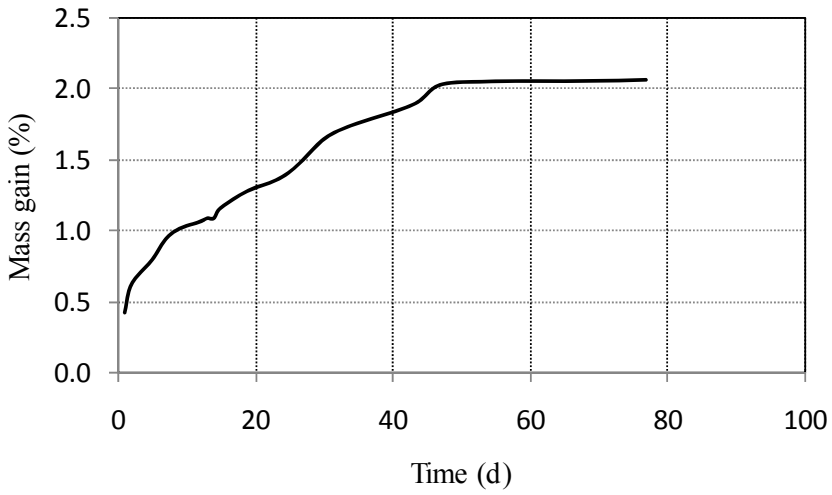

Figure 3.30. Mass gain of GFRP rebars as a function of time.

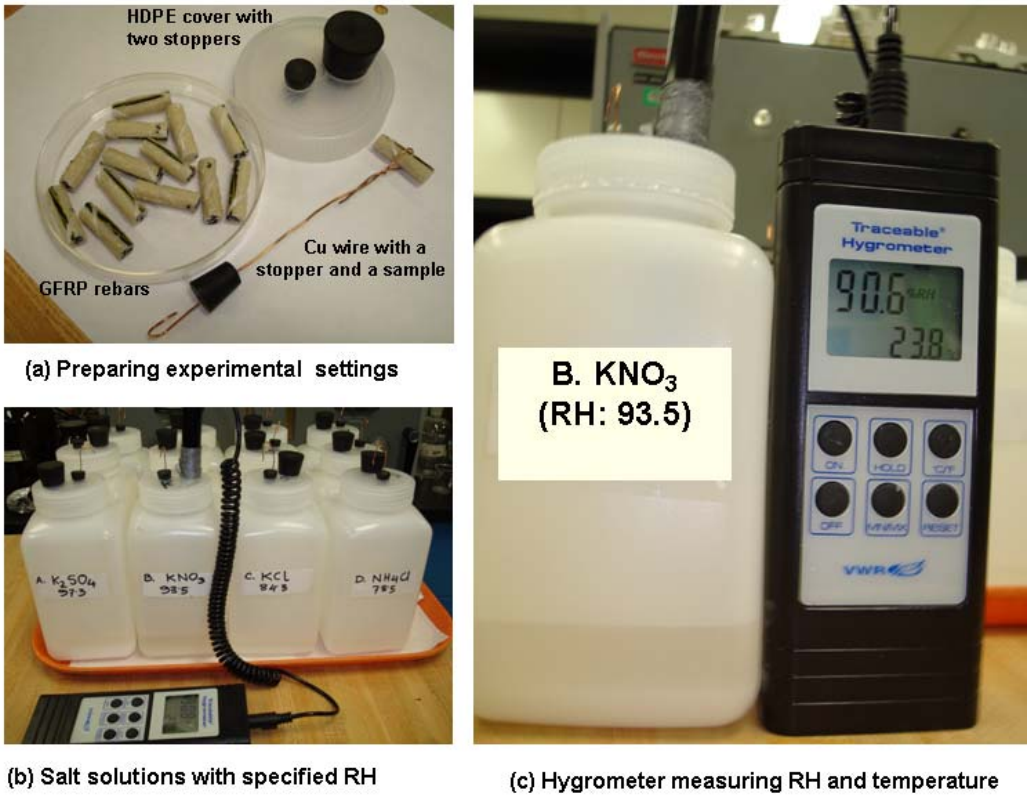

Figure 3.31. Configuration of the RH chambers and probing device.

3.5.4. Salt solutions preparation

A saturated solution of a specific salt creates a specific RH. The environment of RH is created by adding water to pure salts. Stirring the mixture dissolves a certain amount of salt to saturate the solution and the extra salt will be deposited at the bottom. To prepare a specific salt solution with a given equilibrium RH, the European standard (1996) was used. The saturated salt solution provides specific humidity conditions by absorbing or giving off moisture to the vapour space above the solution. In this study, a hygrometer probe with an accuracy of ±1% previously calibrated with saturated salt solutions over the range 10% -100% was used to measure the experimental RH in the chambers. A list of the salts used to produce the saturated salt solutions and corresponding equilibrium RH is shown in Table 3.5. To reach the theoretical equilibrium RH of a specific salt solution, the following conditions were maintained as recommended in the literature (Hygrodynamics Inc. 1964).

1. Water level on un-dissolved salts was kept as minimum as possible. Higher water levels lead to lower RH than anticipated.
2. Large solution surface and small vapor space were maintained to achieve the required RH of a specific salt.
3. Analytical grade salts and deionized water were used to prepare all salt solutions.
4. An air tight environment was created to reach and maintain the theoretical equilibrium of a specific salt.

Table 3.5. RH values produced by the saturated solutions of different salts.

Salt	Chemical formula	RH values at room temperature (22 ± 0.5 °C) (%)
Potassium nitrate	KNO_3	92.6
Potassium chloride	KCl	83.6
Sodium chloride	NaCl	74.5
Magnesium nitrate	$MgNO_3$	53.1
Potassium carbonate	K_2CO_3	42.1
Magnesium chloride	$MgCl_2$	30.7
Potassium acetate	CH_3COO-K	23.5
Sodium hydroxide	NaOH	8.1

3.5.5. Methods

To observe the mass changes of GFRP rebars at different RH, samples were hung at the RH levels shown in Table 3.5 inside the humidity chambers. On the one hand, for the mass loss calculation, saturated samples (W_b) were hung in the RH chambers until they reached a constant mass (W_i) while drying. On the other hand, for the mass gain calculation, dried samples (W_b) were exposed to similar RH chambers until they reached a constant mass (W_i) while wetting. The percent of mass loss and mass gain were calculated using Equation 3.3, whereas the moisture diffusivity was calculated using Equation 3.4.

CHAPTER FOUR
GFRP REBARS IN ACCELERATED AGEING CONDITIONS (PHASE 1)

4.1. Overview

GFRP rebars exposed to highly alkaline solutions will be interacting with all water molecules (H_2O) and any ions (M^+, H_3O^+, and OH^-) produced by dissolving metal hydroxides in water. An important interaction of solution species with the GFRP samples is related to the potential ingress of alkali ions into the rebars, which could cause a degradation of the E-glass fibres. The ingress of chemical species can be explained by molecular diffusion and advective transport (Bird et al. 2007; Tosun 2007). The performance of GFRP rebars under accelerated ageing conditions has mostly been studied by assessing the loss of strength or some other relevant material property of rebars (Chen et al. 2006; Dejke and Tepfers 2001; Murphy et al. 1999; Porter et al. 1997; Katsuki and Uomoto 1995). The strength loss of GFRP rebars, for instance, has been shown to be larger in alkali solutions than in water (Chin et al. 1999; Chin et al. 1997). However, the mechanisms of how alkali solutions affect the strength loss are not clearly elucidated. Therefore, an attempt was made in this study to understand the penetration of water and alkali ions into GFRP rebars and how they affect the potential degradation of fibre, matrix, and their interface under accelerated ageing conditions. In the following sections, findings about the potential penetration of alkali ions into the rebars, together with their subsequent effect on the VE matrix, E-glass fibre, and their interphase are presented.

4.2. Penetration of harmful species

The presence of penetrating alkali ions into GFRP rebars was investigated initially by X-ray mapping of BE images and crosschecked by line EDS scans as described in Section 3.2.7.

4.2.1. Assessment of potential alkali ions penetration by X-ray mapping

X-ray mapping for alkali ions, such as Na, K, and Ca were performed for unconditioned samples once and for conditioned samples at the intervals of 1, 3, and 12 months. The alkali ions under investigation were continuously available in the exposure environments where the samples were immersed. On the other hand, these elements are either totally absent from the polymer matrix of unconditioned samples or only present as filler. It has been shown that alumino-silicate phosphate (ASP) is actually present in the polymer matrix as a filler in GFRP rebars (Bank et al. 1998). This filler contributes only Al and none of the other alkali ions present in the considered solutions, such as Na, K, and Ca. If any alkali ions had penetrated, they should be present at some points of the rebar sample, especially those closer to the outer boundary. The experimental results after each interval are discussed in the following paragraphs.

Findings after 1 month

Two major issues were considered when examining samples after all considered intervals: (i) the potential penetration of alkali ions into the rebars, and (ii) the most aggressive exposure conditions. Among the three alkali ions in the exposure solutions, Na is the smallest alkali ion, and therefore the possibility of Na penetration into GFRP rebars should be higher than any other alkali. The exposure temperatures for immersed samples were 23 °C, 50 °C, was 75 °C; as discussed in Section 3.2.3. As a result, the GFRP samples immersed in the NaOH solution at 75 °C should have the strongest possibility of ions penetration into GFRP rebars, because the solution contains Na ions which have the smallest diameter as compared to the other ions present in solution. Therefore, GFRP samples immersed in NaOH solution at 75 °C were examined first after one month to observe whether any Na ions had penetrated the rebars. To answer the question as to whether Na had penetrated or not, an X-ray mapping for Na was carried out.

A typical example of a BEI image for a sample immersed in a NaOH solution at 75 °C for one month is shown in Figure 4.1a, and the X-ray mapping on the same image for Na is shown in Figure 4.1b. If Na had penetrated into rebars, it would have been observed in the matrix closer to the boundary in Figure 4.1b; however, no Na ions were detected. A similar technique was utilized to examine other alkali ions, such as K and Ca. Since the smallest alkali (Na) did not penetrate, it is unlikely that other alkali ions (K and Ca) bigger than Na could have penetrated into the rebars. To remove even that little uncertainty, samples immersed in KOH and $Ca(OH)_2$

solutions at 75 °C were examined to assess the penetration of K and Ca, respectively, after one month of exposure. Typical BE images for samples immersed in a KOH and $Ca(OH)_2$ solution at 75 °C for one month are shown in Figures 4.2a, and 4.3a, respectively. The X-ray mappings on those images for K and Ca are shown Figures 4.2b, and 4.3b, respectively. No alkali ions were observed within the GFRP samples even very close to their outer boundaries.

Another question that still remained unanswered was how the alkali ions would behave in mixed alkali solutions, which are more representative of concrete pore solutions. To answer the question of whether the smallest alkali (Na) from mixed alkali solutions penetrated into rebars or not, BE images of a sample immersed in a mixed alkali solution at 75 °C for one month were examined, as shown in Figure 4.4a, and the X-ray mapping on the same image for Na is shown in Figure 4.4b. As can be seen in Figures 4.4a and 4.4b, no Na ions from the mixed alkali solution penetrated into rebars. Therefore, it can be concluded that bigger alkali ions K and Ca from mixed alkali ions solutions would not penetrated into GFRP rebars.

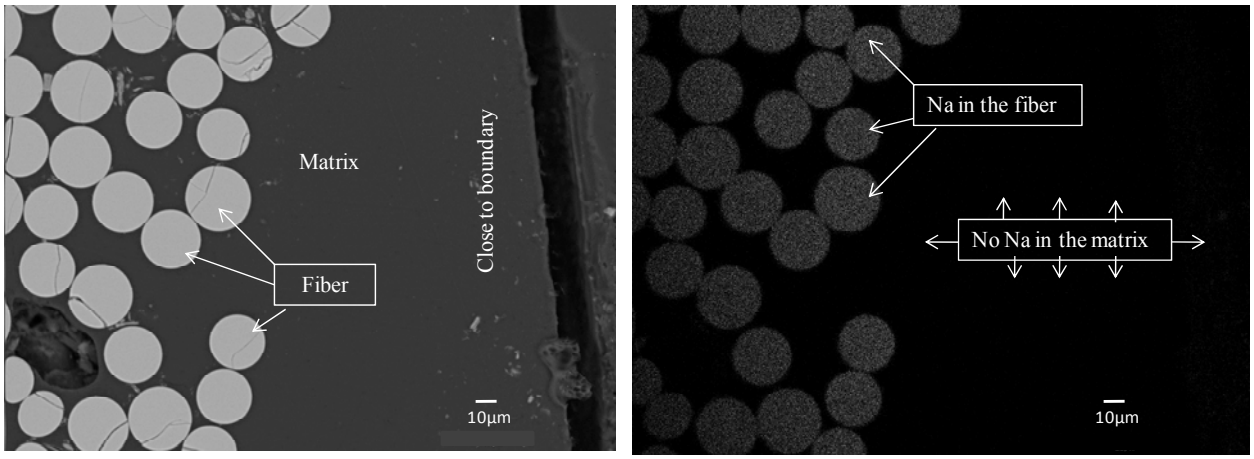

(a) (b)

Figure 4.1. Investigating the presence of Na ions: (a) a BEI of a conditioned sample exposed to a NaOH solution at 75 °C for one month (x500) and (b) an X-ray mapping of the same image for Na ions (x500).

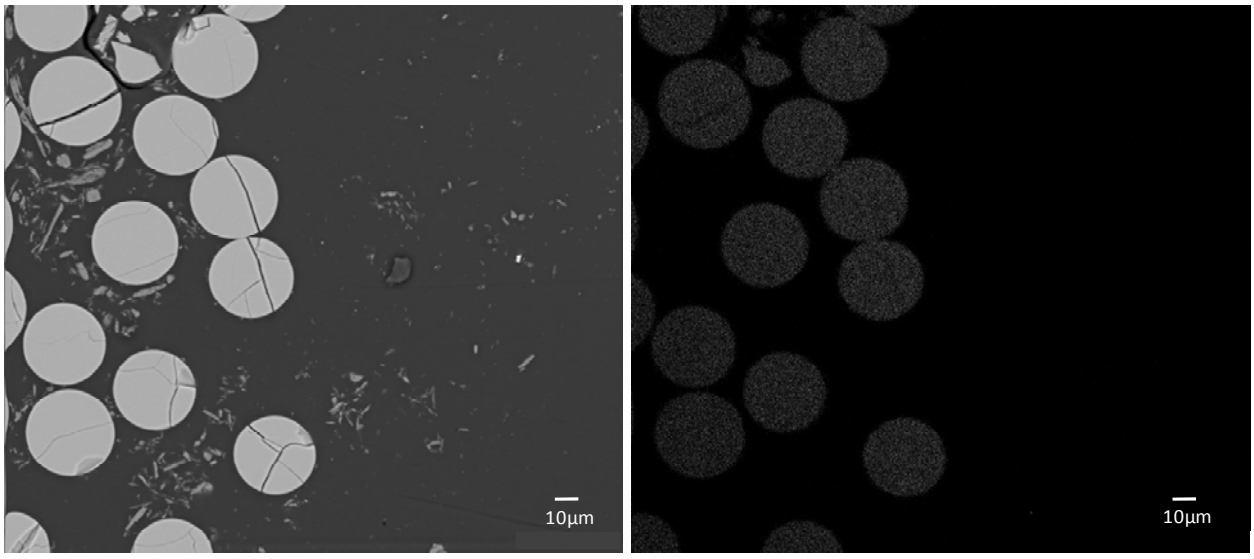

(a) (b)

Figure 4.2. Investigating the presence of K ions: (a) a BEI of a conditioned sample exposed to a KOH solution at 75 °C for one month (x500) and (b) an X-ray mapping of the same image for K ions (x500).

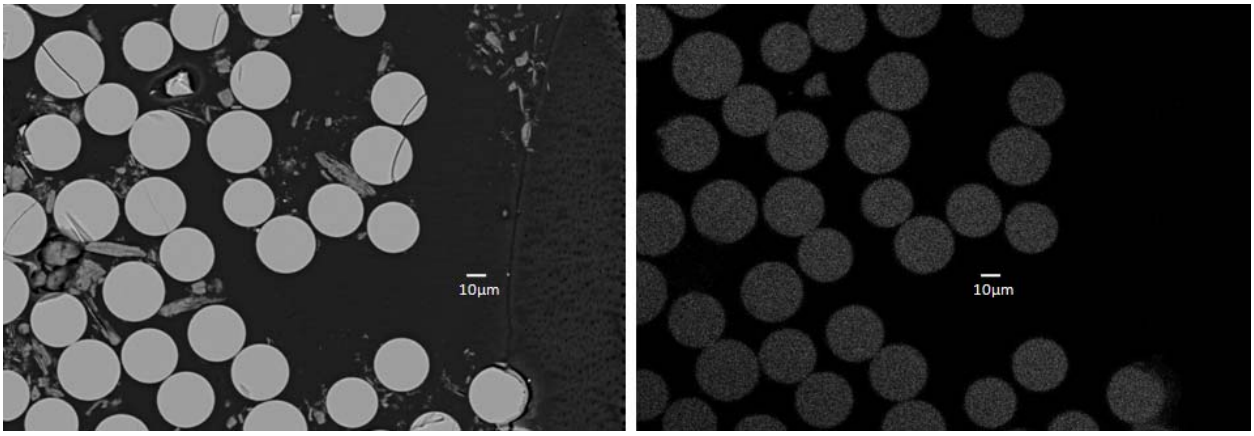

(a) (b)

Figure 4.3. Investigating the presence of Ca ions: (a) a BEI of a conditioned sample exposed to a Ca(OH)2 solution at 75 °C for one month (x500) and (b) an X-ray mapping of the same image for Ca ions (x500).

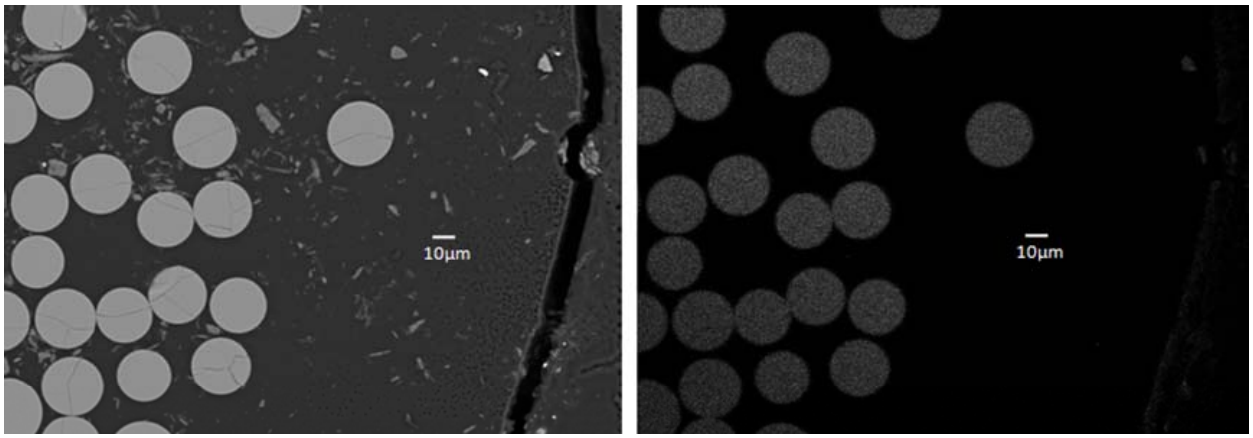

(a) (b)

Figure 4.4. Investigating the presence of Na ions: (a) a BEI of a conditioned sample exposed to a mixed alkali solution at 75 °C for one month (x500) and (b) an X-ray mapping of the same image for Na ions (x500).

After analyzing all potential cases discussed above, no alkali ions were observed to have penetrated after one month of exposure at 75 °C. Therefore, the probability of any alkali ions penetrating for other exposure temperatures (23 °C and 50 °C) is unlikely. Hence, it can be concluded that no alkali ions penetrated into any samples at all exposure conditions after one month.

Findings after 3 months

As no alkali ions penetrated after one month of exposure, samples were examined again after three months. Again, samples with the greatest potential for ion penetration were considered, i.e. the samples in NaOH solution at 75 °C, and the samples conditioned in mixed alkali solution at 75 °C. The BE images of the samples immersed in NaOH and mixed alkali solutions at 75 °C for 3 months were examined, and are illustrated in Figures 4.5a, and 4.6a, respectively. The X-ray mappings on the same images for Na are shown in Figures 4.5b and 4.6b. No Na penetrated into either sample. Therefore, it can be concluded that no alkali ions penetrated any of the samples at all considered temperatures after 3 months.

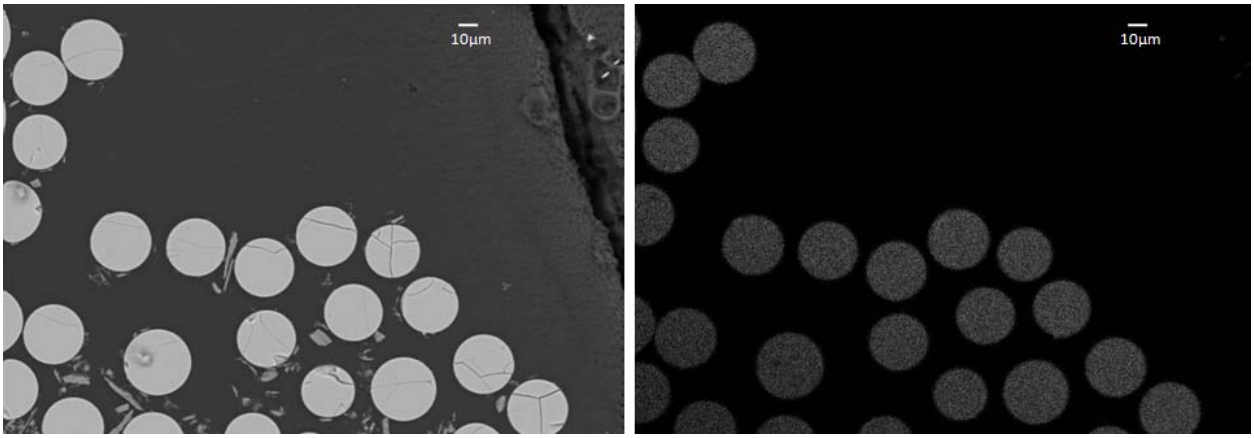

(a) (b)

Figure 4.5. Investigating the presence of Na ions: (a) a BEI of a conditioned sample exposed to a NaOH solution at 75 °C for three months (x500) and (b) an X-ray mapping of the same image for Na ions (x500).

Findings after 12 months

Similar experiments were conducted for the samples immersed in NaOH and mixed alkali solutions at 75 °C after 12 months. The BE images of those samples are shown in Figures 4.7a and 4.8a. The X-ray mappings on the same images for Na are shown in Figures 4.7b and 4.8b. No Na ions penetrated in to either sample. Therefore, it can be concluded that no alkali ions penetrated, even after 12 months of exposure at 75 °C.

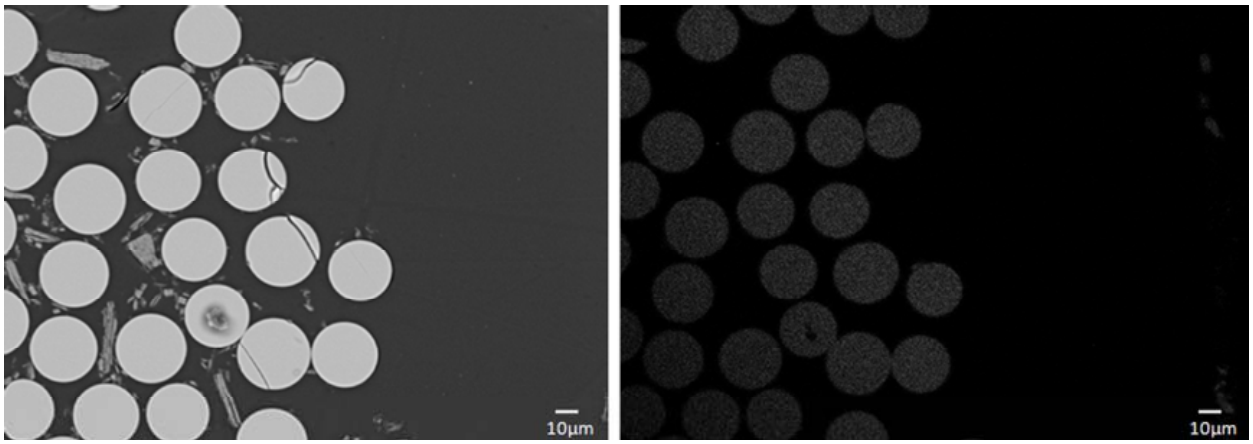

(a) (b)

Figure 4.6. Investigating the presence of Na ions: (a) a BEI of a conditioned sample exposed to a mixed alkali solution at 75 °C for three months (x500) and (b) an X-ray mapping of the same image for Na ions (x500).

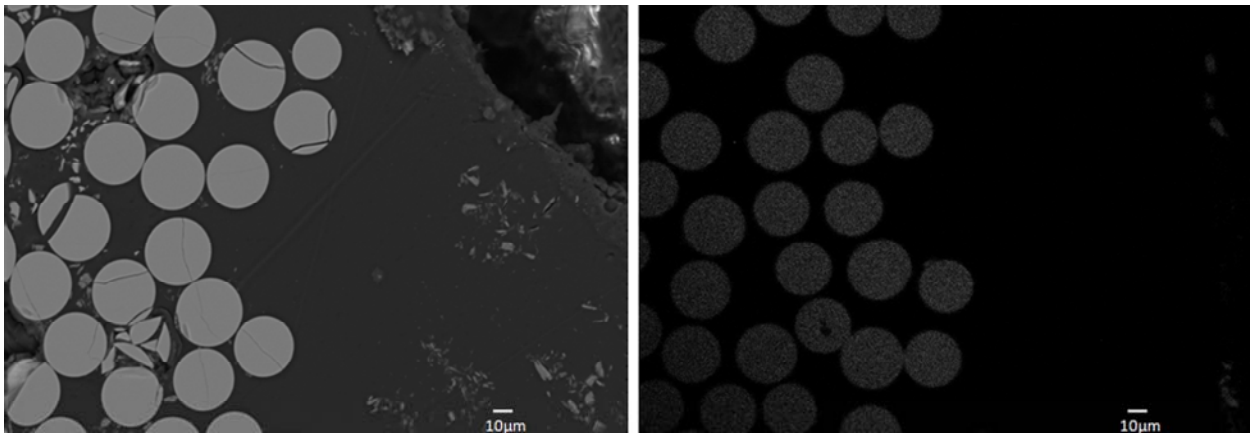

(a) (b)

Figure 4.7. Investigating the presence of Na ions: (a) a BEI of a conditioned sample exposed to a NaOH solution at 75 °C for three months (x500) and (b) an X-ray mapping of the same image for Na ions (x500).

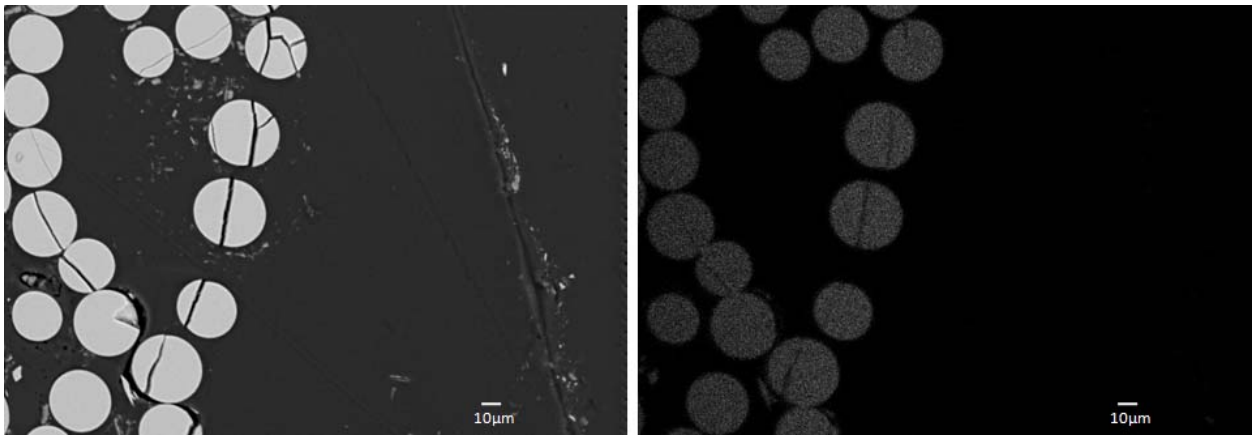

(a) (b)

Figure 4.8. Investigating the presence of Na ions: (a) a BEI of a conditioned sample exposed to a mixed alkali solution at 75 °C for three months (x500) and (b) an X-ray mapping of the same image for Na ions (x500).

After observing the above scenarios, one can conclude that no alkali ions had penetrated into GFRP rebars from any types of exposure solutions at elevated temperatures after 12 months of exposure.

4.2.2. Penetration of alkali ions crosschecked by a line EDS

The methods of detecting alkali ions in GFRP rebars are discussed in Section 3.2.7. Given the findings of the previous section, a more precise line EDS scan for Na was also conducted for the samples that were considered most vulnerable to chemical attacks.

As discussed in Section 4.2.1, Na has the highest probability of penetration due to its smallest size among other alkali ions. In addition, the most aggressive situation is the highest temperature (75 °C). Therefore, the samples immersed in NaOH solution at 75 °C were examined with the line EDS after 1, 3, and 12 months. The line EDS scans of those samples conditioned in NaOH solutions for 1, 3, and 12 months are shown in Figures 4.9, 4.10 and 4.11, respectively. All samples showed high concentrations of Na on fibres and no/low concentration in the matrix.

As none of the alkali ions was detected in the matrix of tested samples at all intervals by X-ray mappings of BE images and crosschecked with a line EDS scan, it can be concluded that alkali ions had not penetrated through the GFRP rebars under the considered exposure conditions. However, since the GFRP rebars gained moisture, as discussed in Section 3.4.2, water molecules must have been able to penetrate. Hence, for all practical purposes, the outer polymeric layer of GFRP rebars seems to be acting as an effective semi-permeable membrane allowing water to penetrate but blocking alkali ions.

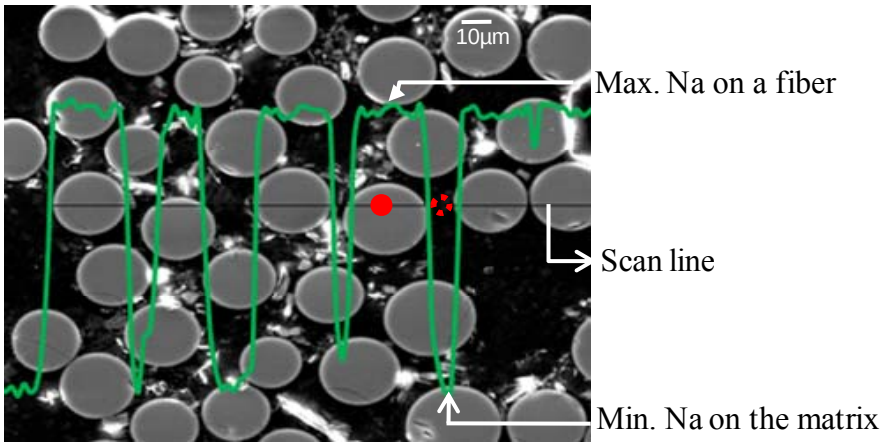

Figure 4.9. Variation of Na counts along a line by an EDS of a conditioned sample immersed in a NaOH solution at 75 °C for one month (x500).

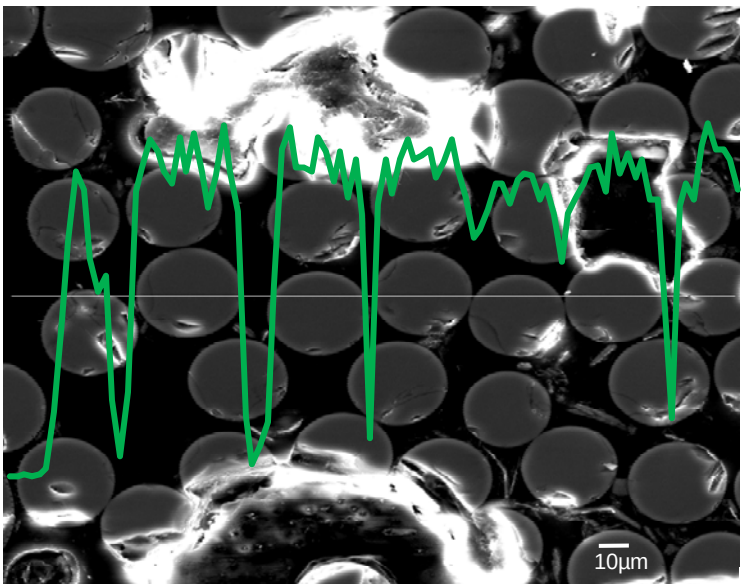

Figure 4.10. Variation of Na counts along a line by an EDS of a conditioned sample immersed in a NaOH solution at 75 °C for nine months (x500).

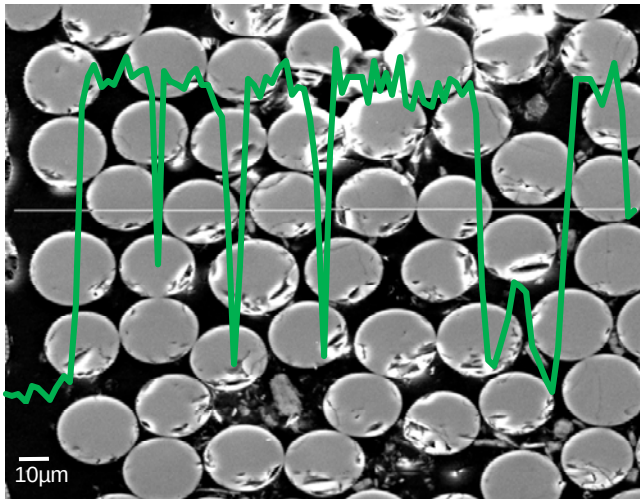

Figure 4.11. Variation of Na counts along a line by an EDS of a conditioned sample immersed in the mixed alkali solution at 75 °C for 12 months (x500).

4.3. Deterioration at the fibre matrix interphase

The fibre-matrix interphase is the critical region where several kinds of deterioration can occur. The deterioration can occur due to any of the following reasons: (i) debonding at the interphase, (ii) deterioration of polymer matrix, and (iii) deterioration of fibres. The following section

discusses the experimental results obtained by observing the deterioration fibre-matrix interphase.

4.3.1. Examining the Debonding at the fibre-matrix interphase by an SEM

Debonding of fibres from the matrix was assessed by analyzing highly magnified SEM images of conditioned samples after 1, 3, and 12 months of exposure. It is expected that samples immersed in the highest temperatures (75 °C) are more prone to chemical attacks than the samples immersed in lower temperatures (23 °C and 50 °C). Therefore, the samples immersed in deionized water, NaOH, KOH, $Ca(OH)_2$, and mixed alkali solutions at 75 °C for one month were analyzed. Their highly magnified SEM images are shown in Figures 4.12, 4.13, 4.14, 4.15, and 4.16, respectively. None of the samples showed any sign of debonding. Therefore, it is unlikely that any samples immersed in lower temperatures (23 °C and 50 °C) would show debonding. Hence, it was concluded that no debonding was observed after one month of exposure for any samples.

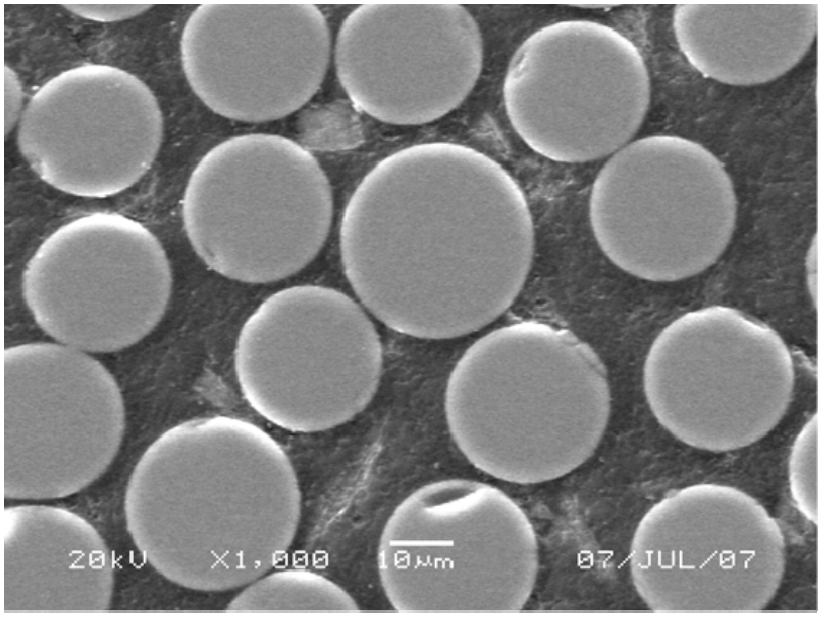

Figure 4.12. SEM images showing no debonding characteristics at fibre-matrix interphase of GFRP samples exposed at 75 °C for one month for a conditioned sample (x1,000) in a deionized water.

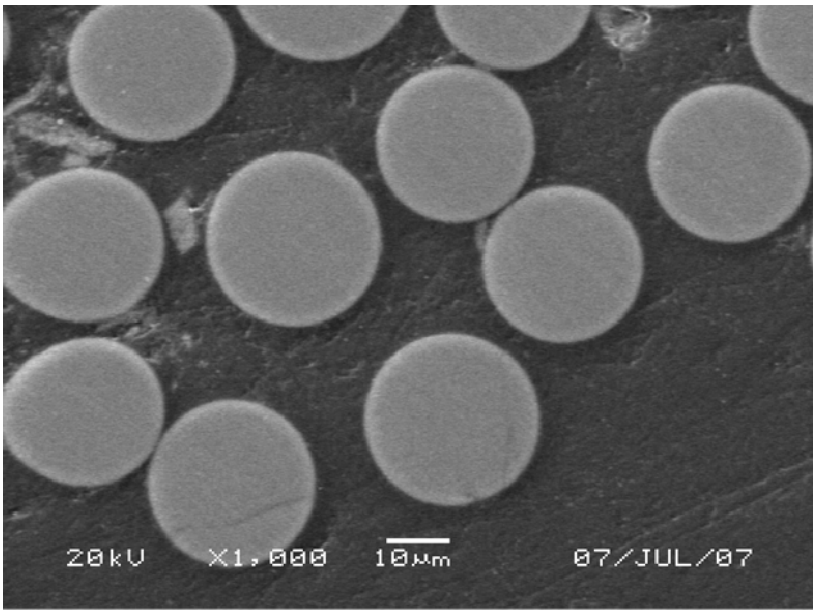

Figure 4.13. SEM images showing no debonding characteristics at fibre-matrix interphase of GFRP samples exposed at 75 °C for one month for a conditioned sample (x1,000) in a NaOH solution.

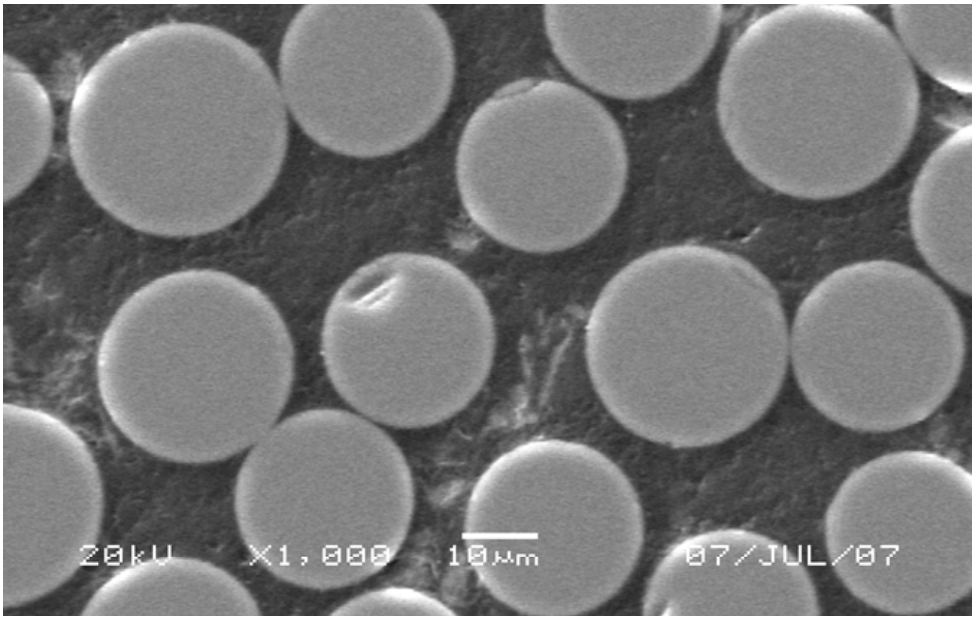

Figure 4.14. SEM image showing no debonding characteristics at fibre-matrix interphase of GFRP samples exposed at 75 °C for one month for a conditioned sample (x1,000) in a KOH solution.

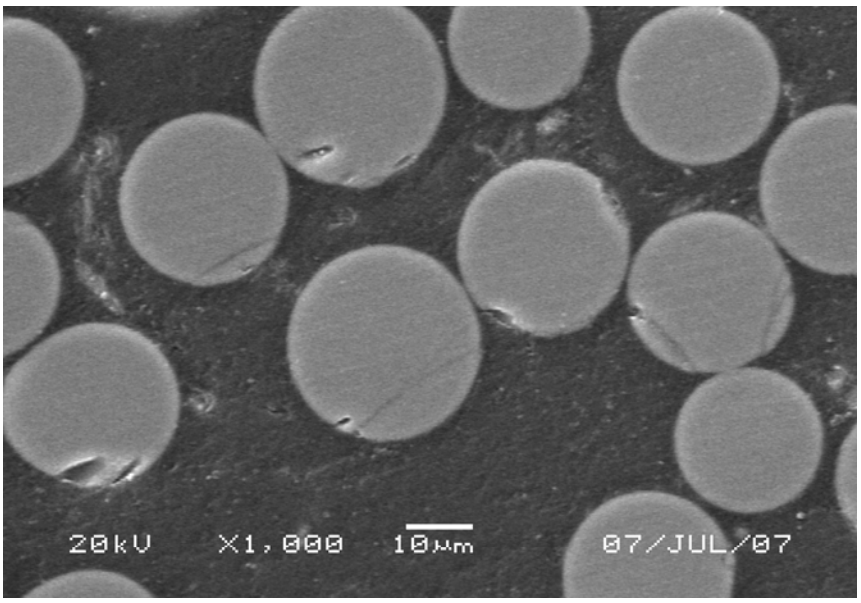

Figure 4.15. SEM image showing no debonding characteristics at fibre-matrix interphase of GFRP samples exposed at 75 °C for one month for a conditioned sample (x1,000) in a $Ca(OH)_2$ solution.

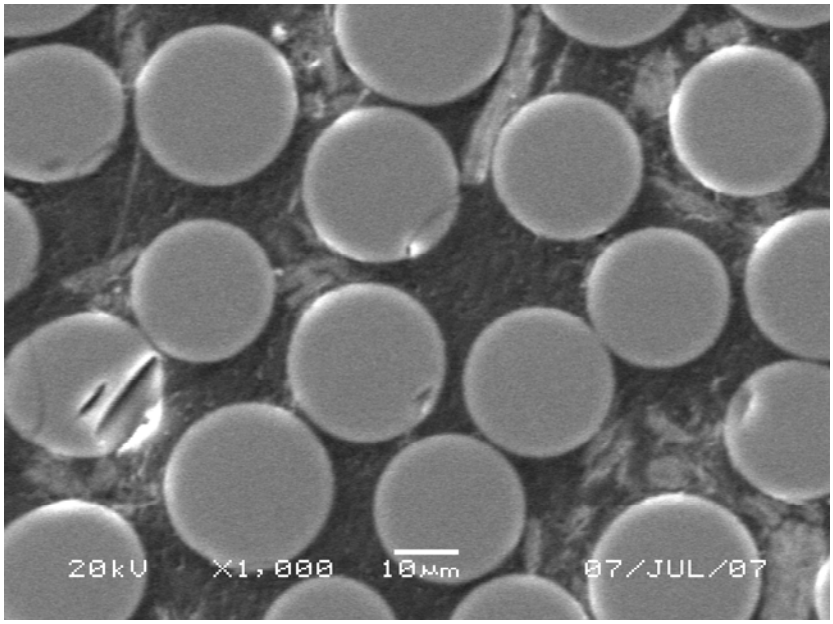

Figure 4.16. SEM image showing no debonding characteristics at fibre-matrix interphase of GFRP samples exposed at 75 °C for one month for a conditioned sample (x1,000) in a mixed alkali solution.

A similar experiment was conducted after 3 months for those samples conditioned in the highest temperature, for the same reasons explained above. Samples immersed in deionized water, NaOH, KOH, $Ca(OH)_2$, and mixed alkali solutions at 75 °C for three months were analyzed. Their highly magnified SEM images are shown in Figures, 4.17, 4.18, 4.19, 4.20, and 4.21, respectively. As was observed after one month, no fibre-matrix debonding was observed after three months. Moreover, the highly magnified SEM images of two samples most vulnerable to attack – immersed in NaOH and mixed alkali solutions – had shown no signs of debonding. The reasons for selecting these two samples for the high magnification are discussed in Section 4.1.1. Observing the scenarios after three months, one can conclude that no signs of debonding at the fibre-matrix interphase for any samples in any exposure conditions are present.

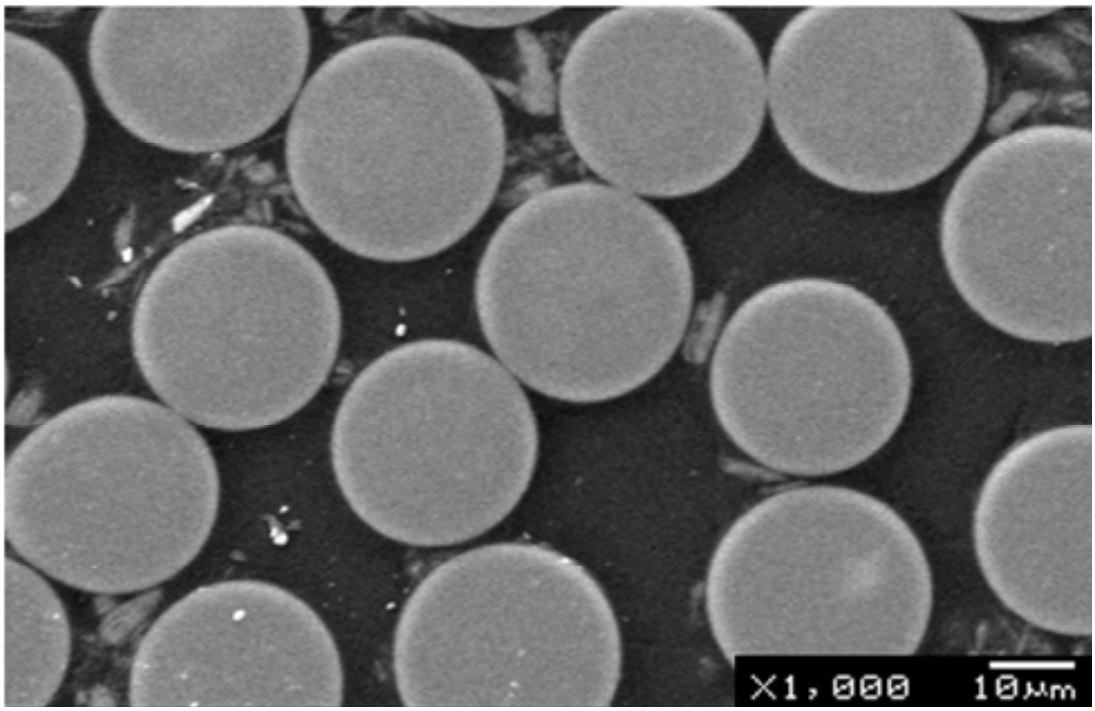

Figure 4.17. SEM image showing no debonding characteristics at fibre-matrix interphase of GFRP samples exposed at 75 °C for 3 months for a conditioned sample (x1,000) in deionized water.

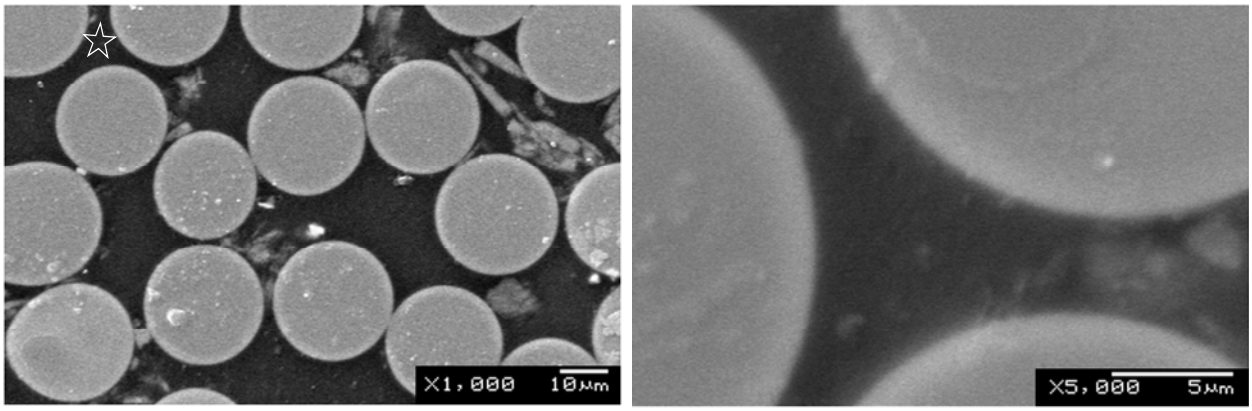

(a) (b)

Figure 4.18. SEM images showing bonding characteristics at fibre-matrix interphase of GFRP samples exposed at 75 °C for 3 months: (a) a conditioned sample (x1,000) in a NaOH solution showing no debonding, (b) the same conditioned sample at higher (x5,000) magnification. The highly magnified portion is shown by a star on image 'a'.

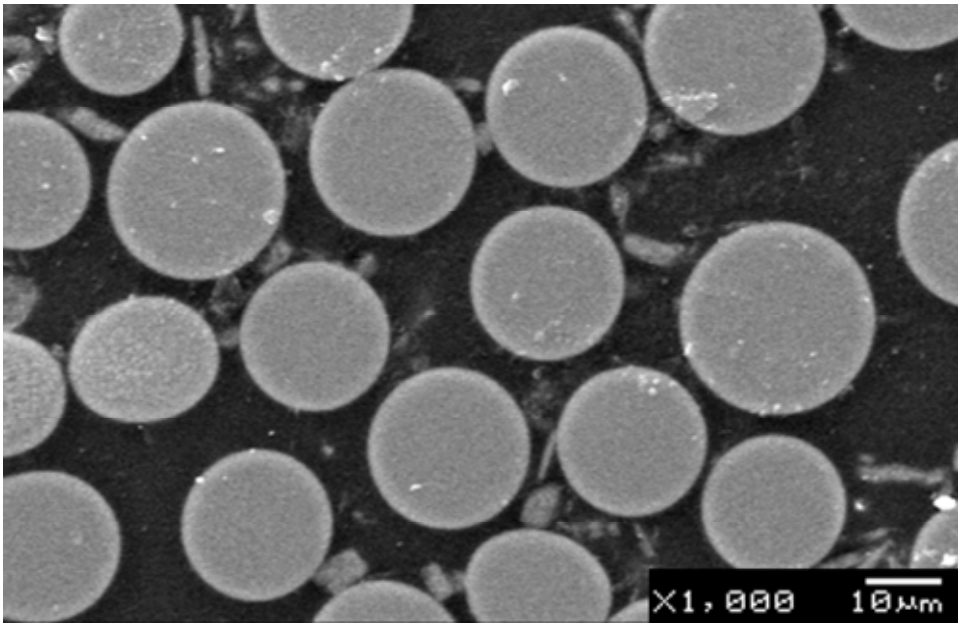

Figure 4.19. SEM image showing no debonding characteristics at fibre-matrix interphase of GFRP samples exposed at 75 °C for 3 months for a conditioned sample (x1,000) in a KOH solution.

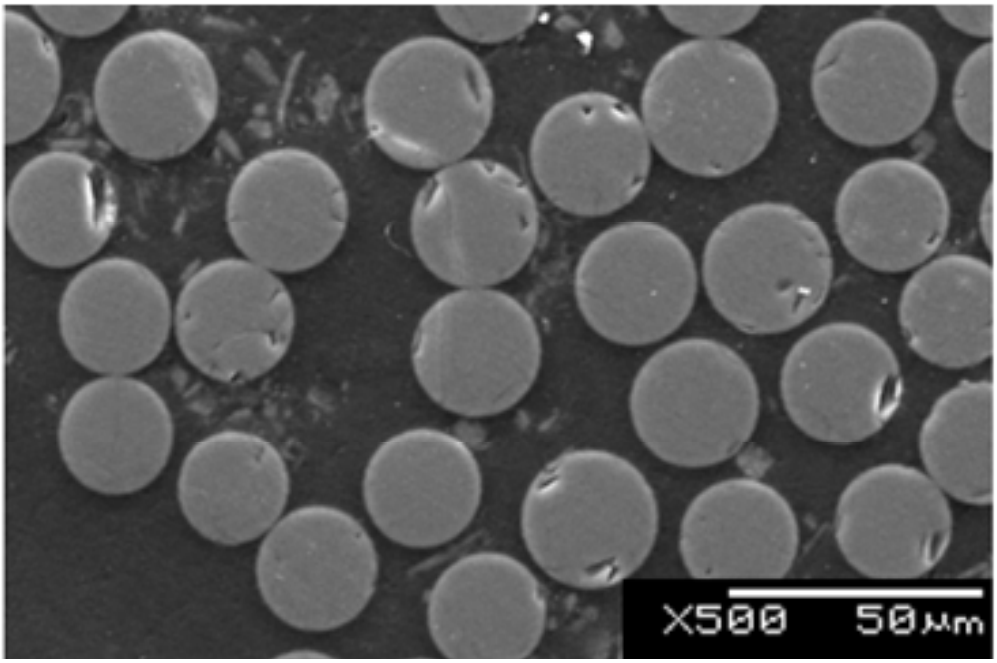

Figure 4.20. SEM image showing no debonding characteristics at fibre-matrix interphase of GFRP samples exposed at 75 °C for 3 months for a conditioned sample (x500) in a $Ca(OH)_2$ solution.

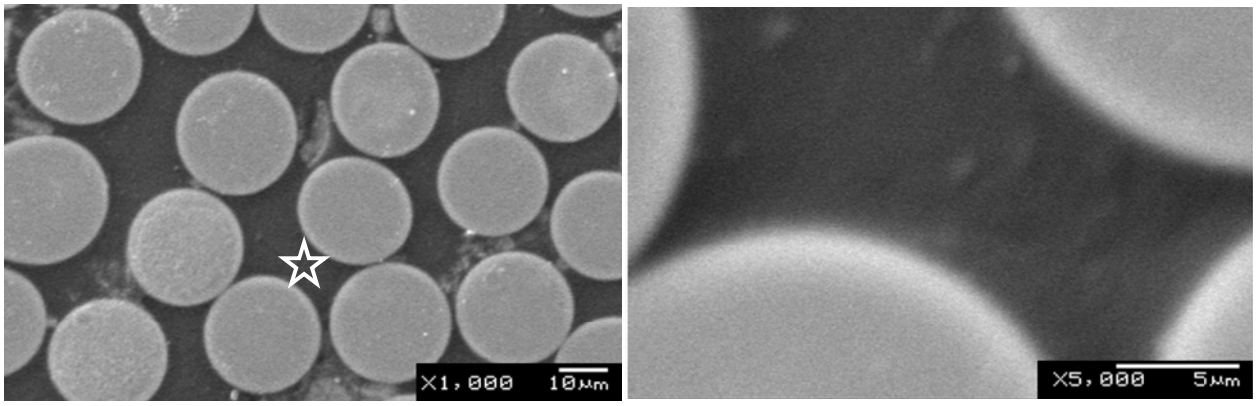

(a) (b)

Figure 4.21. SEM image showing bonding characteristics at fibre-matrix interphase of GFRP samples exposed at 75 °C for 3 months: (a) a conditioned sample (x1,000) in a mixed alkali solution shows no debonding, (b) the same conditioned sample at higher (x5,000) magnification. The highly magnified portion is shown by a star on image 'a'.

Although most samples did not show any sign of debonding for all exposure conditions after three months of study, SEM images of samples conditioned at 75 °C showed signs of debonding at the fibre matrix interphase after 12 months. Samples immersed in deionized water, NaOH, KOH, $Ca(OH)_2$ and mixed alkali solutions at 75 °C for one month were analyzed and their highly magnified SEM images are shown in Figures 4.22, 4.23, 4.24, 4.25, and 4.26, respectively. Irrespective of exposure solutions, all samples immersed at 75 °C showed clear signs of debonding. In other words, debonding was observed only in samples exposed to 75 °C, and seems to be the same regardless of whether the conditioning solution had alkali ions or not.

Interestingly, samples exposed to lower temperatures did not show any sign of debonding. Figures 4.27 and 4.28 are SEM image showing no signs of debonding at fibre-matrix interphase of GFRP samples conditioned in solutions at 50 °C after 12 months of exposure in a NaOH and mixed alkali solutions.

Deterioration at the fibre-matrix interphase can be explained with the deterioration mechanisms of the rebars' constituents, such as fibre, matrix, and sizing. Among all adhesion theories, the chemical bonding theory provides an explanation for the most significant mechanism contributing to the binding of fibres to the matrix. Choice of an appropriate coupling agent in sizing seems to be a major controlling factor. The fibre-matrix interphase is a critical area where many kinds of potential deterioration mechanisms can take place in FRP composites. Fibres and the matrix constitute a major portion of the composite, while sizing used to promote the fibre-matrix adhesion represents only about two percent by weight (Thomason and Dwight 2000). However, they greatly affect the performance of GFRP rebars (Marsden 1990). Deterioration at the interphase relies to a large extent on the performance of sizing and exposure conditions. It is believed that debonding at the fibre-matrix interphase, observed at 75 °C, is very likely due to hydrolysis of the fibre sizing by water at that high temperature.

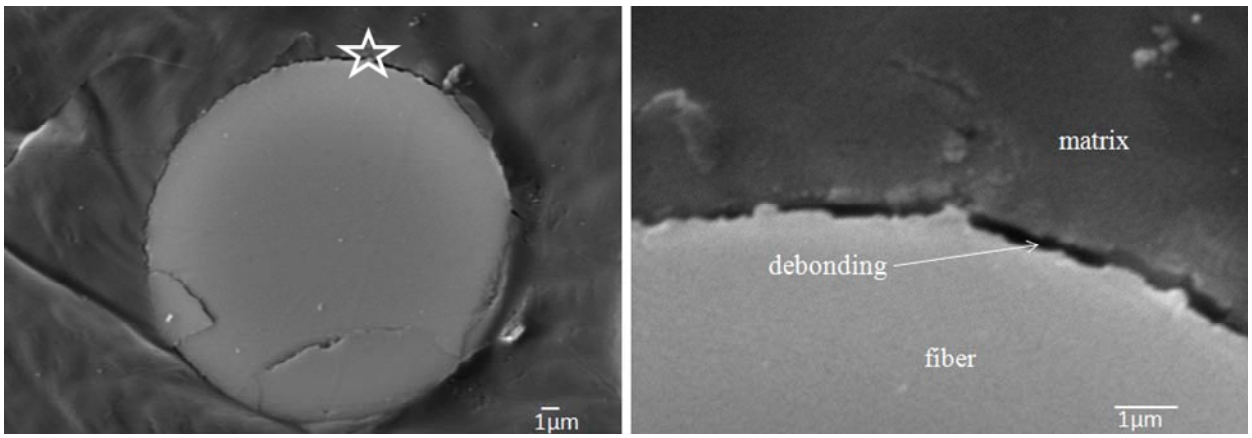

(a) (b)

Figure 4.22. SEM images showing debonding characteristics at fibre-matrix interphase of GFRP samples exposed at 75 °C for 12 months: (a) a conditioned sample (x1,000) in deionized water shows clear debonding, (b) the same conditioned sample at higher (x5,000) magnification. The highly magnified portion is shown by a star on image 'a'.

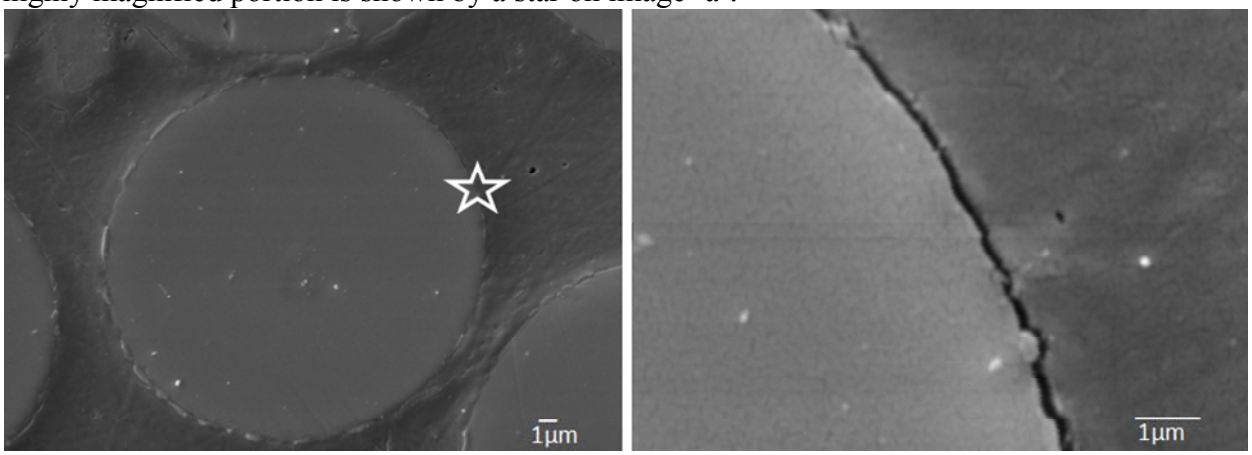

(a) (b)

Figure 4.23. SEM images showing debonding characteristics at fibre-matrix interphase of GFRP samples exposed at 75 °C for 12 months: (a) a conditioned sample (x1,000) in a NaOH solution shows clear debonding, (b) the same conditioned sample at higher (x5,000) magnification. The highly magnified portion on is shown by a star on image 'a'.

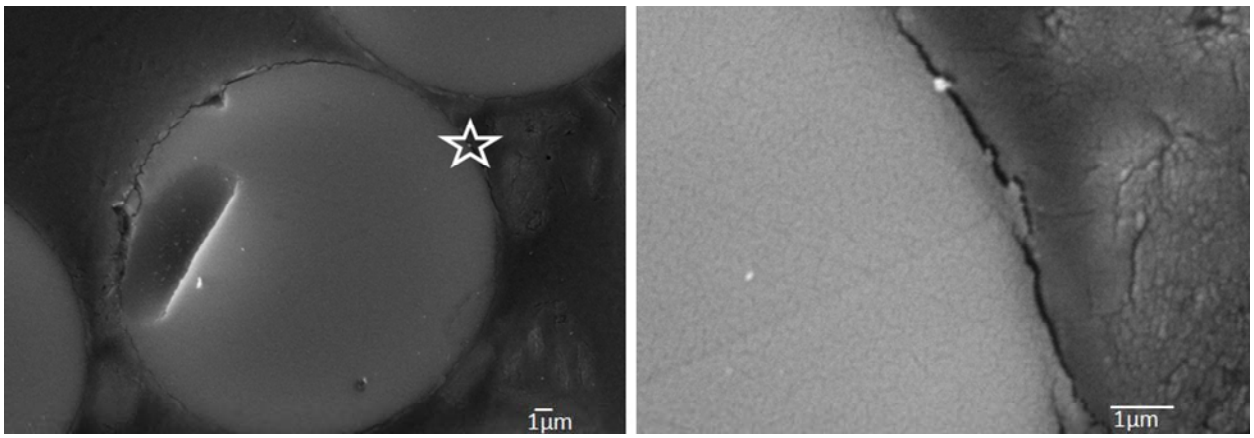

(a) (b)

Figure 4.24. SEM images showing debonding characteristics at fibre-matrix interphase of GFRP samples exposed at 75 °C for 12 months: (a) a conditioned sample (x1,000) in a KOH solution shows clear debonding, (b) the same conditioned sample at higher (x5,000) magnification. The highly magnified portion is shown by a star on image 'a'.

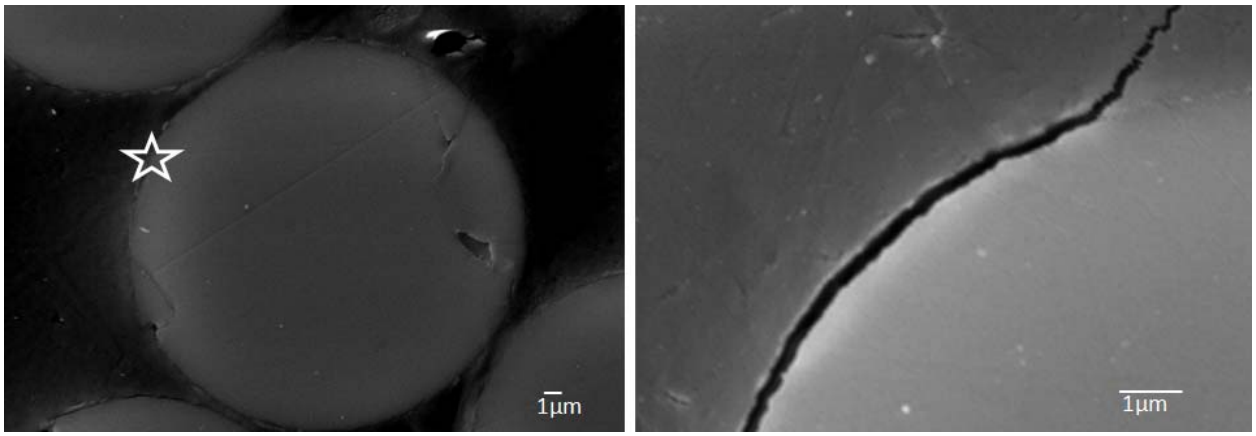

(a) (b)

Figure 4.25. SEM images showing debonding characteristics at fibre-matrix interphase of GFRP samples exposed at 75 °C for 12 months: (a) a conditioned sample (x1,000) in a $Ca(OH)_2$ solution shows clear debonding, (b) the same conditioned sample at higher (x5,000) magnification. The highly magnified portion is shown by a star on image 'a'.

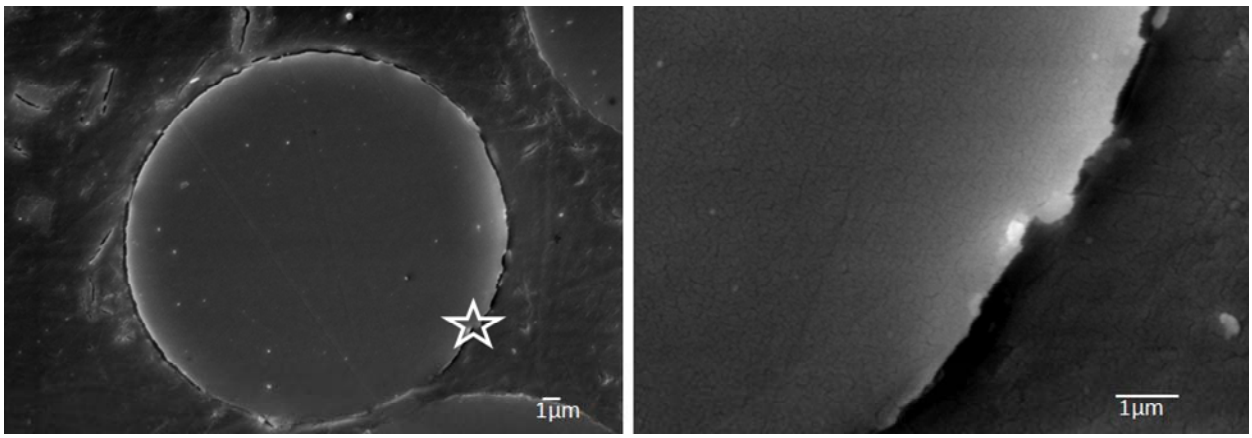

(a) **(b)**

Figure 4.26. SEM images showing debonding characteristics at fibre-matrix interphase of GFRP samples exposed at 75 °C for 12 months: (a) a conditioned sample (x1,000) in a mixed alkali solution shows clear debonding, (b) the same conditioned sample at higher (x5,000) magnification. The highly magnified portion is shown by a star on image 'a'.

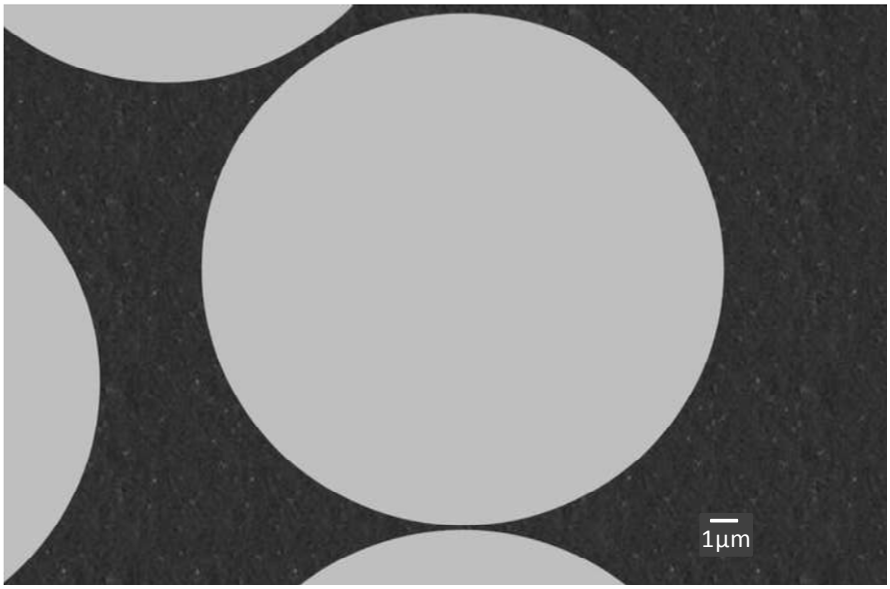

Figure 4.27. Typical SEM image showing no sign of debonding at fibre-matrix interface of GFRP samples conditioned in a NaOH solution at 50 °C after 12 months of exposure.

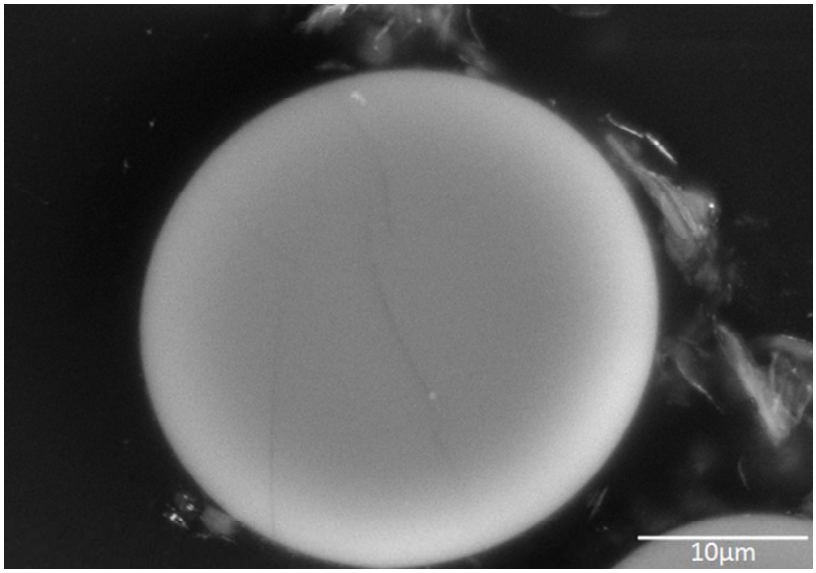

Figure 4.28. Typical SEM image showing no sign of debonding at fibre-matrix interphase of GFRP samples conditioned in a mixed alkali solution at 50 °C after 12 months of exposure.

Exposure conditions that can affect the performance of sizing include a high pH solution, temperature, applied stress, etc. Moreover, defects produced by the fabrication of rebars and the experimental sample preparation expedite the deterioration steps. The degradation of the fibre-matrix interphase by hydrolysis of fibre sizing, and potential subsequent debonding, is not expected in mild exposure conditions (with temperatures lower than 50 °C) even when the pH is about 13. Fibre-matrix debonding can also be triggered either by sample preparation, manufacturing defects, or a combination of both.

Though, none of the major constituents had been observed to deteriorate in this study, significant loss of strength in FRP rebars subjected to harsh environments has been reported by several researchers (Chen et al. 2006; Dejke and Tepfers 2001; Murphy et al. 1999; Porter et al. 1997; Katsuki and Uomoto 1995). The difference in the findings can be explained by the fact that most of those studies considered either weaker materials (such as polyester resins, lower grade VE matrices, different fibre sizing, etc.), harsher exposure conditions (higher temperatures), or the presence of stress or strain, etc.

It is expected that if exposed to harsher environments under accelerated ageing conditions (temperatures around 70 °C in the presence of permanent stress), even the GFRP evaluated in this study could show some signs of degradation, as has been reported in the literature (Benmokrane et al. 2006). The findings of this kind of accelerated tests are, however, in contradiction with a recent field study (Mufti et al. 2007, Mufti et al. 2005, Benmokrane and Cousin 2005), where the glass fibres, the polymer matrix, as well as the GFRP/concrete interface have been shown to remain intact after 6-8 years of service inside concrete. These findings confirmed that the results of accelerated laboratory studies in alkaline solutions, cannot be easily extrapolated to field performance evaluation. Hence, more research is still needed to fully comprehend, explain and quantify the root causes of the behavior exhibited by GFRP composites under accelerated ageing conditions and field conditions, especially in the presence of stress. The rational as to why most design codes keep stress in GFRP rebars around 25% of ultimate stress is mostly based on results of accelerated ageing conditions, knowing that a serious lack of understanding of how those tests could relate to field performance of GFRP inside concrete still exists. This lack of knowledge has led to what may be a sub-optimal, and hence uneconomical, use of these materials by the construction industry.

4.3.2. Assessing the deterioration of the polymeric matrix by an FTIR

The chemical resistance of any polymer matrix depends on the chemical nature of the long molecular chains. The ester bonds in the long polymeric chain are the weakest bonds. The chain scission at the ester bonds occurs by hydrolysis and/or saponification reactions, shown by Eqs. 4.1 and 4.2.

During hydrolysis of esters, OH^- attacks the ester linkage and the long polymeric chain is broken. Changes of hydroxyl groups in the polymer matrix indicate ester hydrolysis. The extent of hydrolysis reactions is measured by determining the ratios of band areas of OH at 3540 cm^{-1} and CH at 2900 cm^{-1} in FTIR spectra (Wade 2003; Benmokrane et al. 2006).

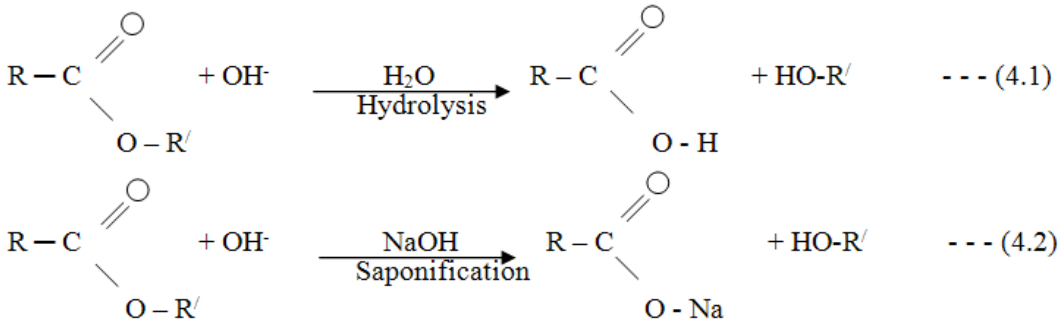

R denotes for alkyl group, whereas $R^{/}$ represents the long polymeric chain

As the CH content is considered constant, any change in the OH/CH should be due to hydrolysis and/or saponification. Thus, the higher OH/CH of conditioned samples over the unconditioned sample will be an indication of matrix degradation. The FTIR spectra of unconditioned and conditioned specimens are shown in Figures 4.29 – 4.34. Spectra obtained from unconditioned specimens are compared with those of conditioned specimens (Table 4.1) and no significant changes in band ratios have been observed in any conditioned specimens. Interestingly, the specimen from a mixed alkali solution, which is the closest representation of concrete pore solution, showed exactly the same band ratio of 1.05 with an unconditioned specimen even at 50 °C. Hence, no major deterioration of the matrix had occurred at 50 °C for most samples even after one year of exposure. These findings of FTIR analyses are similar to those of SEM analyses for the samples immersed in 50 °C for one year. However, the FTIR analysis for samples conditioned for one year and 75 °C was not possible, due to the shortage of samples.

Table 4.1. Band Ratios (OH/CH) of unconditioned and conditioned specimens after 12 months of exposure.

Sample Exposure environments	Uncondi-tioned specimen	Conditioned specimens				
		$Ca(OH)_2$ soln. at 23 °C	NaOH soln. at 50 °C	KOH soln. at 50 °C	$Ca(OH)_2$ soln. at 50 °C	Mixed alkali soln. at 50 °C
OH/CH	1.05	1.11	1.18	1.10	1.09	1.05

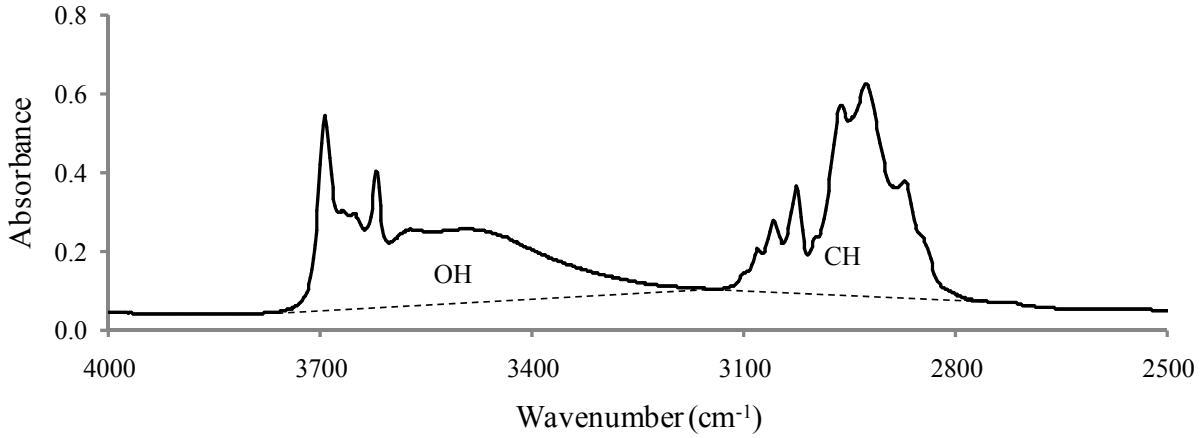

Figure 4.29. Typical FTIR spectra obtained for an unconditioned (control) GFRP rebar sample.

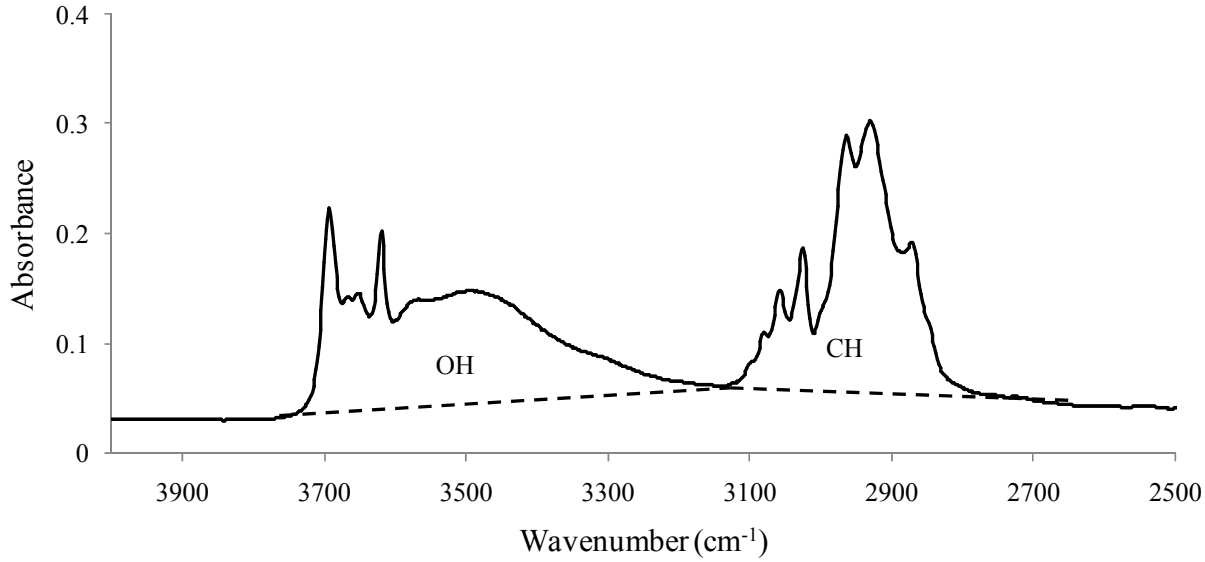

Figure 4.30. Typical FTIR spectra obtained for a conditioned specimen in a mixed alkali solution at 23 °C for one year.

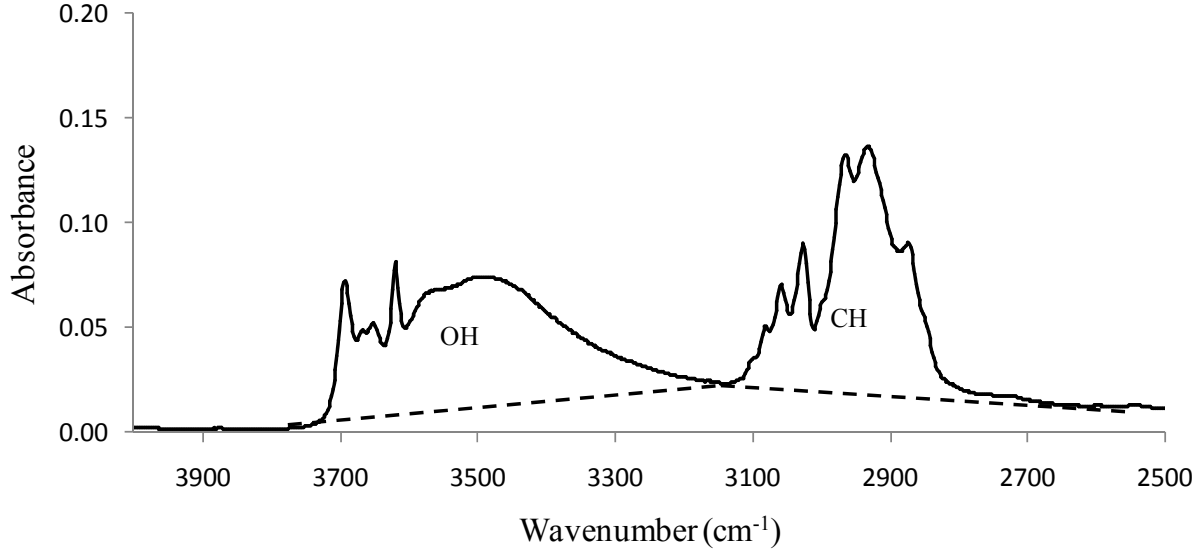

Figure 4.31. Typical FTIR spectra obtained for a conditioned specimen in a NaOH solution at 50 °C for one year.

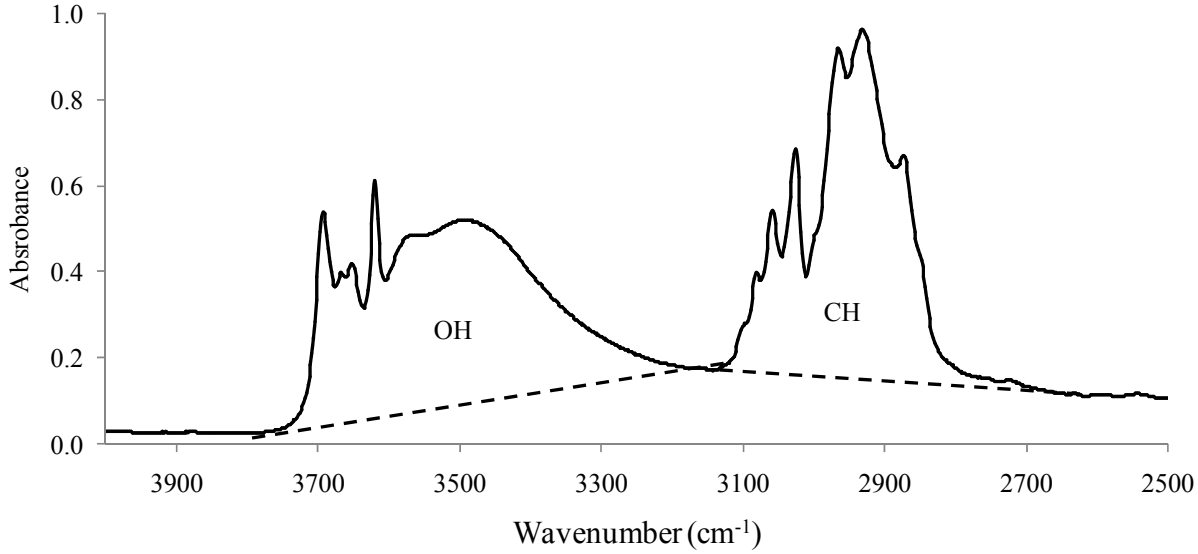

Figure 4.32. Typical FTIR spectra obtained for a conditioned specimen in a KOH solution at 50 °C for one year.

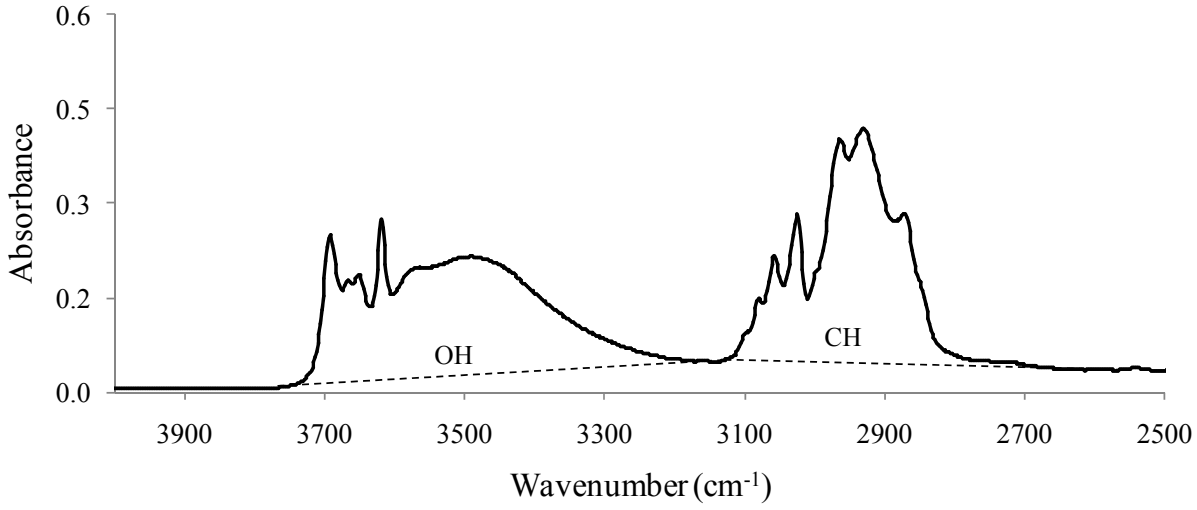

Figure 4.33. Typical FTIR spectra obtained for a conditioned specimen in a $Ca(OH)_2$ solution at 50 °C for one year.

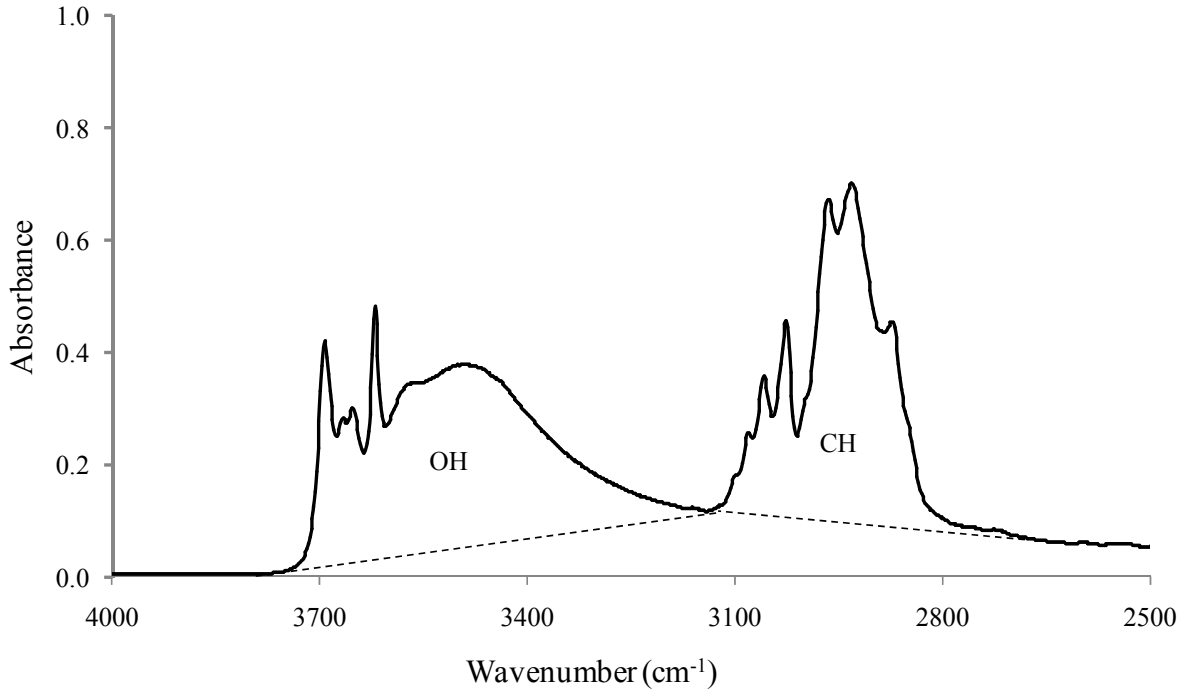

Figure 4.34. Typical FTIR spectra obtained for a conditioned specimen in a mixed alkali solution at 50 °C for one year.

Sample preparation for the FTIR analysis may have contributed to OH/CH band measurements for any specimen. The contents of fibre and matrix in a small amount of FTIR samples might affect the intensity and shape of the absorption bands. Robert et al. (2009)

observed that no deterioration of matrix occurred by the FTIR analysis after immersing 12.7 mm diameter mortar-wrapped samples in water for 240 days at 50 °C. The OH/CH in their study was 0.25 compared to 0.21 for unconditioned samples. The FTIR spectra obtained in the current experiment showed two small additional peaks over 3600 cm^{-1} in comparison to other studies of GFRP rebars (Mufti et al. 2007; Benmokrane and Cousin 2005). The literature shows (Wade 2003) that such peaks might be due to the presence of silicon hydroxide (≡Si-OH) in the silicon networking of E-glass fibre in specimens. They might have been introduced into the specimens from the sample preparation process and/or the fillers in the matrix. During GFRP rebar fabrication, Aluminum Silicate Phosphate (ASP 400) is mixed with VE resin. The Si in fillers may have contributed additional peaks in the FTIR spectra. However, as both unconditioned and conditioned specimens had similar additional peaks, their effects on the overall band measurement are not considered to be very significant.

4.3.3. Assessing the deterioration of glass fibres by a point EDS

E-Glass fibres are known to deteriorate in moist, acidic and alkaline environments when unprotected. This is not necessarily the case for GFRP composites where the polymer matrix is supposed to protect the fibres. The question being addressed in this study is about what kind of protection does the VE matrix provide to the E-glass fibres of the GFRP composite under consideration?

Reviews of fibre degradation in alkaline environments are available in the published literature (Nkurinziza et al. 2005, Onofrei 2005, Chong 1998, Sen et al. 2002, and Yilmaz and Glasser 1991) and will not be repeated here. Fibre dissolution in water, as shown by Equation 4.3, is termed leaching. By this process, alkali ions are extracted out from the glass structures and the leaching process continues as long as alkali ions are available in the glass structure. Those alkali ions are Ca^{2+}, Al^{3+}, K^{1+}, and Mg^{2+}, typically available in fibre composition (Barkatt 2001). The hydroxide ions produced by the leaching process (Equation 4.3) increases the pH of alkaline environment and once the pH exceeds nine it affects Si networks (Si-O-Si and Si-O-Na/K) according to Equation 4.4 (Sonawala and Spontak 1996). The second reaction product (SiO^-) of Equation 4.4 can further react with water molecules to produce OH^- as shown in Equation 4.5.

All the glass degradation processes (Equations. 4.3, 4.4 and 4.5) produce SiOH, which is a gel type product, less dense than the original glass structure. This gel can transport water and

alkali ions, which accelerate the fibre degradation (Tannous and Saadatmanesh 1999). Since silica is not supposed to be present in the matrix, an elemental analysis by point EDS of the matrix very close to the fibre-matrix interface should be able to detect the presence of silica coming from glass dissolution. SEM was also used to detect any sign of fibre degradation, as discussed in Section 4.2.1.

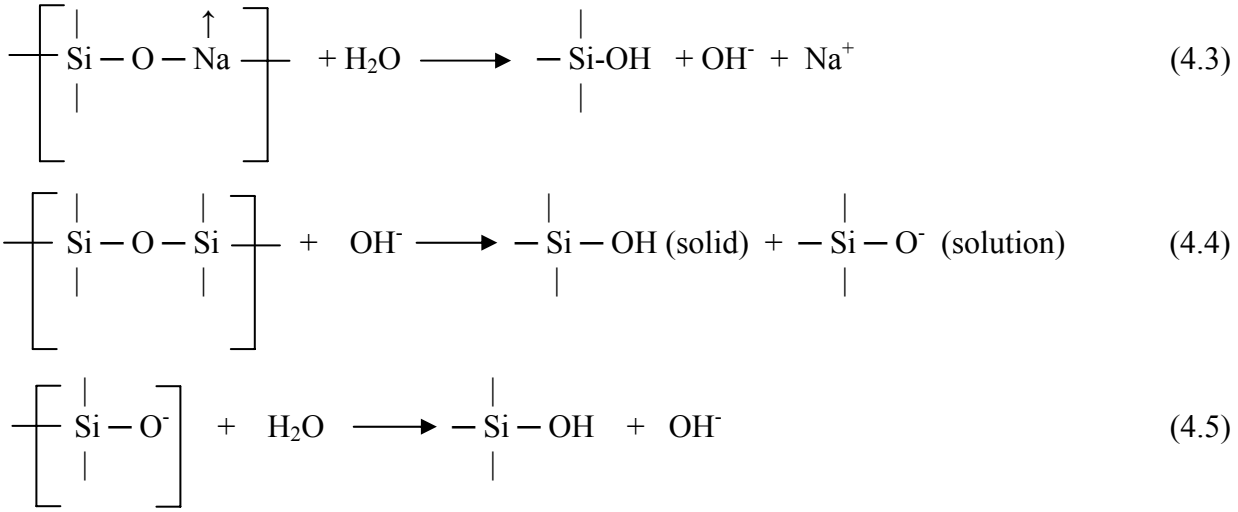

As can be seen in Figure 4.35, no silica could be detected in the matrix of either the unconditioned (i.e. control) sample or that of the conditioned samples, even after one year of exposure to alkali solutions at 75 °C. Similar results were obtained for the other conditioned samples. Figure 4.36, on the other hand, shows that the composition of the fibre does not include zirconium, hence confirming that the fibre is a regular E-glass fibre and not an AR-glass fibre (Alkali Resistant glass). A close look at the sample shown in Figure 4.23 and exposed to a similar solution and temperature shows that, although some debonding had occurred at the fibre-matrix interface, no typical visual sign of glass dissolution can be seen. Similar trends were observed for the samples exposed to pure water and the other alkaline solutions. In other words, debonding was observed only in samples exposed to 75 °C. The fibre-matrix debonding seems to be the same regardless of whether the conditioning solution had alkali ions or not. No debonding was observed in all samples for conditioning times shorter than three months. Therefore, it can be concluded that the E-glass fibres did not degrade in the considered exposure environments. However, deterioration of glass fibres in GFRP rebars under accelerated ageing conditions has

been reported by many researchers (Sen et al. 2002, Valter and Ralejs 2001, Swit 2000, and Chong 1998). This is not necessarily in contradiction with the findings of the current study as fibre deterioration in GFRPs is a complex process controlled both by internal and external factors. Internal factors include the type and quality of rebar constituents, such as fibres, matrix, fillers and sizing, and fibre volume fraction. In addition, the manufacturing method of rebars and curing process affects the overall strength. External factors include exposure conditions, temperature, applied stress and duration.

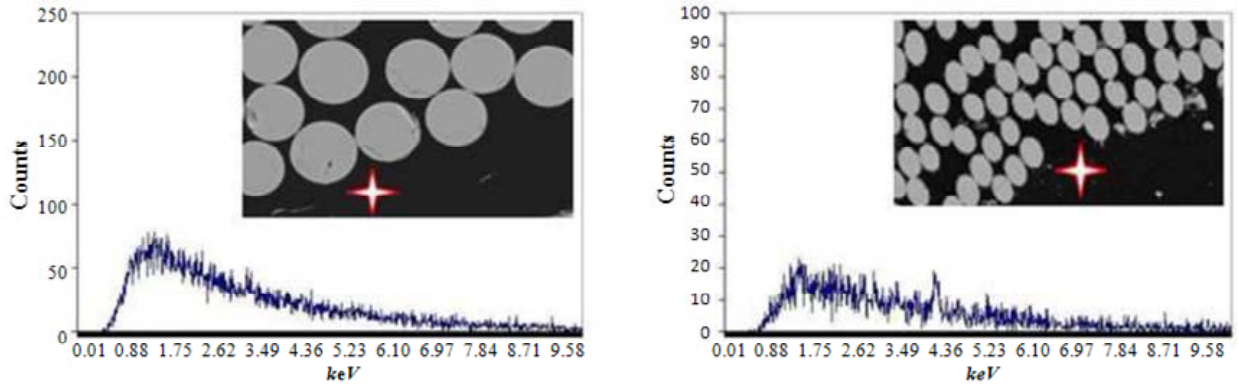

(a) (b)

Figure 4.35. Point EDS scans of the matrix near the outer surface of the sample: (a) an unconditioned sample and (b) a sample conditioned in a NaOH solution at 75 °C for 1 year.

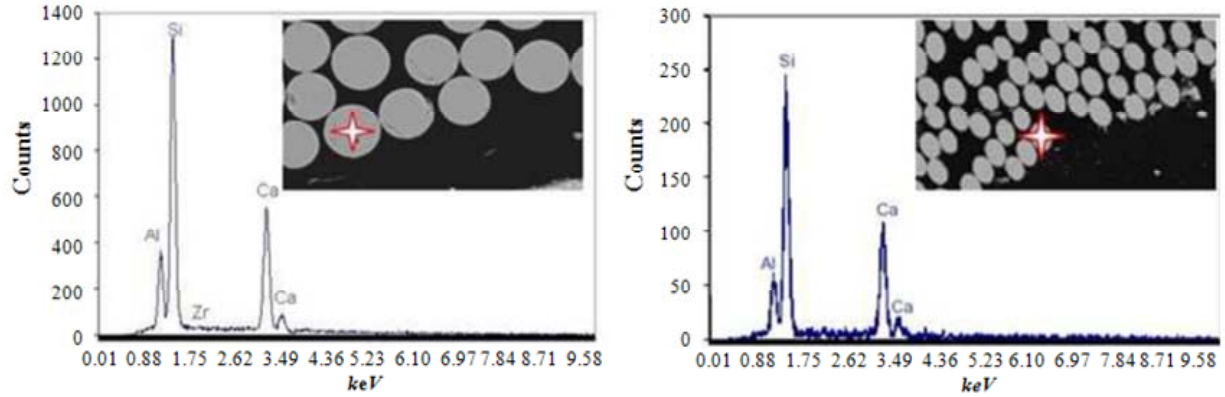

(a) (b)

Figure 4.36. Point EDS Scans on the glass fibre near the outer surface of the sample (a) an unconditioned sample and (b) a sample conditioned in a NaOH solution at 75 °C for 1 year.

4.4. Summary and conclusions

The possible penetration of alkali ions and subsequent degradation of the fibre, matrix, and fibre-matrix interphase have been evaluated for an E-glass--VE FRP composite. GFRP bar samples were exposed to neutral water and various alkaline solutions ($12.5 < pH < 13.8$) with a maximum temperature of 75 °C before being tested at 1, 3, and 12 months. The findings are summarized as follows:

1. Penetration of alkali ions into GFRP rebars was assessed by X-ray mapping and crosschecked by line EDS, and sometimes point EDS, scans. The results showed that no alkali ions penetrated into the rebars for all pH values and temperatures considered.
2. The deterioration of the VE matrix was investigated by an FTIR analysis. These analyses showed no deterioration in the matrix even after 12 months of exposure to simulated concrete pore solutions. This finding suggests that the VE resin evaluated in this study has an intrinsic chemical resistance against water and alkaline solutions, even at 50 °C.
3. Highly magnified SEM images at fibre-matrix interphase, together with point EDS scans close to the interface, have shown that no detectable glass fibre degradation has taken place. No evidence of silica dissolution could be found in the vicinity of glass fibres.

In light of the above findings, one can conclude that the VE polymer matrix effectively acts as a semi-permeable membrane in GFRP composites allowing water molecules, while blocking harmful alkali ions. This fact should remain true as long as the outside 50 μm protective resin layer is present and remains undamaged.

Although the degradation of either the fibre or matrix themselves does not seem to be an issue for the GFRP composite evaluated in this study, their interface might be more prone to damage initiation under extreme conditions. Fibre-matrix debonding has been observed for the samples exposed to pure water and to the other alkaline solutions when exposed to 75 °C and seems to be the same regardless of whether the conditioning solution had alkali ions or not. Knowing the susceptibility of E-glass fibres to alkali ions, this is another confirmation that no alkali ions have reached the fibres. It is believed that debonding at the fibre-matrix interface, observed at 75 °C, is very likely due to hydrolysis of the fibre sizing by water at that high temperature

CHAPTER FIVE
INTERPHASIAL EFFECTS ON THE PROPERTIES OF FRP COMPOSITES (PHASE 2)

5.1. Overview

The fibre-matrix interphase is a most critical region controlling the properties of FRP composites, as load transfer between fibre and matrix takes place through their interphase. As has been observed in the accelerated ageing tests in Phase 1, debonding occurred at the fibre-matrix interphase only for those samples conditioned for 12 months at 75 °C, although no alkali ions had penetrated into GFRP rebars. A recent theoretical study suggests that the fibre-matrix interphase is the most likely source for damage initiation and subsequent performance deterioration in high performance composites, such as VE-E-glass systems (Boulfiza and Banthia 2009). The probable reason for fibre-matrix debonding at the aggressive exposure conditions is the hydrolysis of sizing at the interphase. Therefore, an attempt was made in Phase 2 to study the effects of sizing at the interphase and subsequently the effects of sizing on the properties of GFRP composites. In this study, GFRP custom plane sheets were produced by a Vacuum Infusion Process (VIP). Use of the custom sheets instead of actual rebars would allow one to study, understand, and ultimately model the behavior of GFRP composites more effectively than the current models, as discussed in section 3.3.2.

The study of the influence of sizing on the properties of composites is as old as the application of composites. Several researchers have studied the effects of sizing in fibre-matrix composites. Sonawal and Spontak (1996) observed the increased moisture gain by glass reinforced polyester matrix with temperature. Zhang and Morgan (1993) did the same for carbon fibre embedded in epoxy composites. However, the study of sizing on glass fibres embedded in VE matrix composites (GFRP rebars) demands special attention due to their recent applications in infrastructure. Although the effects of moisture on composites are available in the literature (Karbhari and Zhang 2003; Thomason 1995; Schutte 1994; Plueddemann 1991; Apicella et al. 1983), the effects of sizing on the properties of GFRP composites are scantly addressed.

Therefore, this experiment was aimed at investigating the effects of sizing on the properties of GFRP composites by immersing sized and de-sized specimens in deionized water at different temperature, and determining moisture gain, moisture diffusivity, and tensile strength.

5.2. Effects of sizing on moisture up-take by GFRP sheets

The mass gain behaviour of GFRP sheets as a function temperature is shown in Figure 5.1. Following their exposure to deionized water, the GFRP custom plane sheets continued taking up moisture until they become saturated with deionized water. All sheets showed a typical Fickian behavior by developing linear, concave, and plateau regions in the mass gain curves with time. However, sheets exposed to higher temperatures showed that behaviour faster. The detailed mass gain data for both sized and de-sized specimens immersed in water at 4 °C, 23 °C, and 50 °C are shown in Table A1 in Appendix A.

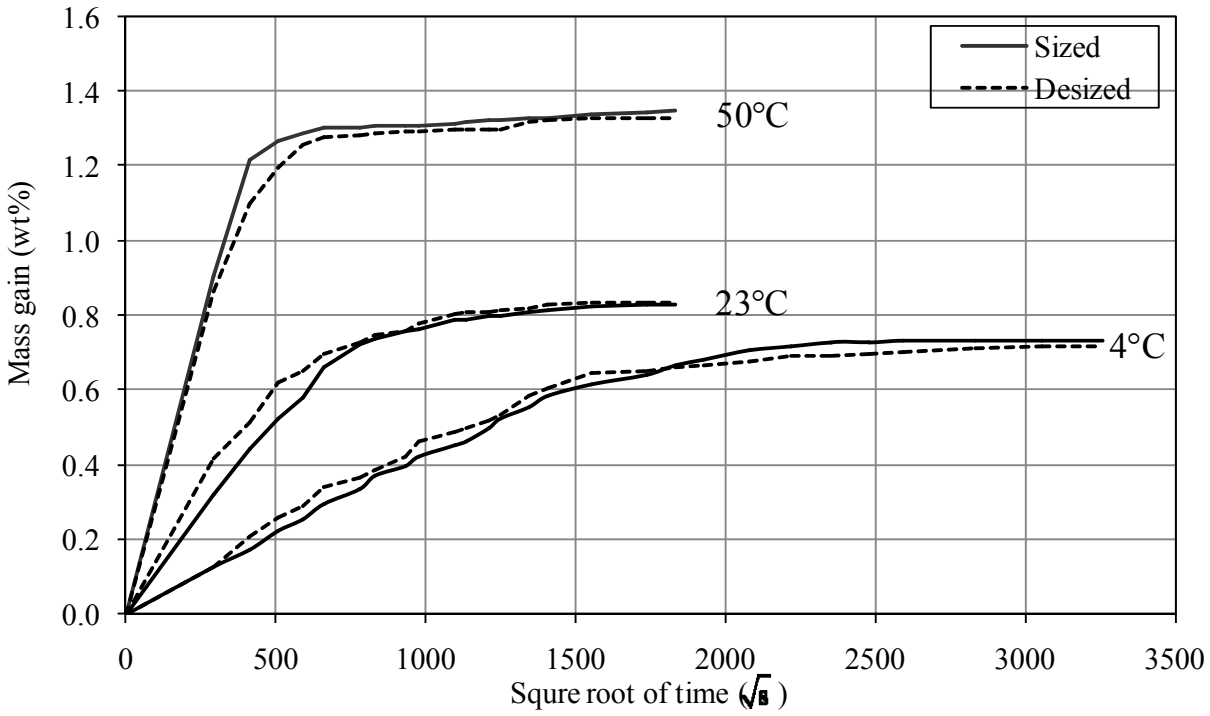

Figure 5.1. Moisture gain of sized and de-sized GFRP plane sheets as a function of immersed times.

The moisture gain-time curve reveals that temperature has a direct impact on both the amount of water absorbed (moisture gain) and how fast it takes place (moisture diffusivity) for

both sized and de-sized specimens. These characteristics increased with temperature for both types of specimens. For instance, the maximum moisture gains by the sized specimens were 0.73%, 0.83%, and 1.35% at 4 °C, 23 °C, and 50 °C, respectively. Moreover, the moisture diffusivities also increased with temperature with values of 0.324 x 10^{-7} mm^2/s, 1.11 x 10^{-7} mm^2/s, and 38.2 x 10^{-7} mm^2/s at 4 °C, 23 °C, and 50 °C, respectively (Table 5.1). Due to the greater moisture diffusivity at the higher temperatures, the specimens at higher temperatures were equilibrated faster than those at lower temperatures. However, the sized and de-sized specimens showed similar behaviors of moisture gain and moisture diffusivity at all exposure temperatures considered in this study. For instance, the maximum moisture gain at 23 °C for the sized specimen was 0.83%, which is very close to the de-sized specimen, 0.84%, at the same temperature. Similarly, the moisture diffusivity at 23 °C for the sized specimen was 1.1 x10^{-7} mm^2/s, which is also very close to the diffusivity of the de-sized specimen, 1.2 x $10^{-7}mm^2/s$, at the same temperature. However, the sizing effect on diffusivity at higher temperature (50 °C) was observed, as it was 38.2 x 10^{-7} mm^2/s for sized specimens and 47.0 x 10^{-7} mm^2/s for de-sized ones. The overall moisture uptake results with respect to maximum moisture gain, diffusivity coefficients, and the duration of experiment for both sized and de-sized GFRP custom plane sheets are listed in Table 5.1.

Table 5.1. Moisture gain characteristics of GFRP custom plane sheets.

Temperature of deionized water (°C)	GFRP Sheets with sized fibreglass mat			GFRP Sheets with de-sized fibreglass mat		
	Maximum moisture gain (wt%)	Coefficient of diffusion (x10^{-7}) mm^2/s	Duration of Experi -ment (days)	Maximum moisture gain (wt%)	Coefficient of diffusion (x10^{-7}) mm^2/s	Duration of Experi -ment (days)
4	0.734	0.324	123	0.720	0.324	123
23	0.828	1.11	39	0.836	1.24	39
50	1.350	38.2	39	1.327	47.0	39

5.3. Effects of sizing on the strength of GFRP sheets

5.3.1. The relation of load with displacement

A typical load-displacement curve for a GFRP custom plane sheet specimen is shown in Figure 5.2. All specimens showed similar kinds of load-displacement curves. Each curve has two parts: a linear elastic phase followed by a sudden breakage of the specimen. The specimen started bearing load until it broke at 'B'. This part (AB) of the curve has a positive slope, where displacement increased with load. At the breaking point, all types of bond scissions start to occur. Weak bonds, such as van der Waals bonds break first followed by the covalent bonds which continue to stress with increasing load until they reach their breaking load. The breaking load of a GFRP sheet specimen is the ultimate load, which was used to calculate the tensile strength of each specimen, as presented in Section 5.3.2.

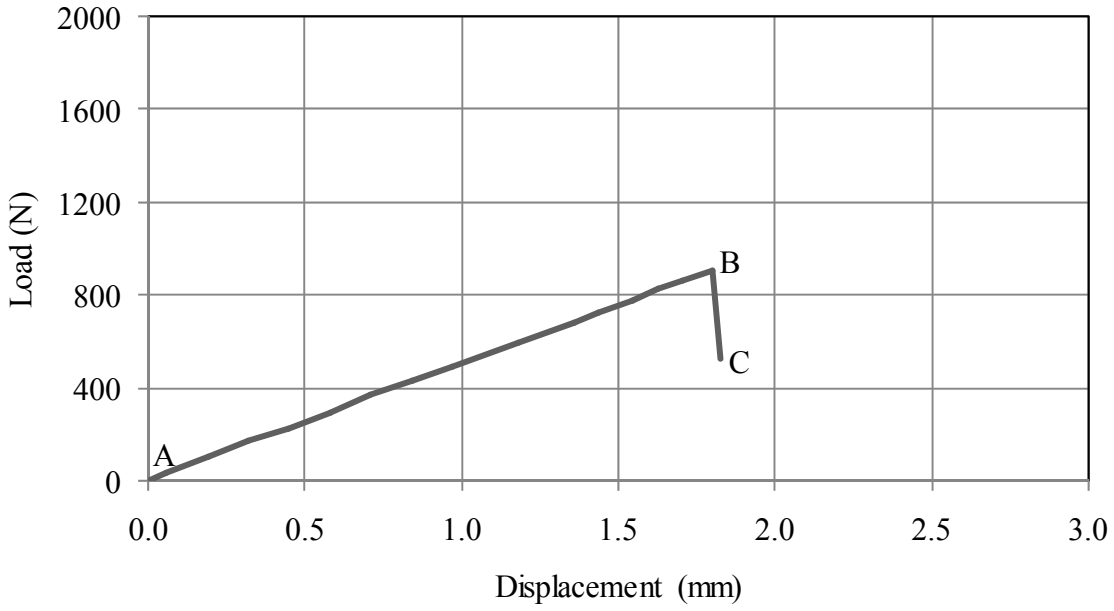

Figure 5.2. A typical load-displacement curve for GFRP sheet specimens.

The mechanical properties of sized and de-sized specimens in the as-produced condition at 23 °C, wet condition at 23 °C, and wet condition at 50 °C are listed in Tables 5.2-5.7. A summary of their mechanical properties is also shown in Table 5.8. At each exposure condition, sized specimens showed a greater load bearing capacity than the de-sized ones, as shown in Figures 5.3 to 5.5. The slipping of the specimens from the grip of tensile machine might have created the

irregular behaviour shown in Figures 5.3 to 5.5. The breaking loads for sized and de-sized specimens that were exposed to deionized water at 23 °C were 1300 N and 700 N, respectively. Moreover, irrespective of specimen types, the breaking load was observed to decrease with the severity of exposure conditions as shown in Table 5.8. As a result, it is clear that sizing plays a pivotal role in the load bearing capacity of GFRP composites, even in harsh conditions.

Table 5.2. Mechanical properties of sized GFRP sheet specimens in the as-produced condition at 23 °C.

Sample No.	Width (mm)	Thickness (mm)	Area (mm^2)	Max load (N)	Extension at max load (mm)	Tensile strength (MPa)
1	20.00	1.35	27.00	1680.52	2.89	62.24
2	19.00	1.24	23.56	1400.04	2.28	59.42
3	21.30	1.25	26.63	1850.43	4.00	69.50
4	20.10	1.28	25.73	1643.67	3.06	63.72
Avg.	20.10	1.28	25.73	1643.67	3.06	63.72
Std. dev.	0.94	0.05	1.54	185.71	0.71	4.25

Table 5.3. Mechanical properties of de-sized GFRP sheet specimen in the as-produced condition with 23 °C.

Sample No.	Width (mm)	Thickness (mm)	Area (mm^2)	Max load (N)	Extension at max load (mm)	Tensile strength (MPa)
1	20.00	1.25	25.00	1314.23	2.19	52.57
2	22.00	1.25	27.50	1212.92	1.83	44.11
3	20.50	1.30	26.65	1215.80	2.27	45.62
Avg.	20.83	1.27	26.38	1247.65	2.10	47.43
Std. dev.	1.04	0.03	1.27	57.68	0.23	4.51

Table 5.4. Mechanical properties of sized GFRP sheet specimen conditioned at deionized water and 23 °C.

Sample No.	Width (mm)	Thickness (mm)	Area (mm^2)	Max load (N)	Extension at max load (mm)	Tensile strength (MPa)
1	20.00	1.35	27.00	1680.52	2.89	62.24
2	20.00	1.25	25.00	1314.23	2.19	52.57
3	20.53	1.20	24.64	1286.8	2.23	52.23
Avg.	20.18	1.27	25.55	1427.18	2.44	55.68
Std. dev.	0.31	0.08	1.27	219.82	0.39	5.68

Table 5.5. Mechanical properties of de-sized GFRP sheet specimen conditioned at deionized water and 23 °C.

Sample No.	Width (mm)	Thickness (mm)	Area (mm^2)	Max load (N)	Extension at max load (mm)	Tensile strength (MPa)
1	21.60	1.30	28.08	887.05	1.47	31.59
2	19.50	1.30	25.35	882.01	1.69	34.79
3	20.00	1.30	26.00	648.94	1.32	24.96
Avg.	20.37	1.30	26.48	806.00	1.49	30.45
Std. dev.	1.10	0.00	1.43	136.04	0.19	5.01

Table 5.6. Mechanical properties of sized GFRP sheet specimen conditioned at deionized water and 50 °C.

Sample No.	Width (mm)	Thickness (mm)	Area (mm^2)	Max load (N)	Extension at max load(mm)	Tensile strength (MPa)
1	19.00	1.22	23.18	972.68	1.99	41.96
2	20.10	1.35	27.135	1403.88	2.45	51.74
3	20.60	1.35	27.81	1054.80	2.30	37.93
Avg.	19.90	1.31	26.04	1143.79	2.25	43.88
Std. dev.	0.82	0.08	2.50	228.96	0.23	7.10

Table 5.7. Mechanical properties of de-sized GFRP sheet specimen conditioned at deionized water and 50 °C.

Sample No.	Width (mm)	Thickness (mm)	Area (mm^2)	Max load (N)	Extension at max load(mm)	Tensile strength (MPa)
1	20.50	1.35	27.68	754.34	1.63	27.26
2	20.80	1.40	29.12	672.18	1.36	23.08
3	22.50	1.35	30.38	1055.94	1.71	34.76
Avg.	21.27	1.37	29.06	827.49	1.57	28.37
Std. dev.	1.08	0.03	1.35	202.07	0.18	5.92

Table 5.8. Summary of the mechanical properties of GFRP sheet specimens at several exposure conditions.

Exposure environments	Sample type	Width (mm)	Thickness (mm)	Area (mm^2)	Max load (N)	Extension at max load (mm)	Tensile strength (MPa)
As received at 23 °C	sized	20.10 (±1.15)	1.28 (±0.06)	25.73 (±1.89)	1644 (±227)	3.06 (±0.87)	63.72 (±5.20)
	de-sized	20.83 (±1.04)	1.27 (±0.03)	26.38 (±1.27)	1248 (±58)	2.10 (±0.23)	47.43 (±4.51)
Immersed in deionized water at 23 °C	sized	20.18 (±0.31)	1.27 (±0.07)	25.55 (±1.27)	1427 (±220)	2.44 (±0.39)	55.68 (±5.68)
	de-sized	20.37 (±1.10)	1.30 (±0.00)	26.48 (±1.43)	806 (±136)	1.49 (±0.19)	30.45 (±5.01)
Immersed in deionized water at 50 °C	sized	19.90 (±0.82)	1.31 (±0.08)	26.04 (±2.50)	1144 (±229)	2.25 (±0.23)	43.88 (±7.10)
	de-sized	21.27 (±1.08)	1.37 (±0.03	29.06 (±1.35)	827 (±202)	1.57 (±0.18)	28.37 (±5.92)

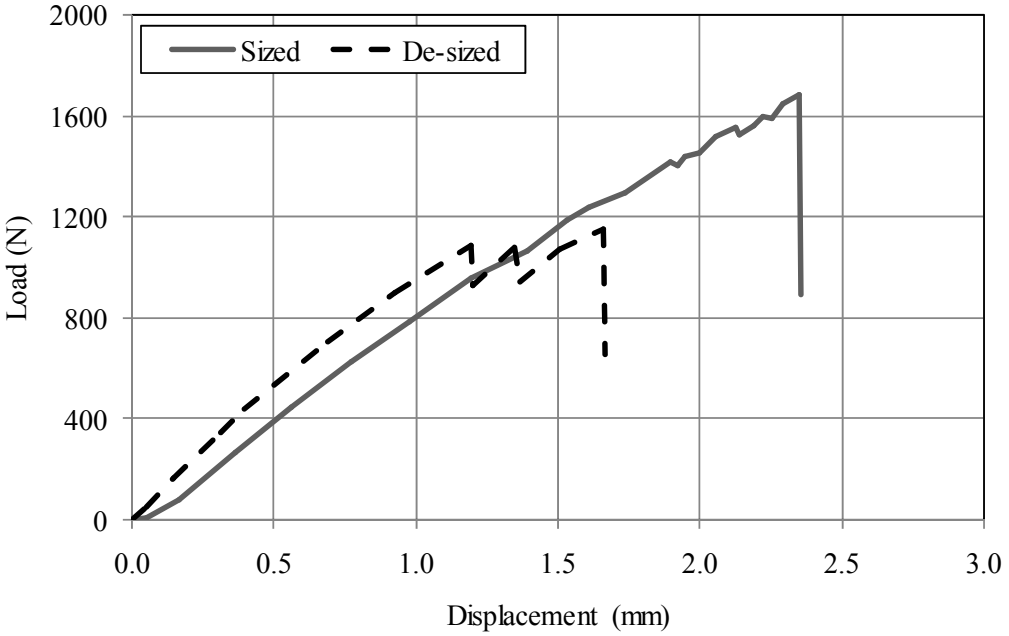

Figure 5.3. The load-displacement curves for GFRP sheet specimens at as produced condition with 23 °C.

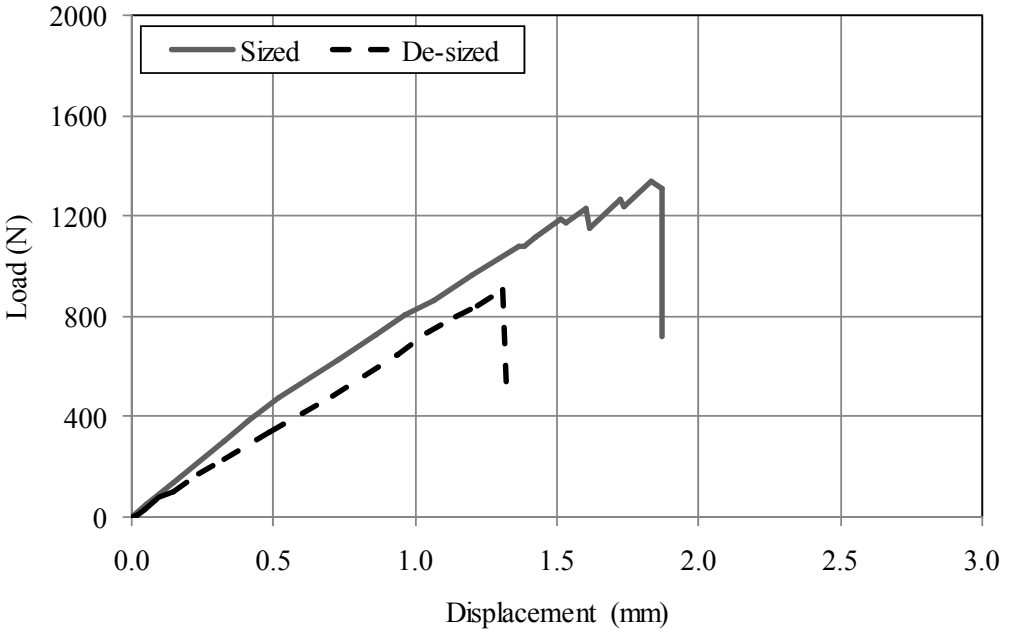

Figure 5.4. The load-displacement curves for GFRP sheet specimens saturated with deionized water at 23 °C.

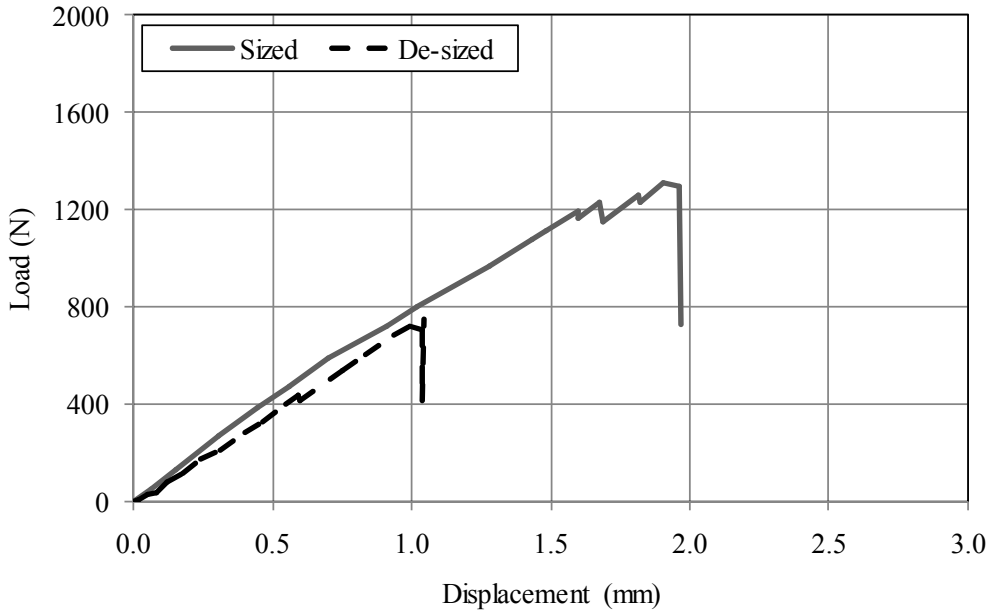

Figure 5.5. The load-displacement curves for GFRP sheet specimens saturated with deionized water at 50 °C.

5.3.2. Tensile strength

The tensile strength of GFRP custom plane sheets varied with the exposure environment and the specimen type as shown in Figure 5.6. The exposure involved immersion of both specimens in de-ionized water at 23 °C and 50 °C to create an equilibrium condition. The higher the temperature, the higher the strength loss caused by the maximum mass gain. For instance, the sized specimens lost 13% of their strength at 23 °C, and 31% at 50 °C when equilibrated with deionized water, as compared with as-produced strengths. On the other hand, the de-sized specimens lost strength by 36% at 23 °C, and 40% at 50 °C when equilibrated with deionized water. Sized specimens in any particular exposure environment performed better than de-sized specimens in terms of retaining strength. For example, sized specimens were 34% stronger at as-produced conditions, 83% stronger in the wet condition at 23 °C and 55% stronger in the wet

condition at 50 °C than the de-sized ones.

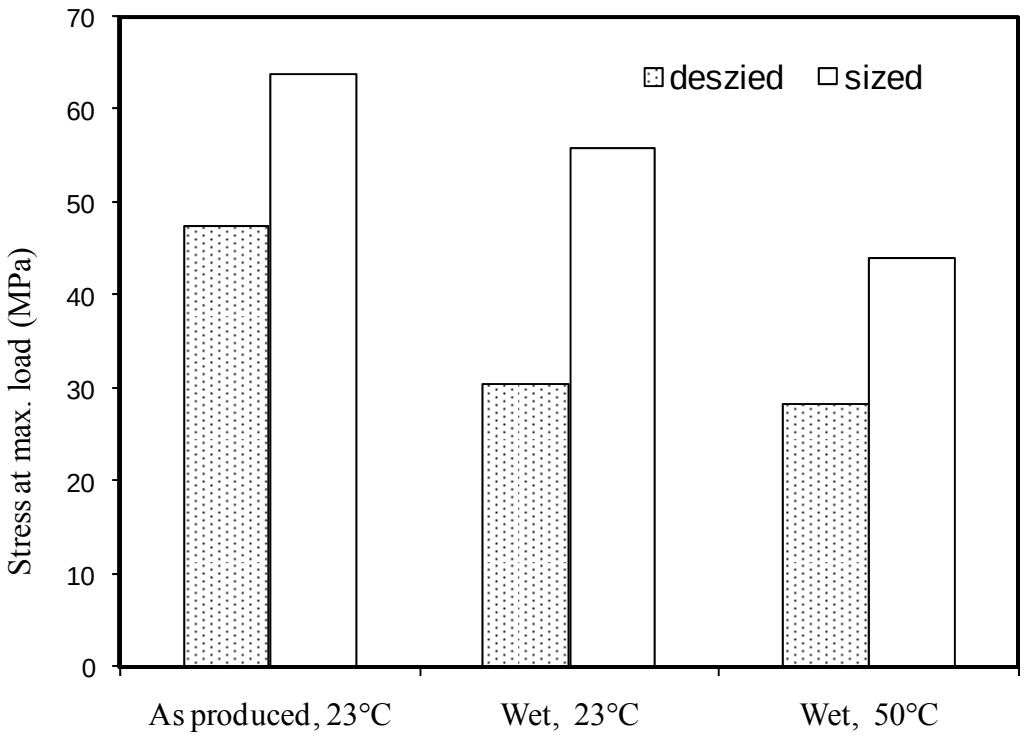

Figure 5.6. Effect of sizing on the tensile strength GFRP custom plane sheet specimens at various exposure environments.

In spite of showing different behaviors in tensile strength retention, both sized and de-sized specimens of GFRP custom plane sheets showed similar behaviors of moisture gain and moisture diffusivity. The strength loss difference is significant after exposing sized and de-sized composites in deionized water at 23 °C. For instance, the sized specimen in this study was 83% stronger than the de-sized one. Marsden (1990) has also observed similar trends of strength loss in composites. In that study, polyester composites impregnated with fibreglass and silane coupling agent were over 100% stronger at wet conditions in terms of flexural strength than similar composites without silane. As moisture diffused into the composites and traversed the fibre matrix interphase, adhesions weakened the bonding mechanisms, which ultimately resulted in lower strength. Thus, sizing elements, including coupling agents and others, seem to play a significant role in strength retention even at adverse exposure environments by maintaining the fibre-matrix bond at the interphase.

5.4. Bonding mechanism at the fibre-matrix interphase

The overall strength of a GFRP composite depends on the effectiveness of its components: glass fibres, a polymer matrix, and a sizing. Fibres in GFRP rebars are the main strength contributing element, whereas the matrix protects fibres from the ambient environment and distributes stress from one fibre to another. Although a minor element, sizing contributes enormously to the strength in GFRP rebars by forming interphasial bonds between fibres and matrix. The interphase of GFRP rebars consists of three segments shown, schematically in Figure 5.7. The left segment is the glass fibre, while the right one is a polymer matrix (resin), and the middle one is sizing, which holds fibres and the matrix together. Sizing is a complex mixture of different elements that perform specific function at the fibre-matrix interphase, as discussed in Section 2.3. All sizing elements ultimately work together to retain the strength of interphasial bonds.

The bonding between fibres and a matrix at an interphase is explained by adhesion theories (Petrie 2007; Jang 1994). Once sizing is applied during a fibre-fabrication, the coupling agent in the sizing acts as a bridge between fibres and a polymer matrix to bond them. Organo-silane, the active ingredient of sizing, has two reactive ends: a silicon end and a long chain polymeric end. The chemically reactive silicon end develops covalent bonding networks with the silanol functional groups on the surface of a glass fibre. The silane reactions on the surface of a glass fibre are shown in Figure 5.8 (Jones 2003). After embedding the sized fibres into the polymer matrix, the diffusion of polymer matrix molecules (resin) occurs toward the surfaces of fibres. The sizing elements from the other side diffuse into the polymer matrix molecules (Figure 5.7). Finally, the long polymeric chain forms bonds with the polymer matrix. The chemical bond is the predominate bond in maintaining fibre-matrix adhesion at the interphase. Besides the chemical bonds, van der Waals forces contribute to the fibre-matrix adhesion by adsorption and wetting characteristics. The poorer the wetting of the polymer matrix on the fibres, the weaker will be the adhesion. Moreover, mechanical interlocking between fibres and a matrix creates physical bonds at the fibre-matrix interphase. The voids and pores on the fibre surface allow stronger mechanical bonding. The bonding mechanisms in sized specimens are different from de-sized ones. In sized specimens, diffusion, chemical bonding, adsorption and wetting theories may explain the bonding mechanisms, whereas in de-sized specimens, mechanical interlocking theory may explain the bonding mechanisms.

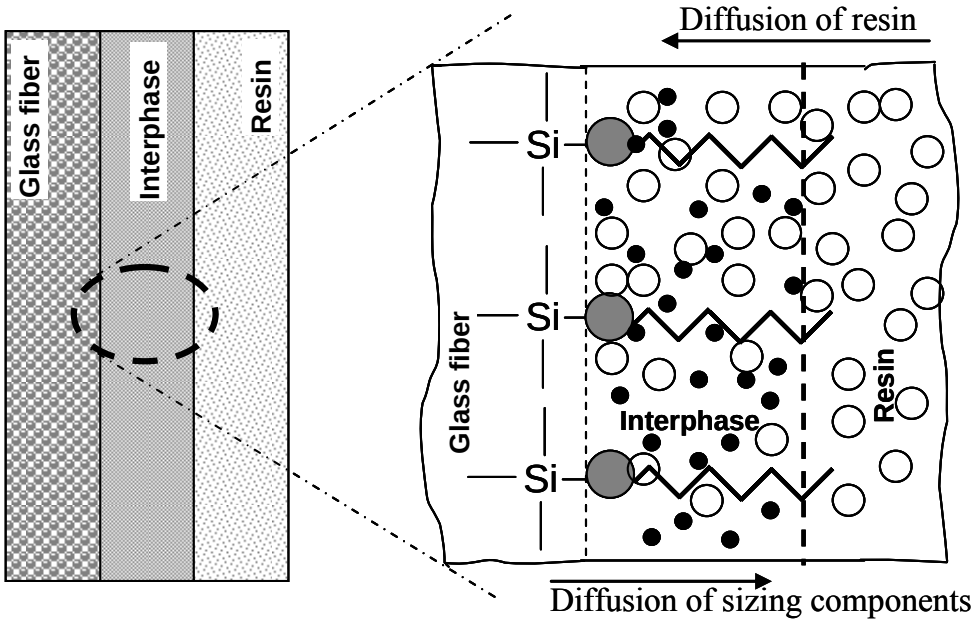

, silane coupling agent; O, resin; and ●, other constituent of sizing, such as, film former, antistatic agent, lubricant, etc.

Figure 5.7. A schematic representation of a fibre matrix interphase. (a) Interphase network between fibre and matrix in GFRP composite fibre-matrix composite, (b) Projected view of fibre-matrix interphase showing different components of sizing.

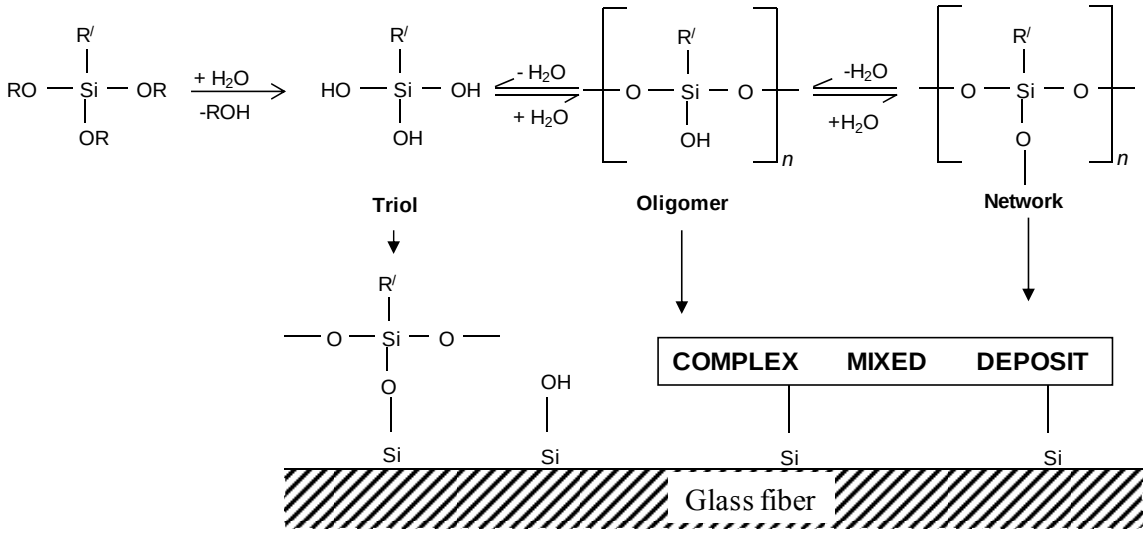

R denotes an alkyl group, whereas $R^{/}$ represents the long polymeric chain

Figure 5.8. Silane reactions on the surface of glass fibre.

The interphase has some of the vulnerable sites for deterioration in fibre-matrix composites. In moist environments, water molecules diffuse through the matrix, and remain preferentially at the fibre-matrix interphase (Callister 2007). The effects of water molecules at the interphase can be characterized by the physical, physicochemical, and chemical aspects. Water molecules at the interphase affect the physical bonds by causing swelling. As a consequence of swelling, chain separation might occur, which weakens the interphase bond strength (Callister 2007). This can be explained by breaking the weak secondary bonds, such as van der Waals bonds. Not only physical bonds, but also any kind of bonds can be hydrolyzed by water molecules present at the fibre-matrix interphase (Plueddemann 1991). However, sizing present at the interphase delays the bond breaking. Andrews et al. (1982) studied the bond performance of epoxy-glass in 80 °C water for both sized and de-sized specimens, and observed that failure was delayed due to the silane coupling agents.

As sizing is compatible with the matrix, a fraction of the sizing dissolves in the matrix and the remaining sizing stays bound to the fibre. The amount of bound sizing is related to the strength of the fibre matrix interphase (Thomason 1995; Tanoglu et al. 2001). A series of analytical experiments were conducted by Thomson (1995) to quantify the amount of coupling agents on E-glass fibre. A similar kind of experiment was conducted by Tanoglu et al. (2001) to identify the bound and soluble part of sizing from en E-glass-epoxy amine composite using a nuclear magnetic resonance (NMR) technique. Both studies showed that the amount of coupling agent present at the fibre-matrix interphase is related to the interfacial strength.

The decline of specimen strength is related to the severity of exposure environment, as shown in Figure 5.6. However, the overall strength of sized specimens over the de-sized ones is due to the bonding characteristics of organo-silane which binds to both the fibres and the polymer matrix. In the long run, the chemical bonds of organo-silanes at the fibre-matrix interphase are susceptible to hydrolytic damage. This damage can significantly be reduced by selecting a proper matrix, processing conditions, and by applying gel coats and protective coatings, as suggested by Karbhari et al. (2003).

5.5. Summary and conclusions

The sizing effects at the fibre-matrix interphase of a GFRP composite were evaluated in this study. To make the experiment effective and convenient, GFRP custom plane sheets were tested in place of GFRP rebars. GFRP sheets with sized and de-sized glass fibres were produced by a vacuum infusion process. The desizing technique was developed in the Materials lab. Both sized and de-sized specimens were immersed in deionized water at different temperatures and tested. The changes of properties with respect to moisture gain characteristics and strength loss were addressed in this study by distinguishing the effects of sizing.

Moisture gain experiments allowed assessing the effects of sizing on moisture uptake and moisture diffusivity by GFRP sheets. Both types of specimens showed a Fickian behaviour of moisture gain until they reached equilibrium. The percent of moisture uptake and moisture diffusivities increased with temperature for both types of specimens. Although both sized and de-sized specimens showed similar characteristics of moisture uptake and moisture diffusivity at any particular temperature, they are differed in terms of tensile strength under adverse exposure environments.

The tensile strengths of both kinds of specimens demonstrated the effect of sizing on the strength of composites. It was identified that sizing in GFRP sheets played a major role in retaining the tensile strength due to the strong interphasial bonds between E-glass fibre and VE resin. However, the interphase bonding was shown to be affected by the severity of exposure environments. Although the weak van der Waals bonds seem to have been affected by the exposure environments, the strong covalent bonds still managed to contribute in retaining the tensile strength of sized specimens. Conversely, de-sized specimens exhibited lower strength due to the weaker fibre-matrix bonds. Therefore, sizing is one of the main contributors to strength retention by maintaining the fibre-matrix bond at the interphase for sized specimens under severe exposure environments.

The experimental results for tests on the GFRP custom plane sheets are a step forward towards understanding the sizing effects on GFRP composites. However, to extrapolate this result to GFRP composites, fibre volume fraction, manufacturing, and curing process have to be addressed with a greater attention.

CHAPTER SIX
EFFECTS OF RELATIVE HUMIDITY ON GFRP COMPOSITES (PHASE 3)

6.1. Overview

Penetration of harmful species (H_2O and alkali ions) from a concrete solution may cause fibre debonding and strength loss. It was observed in Phase 1 that water had penetrated into GFRP rebars, but not alkali ions. Mass gain tests of rebars have confirmed the water penetration. Water saturated GFRP custom plane sheets have shown less strength retention over dried ones in Phase 2. It seems that at relative humidity (RH) has an effect on the properties of GFRP composites. Moreover, GFRP rebars are not always exposed to 100% RH environments. Therefore, an attempt was made to observe the mass change characteristics of GFRP rebars during drying and wetting under different RH environments. In addition, the thermal effects on mass gain were studied for GFRP rebars and GFRP custom plane sheets.

6.2. Effects of RH on drying of GFRP rebars

Water saturated GFRP rebars were hung in the pre-installed RH chambers. The preparation of samples, RH environments, and the configuration of RH chambers and probing device are discussed in Section 3.4. Moisture loss of each sample was measured until it reached a constant mass. The moisture loss of samples as a function of time for all RH chambers is shown in Figure 6.1. The raw data of moisture loss for GFRP rebars while drying at all RH is included in Table A.2 in Appendix A.

A similar type of moisture loss behaviour has been observed for each sample at all RH. The moisture loss was rapid at the beginning of the experiment before becoming slow with time. Though all samples reached constant masses within 36 days while drying, they took about three months to be water saturated. Samples at different RH showed different moisture loss properties. It has been observed that the moisture loss increased with decreasing RH. For instance, moisture

losses of 1%, 1.7%, and 2.5% have been observed at 94% RH, 53% RH, and 9% RH, respectively. The maximum moisture loss by the GFRP rebar samples hung at different RH is shown in Figure 6.2.

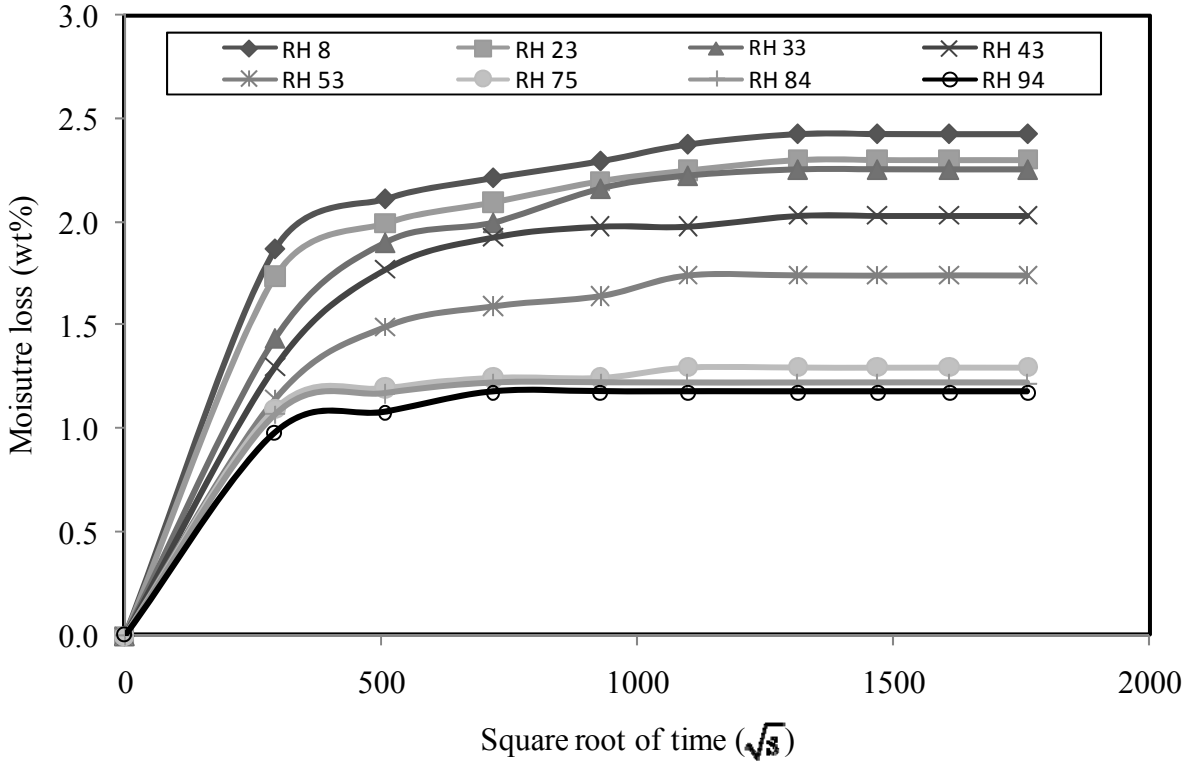

Figure 6.1. Mass loss of water saturated GFRP rebars at different RH.

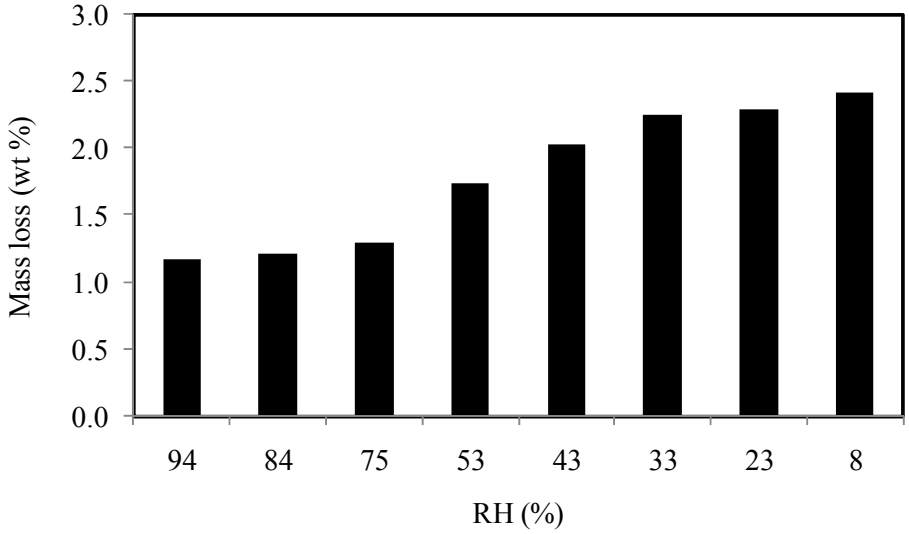

Figure 6.2. Maximum mass loss by GFRP rebars at different RH.

6.3. Effects of RH on wetting of GFRP rebars

Oven dried GFRP rebars were hung in the pre-installed RH chambers. The preparation of samples, RH environments, and the configuration of RH chambers and probing device are discussed in Section 3.4. The maximum moisture gain of each sample at any exposure environment was measured until they reached equilibrium. The obtained data was utilized to calculate the percent moisture gain for the GFRP rebars.

The moisture gain as a function of time for all RH (9%-100%) is shown in Figure 6.3. A similar trend of moisture uptake was observed at all RH exposure environments. The moisture uptake process in higher RH chambers was so sluggish that it took about two years for few samples to reach equilibrium. However, the samples at the lower RH equilibrated relatively fast. For instance, the samples at 9% RH, 43% RH, and 94% RH took 0, 412, and 672 days, respectively, to be equilibrated. Another noticeable difference in mass gain was identified for rebars immersed in 100% RH and other RH values (9%-94%) as shown in Figure 6.4. Though 100% RH is close to 94% RH, the maximum mass gain by the rebars immersed in water (RH 100%) is four times higher than those hung in 94% RH chamber.

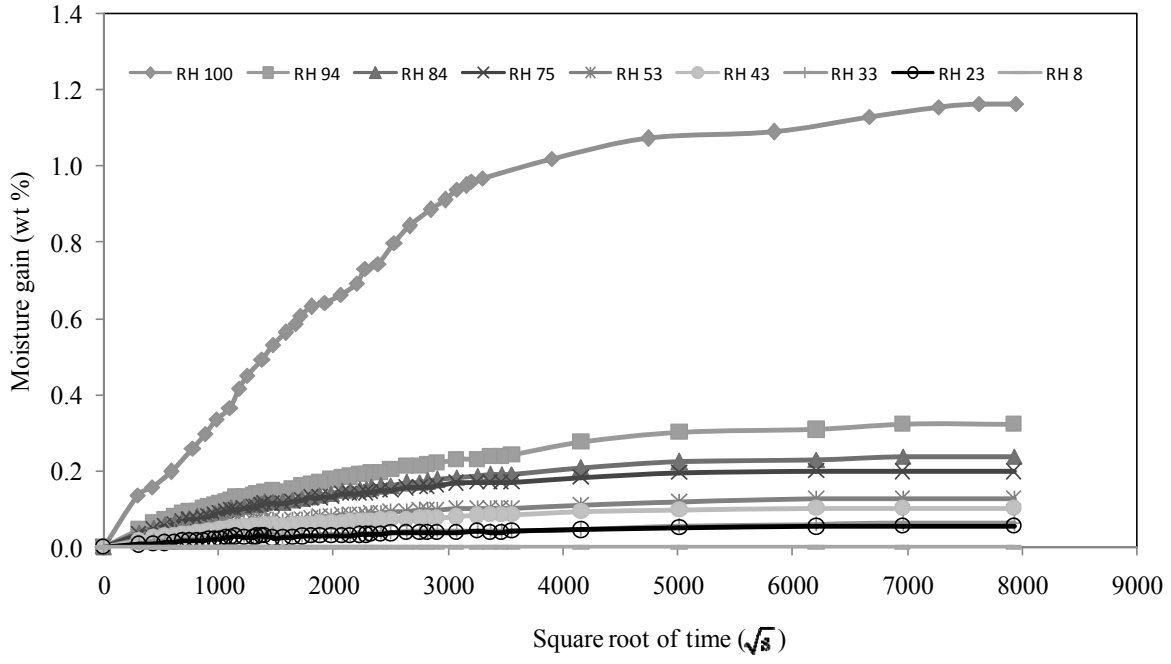

Figure 6.3. Moisture gain of dried GFRP rebars at different RH.

Taking a longer time for gaining a maximum moisture at higher RH is a positive attribute as it pertains to the durability of GFRP rebars as well as rebars embedded in concrete, as most deterioration types depend on the moisture saturation and the longer saturation times should help prolong their service life. The raw data of moisture gain for GFRP rebars during the wetting process at all RH values are included in Table A.3 in Appendix A.

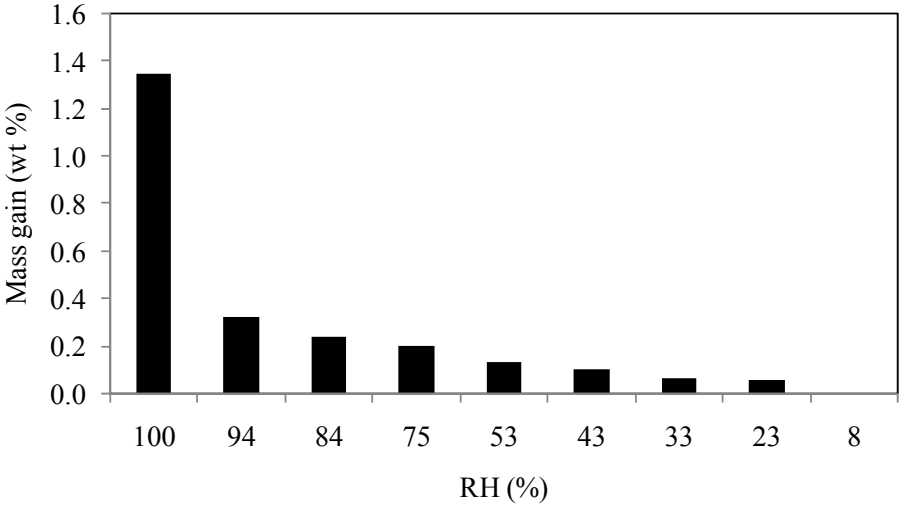

Figure 6.4. Maximum mass gain by GFRP rebars at different RH.

6.4. Hysteretic effects

The effects of drying and wetting on GFRP rebars at different RH values were discussed in Sections 6.2 and 6.3, respectively. As shown in Figure 6.5, mass change data at different RH values showed a hysteretic effect.

Any hysteretic effect depends on several factors, such as the inconsistency of composites pores, connectivity of pores, contact angles of liquid and solid, and air entrapment (Hillel 1982). The moisture hysteretic effect of GFRP rebars can be explained with an ink bottle effect by considering water transport phenomenon in a porous medium. The flow of water inside the pores is related to the degree saturation in the porous medium. Various stages of moisture transport through a typical pore are illustrated in the literature as shown in Figure 6.6 (Illston 1994).

Moisture is adsorbed onto the dry surfaces of the pores at low humidity (a). As the humidity increases the moisture adsorption on the pore surface is completed, and vapour starts condensing. Condensed vapour (water) creates a hindrance to free movement of moisture (b)

through the pores. Liquid flow through the pores occurs due to pressure gradients, initially through the incompletely saturated state (c), and finally through the completely saturated state (d). Movement of ions and dissolved substance in water saturated pores can move due to concentration gradients. The moisture hysteretic effect should be good for the longer durability of GFRP rebars due to a lesser contact of moisture with rebars.

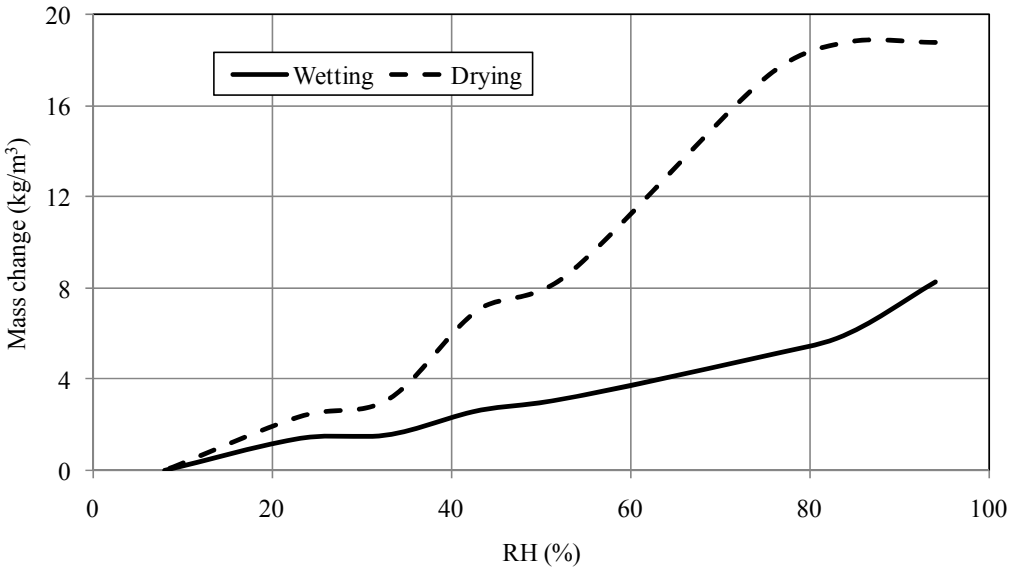

Figure 6.5. A moisture hysteresis of GFRP rebars during wetting/drying at different RH.

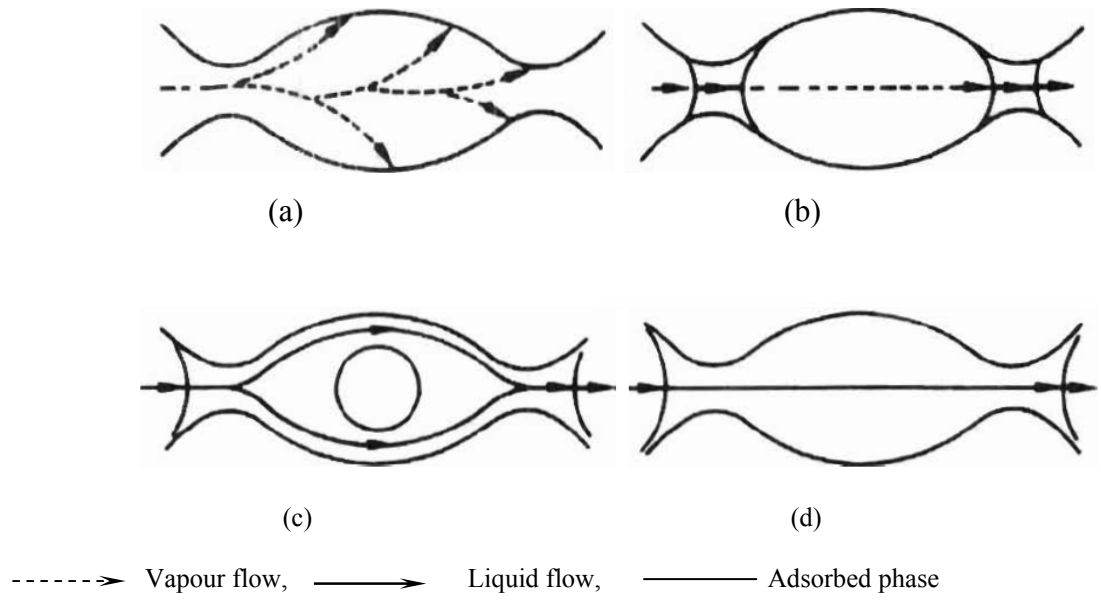

Figure 6.6. Various stages of moisture transport in a typical pore (adapted from Illston1994).

6.5. Effects of water on GFRP rebars

Water saturated FRP composites retain less strength over the dried ones. The effects of water on strength retention for GFRP rebars have been reported by several researchers (Karbhari and Zhang 2003; Marom and Broutman 1981; Zheng and Morgan 1993; Katuiki and Uomoto 1995). However, the moisture gain characteristics of GFRP rebars at elevated temperatures has scantily been reported. Therefore, this study was conducted with the following objectives:

i) to study the water gain characteristics of GFRP rebars at different temperatures, and
ii) to compare the temperature effects on the water uptake of GFRP rebars and GFRP custom plane sheets.

GFRP rebars with 50 mm length and 13.16 mm diameter were cut, dried, weighed, and immersed in deionized water. The rebars were exposed to similar exposure temperatures as for the GFRP custom plane sheets, i.e. 4 °C, 23 °C, and 50 °C. A similar method to that one discussed in Section 3.3.7 was used to determine the moisture gain of GFRP rebars at all exposure conditions.

6.5.1. Water gain characteristics of GFRP rebars at different temperatures

Moisture gain continued for all samples with time as shown in Figure 6.7. Like most composite materials, GFRP rebars showed Fickian behavior of water absorption at lower temperatures. Rebars continued gaining moisture until they became saturated. However, the samples with higher exposure temperature showed non-Fickian behavior. The samples with higher exposure temperature saturated faster than the lower temperature ones. The effects of temperature on moisture gain are discussed in the following section.

Samples immersed in higher temperatures absorbed higher amounts of water but saturated faster than those immersed at lower temperatures. The maximum moisture gain for the samples immersed in 50 °C, 23 °C, and 4 °C were 2.44%, 1.16%, and 0.7%, respectively. Also, the samples immersed in those exposure environments took 260, 610, and 730 days, respectively, to reach equilibrium. High exposure temperatures have an impact on the bonding characteristics of E-glass fibres with the VE matrix in GFRP rebars, as discussed in Section 5.4. When rebars

are soaked in water at elevated temperatures, some dissolution might take place at the fiber matrix interphase, which could increase diffusivity by capillary uptake along the fibers. Thus, higher exposure temperatures allow gaining a larger amount of moisture in a shorter period of time. The raw data of moisture gain for GFRP rebars immersed in deionized water is included in Table A.4 in Appendix A.

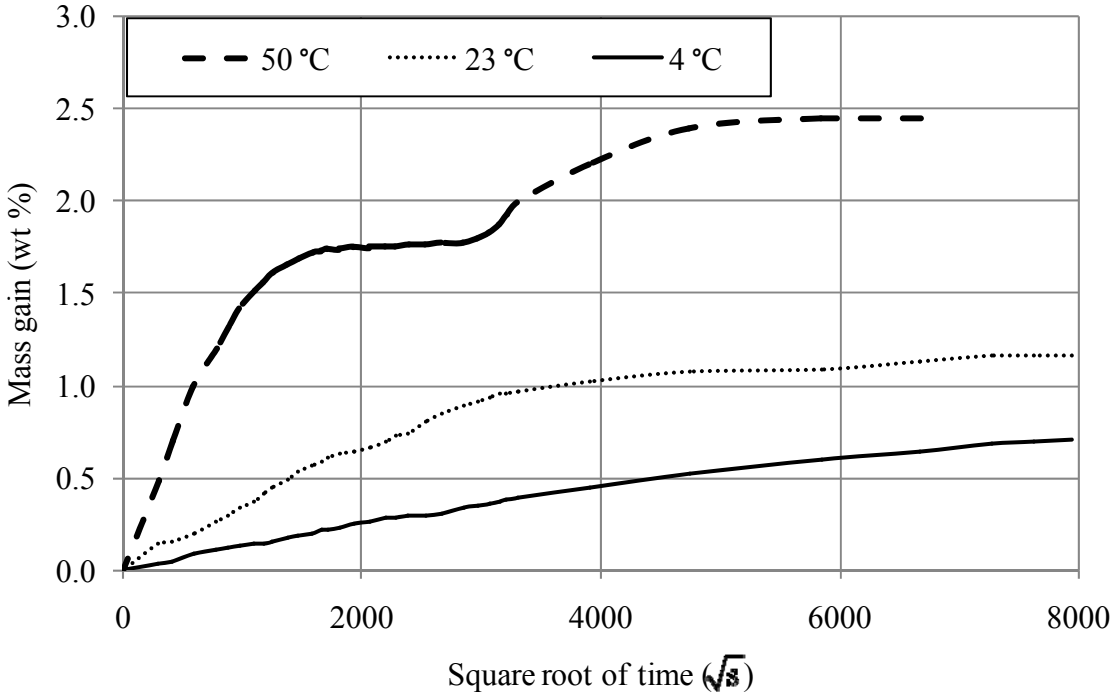

Figure 6.7. Mass gain of GFRP rebars at various exposure temperatures as a function of immersion time.

6.5.2. Effects of temperature on GFRP rebars and GFRP custom plane sheets

Temperature has direct effects on the mass gains in FRP composites. The mass gain characteristics of GFRP custom plane sheets and GFRP rebars are discussed in Sections 5.2 and 6.4.1, respectively. A comparison of the moisture gain characteristics for GFRP rebars and GFRP custom plane sheets is drawn in Table 6.1.

The moisture gain of rebars and sheets has been observed to increase with temperature (Figure 6.8). Among others, two major factors that affect those properties are composition and manufacturing methods.

Although the basic ingredients for both rebars and sheets were similar, their minor ingredients were different. A typical composition of GFRP rebars is E-glass fibre 62%, VE 31%, filler 6% and catalyst 1% (Bank et al. 1998), whereas the composition of a GFRP custom plane sheet was E-glass fibre 13%, VE 86% and catalyst 1% (section 3.3.4). The presence of more ingredients has made the rebar more inhomogeneous than the custom plane sheet. Moreover, the outer surface of a GFRP rebar is composed of sand, VE matrix, and a helical wrapping to produce a rough surface which provides better gripping with concrete.

Table 6.1. A comparison of moisture gain characteristics of GFRP custom plane sheets and GFRP rebars.

Temperature of deionized water (°C)	GFRP rebars		GFRP Sheets	
	Maximum moisture gain (wt%)	Duration of experiment (days)	Maximum moisture gain (wt%)	Duration of experiment (days)
4	0.7	730	0.74	123
23	1.16	730	0.83	39
50	2.44	515	1.35	39

Conversely, the absence of fillers and the manufacturing technique of the custom sheet produced the homogenous sheets with polished outer surface as only VE is present at that location. As a result, the inhomogeneous and rough rebar surface allowed higher amounts of water ingress in GFRP rebars at all exposure temperatures than those in GFRP sheets. The manufacturing technique for rebars and sheets was different. The rebar was manufactured with a pultrusion technique, whereas the sheet was-produced with a vacuum infusion process (VIP). Both manufacturing techniques run with different operating conditions that affect the properties of FRP composites. The pultrusion process operates at higher temperatures with a greater speed and cures at an elevated temperature, whereas the VIP runs at a vacuum with lower infusion speed and cures at room temperature. Both operating and curing conditions affect the properties of FRP composites. It has been observed that a VE matrix, if cured at higher temperatures, absorbs less water than those cured at lower temperatures (Azom 2010). Higher temperature curing allows more cross linking to develop between the long polymeric chains, while the lower

temperatures curing provide incomplete curing reactions. Thus, irrespective of composition and manufacturing techniques, the mass gain of FRP composites increases with exposure time and temperature.

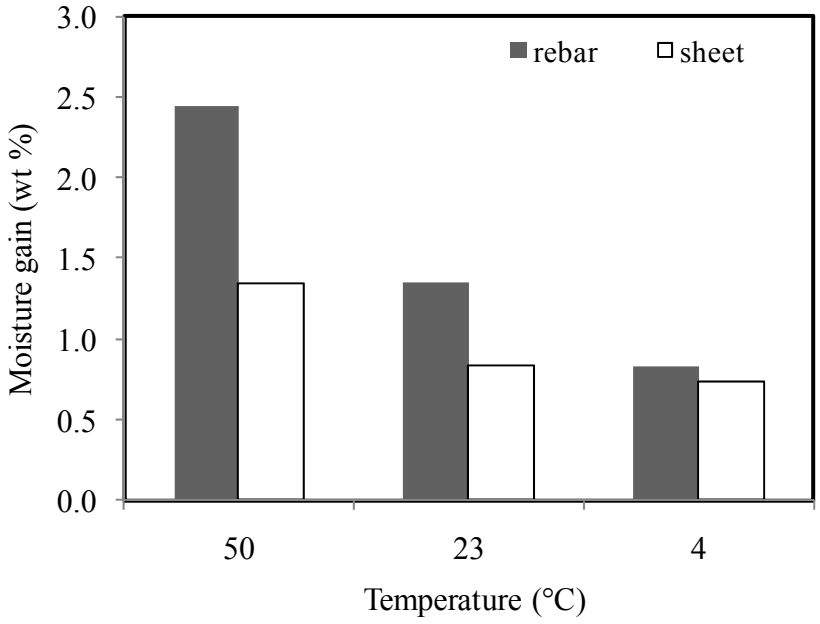

Figure 6.8. A comparison of mass gain for GFRP rebars and GFRP sheets at various exposure temperatures.

6.6. Summary and Conclusions

The effects of exposure environments (RH and temperature) on moisture uptake by GFRP composites were investigated in this study. The effects of RH on drying and wetting of GFRP rebars were studied by exposing them to different RH environments. The mass change characteristics with time were identified for both drying and wetting experiments and a hysteretic effect was observed. Moreover, the effects of temperature on GFRP rebars were studied and compared with those of GFRP custom plane sheets by immersing rebars in deionized water at 4 °C, 23 °C, and 50 °C.

During drying of saturated GFRP rebars, the moisture loss was observed to increase with time but decrease with increasing RH, for all RH conditions considered in this study. Although the rebars took three months to reach equilibrium, it took less than 36 days to dry the rebars at all

RH chambers. Rebars at 94% RH took a maximum of 10 days to become dry and those at 9% RH took a maximum of 36 days. Drying releases free water from the rebars immediately and hence relieves the rebars from its adverse effects.

During wetting of oven dried GFRP rebars considered here, the moisture gain was observed to increase with time and RH, at all RH environments. Oven dried rebars at 9% RH equilibrated almost immediately, whereas rebars at 94% RH equilibrated after 730 days. Keeping rebars away from the higher RH should be a good practice for the longer durability of rebars.

A clear hysteretic effect of moisture on GFRP rebars was observed by plotting mass changes (during drying and wetting) as a function of RH. The moisture hysteresis controls the hydrolytic properties of rebars that ultimately affects the durability of GFRP composites.

GFRP custom plane sheets and GFRP rebars are directly affected by the exposure temperatures. The moisture gain is found to increase with temperature for both composites. However, the rebars took a longer period of time to become saturated (730 days at 23 °C) than the sheets (39 days at 23 °C). The slow saturation process should be beneficial for the longer durability of rebars. The moisture gain characteristics for both composites are affected by their elemental composition, manufacturing, and curing processes.

Exposure environments, such as RH and temperature have direct effects on the mass gain properties that control the durability GFRP composites. Exposure to lower RH and temperature should be beneficial to GFRP rebars since their water uptake would be reduced under such environments.

CHAPTER SEVEN

PREDICTION OF GFRP PERFORMANCE

7.1. Background

The earlier Chapters discussed the performance of GFRP composites in various exposure conditions at a lab-scale. It was observed that the VE resin acts as a semi permeable membrane that allows water molecules to penetrate but not alkali ions (Kamal and Boulfiza 2011; Kamal and Boulfiza 2008). As water diffuses through VE matrix and reaches the fibre-matrix interphase, the effects of water on the properties of composites were discussed. It was observed that the sizing at the fibre-matrix interphase controls the strength of GFRP composites (Kamal et al. 2010). In the same study, it was further observed that mass gain in GFRP composites increased with the increase of RH and temperature. However, predicting the performance of GFRP composites is yet to be discussed. Based on the experimental results, a theoretical approach was developed to address the deterioration mechanisms of GFRP composites. In connection with this approach, the objectives of this study were: (i) to determine the diffusion coefficient of GFRP composites using a Fickian Model, (ii) to assess the validity of an Arrhenius dependence of the moisture diffusivity in GFRP composites on the exposure temperature, and (iii) to assess whether the possibility of a microblister formation and propagation at the fiber-matrix interface can serve as a mechanism to explain the root cause of interphase deterioration of GFRP composites.

7.2. Materials and methods

In this study, GFRP composite samples used were GFRP rebars and GFRP sheets. The rebar samples had a diameter of 13.16 mm and a length of 50 mm, while the sheet samples had dimensions of 125 mm x 20 mm x 1.25 mm. Both kinds of samples were immersed in water with temperatures of 4 °C, 23 °C, and 50 °C. The moisture gain data with respect to time at various

water temperatures were utilized to determine the moisture diffusivity for GFRP composites. The experimental settings, sample preparation, and exposure conditions were discussed elaborately in Chapter 3.

7.3. Fickian model

Water uptake in composite materials can be modeled/predicted using diffusion theories. It has been observed that Fick's laws can be utilized for a fibre-matrix composite to predict water uptake (Shen and Springer 1976). Fick's second law assumes that water penetrates due to a concentration gradient (Crank 1979), δC/δx, so that the water uptake as a function of time in a plane sheet is given by Equation 7.1.

$$\frac{\partial C}{\partial t} = \frac{\partial}{\partial x}\left(D\frac{\partial C}{\partial x} \right) = D\frac{\partial^2 C}{\partial x^2} \tag{7.1}$$

where, D is a diffusion coefficient with the direction of diffusion. Fick's law of diffusion is discussed elaborately in Chapter 2.

For a cylindrical composite, where diffusion is radial everywhere, the diffusion Equation is more conveniently solved in cylindrical coordinates, where it takes the form of Equation 7.2, as shown in Crank (1979). In this Equation, the concentration is a function of the cylindrical radius (r) and the diffusing time (t).

$$\frac{\partial C}{\partial t} = \frac{1}{r}\frac{\partial}{\partial r}\left(rD\frac{\partial C}{\partial r} \right) \tag{7.2}$$

It has been discussed in Crank (1979) that the transfer rate of a diffusing substance over a unit area is proportional to the concentration gradient normal to the section. However, the solutions to the diffusion Equations will be different according to the boundary conditions of the samples.

For a sheet (plate) sample, Crank (1979) solved the diffusion Equation to get Equation 7.3 considering the following boundary conditions:

(a) The diffusing substance is uniformly distributed with a concentration of C_0

(b) The value of x at the sheet surface is zero and increases with a distance into the plate

(c) The time is zero before the diffusion process starts.

These boundary conditions are simply stated below and shown schematically in Figure 7.1.

$x = 0$, C_1 = Constant

x = h, at C_2

where

C_1 : the concentration of diffusing substances at location $x = 0$

C_2 : the concentration of diffusing substances at location $x = h$

h : the plate thickness

The solution to Equation 7.1 is normally obtained in terms of concentration distribution of the diffusing species in space and time over the considered domain (a plate in this case), C=C(x,t). Integrating C(x,t) over the thickness of the plate, h, at any given time t, gives the total amount of diffusing substance, M_t, which has entered the plate at time t. After an infinite interval of time, the steady state condition is reached. During this time, the mass change is shown in Crank (1979) to be governed by Equation 7.3.

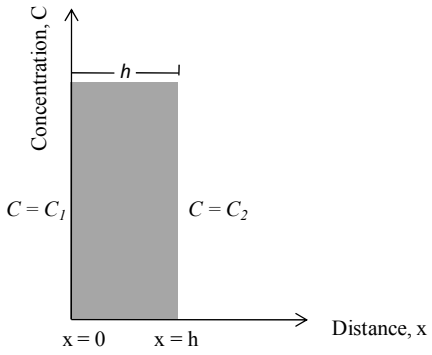

Figure 7.1. A schematic showing typical boundary conditions for diffusion through a plate.

$$\frac{M_t}{M_\infty} = 1 - \frac{8}{\pi^2}\sum_{n=0}^{\infty}\frac{1}{(2n+1)^2}\exp\left[-D(2n+1)^2\pi^2 t/h^2\right] \qquad (7.3)$$

where

M_t : the quantity of diffusing substance after time, t (wt%)

M_∞ : the respective quantity after an infinite length of time (wt%)

D : diffusivity/ the diffusion coefficient (m^2/s)

h : thickness of the plate (m)

n : number of terms in the series.

To determine how many terms would be needed in a practical implementation of the solution shown in Equation 7.3, the number of terms (n) considered in the series was varied from 0 to 4. However, after using n = 1, the mass gain points superimposed on a single line with time, as shown in Figure 7.2.

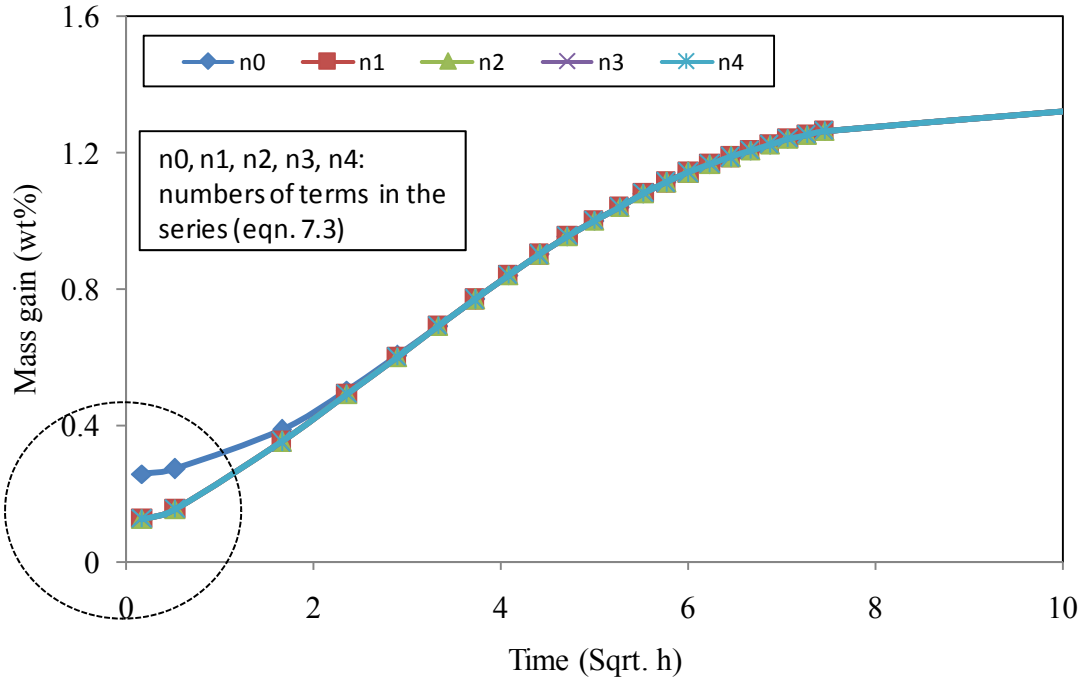

Figure 7.2. Effects of the number of terms, n, in the series on the mass gain for the sheet sample.

For a cylindrical sample, Crank (1979) has solved the diffusion Equation to get Equation 7.4 considering the following boundary conditions that are schematically shown in Figure 7.3.

$C = C_0$, $r = a$, $t \geq 0$

$C = f(r)$ $0 < r < a$, $t = 0$

$f(r) = C_1$, Considering the initial concentration is uniform throughout the cylinder

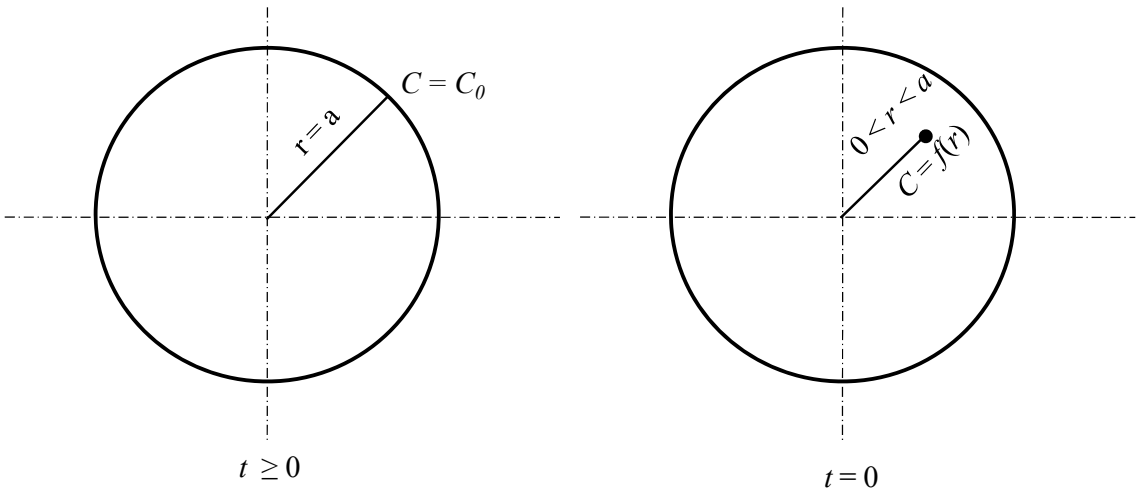

Figure 7.3. A schematic showing the boundary conditions for diffusion through a cylinder.

Just as in the case of the plate, the solution to Equation 7.2 is normally obtained in terms of concentration distribution of the diffusing species in space and time over the considered domain (a cylinder in this case), C=C(r,t). Integrating C(r,t) over the cylindrical radius, a, at any given time t, gives the total amount of diffusing substance, M_t, which is shown in Crank (1979) to be represented by Equation 7.4.

$$\frac{M_t}{M_\infty} = 1 - \sum_{n=1}^{\infty} \frac{4}{a^2 \alpha_n^2} \exp(-D\alpha_n^2 t) \tag{7.4}$$

where

M_t : the quantity of diffusing substance after time, t (wt%)

M_∞ : the respective quantity after an infinite length of time (wt%)

D : diffusivity/ the diffusion coefficient (m^2/s)

a : radius of the sample (m)

α_n : roots of Equation $J_o = 0$, where J_o (x) is the Bessel function of zero order of the first kind (Crank 1979).

Bessel functions are described elsewhere in more detail (BMTA 1937). For calculation purposes, the first ten roots of the Bessel function of the first kind of order zero were used in the simulations presented in this study.

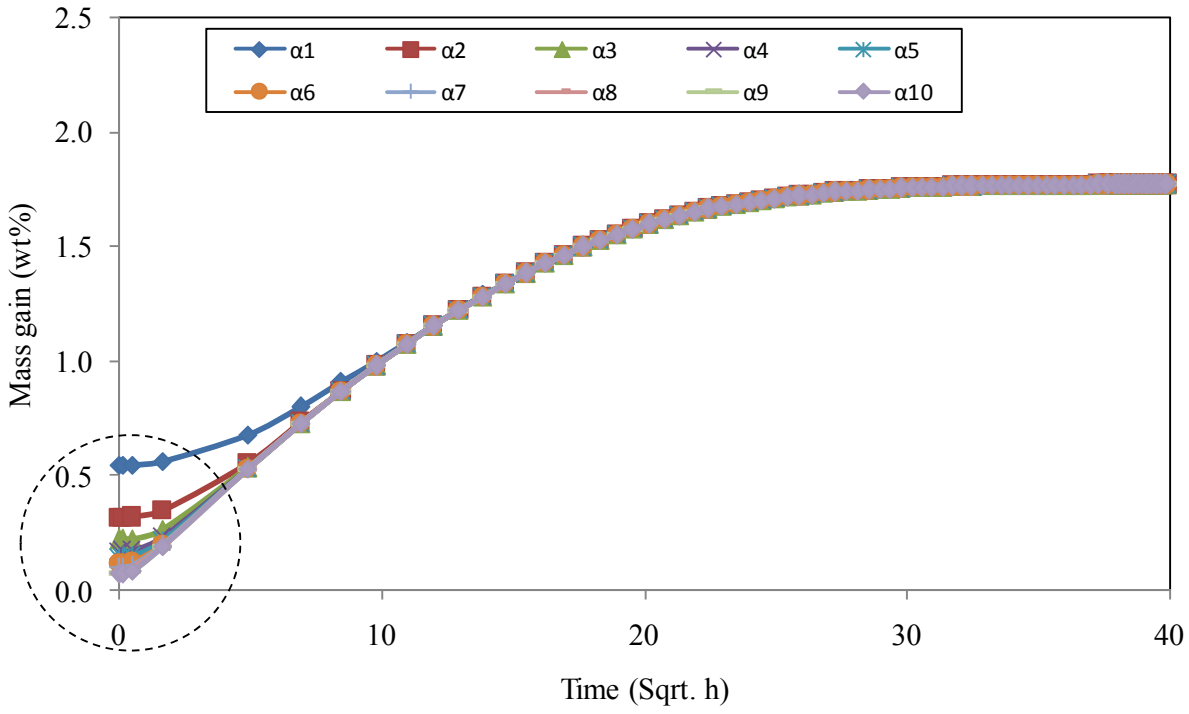

Figure 7.4. Effects of 'α_n' in the series on mass gain for the GFRP rebar sample exposed at 50 °C.

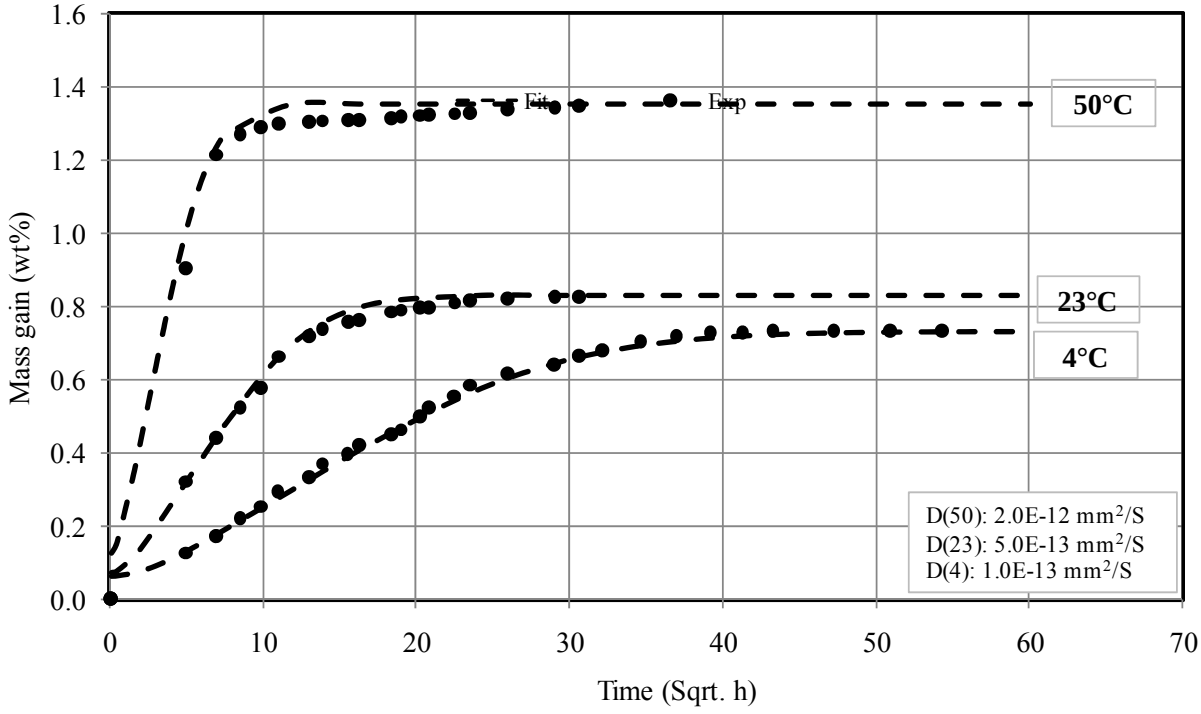

(a)

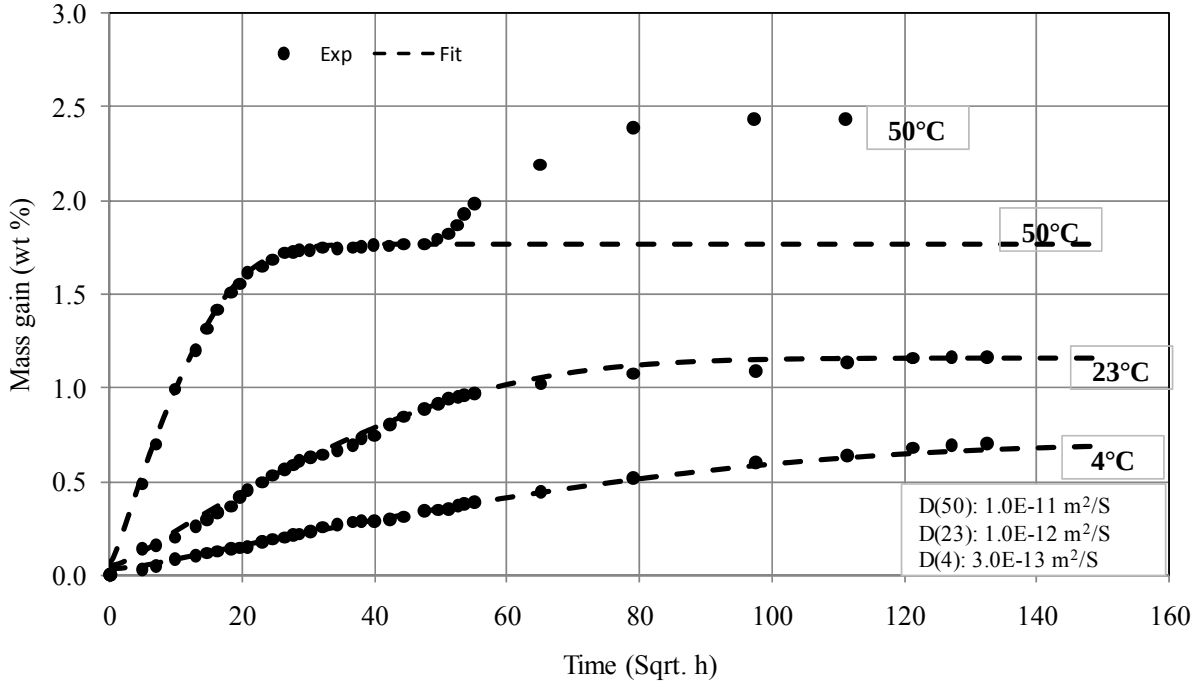

(b)

Figure 7.5. Mass gain of GFRP composites as a function of time at different exposure conditions: (a) GFRP sheets, and (b) GFRP rebars.

With the increase of α terms, the mass gain is observed to become more accurate at shorter times. However after α_6 the mass gain change is practically insignificant, as shown in Figure 7.4. Moisture absorption (%M) as a function of time (sqrt. of hours) for both GFRP rebars and sheets is shown in Figure 7.5. The fit curves were obtained by fitting Equations 7.3 and 7.4 to the experiential data. M_∞ and D were determined at different temperatures for the best-fit curves as shown in Table 7.1.

Table 7. 1. Maximum moisture (M_∞) and diffusion coefficients (D) of GFRP composites at different exposure temperatures.

Temperature	**GFRP sheets**		**GFRP rebars**	
(°C)	Max moisture M_∞ (%)	Diffusion coefficient D (m^2/s)	Max moisture M_∞ (%)	Diffusion coefficient D (m^2/s)
4	0.7338	$1x10^{-13}$	0.7037	$3x10^{-13}$
23	0.8281	$5x10^{-13}$	1.1621	$1x10^{-12}$
50	1.3502	$2x10^{-12}$	1.7691	$1x10^{-11}$

Both types of samples show a similar trend of higher mass uptake with increased temperature. However, the rebars at 50 °C show anomalous (Non-Fickian) behaviour in the experiment. Inhomogeneous components (sands, helical wrapping, and VE resin) at the outer layer of rebars might have had an effect on the larger amount of water uptake than expected by the Fickian model. This kind of anomalous behaviour of moisture uptake has been observed in the published literature (van der Wal and Boulfiza 2007). In their study, GFRP rebars were immersed at pH 7 and pH 14 at 40 °C and 70 °C.

7.4. Temperature effects on diffusivity

The temperature dependence of the diffusivity in GFRP composites was studied by immersing GFRP composites in water at 4 °C, 23 °C, and 50 °C. Assuming an Arrhenius dependence of diffusivity on temperature, as shown in Equation 7.5 (Rabek 1980), the activation energy and the pre-exponential factor can be determined by fitting the experimental data discussed in the previous Chapters.

$$D = D_0 . \exp\left(-\frac{E_a}{RT} \right) \tag{7.5}$$

where,

D : Diffusion coefficient/diffusivity (m^2/s)

D_0 : Pre-exponential factor (m^2/s)

R : Ideal gas constant (8.314 *J/mol-K*)

T : Temperature (K)

E_a : Activation energy for diffusion (*J/mol*)

By taking the natural log of both sides of Equation 7.5 and after simplification, Equation 7.6 can be obtained.

$$\ln D = -\frac{E_a}{R} . \frac{1}{T} + \ln D_0 \tag{7.6}$$

It is a linear Equation. Now, by plotting the values of the natural logarithm of diffusion coefficient as a function of the reciprocal of temperature, one can get the pre-exponential factor (D_0) from the intercept of the Equation at X=0 and activation energy (E_a) from the slope.

By plotting the values of D and T from Table 7.1, the ln(D) vs. 1/T curves are as shown in Figure 7.6. Using a regression analysis (the method of least squares), D_0 and E_a for the sheet were 1.33×10^{-4} m^2/S and 48.16 kJ/mol, respectively; the corresponding parameters for the rebar samples were 1.53×10^{-2} kJ/mol and 57.1 kJ/mol, respectively.

As can be seen in Figure 7.6, the dependence of diffusivity on temperature does follow the Model (linear relationship between ln(D) and 1/T) in the range of temperatures evaluated in this study. Another water uptake study has been carried out earlier for similar GFRP rebar samples immersed in water at 40 °C and 70 °C (van der Wal and Boulfiza 2007). The diffusivity data obtained from that study were 5×10^{-12} m^2/s at 40 °C and 2.41×10^{-11} m^2/s at 70 °C. By plotting the data from that study together with the experimental data obtained in this study, a linear relationship between ln$D$ and 1/T was obtained, as shown in Figure 7.7, confirming that Arrhenius law applies in this entire range of temperatures.

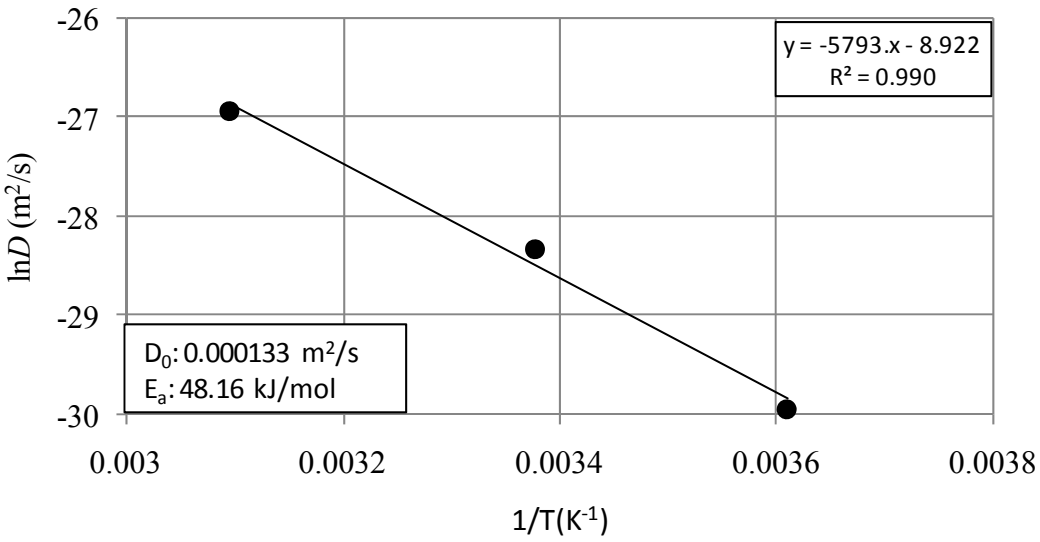

(a)

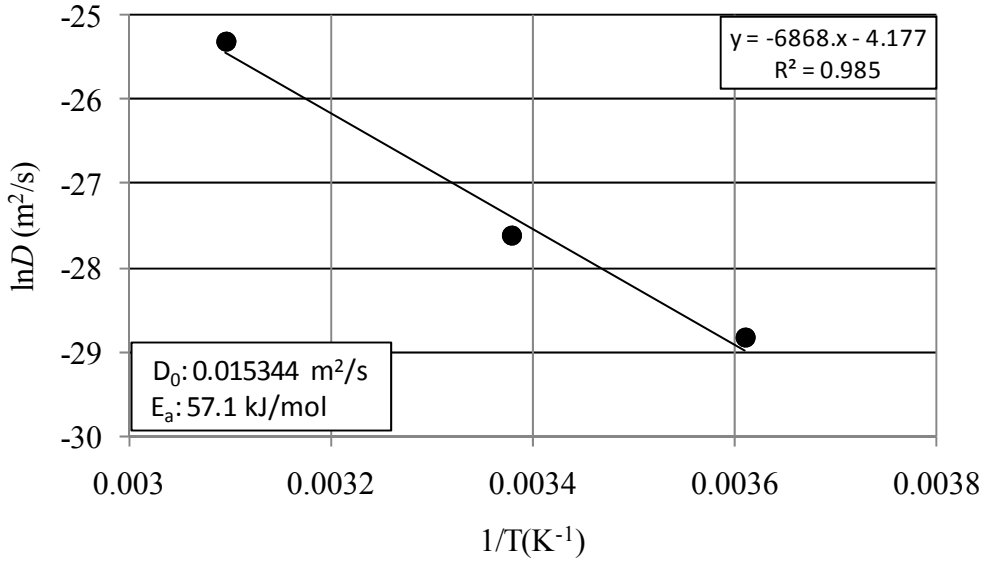

(b)

Figure 7.6. Determining D0 and Ea: (a) GFRP sheets and (b) GFRP rebars.

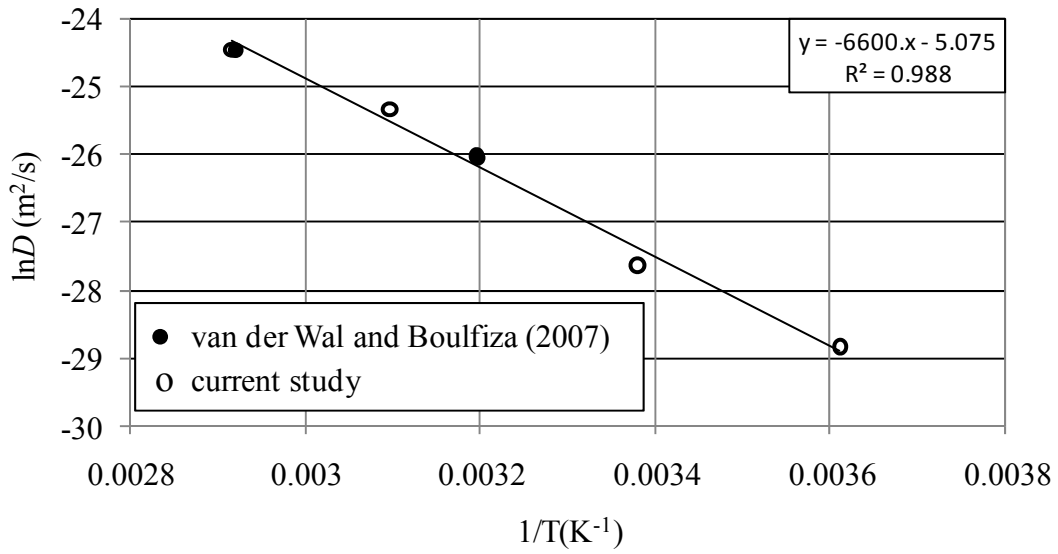

Figure 7.7. Relationship between ln*D* and *1/T* for 23 °C ≤ T ≤ 70 °C.

7.5. Microblister formation: the mechanism behind the behaviour of GFRP composites

7.5.1. Introduction

Generally, water absorption of FRP composites results in detrimental effects on the strength of composites. Strength loss of FRP composites due to water absorption is addressed in Chapter 5. However, the root cause of strength loss was not addressed. It is discussed in this section.

The deterioration of engineering properties of any composite material can always be related to either matrix degradation, fiber degradation, interface/interphase degradation, or any combination of these. As has been shown in the previous Chapters, no matrix or fiber degradation was observed for the VE matrix and E-glass fiber used under all environmental exposure conditions considered in this study. Moreover, no alkali ions were detected inside the GFRP composite for all alkali solutions and temperatures investigated (pH up to 13.7 and temperature up to 75 °C) and no fiber-matrix debonding could be detected for any sample for temperatures up to 50 °C. However, many samples showed signs of fiber-matrix debonding at 75 °C after 12 months of exposure. Also, mass gain data confirmed the penetration of water into the GFRP composites which would eventually reach the fibre-matrix interphase and possibly react with it (Kamal and Boulfiza 2011). A closer look at Figure 7.8b shows that the degradation is basically a physical separation, or debonding, of the matrix from the fiber without any sign of chemical degradation to either constituent; this was also confirmed with the other chemical tests

(FTIR, EDS, etc.) presented in earlier Chapters. The same observation was made for all samples exposed to 75 °C irrespective of the nature of the solution used. In other words, it did not matter whether it was simply pure water or a highly alkaline solution. This is consistent with earlier findings, presented in the previous Chapters, that no alkali ions penetrated the GFRP samples because, otherwise, signs of E-glass dissolution would have been detected.

At this point, it is worth noting that some published data in the technical literature (although usually from studies that considered harsher conditions of temperature and/or the presence of stress) reported severe matrix cracking and fiber dissolution following exposure to alkali ions (Kim et al. 2009; Chen et al. 2007; Chen et al. 2006; Mukherjee and Arwikar 2005; Karbhari and Zhang 2003; Chin et al. 2001; Dejke and Tepfers 2001; Zhang and Karbhari 1999). This severe degradation was also accompanied by significant losses in the tensile strength of GFRP, as one would logically expect. Given the high intrinsic chemical resistance of the VE resins evaluated in this study against water and various chemical solutions, one wonders what possible mechanism(s) might actually be at the origin of this marked change in bahaviour.

Since both matrix and fiber did not suffer any damage up to75 °C, while their interface started to show signs of debonding, any likely candidate mechanism that can potentially explain this transition in behaviour must be related to some degradation at the interface/interphase of the GFRP composite. Knowing that decomposition of a water soluble part of sizing at the fiber-matrix interface has been reported elsewhere in the literature (Tanoglu et al. 2001; Nagae and Otsuka 1996), it is proposed here to evaluate the possibility of microblister formation and growth at the fiber matrix interface as a possible mechanism that can explain and control the long-term behaviour of GFRP composites.

Interphase deterioration due to microblister formation following moisture diffusion and osmosis in composite materials has been reported by some researchers (Bradley and Grant 1995, Mohd Ishak and Lim 1994, Kinloch 1986, and Walter and Ashbee 1982). The detrimental effects of such a microblister growth may cause dimensional changes of the composite that can possibly lead to matrix cracking, leaching out of reaction products, and composition components. A schematic of a fibre-matrix interphase in a GFRP rebar is shown in Figure 7.8a. Models based on diffusion and osmotic theory were developed for the growth of water-filled microblisters at the interface (Walter and Ashbee 1982). Macroscopic solutions can form at the interface, under harsh environments, as a result of either reaction or intrinsic poor adhesion, giving rise to an

osmotic pressure with subsequent microblister formation. Knowing that microdefects always exist at the interface (due for instance to imperfect wetting of the E-glass by sizing), it is proposed here to assess whether those microdefect locations could serve as sites for potential formation and growth of a microblister (local osmotic cells). The possible decomposition of water soluble sizing at the fibre-matrix interface and its contribution to the strength loss of GFRP composites will be discussed in this section.

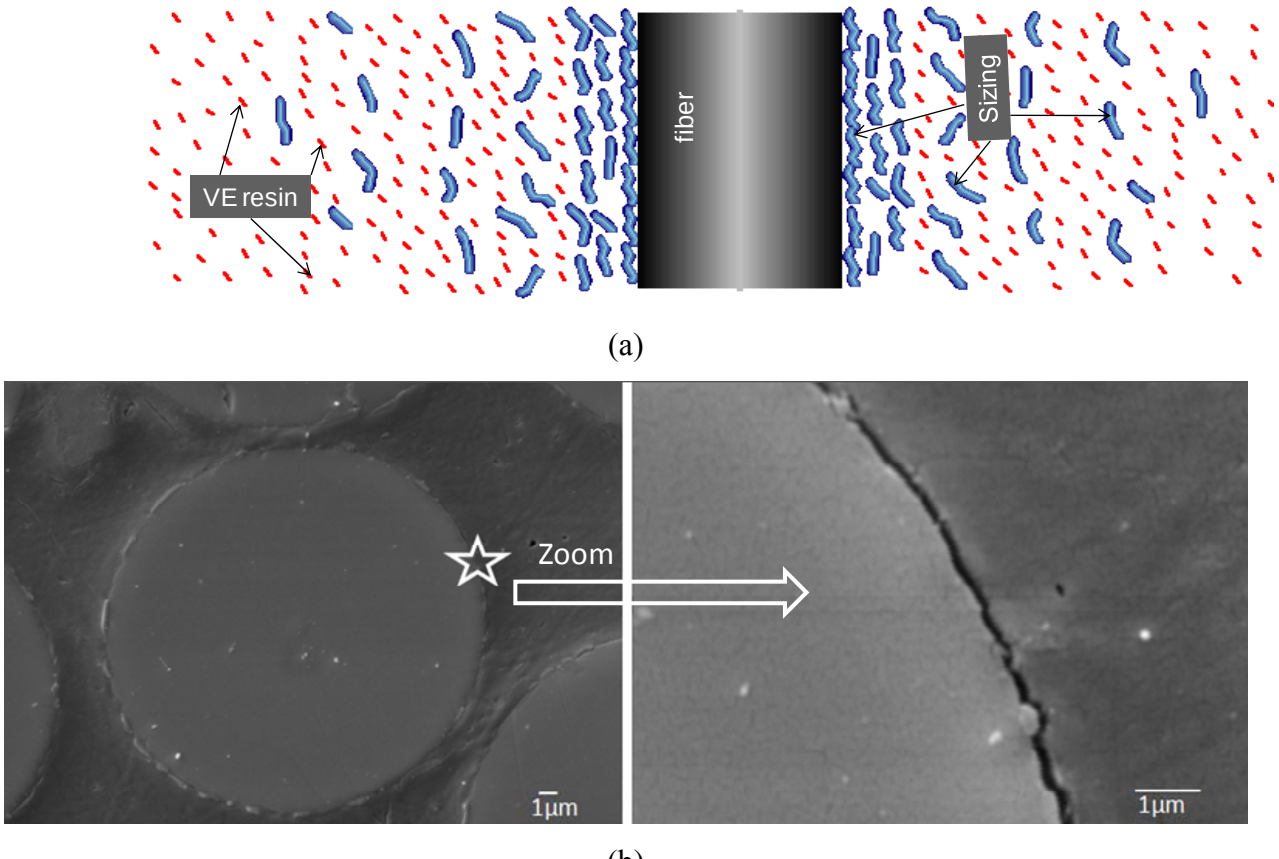

(a)

(b)

Figure 7.8. A fibre matrix interphase in GFRP composite: (a) schematic elevation view, and (b) a SEM view of interphase deterioration after 1 year of exposure at 75 °C.

7.5.2. Background

It has been observed that molecular diffusion of water occurs through FRP composites. The outside epoxy resin layer allows water to traverse into FRP through nanovoids. This is due to the presence of larger size nanovoids, of 5-10 Å diameters, in epoxy resins than the size of water

molecules, 2.6Å (Soles and Yee 2000). Moisture gain of FRP composites also confirms the water penetration (Kamal et al. 2010; Karbhari and Zhang 2003; Thomason 1995; Schutte 1994; Plueddemann 1991; Apicella et al. 1983). Water molecules reach at the fibre-matrix interphase through the networking of epoxy nanopores and thus get a chance to interact with sizing (Soles et al. 2000).

A fiber matrix interphase comprised three segments, as discussed in Chapter five. A fibre-sizing interphase is on one side, with predominately covalent bonds (Figure 5.8, Chapter five). In the middle, an interphase of oligomers that contains elements of sizing, such as silane coupling agent, film former, antistatic agent, lubricant, etc. (Figure 5.7, Chapter five). They are mainly bonded together by weak physical bonds, such as hydrogen bonds and van der Waals attractions. The other end is the sizing-epoxy interphase with predominantly covalent bonds. As the covalent bonds are stronger than those physical bonds, the middle section of the interphase (oligomers) is the vulnerable section for sizing-water interaction to produce a microscopic solution. The microscopic solution may change the osmotic pressure and create a potentially favourable environment for microblister formation and growth.

7.5.3. Analysis of microblister formation

The microblister growth depends on three factors: osmotic pressure, interfacial strength of the matrix and sizing, and the elastic force of the composite (Walter and Ashbee 1982, van der Wal 2006). In this section, how the interfacial and elastic energy are linked with osmotic and critical pressures are presented.

Microblister expansion involves a change in two types of energy: elastic energy of the VE resin and interfacial surface energy. Elastic energy is expressed with an osmotic pressure (P_{os}) and a microblister volume change (dV) in Equation 7.7 (Williams 1969; van der Wal 2006). Again, the volume change (dV) of a penny shaped microblister can be expressed with a microblister disc surface area (A) and the deflection of the microblister [$\omega(r)$] shown in Equation 7.8. The change of deflection as a function of osmotic pressure can be represented by Equation 7.9 (Timoshenko and Woinowsky-Krieger 1959).

$$dE_{\text{elastic}} = P_{os}.dV \tag{7.7}$$

$$dV = d\omega(r).A = d\omega(r).\pi r^2 \tag{7.8}$$

$$\omega(r) = \left(\frac{1}{64}\right).\left[\frac{p.12.\left(1-v^2\right)}{E.h^3}\right].\left(r_{\max}^2 - r^2\right) \qquad r_{\max} \le h \tag{7.9}$$

where,

P_{os} : Osmotic pressure (Pa)

V : molar volume of water in a microblister (m^3/mol)

E_{elastic} : elastic energy (J/m^2)

$\omega(r)$: deflection of a microblister, μm

A : microblister surface area, μm^2

r : microblister radius, μm

p : pressure of a microblister, Pa

υ : Poisson's ratio

E : Young's modulus, Pa

h : outer layer thickness of a GFRP composite, μm

$r_{\max}$: max radius of a microblister, μm

The change of the opposing surface energy can be expressed in terms of the adhesion energy (σ) and the change of surface area (dA), as shown in Equation 7.10.

$$\mathrm{d}E_{\text{surface}} = -\sigma.\mathrm{d}A \tag{7.10}$$

Thus, the resulting total energy is expressed as:

$$\mathrm{d}E = \mathrm{d}E_{\text{elastic}} + \mathrm{d}E_{\text{surface}} \tag{7.11}$$

The total energy corresponds to a minimum microblister size at equilibrium. That equilibrium energy can be expressed in terms of a critical pressure (Williams 1969), as shown in Equation 7.12.

$$P_{cr_i} = \left[\frac{32}{3.\left(1-v^2\right)}.\left(\frac{h}{r_i}\right)^3.\frac{E.\sigma}{r_i}\right]^{0.5} \tag{7.12}$$

Osmotic pressure at the fibre-matrix interphase of the composite develops following a change in the microscopic solution, which is developed by the reaction of sizing with water. The newly developed reaction product could change the osmotic pressure that offers the potential environment for a microblister formation. For simplicity, the microscopic solution for the microblister formation is considered as a dilute solution. The osmotic pressure, P_{os}, is a function of molar volume of water, *Uw*, the mole fraction of water in that microscopic solution, X_i, the ideal gas constant, *R*, and the temperature, *T*, as described in McBride (1994) and is shown in Equation 7.13.

$$P_{os} = -\left(\frac{RT}{U_w}\right)\ln X_i \tag{7.13}$$

Molar volume of water changes with the exposure temperatures (4 °C-75 °C). The estimated molar volume of water (m^3/mol) is 1.802E-05, 1.806E-05, 1.823E-05, 1.848E-05 at 4 °C, 23 °C, 50 °C, and 75 °C, respectively. The molar volume of water at different temperatures was obtained by dividing the molar mass of water (18.016 g) by the molar density of water at those temperatures. The molar density of water at different temperatures is available in the literature (Lide 2007).

The mole fraction of water (X_0) depends on the number of moles of water that react with silane coupling agent at the fibre-matrix interphase. As illustrated in Chapter 5, one mole of silane coupling agent reacts with four moles of water. Thus, the estimated initial mole fraction of water in the microblister is 0.8.

The growth of a microblister size is related to the dilution of water in the microblister. The dilution of water is represented by Equation 7.14, with the initial and final radii of the microblister being denoted by r_o and r_i, respectively.

$$X_i = 1-\left[\left(\frac{r_0^2}{r_i^2}\right).\left(1-X_0\right)\right] \tag{7.14}$$

7.5.4. Conditions of microblister simulation

As explained earlier, macroscopic solutions can form at the interface as a result of either reaction or intrinsically poor adhesion (like microdefects due to imperfect wetting of the E-glass by sizing). Those microdefect locations could serve as sites for potential formation and growth of a microblister, following the formation of local osmotic cells. In GFRP rebars, bulk fibres are typically surrounded by 50 μm VE coatings. Therefore, the potential region for the first possible microblister nucleus is under the outside VE resin layer of FRP composites. Thus, the thickness of the outer layer for the GFRP rebars should be 0.05×10^{-3} m, and for the GFRP sheets should be 0.45×10^{-3} m (dimensions of GFRP sheet as discussed in Chapter 3).

A typical GFRP rebar contains glass fibers with a diameter of 5-10 μm (ISIS 2003). Usually, the thickness of sizing over glass fibers is about 2 volume percent of fibre. Thus, a glass fibre with a diameter of 6 μm that carries about 2 percent (by volume) of sizing would have a layer thickness of approximately 0.1 μm. For simulation purposes, the initial nucleus diameter is also considered to be 0.1 μm. This nucleus should contain the reaction products of sizing and water. And the amount of water in the nucleus is based on the reaction equilibrium conditions of sizing and water.

Young's modulus of cast VE resin is estimated as 3×10^{9} Pa for the highest exposure temperature (75 °C) based on the reports of Asland (2004) and Curry and Rolston (2007). Poisson's ratio of VE resin is reported as 0.4 for room (Cease et al. 2006).

The adhesion energy for glass fibre-VE resin interface is hard to assume. Therefore, conservatively low adhesion energy of 0.001 J/m^2 was used to simulate the strength loss because of the sizing-water reaction (Lee 1992).

7.5.6. Microblister simulation

The possibility of blister growth at the fiber matrix interface is evaluated in this section. In order for a blister to grow, the osmotic pressure that develops inside the interface microdefect (represented by Equation 7.13) must be higher than the critical pressure of the system (represented by Equation 7.12). A graphical representation of the critical pressure as a function of microblister radius (Equation 7.12) is shown in Figure 7.9 for GFRP sheets and GFRP rebars. Basically, both types of composites – GFRP sheet and GFRP rebar - produce curves with similar trends. However, the critical pressure in the GFRP sheet is about one order of magnitude higher

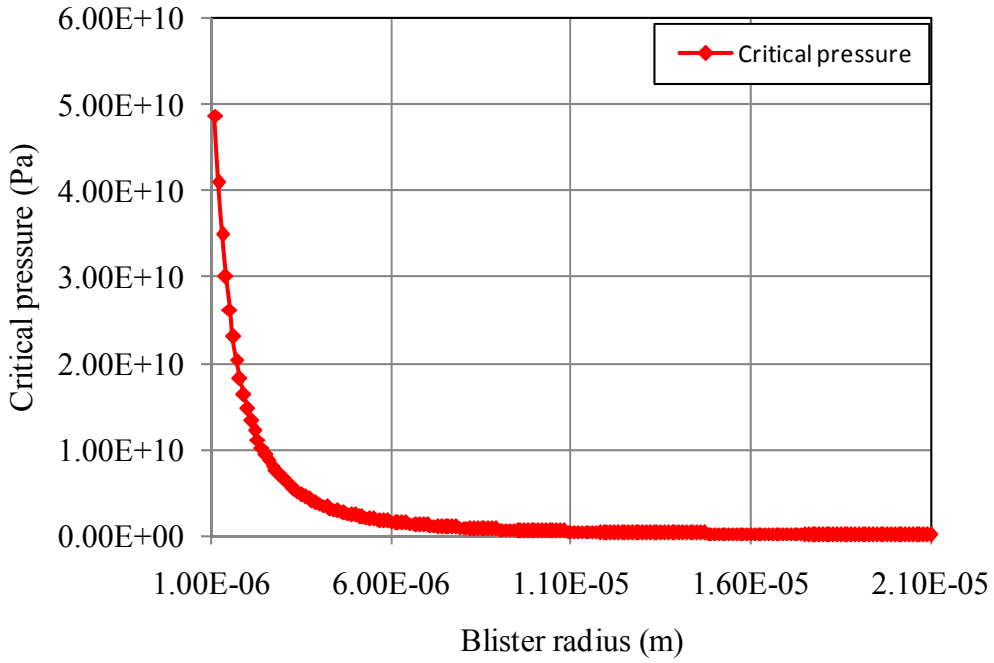

(a)

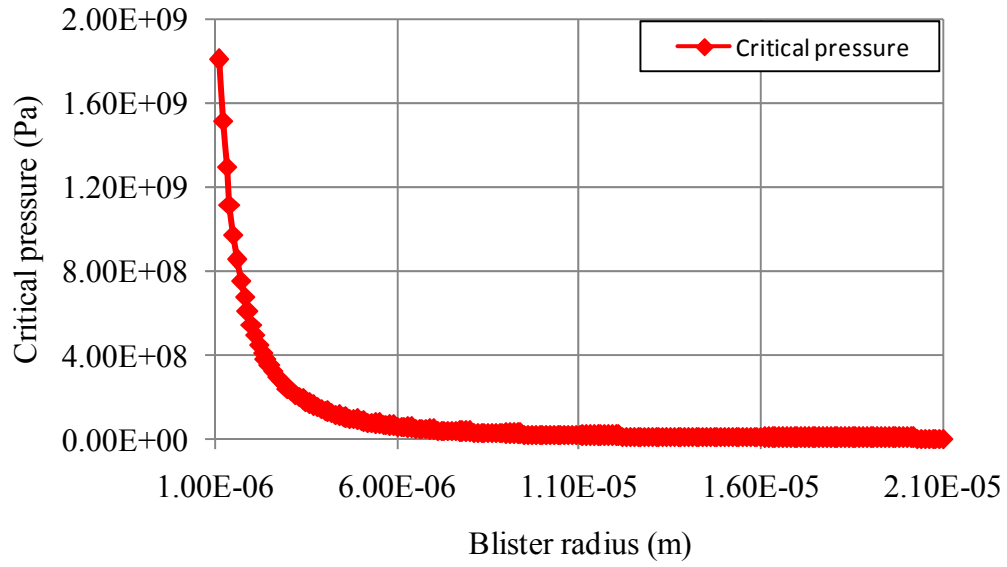

(b)

Figure 7.9. Critical pressure of a growing microblister as a function of microblister radius: (a) GFRP sheets and (b) GFRP rebars.

than that of the GFRP rebars. This difference is due to the thickness of the outer layers for the two composites. The GFRP sheets, with a thicker outer layer (0.45×10^{-3} m), generate a greater critical pressure than the GFRP rebars, with a thinner outer layer (0.05×10^{-3} m). With higher critical pressure, the chance of microblister formation is generally lower. This result shows the importance of the thickness of the outer layer; the thicker the outer layer surrounding an FRP composite, the lower a chance of microblister formation.

In both cases, there is a large critical pressure. Now, we need to assess whether an equilibrium reaction of water with sizing could generate a sufficient osmotic pressure to let a microblister grow and overcome such a large critical pressure. A graphical representation of the osmotic pressure as a function of microblister radius (Equation 7.13) is shown in Figure 7.10.

Again, both types of composites – GFRP sheet and GFRP rebar - produce curves of similar trends showing decreasing osmotic pressure with increasing microblister size. In terms of magnitude, both composites (GFRP sheets and GFRP rebars) develop similar osmotic pressures under similar defect geometries and initial conditions. However, it is worth noticing that the kinetics is different; it would be faster for the osmotic pressure to develop in the GFRP rebars than the corresponding pressure in the sheets because of the difference in thickness of the outer layer. Moreover, the osmotic pressure is shown to be higher at higher temperatures, as expected for both composites.

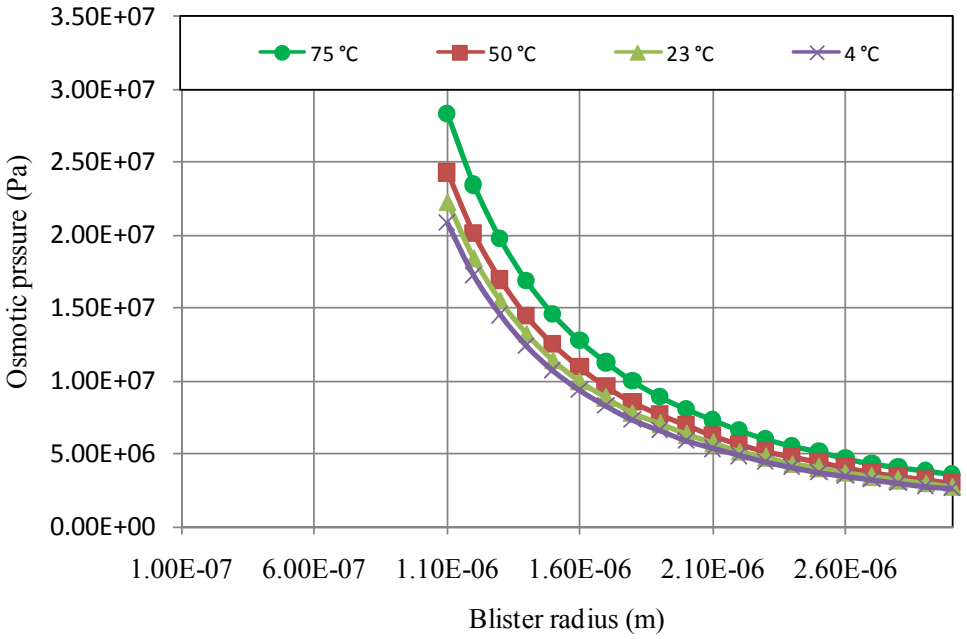

(a)

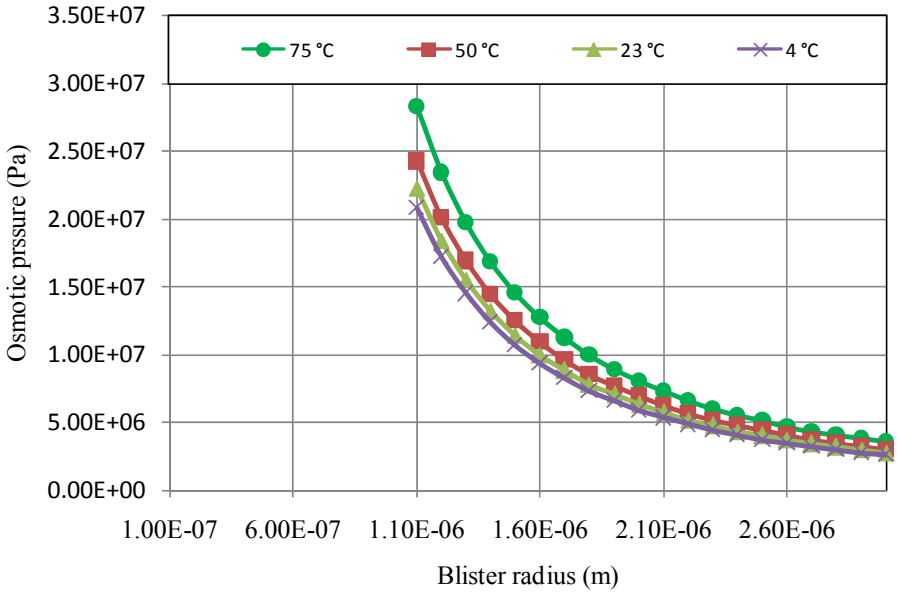

(b)

Figure 7.10. Osmotic pressure of growing microblisters as a function of microblister radius: (a) GFRP sheet and (b) GFRP rebar.

7.5.7. Analysis

A comparison of osmotic pressures with the critical pressures for both GFRP sheets and GFRP rebars is shown in Figure 7.11. The simulation parameters used correspond to a temperature of 75 °C as reported in Table 7.2. In both cases, the osmotic pressure is found to be much smaller than the critical pressure needed for the blister to grow. Thus, the possibility of change in volume, or matrix cracking, for the GFRP composite in water is virtually zero at the exposure temperatures considered in this study.

Table 7.2. Simulation conditions to cause microblister formation and growth in GFRP rebars

Pressure type	Simulation parameters	Simulation conditions at 75 °C*	Simulation conditions at 95 °C**
Osmotic pressure	Molar vol. of water, U_w (m^3/mol)	1.848E-05	1.867E-05
	Mole fraction of water in microblister, X_0	0.8	0.8
	Gas const., R ($J/mol\text{-}K$)	8.314	8.314
	Temperature, T ($°K$)	348	368
Critical pressure	Outer layer thickness of composite, h (m)	5.00E-05	5.00E-05
	Initial disc radius of the microblister, r_o (m)	1.00E-07	8.00E-07
	Young's Mod., E (Pa)	3.00E+09	3.00E+08
	Poisson's ratio (υ)	0.40	0.45
	Adhesion energy, σ (J/m^2)	0.001	0.000001

* Experimental conditions, ** considering accumulated effects all factors, such as sustained load, high pH solutions on the simulation parameters.

However, it has been shown that sizing decomposes in water in the composite at 75 °C, and this is expected to influence the mechanical strength of the composite. This dissolution of glass fibre sizing in water has also been observed elsewhere in the literature (Tanoglu et al. 2001; Nagae and Otsuka 1996). The retention of the mechanical properties of the GFRP rebars can be estimated using a Dynamic Mechanical Analysis (DMA). This technique is used to determine the viscoelastic properties of materials. An oscillating force is applied to the sample to determine various properties, such as storage modulus, loss modulus, glass transition temperature, etc. Van der Wal and Boulfiza (2007) conducted a DMA test for GFRP rebars by applying an oscillating force at 1 Hertz and 25 °C, and measuring the material's response. The results of the measurements were as follows:

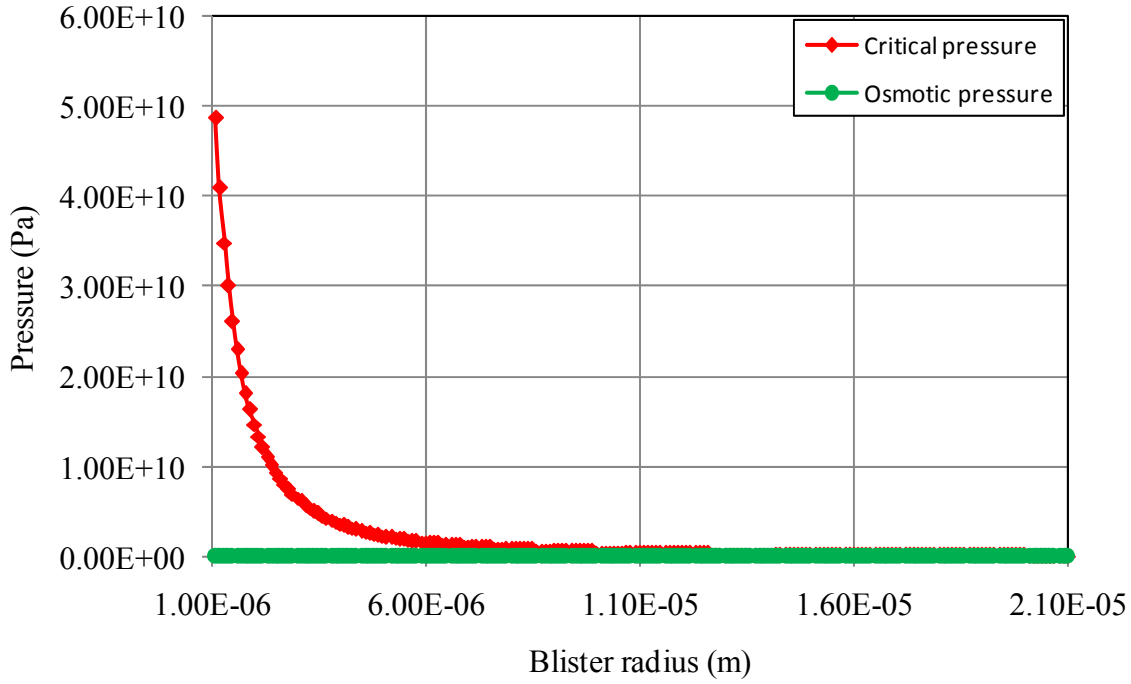

(a)

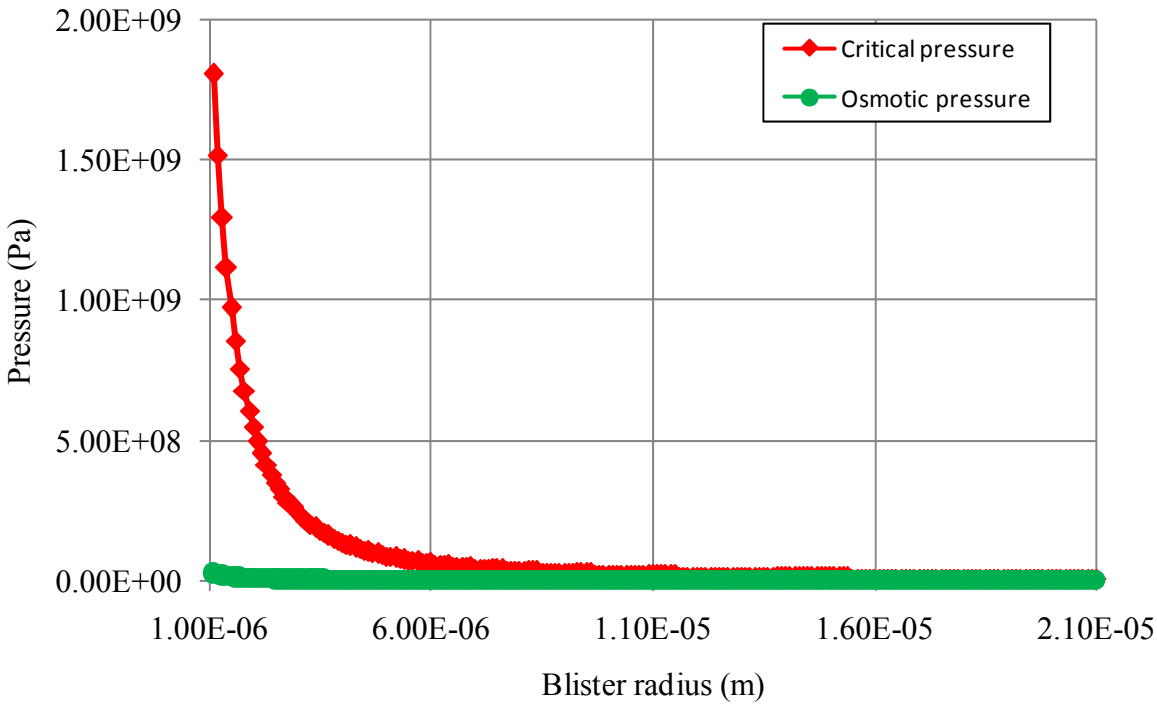

(b)

Figure 7.11. Pressure profile of growing microblister: (a) GFRP sheet and (b) GFRP rebar.

- Unexposed sample: E storage: 27 GPa / E loss: 1.0 GPa
- Sample exposed to pH 7 and T=70 °C: E storage: 25 GPa / E loss: 1.0 GPa
- Sample exposed to pH 14 and T=70 °C: E storage: 25 GPa / E loss: 1.0 GPa

One can easily see that the storage modulus of the exposed samples is slightly lower than that of the unexposed samples, due to decomposition of sizing. However, it is worth noticing that no difference exists between the solution with pH 7 and that with pH 14. In a viscoelastic material, the storage modulus measures the stored energy, representing the elastic portion, while the loss modulus measures the energy dissipated as heat, representing the viscous portion. This result is consistent with published data about the loss of mechanical strength in GFRP composites due to moisture absorption (Yeol-Kim et al. 2007, Chen et al. 2006; Dejke and Tepfers 2001; Murphy et al. 1999; Porter et al. 1997; Katsuki and Uomoto 1995).

7.6. Parametric study of the microblister model

The microblister simulations shown in the previous section used exposure conditions to match those of GFRP samples (rebars and sheets) immersed in deionized water at 75 °C (Among all exposure temperatures, 4 °C, 23 °C, 50 °C, and 75 °C, the highest temperature (75 °C) was used for the first simulation). The rest of the needed simulation parameters used are shown in Table 7.2. Generally, a model is not equally sensitive to all input parameters. Analyzing the model's predictions in relation to variations in the input parameters allows one to find out what quantities have the greatest impact on the studied output. In this section, the influence of the model parameters that can affect a blister growth in GFRP rebars on the critical pressure and osmotic pressure are analysed. This information will also be used to investigate the impact of some possible manufacturing imperfections (such as uncertainty in the material properties or in geometric properties such as the thickness of the outer layer VE matrix, etc.). Prior to the analysis, a brief discussion of the simulation parameters and how they vary with temperature is in order.

With an increase in temperature, the density of water will decrease and its volume will increase. The molar volume of water is estimated to be 1.848×10^{-5} m^3/mol at 75 °C and 1.873×10^{-5} m^3/mol at 95 °C.

Young's modulus: Young's modulus of cast VE resin is reported as 3.2×10^9 Pa at room temperature (Asland 2004; Curry and Rolston 2007). Young's modulus of VE resin was estimated as 3.2×10^9 Pa at 66 °C, 2.65×10^9 Pa at 93 °C, drastically decreased after 100 °C, and finally becoming almost zero at 130 °C, from the modulus vs. temperature profile reported in Curry and Rolston (2007). It is worthy to note here that the *Tg* of VE resin is in between 110~135 °C, as reported in Herzog et al. (2005) and Ashland (2004). At *Tg*, the Young's modulus of VE should be minimum. The impact of other factors will certainly aggravate the situation even at lower temperature. Therefore, Young's modulus of cast VE resin was considered to 3.00×10^8 Pa at 95 °C (considering accumulated effects of other factors) in place of 3.00×10^9 Pa at 75 °C(experimental conditions).

Poisson's Ratio: Poisson's ratio of cast VE resin is reported to be 0.4 at room temperature (Cease et al. 2006). Just like the Poisson ratios of most materials, which increase with temperature (SM 2011), the Poisson's ratio of VE will also increase. The Poisson's ratio for VE was considered to be 0.45 at 95 °C (considering accumulated effects of other factors) for the purpose of simulation, rather than 0.4.

Adhesion energy: The adhesion energy of VE resin with sizing will be greatly affected by high temperature changes. Composites exposed to high enough temperatures will start to experience of weakening of the fibre-matrix interphase bonds. Aggressive exposure conditions will accelerate the bond scission process and the adhesion energy between fiber and matrix will be very poor. Therefore, very conservative low adhesion energy of 0.000001 J/m^2 was considered at 95 °C (considering accumulated effects of other factors) for the purpose of simulation, in the place of 0.001 J/m^2 at 75 °C (experimental conditions).

The proposed microblister model requires a number of input parameters to be defined before it can be used. These parameters, which originate from basic thermodynamic blister formation theory, can be listed as follows:

Critical pressure parameters

- Geometric Properties
  - Outer layer VE matrix thickness, h (m)
  - Initial disc radius of the blister, r_o (m)
- Material Properties
  - Young's modulus, E (Pa)
  - Poisson's ratio, υ
  - Fiber matrix adhesion energy, σ (J/m^2)

Osmotic pressure parameters

- Temperature, T (K)
- Molar volume of water, U_w (m^3/mol)
- Initial mole fraction of water in blister, X_0

In this Chapter presented so far, the above quantities have been assumed to be constants that are selected within the range of reported values found in the literature. However, experimental studies have shown that these parameters can show significant variations; therefore, the selection of these parameters for modeling purposes can be a challenging task.

A parametric study is carried out to investigate the effect of variations in blister formation parameters on the possibility of blister growth in GFRP composites. The main goal of this investigation was to identify the parameters that have significant influence on degradation. Since there is uncertainty associated with the selection of these parameters, it is intended that the results of this study will provide valuable information to engineers or GFRP manufacturers on the parameters/defects that may play a major role on the performance of GFRP in harsh environments. To achieve this goal, the effect of a single parameter on the blister formation and propagation was studied while all other parameters were kept constant. All simulations were run using the base case model which corresponds to a temperature of 75 °C, as reported in Table 7.2. The parameter under investigation was varied while all other parameters were kept at their base-case values.

7.6.1. Effect of variation in outer layer VE matrix thickness

Four values were considered in this analysis: a very low thickness (10E-6 m), low thickness (25E-6 m), a medium thickness (50E-6 m), and a high thickness (75E-6 m). As can be seen in Figure 7.12, relatively important changes take place in the critical pressure, although it remains much higher than the osmotic pressure for the considered values. This simulation stresses the need to maintain a minimum coverage of the fibers to avoid blister expansion, especially when considering higher temperatures that would necessarily lead to higher osmotic pressures as well.

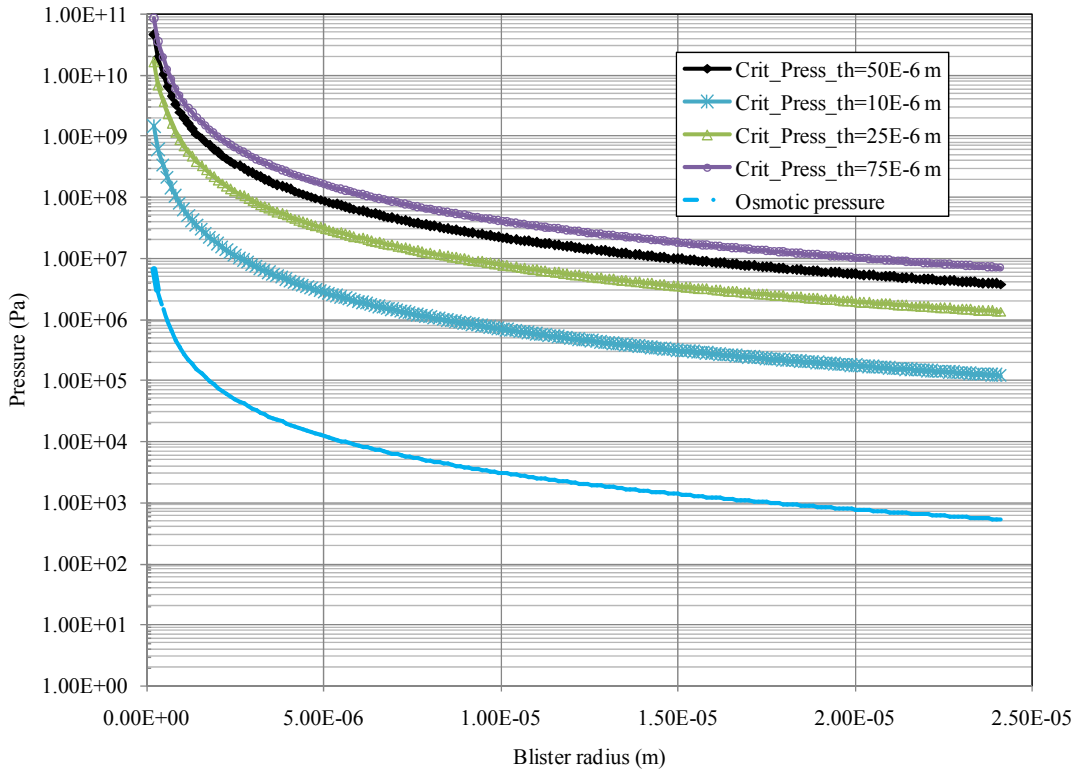

Figure 7.12. Effect of outer later thickness variation on the critical and osmotic pressures for microblister growth in GFRP rebars.

7.6.2. Effect of variation in initial disc radius of the blister

Three values were considered in this analysis: a small initial disc radius ($1.0x10^{-7}$ m), a medium initial disc radius ($1.0x10^{-6}$ m), and a large initial disc radius ($1.0x10^{-5}$ m). As can be seen in Figure 7.13, the three curves are perfectly superposed. The only difference is the starting point

for each curve, which corresponds to the size of the initial defect (i.e., the initial radius of the blister). The three curves have been represented with increasing blister thicknesses so that it would be easier to identify where each one starts. Only relatively small changes take place on the critical pressure, which remains much higher than the osmotic pressure for the considered values.

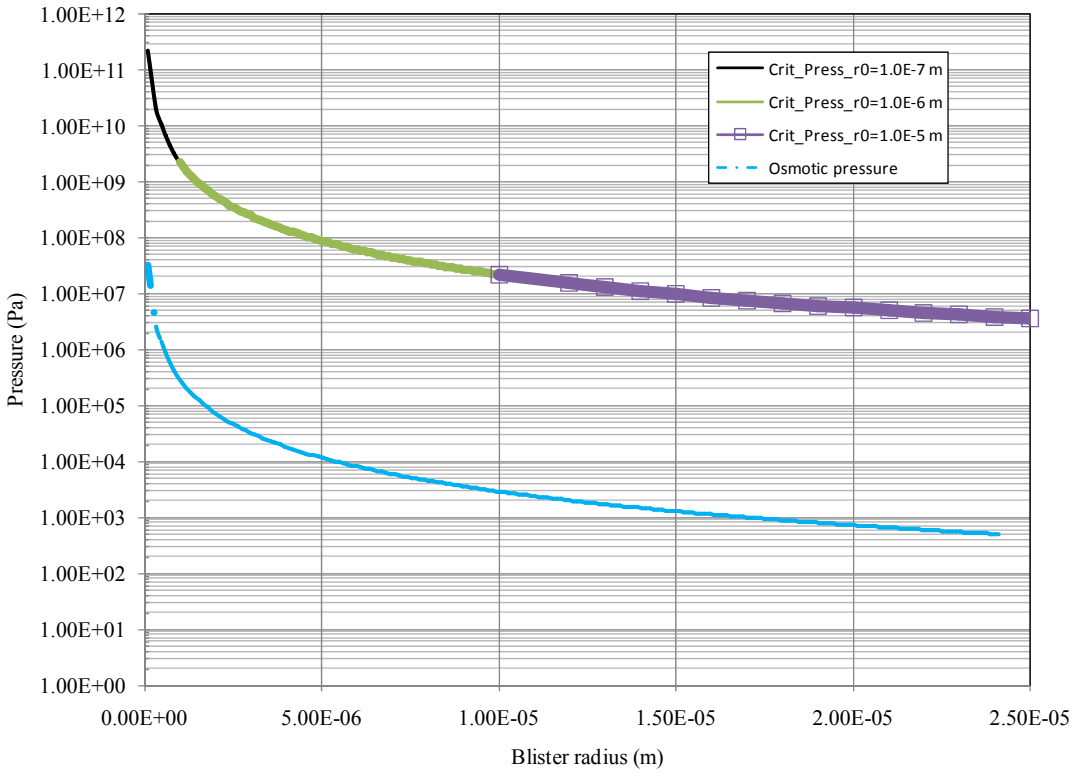

Figure 7.13. Effect of initial defect radius variation on the critical and osmotic pressures for microblister growth in GFRP rebars.

7.6.3. Effect of variation in Young's modulus of the VE layer

Three values were considered in this analysis: a low Young's modulus (1.5 GPa), a medium Young's modulus (3.0 GPa), and a high Young's modulus (6.0 GPa). As can be seen in Figure 7.14, only relatively small changes take place in the critical pressure, which remains much higher than the osmotic pressure for the considered values. The osmotic pressure does not depend on Young's modulus, and hence, is not affected at all by its variation.

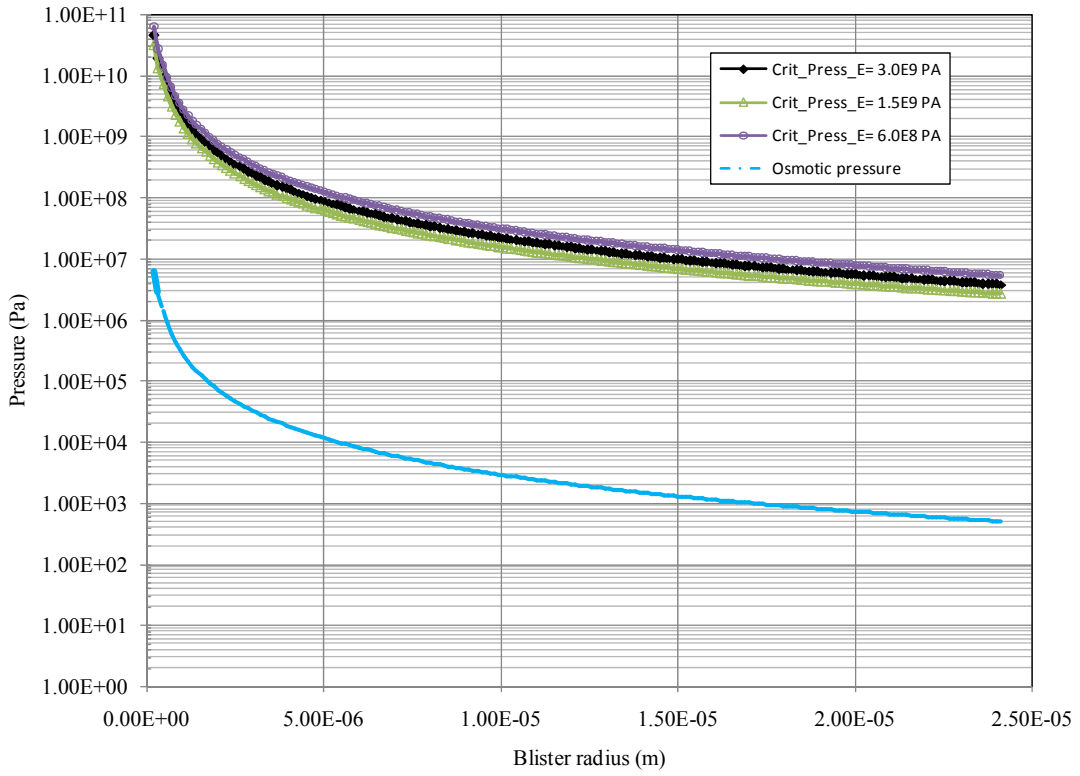

Figure 7.14. Effect of Young's modulus variation on the critical and osmotic pressures for microblister growth in GFRP rebars.

7.6.4. Effect of variation in Poisson's ratio

To evaluate the effect of some uncertainty in the value of Poisson ratio for a certain composite on the critical pressure, three values were considered in this analysis; a low Poisson's ratio (ν=0.35), a medium Poisson's ratio (ν=0.40), and a high Poisson's ratio (ν=0.45). As can be seen in Figure 7.15, the considered variation in Poisson's ratio has virtually no effect on the critical pressure. Hence, it can be concluded that the critical pressure is not very sensitive to Poisson ratio. Consequently, its value does not need to be very accurately known. The osmotic pressure does not depend on Poisson's ratio, and hence, is not affected at all by its variation.

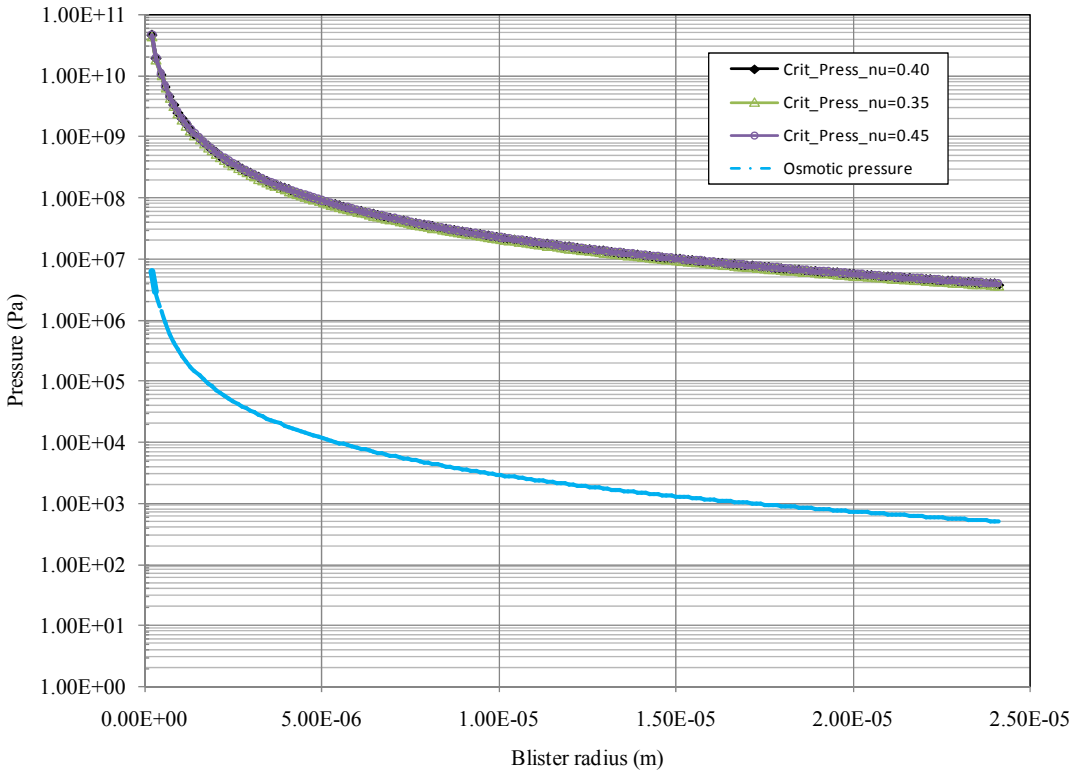

Figure 7.15. Effect of Poisson's ratio variation on the critical and osmotic pressures for microblister growth in GFRP rebars.

7.6.5. Effect of variation in adhesion energy

Three values were considered in this analysis for the fiber-matrix adhesion energy: a low adhesion energy (1.0E-6 J/m^2), a medium adhesion energy (1.0E-3 J/m^2), and a high adhesion energy (1.0E-2 J/m^2). As can be seen in Figure 7.16, relatively important changes take place in the critical pressure, which remains much higher than the osmotic pressure for the considered values. The osmotic pressure does not depend on the adhesion energy, and hence, is not affected at all by its variation.

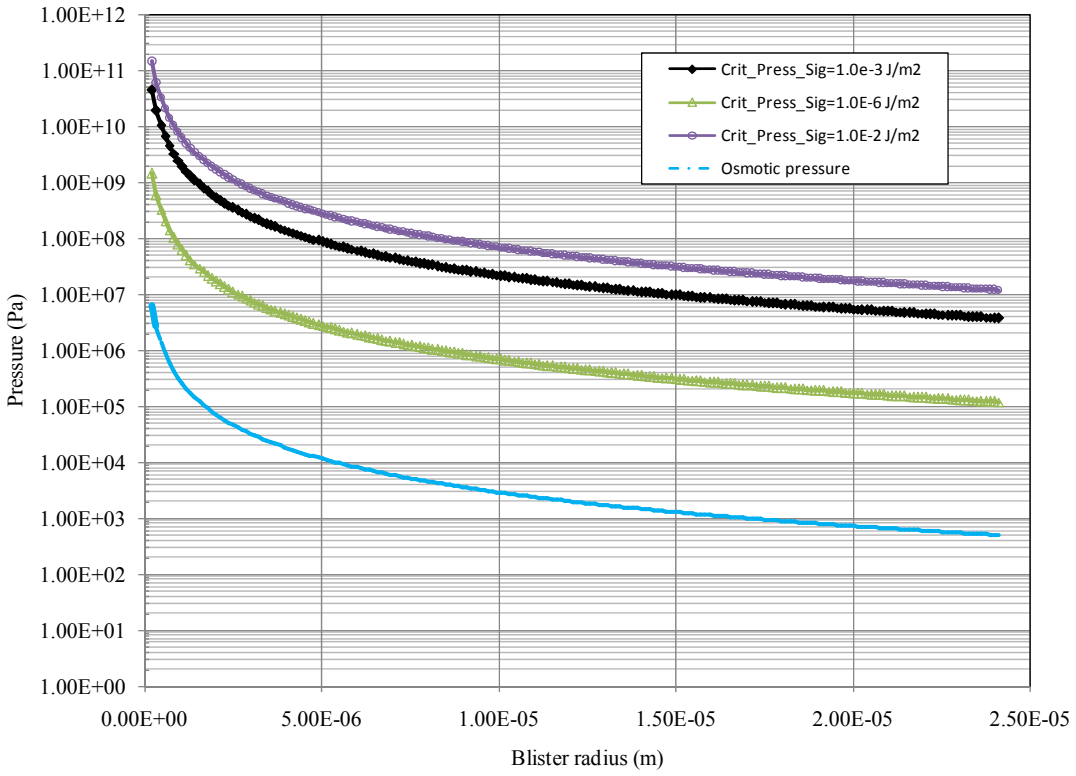

Figure 7.16. Effect of adhesion energy variation on the critical and osmotic pressures for microblister growth in GFRP rebars.

7.6.6. Effect of temperature

Although temperature appears explicitly only in the expression of the osmotic pressure, it is also implicitly present in the expression of the critical pressure as it has significant impacts on all the material properties of GFRP (Young's modulus, Poisson's ration, adhesion energy, etc.). The parameters used in the previous simulations were based on a reference temperature of 75 °C and did not show any potential for blister growth under the simulated conditions, although some sizing dissolution took place at some fiber matrix interfaces. It is proposed here to consider a case where temperature is spiked to a very high value (while remaining below T_g for the VE matrix used in the GFRP composite being evaluated) and see whether a preexisting microblister would be able to grow or not if the changes in material parameters are accounted for. The

temperature of 95 °C was chosen for evaluation and the corresponding properties are shown in Table 7.2.

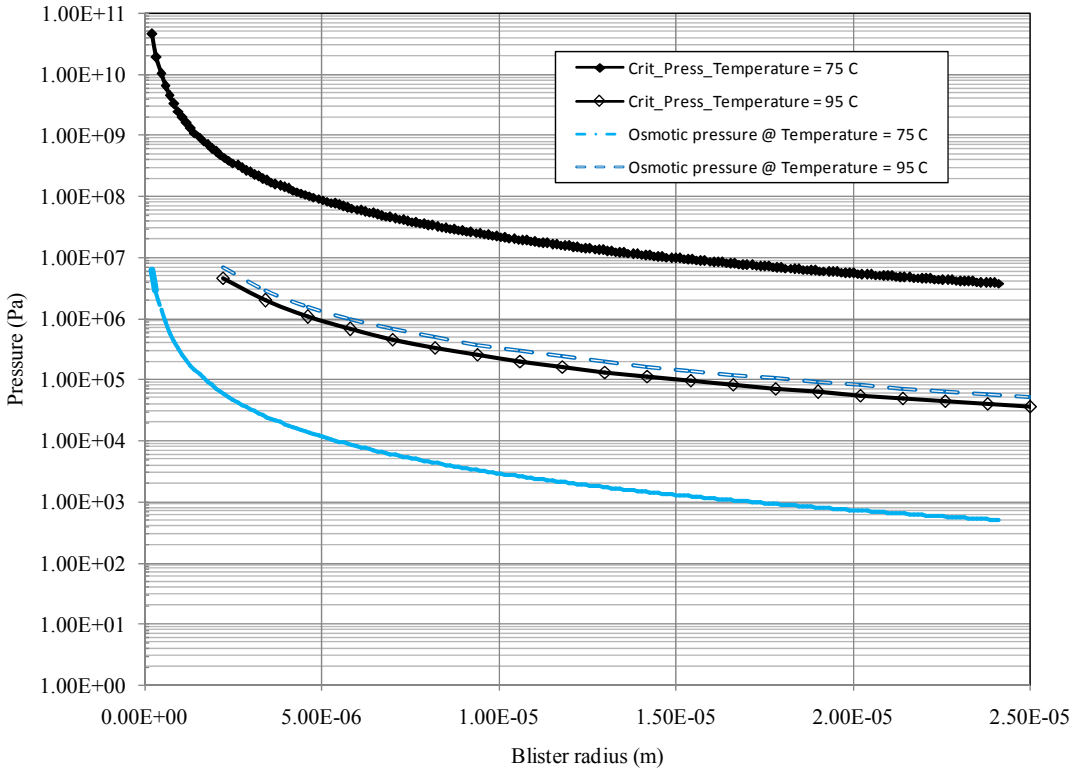

Figure 7.17. Effect of temperature variation on the critical and osmotic pressures for microblister growth in GFRP rebars.

As shown in Figure 7.17, there is a clear shift in microblister behaviour as the temperature increases from 75 °C to 95 °C. As can be easily seen, the conditions for microblister formation and growth are met at 95 °C as the osmotic pressure becomes higher than the critical pressure. Therefore, it is likely that the microblister formation and growth can take place at 95 °C, and lead to volume changes and possibly matrix cracking, as has been observed in some laboratory tests. Figure 7.17 also shows that the GFRP composite evaluated in this study remains very stable until temperature reaches values not too far from the glass transition temperature of the VE matrix. The present model does not take into account the effect of stress coming from applied loads. It is expected that the temperature for blister formation and growth can be lowered

if the applied stress is high enough. This aspect of evaluating the impact of a simultaneous action of applied loads and environmental conditions still remains to be done and could be accomplished by coupling the concept of blister nucleation and growth in an osmotic cell with the stress state in the composite. Ideally, one should use already well established solid mechanics theories such as damage or fracture mechanics and the mechanism of blister formation to predict the entire performance of GFRP composites under all kinds of environments, from the pristine state to ultimate failure. This kind of model would have the ability to capture the transition in behaviour of GFRP composites from a stable condition, with no damage, to conditions where damage can initiate and grow under extreme environments. Indeed, this would be a major departure from service life prediction models based on accelerated ageing tests, where it is typically assumed that the damage mechanisms active under high temperatures are the same as those active at low temperatures and the only effect of temperature is to accelerate the deterioration rate. Based on those models, one would expect to see damage in the GFRP composites right from day one. However, this kind of prediction is in sharp contrast with field observations. A recent study (Mufti et al. 2007) that involved five different projects spread across Canada has confirmed that no signs of degradation could be observed in any of GFRP samples, even after eight years of service. Despite its relative simplicity, the proposed microblister model seems to be able to capture the essential parameters controlling the performance of GFRP composites when exposed to ambient as well as high temperatures.

7.7. Conclusions

The performance of GFRP composites depends on exposure conditions, sustained loads, and ingredient quality, among others. It has been observed that GFRP composites are alkali resistant at harsh exposure conditions, provided that a decent thickness (say about 50 μm) of the outer VE layer exists all around the sample and remains un-cracked. However, the mass gain from aqueous solution confirms the water penetration into GFRP composites. Therefore, the performance of GFRP composites at various immersed water temperatures was predicted in this study and the possibility of microblister nucleation and growth, following the establishment of an osmotic cell, was addressed in terms of adhesion energy, osmotic and critical pressures.

Moisture gain and diffusivity of GFRP sheets and rebars have been shown to increase with increasing time and water temperature. Fickian behaviour has been observed for all

situations, except GFRP rebars at 50 °C, where an anomalous water uptake has been identified. The diffusion coefficient dependence on temperature has been shown to obey an Arrhenius Equation for both composites (GFRP sheets and GFRP rebars).

Based on the thermodynamics of microblister formation and growth, a rational model has been proposed to address the mechanisms of microblister formation at the interphase of FRP composites. Results of the analyses show that the critical pressure that needs to be overcome by the osmotic pressure before a microblister can grow is much higher than the latter one for both GFRP rebar and GFRP sheet samples until 75 °C for the temperatures considered in this study. Thereby, one can conclude that no micromicroblister is formed at the given experimental conditions of samples immersed at a pH 7 with the temperatures of 4 °C, 23 °C, 50 °C, and 75 °C. The same model also predicted that if the temperature is spiked to very high values (around 95 °C), a preexisting microblister would be able to grow, which could eventually lead to matrix volume changes and/or cracking, even if the temperature remains below Tg for the matrix.

CHAPTER EIGHT

CONCLUSIONS AND RECOMMENDATIONS

8.1. Overview

The overall objective of this study was to develop a better understanding of the mechanisms controlling the durability of GFRP composites in concrete, and hence, try to explain some of the "strange behaviours" observed when assessing the service life/performance predictions based on the assumption that the degradation mechanisms from room temperature to Tg are the same and follow Arrhenius law. Indeed, using Arrhenius law to represent the effect of temperature on degradation implicitly assumes that the degradation mechanisms remain the same in the range of the considered temperatures and that the only effect of temperature is to accelerate the rate of degradation. Since it would take too long to observe any degradation under typical service environments, it is an attractive approach to carry out tests at high enough temperatures to cause damage in a relatively short time, and then use Arrhenius law to predict damage behaviours at lower temperatures, especially those representatives of service conditions. An important characteristic of all prediction models based on this kind of approach is that the process of degradation would start from day one. However, predictions of this kind are in sharp contrast with field observations. A recent study (Mufti et al. 2007) that involved five different projects spread across Canada has confirmed that no signs of degradation could be observed in any GFRP samples, even after eight years of service.

To assess the validity of the Arrhenius assumption and identify which degradation mechanisms might change as temperature is increased, the study was divided into three phases. The possibility of the penetration of alkali ions and the deterioration of the three main phases of GFRP composites (matrix, fibre, and their interface) under accelerated ageing conditions were assessed in Phase 1. Results of this phase showed that no alkali ions were observed to penetrate into the GFRP rebars, and that both the VE matrix as well as the E-glass fibre were practically intact. However, some dissolution took place at the fibre-matrix interphase at 75 °C. This loss of interface bond is usually one of the reasons behind strength loss in GFRP composites in

accelerated ageing tests. The cause of debonding at the interphase was investigated in Phase 2. Two main factors that control the strength of FRP composites were identified: sizing and moisture absorption. Finally, the moisture penetration in GFRP rebars was assessed by identifying effects of RH during wetting and drying of GFRP rebars in Phase 3. Based on the findings of the three phase experimental programme, the mechanism of microblister formation and growth at the fibre-matrix interphase was proposed as a mechanism to explain the discrepancy between field observations and performance predictions based on accelerated ageing tests and Arrhenius law. A thermodynamics-based rational model was also proposed to assess the possibility of microblister formation and growth, and to study the parametric effects on the microblister formation at the fibre-matrix interphase. The following sections review the key findings of this study and make recommendations for further research.

8.2. Does the outer VE matrix layer act as a membrane?

The purpose of phase 1 of the experimental programme (discussed in Chapter 4), was to investigate and determine which component of the composite material (vinyl ester matrix, E-glass fibre, their interface) would show signs of degradation under the accelerated ageing conditions considered. GFRP rebars were immersed in five types of simulated concrete pore solutions at 23 °C, 50 °C, and 75 °C, and tested for 1 month, 3 months, and 12 months. Penetration of alkali ions was assessed using X-ray mapping of Backscattered Electron Images (BEI) and crosschecked by line and point Energy Dispersive Spectroscopy (EDS) techniques. The degradation of the polymer matrix was assessed by a Fourier Transform Infrared (FTIR) Spectroscopy, while the degradation of the fibre was investigated by observing highly-magnified Scanning Electron Microscopy (SEM) images at the interphase, and point EDS on fibre and matrix close to the fibre-matrix interface. The effects of harmful chemical species on the fibre-matrix interphase were evaluated by investigating the potential degradation of the fibre-matrix interphase using high resolution SEM pictures.

8.2.1. Key findings

(a) No alkali ions were observed to penetrate into the rebars immersed in deionized water and alkali solutions, at all exposure temperatures, even after 12 months of exposure.

(b) No significant deterioration of the VE matrix was observed for the samples at all exposure conditions, even after 12 months of exposure. This finding suggests that the VE resin evaluated in this study has an intrinsic chemical resistance against water and alkaline solutions.

(c) No significant degradation of the E-glass fibres was observed for the samples at all exposure conditions, even after 12 months of exposure.

(d) No fibre-matrix debonding was observed after one and three months of exposure for any samples. However, debonding showed in some samples after 12 months of exposure. Interestingly, samples immersed in lower temperatures (23 °C and 50 °C) did not show any sign of debonding, but all higher temperature samples (75 °C), irrespective of solution pH, showed debonding.

(e) The above findings confirm that the VE polymer matrix effectively acts as a semi-permeable membrane in GFRP composites allowing water to penetrate, while blocking harmful alkali ions. This fact should remain true as long as the outside protective resin layer (about 50 μm thick) is present and remains undamaged.

8.2.2. Recommendation for further study

(a) All the testing carried out in this study did not involve the effect of external loads. However, structures in the field are subjected, at the same time, to both applied loads and environmental conditions. Hence, it would be very important to see how these findings might change in the presence of stresses due to applied loads. Both static and dynamic loads should be considered, especially fatigue loading which is typically experienced by many structures suffering from steel reinforcement corrosion, such as bridge decks.

8.3. Effect of sizing on strength retention and water uptake

The findings of phase 1, showing that most of the damage was confined to the fibre-matrix interphase under the test conditions considered, stimulated an investigation into the effects of sizing on the strength retention and water up-take of GFRP rebars (Phase 2). The sizing effects on the composite's properties, particularly the tensile strength and moisture gain, was studied using GFRP custom plane sheets, due in part to the unavailability of GFRP rebars with de-sized

glass fibres. The GFRP custom plane sheet was-produced by a Vacuum Infusion Process (VIP) that was specifically developed for this study. Two series of experiments were carried out by immersing sheet specimens (sized and de-sized) in deionized water at 4 °C, 23 °C, and 50 °C. The fibreglass mat was de-sized and the GFRP custom plane sheets were manufactured by the newly developed techniques at a lab-scale. Chapter 5 discusses the effects of sizing at the interphase of GFRP composites. Sizing ingredients at the fibre-matrix interphase control the bond-strength of composites. The key issues to address were (i) the possibility of producing GFRP custom plane sheets with both sized and de-sized E-glass fibres, and (ii) the effects of sizing on the tensile strength retention and water uptake in GFRP composites.

8.3.1. Key findings

The preparation of GFRP custom plane sheets

(a) A newly developed lab-scale vacuum infusion technique was used to produce GFRP custom plane sheets with both sized and de-sized glass fibre mats.
(b) A desizing procedure was also developed to remove sizing from glass fibre mats.

<u>Interphasial effects of sizing</u>

(a) Sized and de-sized specimens showed similar trends of moisture gain when exposed to the same environmental conditions. The percent of mass gain increased with increasing temperature.
(b) Moisture diffusivities were also observed to increase with temperature according an Arrhenius law for both types of specimens.
(c) Sized specimens showed a higher strength retention than the de-sized ones at all exposure conditions. This is believed to be due to the preservation of strong interphasial bonds between fibres and matrix in the case of sized fibres. Organo silane (the active ingredient in sizing) contributes to the development of covalent bonds behind the overall strength retention in the sized specimens.
(d) De-sized specimens exhibited a lower strength due to the weaker fibre-matrix bond formation.

(e) With the increase of temperature, the strength retention characteristics decreased for both types of specimens by breaking the weaker van der Waals bonds at the fibre-matrix interphase.

8.3.2. Recommendation for further study

(a) To make the GFRP sheets more representative of the GFRP rebars, curing them at a higher temperature (but still below the Tg of VE) than the room temperature is recommended.

(b) The fibre-matrix bond strength of GFRP custom plane sheet should be evaluated by indentation and advanced techniques such as X-ray Photoelectron Spectroscopy (XPS) for a better characterization of interfacial phenomena.

8.4. Effects of relative humidity and temperature on water uptake

The effects of sizing on the mass gain and strength retention of GFRP composites were investigated at 100% relative humidity (RH) in Phase 2. However, field service conditions, with respect to RH and temperature, for GFRP composites in concrete are expected to vary with time. Therefore, a further study was conducted to investigate the effects of RH and temperature on the properties of GFRP rebars in Phase 3. The effects of RH were investigated by exposing GFRP rebars to nine RH environments (9%-100%) and taking mass changes during drying and wetting. Moreover, the thermal effects of GFRP rebars on water uptake in deionized water at 4 °C, 23 °C, and 50 °C was studied and compared with those for GFRP custom plane sheets.

Chapter 6 discusses the experimental results of mass changes of GFRP rebars at different RH environments. The key issues to address were (i) the effects of RH on the properties of mass changes (gain and loss) for GFRP rebars during drying and wetting, and (ii) the effects of temperature on the mass transport in GFRP rebars and GFRP sheets.

8.4.1. Key findings

Effects of RH

(a) The mass gain vs RH curves were different for drying and for wetting. This dependence of the mass gain vs RH curve on the direction and history of drying and wetting of a sample is called hysteresis.

(b) The percent of mass gain at 100% RH showed a significant difference from that at other RH environments.

Effects of temperatures

(a) Mass gain and moisture diffusivity were found to increase for both rebars and custom sheets with increasing temperature.

(b) A typical Fickian behaviour of water absorption was observed for GFRP sheet and GFRP rebar samples at all exposure conditions, except for the GFRP rebars at higher temperature (starting at 50 °C), which showed a non-Fickian behaviour for water absorption.

(c) The dependence of the diffusion coefficient on temperature was found to follow an Arrhenius Equation.

(d) GFRP rebars took a longer period of time to become water saturated (more durable) than the plane sheets (less durable) at all exposure environments. The phenomenon of moisture uptake is controlled by the elemental compositions, manufacturing, and curing processes of FRP composites.

8.4.2. Recommendation for further study

(a) Only one type of GFRP rebar was investigated in this study. It would be beneficial to evaluate more of the GFRP rebars available on the market to have a better representation of this reinforcement technology.

8.5. Predicting the performance of GFRP

The deterioration of engineering properties of any composite material can always be related to either matrix degradation, fibre degradation, interface/interphase degradation, or any

combination of these phases. As has been shown in the previous Chapters, no matrix or fibre degradation was observed for the VE matrix and E-glass fibre used under all environmental exposure conditions considered in this study. Moreover, no alkali ions were detected inside the GFRP composite for all alkali solutions and temperatures investigated (pH up to 13.7 and temperature up to 75 °C) and no fibre-matrix debonding could be detected for any sample for temperatures up to 50 °C. However, many samples showed signs of fibre-matrix debonding at 75 °C after 12 months of exposure. On the other hand, it is worth noticing that some published data in the technical literature (although usually under harsher conditions of temperature and/or presence of stress) report severe matrix cracking and fibre dissolution following exposure to alkali ions. This severe degradation is also accompanied by significant losses in the tensile strength of GFRP, as one would logically expect. Such extreme accelerated ageing tests have sometimes been used as a basis for developing service life prediction models. Typically, it is assumed in these kinds of models that the damage mechanisms active at high temperatures are the same as those active at low temperatures and the only effect of temperature is to accelerate the deterioration rate. Based on those models, one would expect to see damage in the GFRP composites right from day one. However, these kinds of predictions are in sharp contrast with field observations. A recent study (Mufti et al. 2007) that involved five different projects spread across Canada has confirmed that no signs of degradation could be observed in any of GFRP samples, even after eight years of service. Despite its relative simplicity, the proposed micoblister model seems to be able to capture the effects of the essential parameters controlling the performance of GFRP composites when exposed to ambient as well as high temperatures.

Chapter 7 discuses the prediction of GFRP performance. Moisture absorption data for GFRP rebars and GFRP sheets were utilized for the prediction study. Samples were immersed in deionized water at 4 °C, 23 °C, and 50 °C and the experiment continued until they were saturated. The key issues to address were (i) Can Fick's model be used to predict moisture absorption, (ii) Can the dependence of temperance on moisture absorption obey the Arrhenius Equation for both composites, and (iii) Can the mechanism of microblister formation and growth at the fibre-matrix interface predict the long-term durability of GFRP composites in concrete and possibly explain the discrepancy between field performance and extreme accelerated ageing conditions.

8.5.1. Key findings

Predicting moisture absorption by a Fickian model

(a) GFRP sheets showed the Fickian behaviour of water absorption at all temperatures. GFRP rebars showed the Fickian behaviour of water absorption except at higher temperature (50 °C). The inhomogeneous outer layer of GFRP rebars may have caused the Non-Fickian behaviour.

(b) The dependence of diffusion coefficient on temperature was found to obey an Arrhenius law in both types of samples (GFRP sheets and GFRP rebars).

Concept of microblister formation

(a) The mechanism of blister formation and growth at the fibre-matrix interface has been proposed to explain the transition in behaviour of GFRP composites from stable condition, with no damage, to conditions where damage can initiate and grow under extreme environments, even below the glass transition temperature of the VE matrix.

(b) As moisture penetrates into the composite and reaches the fibre-matrix interphase, an osmotic cell develops (at locations of poor adhesion and/or reaction product of sizing with water), and can lead to blister formation, under the appropriate conditions.

(c) Based on the thermodynamics of microblister formation, a rational model has been proposed to address the issues of interphase degradation in GFRP composites.

(d) Results of the model's predictions show that the critical pressure, that needs to be overcome by the osmotic pressure before a microblister can grow, is actually much higher than the latter one for both GFRP sheet and GFRP rebar samples up to 75 °C for the temperatures considered in this study. Therefore, one can conclude that no microblister is formed at the given experimental conditions of samples immersed at a pH 7 with the temperatures of 4 °C, 23 °C, 50 °C, and 75 °C.

(e) The same model also predicted that if temperature is spiked to very high values (around 95 °C), a preexisting microblister would be able to grow, which could eventually lead to matrix volume changes and/or cracking, even if the temperature remains below the glass transition temperature of the matrix.

8.5.2. Recommendations for further study

(a) Water diffusivity was shown to obey a Fickian behaviour at low temperatures (typically below 50 °C) but exhibits some anomalous behaviour beyond that value. Although, Fick's laws of diffusion could be used for predicting moisture ingress into the GFRP bars when temperatures remain below 50 °C, they should be used with caution beyond that value. More elaborate diffusion models that can account for the observed behaviour should be identified and used.

(b) It is worth noticing that the present model does not take into account the effect of stress coming from applied loads. It is expected that the temperature for blister formation and growth would be lowered if the applied stress is high enough.

(c) This important aspect of evaluating the impact of a simultaneous action of applied loads and environmental conditions still remains to be done and could be accomplished by coupling the concept of blister nucleation and growth in an osmotic cell with the stress state in the composite. Ideally, one should use already well established solid mechanics theories such as damage or fracture mechanics and the mechanism of blister formation to predict the entire performance of GFRP composites under all kinds of environments, from the pristine state to ultimate failure. This kind of model would have the ability to capture the transition in behaviour of GFRP composites from stable condition, with no damage, to conditions where damage can initiate and grow under extreme environments. Indeed, this would be a major departure from service life prediction models based on accelerated ageing tests, where it is typically assumed that the damage mechanisms active under high temperatures are the same as those active at low temperatures and the only effect of temperature is to accelerate the deterioration rate.

REFERENCES

ACMA. 2004. "Composites basics: Materials." *American Composites Manufacturers Association*. Available in URL: < http://www.mdacomposites.org/mda/>. (Jan. 12, 2008).

Andrady, A. L. 2003. *Plastics and the Environment*. Willey-Interscience: USA.

Andrews, E. H., Pingshen, H. and Vlachos, C. 1982. "Adhesion of epoxy resin to glass." In: *Proc. R. Soc. London A; Mathematical, Physical and Engineering Sciences*, 381, 345-360.

Apicella, A., Migliaresi, C., Nicolais, L. and Roccotelli, S. 1983. "The water aging of unsaturated polyester-based composites: Influence of resin chemical structure." *Compos.*, 14(4), 387–392.

Ashland. 2004. "Derakane 411-350 epoxy vinyl ester resin." *Compo. Polym.* Available in URL: <http://www.derakane.com/> (Jan. 12, 2008).

ASM. 1995. *Engineering Materials Handbook*. ASM International, Desk Ed: The materials information society.

ASM. 1986. *Materials Characterization Handbook*, 9th Ed., Vol.10. ASM International: Metarials Park, Ohio.

ASTM D5229M. "Standard test method for moisture absorption properties and equilibrium conditioning of polymer matrix composite materials." D-5229M-92R04, *ASTM Int.*, West Conshohocken, PA, 2004. p. 65-72.

ASTM D638-10. "Standard test method for tensile properties of plastics." D638-10. *ASTM Int.*, West Conshohocken, PA, 2010. p.1-16.

ASTM E3-01. "Standard Guide for the preparation of metallographic specimens." E3-01. *ASTM Int.*, West Conshohocken, PA, 2007. p.1-13.

ASTM E8. "Standard test methods for tension testing of metallic materials." D-5229M-92R04, *ASTM Int.,* West Conshohocken, PA, 2009. p. 65-72.

Azom 2010. "Resin properties for composite materials." Available in URL: < http://www.azom.com/Details.asp?ArticleID=997#_Degradation_from_Water>. (Jan. 12, 2008).

BAMT. 1937. British Association Mathematical Tables, Vol. 6, Bessel Functions, Cambridge.

Bank, L. C., Barkatt, A. and Gentry, T. R. 1995. "Accelerated test methods to determine the long-term behavior of FRP composite structures: Environmental effects." *J. Reinf. Plast. Compos.*, 14(6), 559– 587.

Bank, L. C., Gentry, T. R., Barkatt, A., Prian, L., Wang, F. and Mangla, S. R. 1998. "Accelerated aging of pultruded glass/vinylester rods." *Proc. 2nd Int. Conf. Comp. Infra.,* ed. H. Saadatmanesh, and M. R. Ehsani, 423-437.

Bank, L. C., Puterman, M. and Katz, A. 1998a. The effect of material degradation of bond properties of FRP reinforcing bars in concrete. *ACI Mats. J.,* Technical Paper, 95M-22.

Bank, L. C., Gentry, T. R., Thomson, B. P. and Russell, J. S. 2003. "A model specification for FRP composites for civil engineering structures." *Const. Build. Mats.*, 17, 405–437.

Barkatt, A. 2001. "Issues in predicting in long-term environmental degradation of fibre reinforced plastics." In: *Environmental Effects on Engineered Materials*, ed. Russell H.J. Marcel Dekker, Inc. NY: USA, 419-458.

Bascom, W. D. 1998. "Fibre sizings." In: *Composites: Engineered Materials Handbook*, Vol 1. ASM International.

Bayrs, E. A. Waldron, P., Dejki, V. Demis, S. and Heddadin, S. 2003. "Durability FRP in concrete – Deterioration mechanisms." *Int. J. Mat. & Prod. Tech.*, 19(1-2): 28-39.

Benmokrane, B., Wang, P., Pavate, T. and Robert, M. 2006. "Durability of FRP composites for civil infrastructure applications." In: *Durability of Materials and Structures in Building and Civil Engineering*, C. W. Yu and J. W. Bull, eds., Whittles Publishing: Dunbeath, Scotland.

Benmokrane, B. and Cousin, P. 2005. "University of Sherbrooke GFRP durability report." *Intelligent Sensing for Innovative Structures (ISIS)*, Canada.

Benmokrane, B., Wang, P., Ton-That, T. M., Rahman, H. and Robert, J. F. 2002. "Durability of glass fibre-reinforced polymer reinforcing bars in concrete environment." *J. Comp. Constr.*, 6(3): 143-153.

Bird R. B., Stewart, W. E. and Lightfoot, E. N. 2007. *Transport Phenomena*, Revised 2nd edition. John Wiley & Sons, Inc: NY/ Chichester/ Weinheim/ Brisbane/ Singapore/ Toronto.

Boulfiza, M. and Banthia, M. 2005. "Durability study Report." *Intelligent Sensing for Innovative Structures (ISIS)*, Canada.

Boulfiza, M. and Banthia, N. 2009. "A chemo-hydro-mechanical model for predicting the long-term performance of GFRP rods in concrete." *A Paper Presented to the Conf. of ISIS Canada network Association*, Toronto, Canada, May 7-8.

Bradley, W. L. and Grant, T. S. 1995. "The effect of the moisture absorption on the Interfacial strength of polymeric matrix composites." *J. Mat. Sci.*, 30: 5537-5542.

Callister, W. D. 2010. *Materials Science and Engineering-An Introduction*, 10th ed. Wiley: NY.

Campbell, F. C. 2004. *Manufacturing Processes of Advanced Composites*. Elsevier Advanced Technology: Oxford, UK.

Carrey, F. A. and Sundberg, R. J. 1990. *Advanced Organic Chemistry*. 3rd ed. Part A: Structure and Mechanism. Plenum Press: NY and London.

Cease. H., Derwent. P. F., Diehl. H. T., Fast, J. and Finley. D. 2006. Measurement of mechanical properties of three epoxy adhesives at cryogenic temperatures for CCD construction, Fermilab Technical Report FERMILAB-TM-2366-A. Available at http://lss.fnal.gov/archive/test-tm/2000/fermilab-tm-2366-a.pdf

Chen, Y., Davalos, J. F. and Ray, I. 2006. "Durability prediction for GFRP bars using short-term data of accelerated aging tests." *J. Comp. Constr*., 10(4): 279-286.

Chen, Y., Davalos, J. F., Ray, I. and Kim, H. Y. 2007. "Accelerated aging tests for evaluations of durability performance of FRP reinforcing bars for concrete structures." *Compo. Struct*., 78(1): 101-111.

Chin, J. W., Aouadi, K., Haight, M. R., Hughes, W. L. and Nguyen, T. 2001. "Effects of water saturated solution and simulated concrete pore solution on the properties of composite matrix resins used in civil engineering applications." *Polym. Compo*., 22(2): 282–297.

Chin, J. W., Nguyen, T. and Aouadi, K. 1997. "Effects of environmental exposure on fibre reinforced plastic-FRP- materials used in construction." *J. Compos. Technol. Res.*, 19(4): 205–213.

Chin, J. W., Nguyen, T. and Aouadi, K. 1999. "Sorption and diffusion of water, salt water, and concrete pore solution in composite matrices." *J. Appl. Polym. Sci.*, 71: 483–492.

Chong, K. P. 1998. "Durability of composite materials and structures." *Proc., 1st Int. Conf. Durability of Fiber Reinforced Polymer for Construction*, B. Benmokrane and H. Rahman, eds., Dept of Civil Engineering, Université De Sherbrooke, Quebec, 1–12.

Chu, W. and Karbhari, V. M. 2005. "Effect of water sorption on performance of pultruded e-glass/vinylester composites." *J. Mat. Civil Eng.*, 17(1): 63-71.

Crank, J. 1979. *Mathematics of Diffusion*. Clarendon Press: Oxford.

Davalos, J. F., Chen, Y. and Ray, I. 2008. "Effect of FRP bar degradation on interface bond with high strength concrete." *Cement Concrt. Comp.,* 30(8):722-730.

Debaiky A. S., Nkurunziza, G., Benmokrane, B. and Cousin P. 2006. "Residual tensile properties of GFRP reinforcing bars after loading in severe environments." *J. Comp. Constr*, 10(5): 370-380.

Dejke, V. and Tepfers R. 2001. "Durability and service life prediction of GFRP for concrete reinforcement." *Pro. 4th Int. Conf. Fibre-Reinforced Plastics for Reinforced Concrete Structures FRPRCS-5*, vol. 1, University of Cambridge, Cambridge. 515–520.

Devalapura, R. K., Greenwod, M. E., Gauchel, J. V. and Humphrey, H. 1998. "Evaluation of GFRP performance using accelerated test methods." *Proc., 1st Int. Conf. on Durability of Fiber Reinforced Polymer for Construction*, B. Benmokrane and H. Rahman, eds., Dept of Civil Engineering, Université De Sherbrooke, Quebec, 107– 116.

Dutta, P. K. 1988. "Structural fibre composite materials for cold regions." *J. Cold Reg. Eng.,* 2(3): 124–134.

Eagles, D. B., Blumentritt, B. F. and Copper, S. L. 1976. "Interfacial properties of Kevlar-49 fiber-reinforced thermoplastics" *J. App. Polym. Sci.*, 20: 435-448.

El-badry, M. M., Abdalla, H. and Ghali, A. 2000. "Effects of temperature on the behavior of fibre reinforced polymer reinforced concrete members: experimental studies." *Can. J. Civ. Eng*., 27: 993–1004.

European standard. 1996. "Determination of hygroscopic sorption curves", *ISO/DIS 1257*.

Flegler, S. L., Heckman Jr. J, W. and Klomparens, K. L. 1993. *Scanning and Transmission Electron Microscopy: An introduction*. Oxford University Press: Oxford, NY.

GangaRao, H. V. S. and Vijay, P. V. 1997. "Aging of structural composites under varying environmental conditions." *Proc., 3rd Int. Symp. on Non-Metallic (FRP) Reinforcement for Concrete Structures (FRPRCS-3)*, Japan Concrete Institute, Sapporo, 91–98.

Goldstein, J., Newbury, D., Joy, D., Lyman, C., Echlin, P., Lifshi, E. Sawyer, L. and Michael, J. 2003. *Scanning Electron Microscopy and X-ray Microanalysis*. 3rd ed. Kluwer Academic/Plenum Publishers: NY, Boston, Dordrecht, London, Moscow.

Gomez, J. and Casto, B.1996. “Freeze/thaw durability of composite materials.” *Proc., 1st Int. Conf. Compos.Infra.,* ICCI, Tuscon, Ariz., 947–955.

Goodman, S. H. 1998. *Handbook of Thermoset Plastics*. 2nd ed., Noyes Publication: New Jersey, USA.

Green, J. 2001. “Flame retardant and smoke suppressants.” In: *Polymer Modifiers and Additives*, J. T. Lutz, and R. F. Grossman, eds., Marcel Dekker Inc.: NY, USA

Greenwood, M. 2002. “Creep-rupture testing to predict long-term performance on durability of fiber reinforced polymer (FRP) composites for construction.” *Proc., 2nd Int. Conf. Durability of Fiber-Reinforced Polymer for Construction (CDCC’02)*, B. Benmokrane and E. El-Salakawy, eds., Montreal, Quebec, 203–212.

Grossman, R. F. 2001. “Coupling agents.” In: *Polymer Modifiers and Additives*, J. T. Lutz, and R. F. Grossman, eds., Marcel Dekker Inc.: NY, USA.

Herzog, B., Gardner, D. J., Lopez-Anido, R. and Goodell, B. 2005. “Glass-Transition temperature based on dynamic mechanical thermal analysis techniques as an Indicator of the adhesive performance of Vinyl Ester Resin”, *J. App. Poly. Sci.* 97: 2221–2229.

Hillel, D. 1982. “Water Hysteresis Prediction Model Based on Theory and Geometric Scaling.” In: Introduction to Soil Physics, Academic Press Inc.: San Diego, Calif.

Hsu, C. P. S. 2011. “Infrared Spectroscopy.” Separation Sciences Research and Product Development Mallinckrodt, Inc. Mallinckrodt Baker Division. Available in URL (www.prenhall.com/settle/chapters/ch15.pdf). (Oct. 25, 2011).

Hygrodynamics Inc. 1964. “Creating and Maintaining Humidities by Salt Solutions”, Hygrodynamics Inc., Technical Bulletin No. 5, Silver Springs, Maryland.

Iglesias, J. G., Gonz´alez-Benito. J., Aznar, A. J., Bravo, J. and Baselgal, J. 2002. “Effect of glass fibre surface treatments on mechanical strength of epoxy based composite materials. *J. Colloid and Interphase Sci.,*250: 251–260.

Illston, J. M. 1994. *Construction Materials: Their Nature and Behaviour*. E and FN Spon: London/Glasgow/New York/Tokyo/Melbourne/Madras.

Irfan, M. H. 1998. *Chemistry and Technology of Thermosetting Polymers in Construction Applications*. Springer: Verlag.

ISIS. 2003. "Educational Module 2: An introduction to FRP composites for construction." Intelligent Sensing for Innovative Structures (ISIS), Canada, A Canadian Network of Centres of Excellence.

Jang, B. Z. 1994. "Interfaces and interphases in composites." *Adv. Poly. Comp: Principle and Applications.* ASM International, Material Park: USA, 37-59.

Jones, F. R. 2003. "Glassfibres." In: *High Performance Fibre*. J. W. S. Hearle, ed., Woodhead Publishing Limited: Cambridge, England.

Jones, F. R. 1994. *Handbook of Polymer-Fibre Composites*, Longman Scientific & Technical: Burnt Mill, Harlow, Essex.

Jones, R. H. 2001. *Environmental Effects on Engineered Materials*, Marcel Dekker, Inc.: NY, USA.

Juska, T. D. and Puckett, P. M. 1997. "Matrix resin and fibre/matrix adhesion." In : *Composite Engineering Handbook*, P. K. Mallick, ed, Marcel Dekker, Inc.: NY, USA.

Kamal, A. S. M. and Boulfiza, M., 2011. "Durability of GFRP rebars in simulated concrete solutions under accelerated aging conditions." *J. Comp. Constr***.** (http://dx.doi.org/10.1061/(ASCE)CC.1943-5614.0000168).

Kamal, A. S. M., Boulfiza, M. and Panigrahi, S. 2010. "Effects of the interphase on the properties of Glass Fibre Reinforced Polymer (GFRP) composites." *Proc. ICCE-18th conf.*, Anchorage, Alaska, USA. July 4-10.

Kamal, A. S. M. and Boulfiza, M. 2008. "On the interactions of fibre reinforced polymer composites with highly alkaline concrete pore solutions." *Proc. Int. Symp. Theortcl. Chemstry., ISTC*, Algiers, 212-218.

Kamal A. S. M., Boulfiza, M., Tripathy, A. C. and Panigrahi, S. 2006. "The effects of synthetic-fibre and natural-fibre on the mechanical and physical properties of FRP rebars in concrete." *Conf. Proc. 1st Int. Struct. Specialty Conference, May 23-26, 2006, Calgary, Alberta, Canada.*

Karbhari, V. M. and Engineer, M. 1996. "Effect of environmental exposure on external strengthening of concrete with composites—Short term bond durability." *J. Reinf. Plast. Compos.*, 15: 1194–1216.

Karbhari, V. M. and Zhang, J. S. 2003. "E-glass/vinylester composites in aqueous environments. I: Experimental results." *Appl. Compos. Mater.*, 10(1): 19–48.

Karbhari, V. M., Chin, J. W., Hunston, J., Benmokrane, B., Juska, T., Morgan, R., Lesko, J. J., Sorathia, U. and Reynaud, D. 2003. "Durability gap analysis for fibre-reinforced polymer composites in civil infrastructure." *J. Comp. Const.*, 7(3): 238-247.

Katsuki, F. and Uomoto, T. 1995. "Prediction of deterioration of FRP rods due to alkali attack in nonmetallic (FRP) reinforcement for concrete structures." *Proc., 2nd Int. RILEM Symp. (FRPRCS-2)*, L. Taerwe, ed., RILEM, Bagneux, France, 82–89.

Kim, H. Y., Park, Y. H., You, Y. J. and Moon, C. K. 2009. "Short-term durability test for GFRP rods under various environmental conditions." *Comp. Sturct.*, 83(1): 37-47.

Kim. D. H. 1995. *Composite Structures for Civil and Architectural Engineering*. E & FN Spon.: London, Glasgow, Winheim, New York, Tokyo, Melbouren, Madras.

Kinloch, A. J. 1986. *Structural Adhesives: Developments in Resins and Primers*. Elsevier Applied Science Publishers Ltd.: London and NY.

Koch, G. H., Brongers, M. P. H., Thomson, N. G., Virmanio Y. P. and Payer J. H. 2005. "Cost of corrosion in the United States." *Handbook of Environmental Degradation of Materials*, M. Kutz, ed., William Andrew Publishing: Norwich, NY, USA.

Lee, H. and Nevile K. 1957. *Epoxy Resins-their Applications and Technology*. McGraw-Hill Book Company, Inc.: NY, Toronto, London.

Lee. S. M. 1992. Handbook of Composite Reinforcements. John Wiley and Sons Ltd.: NY.

Liao, K., Schultheisz, C. R. and Hunston, D. L. 1999. Effects of environmental aging on the properties of pultruded GFRP. *Composites: Part B*, 30: 485–49.

Lide, D. R. 2007. Handbook of Chemistry and Physics. 88th edition, CRC Press.

Lord, H. W. and Dutta, P. K. 1988. "On the design of polymeric composite structures for cold regions applications." *J. Reinf. Plast. Compos.*, 7: 435–458.

Mallick P. K. and Newman, S. 1990. *Composite Materials Technology, Process and Properties*. Oxford University Press: NY, USA.

Marchand, J., Bentz, D., Samson, E. and Maltais, Y. 2001. "Influence of calcium hydride dissolution on the transport properties of hydrated cement systems: calcium hydroxide in concrete." *Materials Science of Concrete. Special Volume, Proceedings*. American Ceramic Society. Workshop on the Role of Calcium Hydroxide in Concrete, November 1-3, 2000, Holmes Beach, Anna Maria Island, Florida, 113-129.

Marom, G. and Broutman, L. J. 1981. “Moisture penetration into composites under external stress.” *Polym. Compos.*, 2(3): 132–136.

Marsden, J. G. 1990. “Organofuctional silane coupling agents.” In: *Handbook of Adhesive*, I. Skeist, ed., 3rd ed., Van Nostrand Reinhold: NY.

Mason, K. F. 2006. “Sizing up fibre sizings.” Available in URL: <http://www.composites world.com/ct/issues/2006/April/1253>.

Massingill, J. L. Jr. and Bauer, R. S. 2000. “Epoxy resins.” In: *Applied Polymer Science 21st Century*, C. D. Craver and C. E. Jr. Carraher, eds., Elsevier: . 393-424.

Mathur, K. K. and Vanderheiden, D. B. 2001. “Fillers: Types, Properties and Performances.” In: *Polymer Modifiers and Additives*, ed., Lutz, J. T. and Grossman, R. F. Marcel Dekker, Inc.: NY, USA.

McBride, M. B. 1994. *Environmental Chemistry of Soils*. Oxford University Press: USA.

Miyano, Y., Nakada, M., Yonemori, T., Silzn, S. and Tsai, S. W. 1999. “Time and temperature dependence of static, creep, and fatigue behavior of FRP adhesive joints.” *Proc. 12th Int. Conf. on Composite Materials*, ICCM, Paris.

Mohd Ishak, Z. A. and Lim, N. C. 1994. Effect of Moisture absorption on the tensile properties of short glass fibre reinforced ply (Butylene Terphthalate), *Poly Eng. Sci*, 34(22): 1645-1655.

Mufti, A. A., Onofrei, M., Benmokrane, B., Banthia, N., Boulfiza, M., Newhook, J., P., Bakht, B., Tadros, G. S. and Brett, P. 2007. “Field study of glass-fibre-reinforced polymer durability in concrete.” *Can. J. Civil Eng.,* 34: 355-366.

Mufti, A., Onofrei, M., Benmokrane, B., Banthia, N., Boulfiza., M., Newhook, J., Baidar, B., Tadros, G. and Brett, P. 2005. "Report on the studies GFRP durability in concrete from field bridge demonstration projects." *Proc. 3rd Int. Conf. on Comp. Constr. (CCC-2005)*, Lyon, Vol. 2, 889-895.

Mukherjee, A. and Arwikar, S. I. 2005. “Performance of glass fibre-reinforced polymer reinforcing bars in tropical environments - Part II: Microstructural tests. ” *ACI Struct. J.*, 102(6): 816-822.

Murphy, J. 1998. *The Reinforced Plastics Handbook*. 2nd edition, Elsevier Advanced Technology.

Murphy, K., Zhang, S. and Karbhari, V. M. 1999. "Effect of concrete based alkaline solutions on short term response of composites." *Proc. 44th Int. Society for the Advancement of Material and Process Engineering (SAMPE) Symposium and Exhibition*, L. J. Cohen, J. L. Bauer, and W. E. Davis, eds., Long Beach, Calif., 2222–2230.

Netcomposites. 2011. "Wet/Hand lay-up process." Available in URL: <http://www.netcomposites.com/education.asp?sequence=56>, (July 15, 2011).

Nagae, N. and Otsuka, Y. 1996. "Effect of sizing agent on corrosion of glass fibre reinforced plastics (GFRP) in water." *J. Mats. Sci. Letters*, 15(83): 83-85.

Nkurunziza, G., Debaiky, A., Cousin, P. and Benmokrane, B. 2005. "Durability of GFRP bars: A critical review of the literature." *Prog. Struct. Engng Mater,* 7: 194–209.

NRC-CNRC. 2008. "Fire resistance of FRP strengthened concrete columns." The Institute for Research in Construction, NRCC 51253, pp2. Available in URL: < http://www.nrc-cnrc.gc.ca/obj/irc/doc/pubs/nrcc51253/nrcc51253.pdf >.

NRC-CNRC. 2010. "Fire Performance of Fibre-Reinforced Polymer Systems Used for the Repair of Concrete Buildings." The Institute for Research in Construction, Construction Technology Update, 74, pp6. Available in URL: < http://www.nrc-cnrc.gc.ca/eng/ibp/irc/ctus/ctus-n74.html >.

Oguocha, I. 2007. Lecture notes on ME 843: Material Characterization, Dept of Mechanical Engineering, University of Saskatchewan.

Onofrei, M. 2005. "Durability of GFRP reinforced concrete from filed demonstration structures, Final report." *ISIS Canada Research Networks*, University of Canada. pp. 195.

Petrie, E. M. 2007. *Handbook of Adhesives and Sealants*. McGral-Hill handbooks: Toronto.

Piggott, M. R., Chua, P. S. and Andison, D. 1985. "The interface between glass and carbon fibers and thermo setting polymers." *Polym Comp.*, 6(4): 242-248.

Plueddemann, E. P. 1991. *Silane Coupling Agents*. 2nd Edition, Plenum Press: NY and London.

Porter, M. L. and Barnes, B. A. 1998. "Accelerated aging degradation of glass fibre composites." *Proc. 2nd Int. Conf. Compo. Infras.* , ICCI, Tuscon, Ariz., Vol., 2, 446–459.

Porter, M. L., Mehus, J., Young, K. A., O'Neil, E. F. and Barnes, B. A. 1997. "Aging for fiber reinforcement in concrete." *Proc., 3rd Int. Symp. on Non-Metallic (FRP) Reinforcement for Concrete Structures (FRPRCS-3)*, Japan Concrete Institute, Sapporo, Vol. 2, 59–66.

Pritchard, G. 1999. *Reinforced Plastics Durability*. Woodhead: Cambridge, U. K.

Pritchard, G. and Speake, S. D. 1987. “The use of water absorption kinetic data to predict laminate property changes.” *Compo.*, 18(3): 227–232.

Rabek, J. F. 1980. “The experimental methods in Polymer chemistry – Physical principles and applications.” John Wiley & Sons Ltd.:

Ray, B. C. 2000. “Temperature effect during humid ageing on interfaces of glass and carbon fibres reinforced epoxy composites.” *J. Colloid & Interface Sci.*, 298: 111-117.

Reardon, E. J. 1992. “Problems and approaches to the prediction of the chemical composition in cement/water systems.” *Waste Management*, 12: 221-239.

Rebenfeld, L. 2000. “Fibres.” *Applied Polymer Science 21st Century*, C. D. Craver and C. E. Jr. Carraher, eds., Elsevier: . 393-424.

Robert, M, Cousin, P. and Benmokrane, B. 2009. “Durability of GFRP reinforcing bars embedded in moist concrete.” *J. Comp. Const.*, 13(2), 66-73.

Schutte, C. L. 1994. “Environmental durability of glass-fibre composites.” *Mater. Sci. Eng., R.*, 13(7), 265–322.

Searle, N. D. 2003. “Environmental effects on polymeric materials.” In: *Plastics and the Environment*, L. A. Anthony, ed., Willey-interscience: USA.

Sen, R., Mullins, G. and Salem, T. 2002. “Durability of E-glass/vinylester reinforcement in alkaline solution.” *ACI Struct. J.*, 99(3): 369–375.

Seymour R. B. 1987. *Polymers for engineering applications*. ASM International: USA.

Shen, C. H. and Springer, G. S. 1976. “Moisture absorption and desorption in composite materials.” *J. Compos. Mat.,* 10(2): 2-16.

Soles, C. L. and Yee, F. 2000. “A discussion of the molecular mechanism of moisture transport in epoxy resins.” *J. Poly. Sci.*, 38: 792-802.

Soles, C. L., Chang, F. T., Bolan, B. A., Hristov, H. A., Gidley, D. W. and Yee, A. F. 2000. “Contributions of the nanovoid structure to the moisture absorption properties of epoxy resins.” *J. Poly. Sci.: Part B:Poly. Phy.*, 36(17): 3035-3048.

Sonawala, S. P. and Spontak, R. J. 1996. “Degradation kinetics of glass-reinforced polymers in chemical environments 1: Aqueous solutions.” *J. Mater. Sci.*, 31: 4745–4756.

SM. 2011. Special Metals, Available in URL: http://www.specialmetals.com/documents/Incoloy%20alloy%20825.pdf> (Aug 26, 2011).

Springer, G. S. 1988. *Environmental Effects on Composite Materials.* Vol. 3, Tecnomic Publishing Co. Inc.: Lancaster, Basel, USA.

Strong, A. B. 2008. "Sizings and coupling agents – the magic of composite performance." Available in URL: < http://www.et.byu.edu/groups/strong/pages/ articles/articles/sizings.pdf > (Jan 12, 2008).

Swain, R. E., Reifsnider, K. L., Jayaraman, K. and El-Zein, M. 1990. "Interface/interphase concepts in composite material systems." *J. Thermoplastic Comp. Mats.*, 3: 13-23.

Swit, G. 2000. "Durability of stressed E-glass fibre in alkaline medium." *Recent Developments in Durability Analysis of Composite Systems*, Reifsneider and Verchery (eds) Cardon, Fukuda, Balkema, Rotterdam, 473–476.

Tannous, F. E. and Saadatmanesh, H. 1999. "Durability of AR glass fibre reinforced plastic bars." *J. Comp. Constr.*, 3(1): 13-19.

Tanoglu, S. Z. M., Mcknight, S. M., Palmese, G. R. and Gillespie, J. W. J. 2001. "Investigation of properties of fibre/matrix interphase formed due to the glass fibre sizings." *J. Ma.t Sci.,* 36: 3041-3053.

Thomason, J. L. 1995. "The interface region in glass fibre-reinforced epoxy resin composites: 3. Characterization of fibre surface coatings and the interphase." *Composites*, 26(7): 487–498.

Thomason, J. L. and Dwight, D. W. 2000. "XPS analysis of the coverage and composition of coatings on glass fibres." *J. Adhe. Sci. Tech*., 14(5): 745-764.

Tillco. 2006. "Fibre glass reinforced plastic rebars." TILLCO. Available in URL : < http://tillco.com/> (Jan. 12, 2008).

Timoshenko, S. P. and Woinowsky-Krieger S. 1959. *Theory of Plates and Shells*. McGraw-Hill: New York.

Topp, P. G. and Devis, J. L. 1982. "Detecting infiltration of water through soil cracks by time domain reflectometry." *Geoderma*, 26: 13-23.

Tosun, I. 2007. *Modeling in Transport Phenomena: A Conceptual Approach*. 2nd edition. Elsevier.

Uematsu, Y., Kitamura, T. and Ohtani, R. 1995. "Delamination of a carbon-fiber reinforced thermoplastic polymer at high temperatures." *Composites Science and Technology 53*, Elsevier Science Limited, Northern Ireland, pp. 333-341.

Valter, T. and Ralejs, T. 2001. "Durability and service life prediction of GFRP for concrete reinforcement." *Proc. 5th Int. Conf. on Fibre-Reinforced Plastics for Reinforced Concrete Structures,* FRPRCS-5, Univ. of Cambridge, Vol. 1, 505–514.

van der Wal, J. S. 2006. "Water resistance of glass and carbon fibre epoxy composites." Presentation for ESAT.

van der Wal, J. S. and Boulfiza, M. 2007. "A step forward in characterizing the performance of GFRP rods in concrete." *Proc. 3rd Int. Conf. on Durability and field applications of fibre reinforced polymer (FRP) composites for construction*, Quibec City, 22-24 May, B. Banmokrane and E. El-Salakawy, eds., University of Sherbrooke, Sherbrooke, Que. 75-82.

WCAS. 2008. "Fourier Transform Infrared Spectroscopy." *Waste coast analytical services*. Available in URL> < http://www.wcaslab.com/tech/tbftir.htm>, (Jan. 12, 2008).

Wade, L. G. Jr. 2003. "Organic chemistry." 5th edition. Pearson Education Inc.: Prentice Hall,

Wallenberger, F. T., Watson, J. C. and Li, H. 2001. "Glass Fibres." In: *ASM Handbook Volume 21: Composites*. ASM International: Materials Park, Ohio, USA.

Walter, E. and Ashbee K. H. G. 1982. "Osmosis in composite materials." *Composites*, Sep, 365-368.

Wang, P. 2005. "Effect of moisture, temperature, and alkaline on durability of E-glass/vinyl Ester reinforcing bars." *Ph. D. Thesis*, Univ. of Sherbrooke, Sherbrooke, Quebec, Canada.

Watt, I. M. 1997. *The Principles and Practice of Electron Microscopy*. 2nd ed., Cambridge University Press:UK

Williams, B., Kodur, V. K. R., Green, M. F. and Bisby, L. 2008. "Fire Endurance of Fibre-Reinforced Polymer Strengthened Concrete T-Beams." *ACI Struc. J.*, 105(1): 60-67.

Williams, M. L. 1969. "The continuum interpretation for fracture and adhesion." *J. Appl. Poly. Sic.*, 13: 29-40.

Yeol Kim, H., Park, Y. H., You, Y. J. and Moon, C. K. 2007. "Short-term durability test for GFRP rods under various environmental conditions." *Compo. Struct.*, 83: 37–47.

Yilmaz, V. T. and Glasser, F. P. 1991. "Reaction of alkali-resistant glass fibres with cement. Part I: Review, assessment, and microscopy." *Glass Tech.*, 32(3): 91–98.

Zaidi, A., Masmoudi, R. 2008. "Thermal Effect on Fiber Reinforced Polymer Reinforced Concrete Slabs." *Can. J. Civil Eng.,* 35(3): 312-320.

Zaske, C. O. and Goodman, S. H. 1998. "Unsaturated polyester and vinylester resins." In: *Handbook of Thermoset Plastics*. 2nd ed., S. H. Goodman, ed., Noyes Publication: New Jersey, USA.

Zhang, S. and Karbhari, V. M. 1999. "Effects of alkaline environments on the durability of E-glass fibre composites for use in civil infrastructure." *Proc. 14th Technical Conf. of the American Society of Composites*, Technomic Publishing Corp.: Lancaster, Pa., 12–20.

Zheng, Q. and Morgan, R. J. 1993. "Synergistic thermal moisture damage mechanisms of epoxies and their carbon fibre composites." *J. Comp. Mat*., 27(15): 1465–1478.

APPENDIX A: RAW DATA

Table A.1. Instantaneous mass (W_i) of GFRP custom plane sheet specimens immersed at different temperatures.

W_b	Days	Instantaneous mass (g)of GFRP sheets immersed in water at **4 °C**					
		Sized specimens			**De-sized** specimens		
		S1	S2	S3	S1	S2	S3
W_i	0	3.1254	3.2268	3.3156	3.4325	3.5996	3.5542
	1	3.1289	3.2308	3.3200	3.4374	3.6042	3.5585
	2	3.1300	3.2324	3.3220	3.4406	3.6071	3.5611
	3	3.1310	3.2339	3.3239	3.4426	3.6088	3.5625
	4	3.1316	3.2350	3.3254	3.4441	3.6100	3.5634
	5	3.1324	3.2363	3.3271	3.4462	3.6118	3.5649
	7	3.1331	3.2375	3.3287	3.4475	3.6128	3.5656
	8	3.1338	3.2387	3.3303	3.4486	3.6136	3.5661
	10	3.1342	3.2396	3.3316	3.4500	3.6147	3.5669
	11	3.1345	3.2404	3.3328	3.4519	3.6163	3.5682
	14	3.1349	3.2413	3.3341	3.4531	3.6172	3.5688
	15	3.1348	3.2417	3.3349	3.4538	3.6176	3.5689
	17	3.1355	3.2429	3.3365	3.4548	3.6183	3.5693
	18	3.1357	3.2436	3.3376	3.4557	3.6189	3.5696
	21	3.1363	3.2447	3.3391	3.4577	3.6206	3.5710
	23	3.1367	3.2456	3.3404	3.4587	3.6213	3.5714
	28	3.1373	3.2467	3.3419	3.4605	3.6228	3.5726
	35	3.1376	3.2475	3.3431	3.4609	3.6229	3.5724
	39	3.1379	3.2483	3.3443	3.4617	3.6234	3.5726
	43	3.1378	3.2487	3.3446	3.4622	3.6236	3.5725
	50	3.1381	3.2495	3.3447	3.4628	3.6239	3.5725
	57	3.1385	3.2499	3.3448	3.4636	3.6244	3.5727
	64	3.1386	3.2503	3.3449	3.4639	3.6244	3.5729
	71	3.1390	3.2503	3.3450	3.4644	3.6246	3.5731
	78	3.1392	3.2504	3.3451	3.4644	3.6249	3.5731
	93	3.1392	3.2504	3.3451	3.4644	3.6253	3.5731
	108	3.1392	3.2504	3.3451	3.4644	3.6255	3.5731
	123	3.1392	3.2504	3.3451	3.4644	3.6255	3.5731

S: Sample

Table A.1. Instantaneous mass (W_i) of GFRP custom plane sheet specimens immersed at different temperatures (cont'd).

	Days	Instantaneous mass (g) of GFRP **sized** specimens immersed in water at **23 °C**				
		S1	S2	S3	S4	S5
W_b	0	3.5871	3.6641	3.9770	3.1750	3.7164
	1	3.5986	3.6763	3.9912	3.1849	3.7305
	2	3.6023	3.6799	3.9955	3.1879	3.7342
	3	3.6056	3.6831	3.9977	3.1907	3.7374
	4	3.6082	3.6850	3.9996	3.1934	3.7383
	5	3.6124	3.6897	4.0056	3.1962	3.7414
	7	3.6135	3.6909	4.0060	3.1972	3.7427
	8	3.6141	3.6912	4.0071	3.1978	3.7436
W_i	10	3.6148	3.6923	4.0078	3.1982	3.7439
	11	3.6144	3.6923	4.0086	3.1985	3.7446
	14	3.6158	3.6927	4.0089	3.1996	3.7452
	15	3.6157	3.6931	4.0091	3.1997	3.7454
	17	3.6158	3.6935	4.0097	3.1997	3.7455
	18	3.6157	3.6939	4.0100	3.1990	3.7458
	21	3.6160	3.6944	4.0104	3.1998	3.7460
	23	3.6162	3.6947	4.0106	3.2000	3.7462
	28	3.6165	3.6949	4.0108	3.2001	3.7465
	35	3.6168	3.6950	4.0109	3.2002	3.7468
	39	3.6168	3.6950	4.0110	3.2002	3.7469

S: Sample

Table A.1. Instantaneous mass (W_i) of GFRP custom plane sheet specimens immersed at different temperatures (cont'd).

	Days	Instantaneous mass (g) of GFRP **de-sized** specimens immersed in water at **23 °C**					
		S1	S2	S3	S4	S5	S6
W_b	0	3.5027	3.8180	3.8754	4.2167	3.8260	3.9160
W_i	1	3.5192	3.8375	3.8923	4.2340	3.8431	3.9347
	2	3.5221	3.8394	3.8961	4.2397	3.8487	3.9377
	3	3.5246	3.8417	3.8996	4.2427	3.8500	3.9407
	4	3.5260	3.8432	3.9010	4.2443	3.8517	3.9421
	5	3.5272	3.8449	3.9026	4.2461	3.8531	3.9431
	7	3.5281	3.8462	3.9040	4.2472	3.8540	3.9445
	8	3.5293	3.8470	3.9046	4.2478	3.8551	3.9455
	10	3.5296	3.8473	3.9054	4.2482	3.8554	3.9457
	11	3.5297	3.8482	3.9064	4.2495	3.8555	3.9466
	14	3.5308	3.8489	3.9065	4.2497	3.8565	3.9471
	15	3.5313	3.8495	3.9068	4.2501	3.8568	3.9472
	17	3.5311	3.8499	3.9071	4.2504	3.8573	3.9476
	18	3.5314	3.8500	3.9072	4.2507	3.8574	3.9478
	21	3.5314	3.8501	3.9073	4.2513	3.8579	3.9482
	23	3.5315	3.8508	3.9075	4.2515	3.8580	3.9485
	28	3.5318	3.8509	3.9077	4.2517	3.8578	3.9489
	35	3.5318	3.8510	3.9077	4.2517	3.8578	3.9489
	39	3.5318	3.8510	3.9077	4.2517	3.8578	3.9489

S: Sample

Table A.1. Instantaneous mass (W_i) of GFRP custom plane sheet specimens immersed at different temperatures (cont'd).

		Instantaneous mass (g) of GFRP **sized** specimens immersed in water at **50 °C**					
	Days	S1	S2	S3	S4	S5	S6
W_b	0	3.7861	3.1803	3.8171	3.2391	3.6584	3.3166
W_i	1	3.8124	3.2038	3.8430	3.2605	3.6843	3.3407
	2	3.8201	3.2103	3.8508	3.2671	3.6918	3.3475
	3	3.8284	3.2166	3.8579	3.2740	3.6995	3.3541
	4	3.8321	3.2196	3.8630	3.2763	3.7037	3.3579
	5	3.8347	3.2211	3.8652	3.2781	3.7062	3.3591
	7	3.8349	3.2212	3.8666	3.2803	3.7057	3.3597
	8	3.8368	3.2215	3.8664	3.2802	3.7058	3.3603
	10	3.8363	3.2214	3.8672	3.2811	3.7059	3.3598
	11	3.8363	3.2214	3.8669	3.2804	3.7068	3.3605
	14	3.8365	3.2213	3.8664	3.2808	3.7066	3.3608
	15	3.8365	3.2214	3.8663	3.2806	3.7063	3.3609
	17	3.8366	3.2219	3.8670	3.2805	3.7065	3.3608
	18	3.8365	3.2222	3.8671	3.2816	3.7065	3.3607
	21	3.8366	3.2222	3.8673	3.2817	3.7065	3.3613
	23	3.8368	3.2222	3.8673	3.2817	3.7066	3.3615
	28	3.8368	3.2219	3.8669	3.2814	3.7066	3.3619
	35	3.8368	3.2220	3.8671	3.2816	3.7071	3.3625
	39	3.8368	3.2222	3.8672	3.2820	3.7075	3.3630

S: Sample

Table A.1. Instantaneous mass (W_i) of GFRP custom plane sheet specimens immersed at different temperatures (cont'd).

	Days	Instantaneous mass (g) of GFRP **de-sized** specimens immersed in water at **50 °C**				
		S1	S2	S3	S4	S5
W_b	0	3.8955	3.3595	3.9955	3.5283	4.0752
W_i	0.5	3.9176	3.3784	4.0183	3.5484	4.0979
	1	3.9293	3.3885	4.0302	3.5589	4.1101
	1.5	3.9342	3.3927	4.0353	3.5634	4.1153
	2	3.9385	3.3964	4.0396	3.5672	4.1197
	3	3.9422	3.3996	4.0435	3.5706	4.1236
	4	3.9446	3.4017	4.0459	3.5728	4.1261
	5	3.9455	3.4024	4.0469	3.5736	4.1270
	7	3.9456	3.4025	4.0469	3.5737	4.1271
	8	3.9458	3.4027	4.0472	3.5739	4.1274
	10	3.9460	3.4029	4.0474	3.5741	4.1276
	11	3.9461	3.4030	4.0475	3.5742	4.1277
	14	3.9461	3.4030	4.0475	3.5742	4.1277
	15	3.9461	3.4030	4.0475	3.5742	4.1277
	17	3.9461	3.4030	4.0475	3.5742	4.1277
	18	3.9463	3.4031	4.0476	3.5743	4.1279
	21	3.9470	3.4038	4.0484	3.5750	4.1287
	23	3.9473	3.4040	4.0487	3.5752	4.1289
	28	3.9473	3.4040	4.0487	3.5753	4.1289
	35	3.9473	3.4040	4.0487	3.5753	4.1289
	39	3.9473	3.4040	4.0487	3.5753	4.1290

S: Sample

Table A.2. Instantaneous mass (W_i) of saturated GFRP rebars while drying at different RH.

W_b	Days	Instantaneous mass (g) of GFRP rebars exposed in different RH								
		PH 8			PH 22			PH 3		
		S1	S2	S3	S1	S2	S3	S1	S2	S3
W_i	0	1.94	2.181	1.844	1.919	2.054	1.88	1.912	2.037	1.859
	1	1.938	2.179	1.842	1.917	2.052	1.878	1.91	2.035	1.857
	3	1.937	2.178	1.841	1.915	2.05	1.876	1.907	2.032	1.854
	6	1.935	2.176	1.839	1.914	2.049	1.875	1.906	2.031	1.853
	10	1.934	2.175	1.838	1.913	2.048	1.874	1.905	2.03	1.852
	14	1.934	2.175	1.838	1.913	2.048	1.874	1.905	2.03	1.852
	20	1.934	2.175	1.838	1.913	2.048	1.874	1.905	2.03	1.852
	25	1.934	2.175	1.838	1.913	2.048	1.874	1.905	2.03	1.852

W_b	Days	Instantaneous mass (g) of GFRP rebars exposed in different RH								
		PH 43			PH 53			PH 75		
		S1	S2	S3	S1	S2	S3	S1	S2	S3
W_i	0	1.922	1.836	1.987	2.115	2.238	1.931	2.01	2.059	1.775
	1	1.897	1.811	1.962	2.091	2.214	1.906	1.988	2.037	1.753
	3	1.888	1.802	1.953	2.083	2.206	1.897	1.986	2.035	1.751
	6	1.888	1.802	1.953	2.081	2.204	1.897	1.985	2.034	1.75
	10	1.888	1.802	1.953	2.08	2.203	1.897	1.985	2.034	1.75
	14	1.884	1.798	1.949	2.078	2.201	1.893	1.984	2.033	1.749
	20	1.883	1.797	1.948	2.078	2.201	1.892	1.984	2.033	1.749
	25	1.883	1.797	1.948	2.078	2.201	1.892	1.984	2.033	1.749
	30	1.883	1.797	1.948	2.078	2.201	1.892	1.984	2.033	1.749
	36	1.883	1.797	1.948	2.078	2.201	1.892	1.984	2.033	1.749

W_b	Days	Instantaneous mass (g) of GFRP rebars exposed in different RH					
		PH 84			PH 94		
		S1	S2	S3	S1	S2	S3
W_i	0	1.962	2.031	1.9431	2.039	1.991	2.075
	1	1.941	2.01	1.9221	2.019	1.971	2.055
	3	1.939	2.008	1.9201	2.017	1.969	2.053
	6	1.938	2.007	1.9191	2.015	1.967	2.051
	10	1.938	2.007	1.9191	2.015	1.967	2.051
	14	1.938	2.007	1.9191	2.015	1.967	2.051
	20	1.938	2.007	1.9191	2.015	1.967	2.051
	25	1.938	2.007	1.9191	2.015	1.967	2.051
	30	1.938	2.007	1.9191	2.015	1.967	2.051
	36	1.938	2.007	1.9191	2.015	1.967	2.051

S: Sample

Table A.3. Instantaneous mass (W_i)of oven dried GFRP rebars while wetting at different RH.

		GFRP rebars exposed in different RH								
		PH 8			PH 22			PH 33		
	Days	S1	S2	S3	S1	S2	S3	S1	S2	S3
W_b	0	17.5893	17.2960	16.9470	16.9077	17.6486	17.5573	17.4082	16.7256	17.5116
	1	17.5893	17.2960	16.9470	16.909	17.6499	17.5584	17.41	16.7272	17.5133
	2	17.5894	17.2960	16.9470	16.9094	17.6502	17.5588	17.4108	16.728	17.5141
	3	17.5895	17.2960	16.9470	16.9097	17.6502	17.5592	17.4112	16.7288	17.5144
	4	17.5893	17.2961	16.9470	16.9104	17.6508	17.5597	17.4116	16.7284	17.5148
	5	17.5893	17.2960	16.9470	16.9104	17.6517	17.5598	17.4117	16.7286	17.5149
	6	17.5894	17.2960	16.9470	16.9108	17.6517	17.5601	17.4122	16.729	17.5154
	7	17.5893	17.2960	16.9470	16.9109	17.6516	17.56	17.4124	16.7291	17.5156
	8	17.5893	17.2962	16.9470	16.911	17.6516	17.56	17.4124	16.7291	17.5156
	9	17.5893	17.2960	16.9470	16.9115	17.6517	17.5603	17.4127	16.7294	17.5158
	10	17.5893	17.2960	16.9470	16.9115	17.6517	17.5605	17.4131	16.7295	17.5161
	11	17.5893	17.2960	16.9472	16.9122	17.652	17.5605	17.413	16.7298	17.5166
	12	17.5893	17.2960	16.9470	16.913	17.6523	17.561	17.4136	16.73	17.5166
	13	17.5893	17.2960	16.9470	16.9135	17.6532	17.5609	17.4136	16.7301	17.5167
	14	17.5893	17.2963	16.9470	16.9138	17.653	17.5613	17.4138	16.7299	17.5172
	16	17.5893	17.2960	16.9470	16.913	17.6531	17.5613	17.4139	16.7303	17.5173
	18	17.5893	17.2960	16.9470	16.9129	17.6534	17.5614	17.4141	16.7301	17.5173
	19	17.5893	17.2960	16.9470	16.913	17.6535	17.5613	17.4141	16.7304	17.5174
	20	17.5894	17.2960	16.9470	16.9134	17.6542	17.5614	17.4139	16.7304	17.5175
	21	17.5893	17.2960	16.9470	16.9136	17.6538	17.5617	17.4137	16.7304	17.518
	23	17.5893	17.2960	16.9471	16.9117	17.6542	17.5597	17.4149	16.7308	17.5168
	26	17.5893	17.2960	16.9470	16.9124	17.6528	17.5607	17.4135	16.7296	17.5169
	29	17.5893	17.2960	16.9470	16.9126	17.654	17.5608	17.4137	16.7297	17.5172
	32	17.5893	17.2960	16.9470	16.9126	17.6542	17.561	17.4137	16.7298	17.5173
W_i	35	17.5892	17.2961	16.9472	16.9133	17.6541	17.5614	17.4139	16.7298	17.5175
	38	17.5893	17.2960	16.9470	16.9133	17.6541	17.5614	17.4144	16.7302	17.5179
	42	17.5893	17.2960	16.9470	16.9132	17.6546	17.5615	17.4147	16.7303	17.518
	46	17.5893	17.2960	16.9470	16.9134	17.6548	17.5614	17.415	16.7305	17.5182
	49	17.5893	17.2960	16.9470	16.9131	17.6551	17.5616	17.4147	16.7304	17.518
	53	17.5893	17.2960	16.9472	16.9136	17.6551	17.5614	17.4151	16.7307	17.5185
	56	17.5893	17.2960	16.9470	16.9138	17.6553	17.5615	17.4148	16.7306	17.5184
	58	17.5893	17.2960	16.9470	16.9139	17.6554	17.5615	17.4151	16.7306	17.5185
	62	17.5893	17.2961	16.9470	16.9141	17.6557	17.5615	17.4154	16.7308	17.5188
	67	17.5893	17.2960	16.9470	16.9145	17.6559	17.5618	17.4155	16.7308	17.5187
	74	17.5893	17.2960	16.9470	16.9152	17.6562	17.5623	17.4159	16.7312	17.5193
	81	17.5896	17.2960	16.9470	16.9152	17.656	17.5623	17.416	16.7314	17.5194
	85	17.5893	17.2960	16.9470	16.9147	17.656	17.5629	17.4158	16.7312	17.5192
	90	17.5893	17.2960	16.9470	16.9152	17.656	17.5627	17.4161	16.7315	17.5195
	101	17.5893	17.2960	16.9471	16.9154	17.6562	17.5626	17.4163	16.7314	17.5196
	113	17.5893	17.2960	16.9470	16.9157	17.6569	17.563	17.4163	16.7316	17.52
	121	17.5893	17.2962	16.9470	16.9149	17.6564	17.5626	17.4162	16.7315	17.52
	128	17.5894	17.2960	16.9470	16.9151	17.6565	17.5624	17.4162	16.7315	17.519
	135	17.5893	17.2960	16.9470	16.9153	17.6574	17.5628	17.4162	16.7312	17.5198
	185	17.5893	17.2960	16.9471	16.9159	17.658	17.5632	17.4171	16.7325	17.5208
	269	17.5894	17.2960	16.9470	16.9165	17.6588	17.5647	17.4186	16.7338	17.5221
	412	17.5894	17.2960	16.9470	16.917	17.6593	17.5652	17.4192	16.7346	17.523
	517	17.5893	17.2960	16.9470	16.9172	17.6595	17.5654	17.4194	16.7349	17.523
	672	17.5893	17.2960	16.9470	16.9172	17.6595	17.5654	17.4194	16.7349	17.523

S: Sample

Table A.3. Instantaneous mass (W_i) of oven dried GFRP rebars while wetting at different RH (Cont'd).

		GFRP rebars exposed in different RH								
		PH 43			PH 53			PH 75		
	Days	S1	S2	S3	S1	S2	S3	S1	S2	S3
W_b	0	17.1724	17.7113	17.4627	16.8324	17.4542	16.849	17.4243	17.0183	17.4513
W_i	1	17.1903	17.7294	17.48025	16.8531	17.4747	16.8725	17.4594	17.0531	17.484
	2	17.1903	17.7294	17.48025	16.8531	17.4747	16.8725	17.4594	17.0531	17.484
	3	17.1901	17.7293	17.48018	16.8529	17.4744	16.8725	17.4583	17.0519	17.4873
	4	17.1894	17.7294	17.4795	16.8519	17.4734	16.8716	17.4578	17.0514	17.4855
	5	17.1886	17.7286	17.4781	16.8501	17.4717	16.8702	17.4557	17.0494	17.4832
	6	17.1869	17.7269	17.4769	16.8485	17.4702	16.8689	17.4538	17.0476	17.4812
	7	17.187	17.727	17.4772	16.8481	17.4701	16.869	17.4541	17.0473	17.4811
	8	17.1869	17.7269	17.477	16.8487	17.4702	16.8691	17.4537	17.0474	17.4811
	9	17.187	17.7256	17.477	16.8486	17.4703	16.8691	17.4534	17.0474	17.4812
	10	17.1867	17.7253	17.4754	16.8483	17.47	16.8688	17.4528	17.0468	17.4816
	11	17.1858	17.7248	17.476	16.8473	17.4695	16.868	17.4519	17.0458	17.4798
	12	17.186	17.7245	17.476	16.8475	17.4693	16.868	17.4513	17.0453	17.4793
	13	17.186	17.7244	17.4759	16.8473	17.4694	16.8679	17.4513	17.0451	17.4793
	14	17.1859	17.7242	17.4743	16.8474	17.4691	16.8673	17.451	17.0448	17.479
	16	17.1852	17.7236	17.4752	16.8466	17.4684	16.8672	17.45	17.044	17.4777
	18	17.185	17.7236	17.4746	16.8465	17.4682	16.8669	17.4496	17.0437	17.4774
	19	17.1846	17.7229	17.4747	16.8459	17.4678	16.8664	17.4491	17.0429	17.477
	20	17.1846	17.723	17.4747	16.8458	17.4676	16.8664	17.4487	17.0428	17.4766
	21	17.1847	17.723	17.4745	16.8456	17.4675	16.8661	17.4487	17.0424	17.4762
	23	17.1845	17.7229	17.4744	16.8453	17.4672	16.866	17.448	17.0422	17.4758
	26	17.1839	17.7226	17.4741	16.8452	17.4671	16.8658	17.4482	17.0423	17.4756
	29	17.1838	17.723	17.4737	16.8448	17.4667	16.8656	17.4469	17.041	17.4749
	32	17.1836	17.722	17.4736	16.8445	17.4664	16.8654	17.4464	17.0402	17.4743
	35	17.183	17.7214	17.4737	16.8436	17.4657	16.8646	17.4464	17.0402	17.4743
	38	17.1827	17.7217	17.4731	16.8435	17.4657	16.8641	17.4455	17.0396	17.473
	42	17.1823	17.7211	17.4731	16.8429	17.465	16.8636	17.4453	17.038	17.4727
	46	17.1817	17.7209	17.4722	16.8428	17.4647	16.8632	17.4441	17.0376	17.4718
	49	17.1832	17.7217	17.4734	16.8435	17.4658	16.8639	17.4434	17.0381	17.4712
	53	17.1825	17.7211	17.4727	16.8431	17.4652	16.8633	17.4443	17.0377	17.472
	56	17.1822	17.721	17.4722	16.8424	17.465	16.8631	17.4435	17.0369	17.4711
	58	17.1823	17.7209	17.4724	16.8426	17.4646	16.8628	17.4425	17.0366	17.4703
	62	17.1822	17.721	17.4724	16.8425	17.4646	16.863	17.4422	17.0364	17.4703
	67	17.1816	17.7208	17.4721	16.8418	17.4642	16.8623	17.4415	17.0356	17.4701
	74	17.1813	17.72	17.4718	16.8419	17.464	16.862	17.4411	17.035	17.4692
	81	17.181	17.7197	17.4715	16.8417	17.4635	16.8615	17.4407	17.0346	17.4687
	85	17.1807	17.7193	17.4713	16.8418	17.4638	16.8615	17.44	17.034	17.4683
	90	17.1806	17.7189	17.4708	16.8408	17.4629	16.8607	17.4393	17.0333	17.4683
	101	17.1797	17.7185	17.4703	16.8405	17.4619	16.8598	17.4385	17.0325	17.4674
	113	17.1798	17.7181	17.4702	16.84	17.4622	16.8596	17.4379	17.032	17.4656
	121	17.1792	17.7178	17.4697	16.8396	17.4617	16.859	17.4375	17.0316	17.4653
	128	17.179	17.7177	17.4696	16.8393	17.4617	16.8587	17.4367	17.0308	17.4647
	135	17.1785	17.7172	17.469	16.839	17.4612	16.8582	17.4361	17.0302	17.464
	185	17.1781	17.7169	17.4687	16.8391	17.4613	16.8578	17.4353	17.0295	17.4632
	269	17.1775	17.7163	17.4683	16.8384	17.4604	16.8574	17.4345	17.0288	17.4622
	412	17.1772	17.7159	17.4677	16.8376	17.4595	16.856	17.4338	17.0278	17.4615
	517	17.1767	17.7156	17.4674	16.8368	17.4587	16.8549	17.4318	17.0261	17.4599
	672	17.1752	17.7145	17.4659	16.8356	17.4572	16.8534	17.4302	17.0242	17.458

S: Sample

Table A.3. Instantaneous mass (W_i) of oven dried GFRP rebars while wetting at different RH (Cont'd).

		GFRP rebars exposed in different RH					
		PH 84			PH 94		
	Days	S1	S2	S3	S1	S2	S3
W_b	0	16.9545	16.7665	17.5169	17.5254	17.4946	17.4019
	1	16.9951	16.8062	17.5582	17.4586	17.5469	17.5853
	2	16.9951	16.8062	17.5582	17.4586	17.5469	17.5853
	3	16.9933	16.8052	17.5541	17.4557	17.5443	17.5833
	4	16.993	16.8038	17.5553	17.4549	17.5433	17.5813
	5	16.9905	16.8012	17.5521	17.4512	17.5392	17.5757
	6	16.9882	16.7984	17.5491	17.4471	17.5352	17.5667
	7	16.9879	16.7985	17.5492	17.4468	17.5352	17.5644
	8	16.988	16.7984	17.5487	17.4468	17.5356	17.564
	9	16.9878	16.798	17.5485	17.4468	17.5349	17.5604
	10	16.987	16.7973	17.5475	17.4455	17.534	17.5629
	11	16.9857	16.7962	17.5461	17.444	17.533	17.5608
	12	16.985	16.7953	17.5455	17.4433	17.5317	17.5601
	13	16.9849	16.7952	17.5453	17.4427	17.5313	17.5598
	14	16.9845	16.7947	17.5445	17.4421	17.5313	17.5596
	16	16.9835	16.7935	17.5434	17.4405	17.5298	17.558
	18	16.9829	16.7932	17.5432	17.4398	17.5282	17.557
	19	16.9824	16.7929	17.5421	17.4389	17.5285	17.5564
	20	16.982	16.792	17.5423	17.4386	17.528	17.556
	21	16.9818	16.7918	17.542	17.438	17.5277	17.5558
	23	16.9811	16.7911	17.5414	17.4371	17.5269	17.555
	26	16.981	16.791	17.5414	17.4366	17.5262	17.5544
	29	16.9801	16.7901	17.5401	17.4354	17.5255	17.5536
	32	16.9792	16.7892	17.5392	17.4344	17.5246	17.5527
W_i	35	16.9781	16.7885	17.5385	17.433	17.5235	17.5519
	38	16.9774	16.788	17.538	17.4319	17.5227	17.551
	42	16.9765	16.7869	17.537	17.4307	17.5213	17.55
	46	16.9757	16.7859	17.5362	17.4297	17.5199	17.5488
	49	16.9756	16.7866	17.5369	17.4301	17.5209	17.5494
	53	16.9757	16.7857	17.5363	17.4287	17.5192	17.5484
	56	16.9751	16.7856	17.5359	17.4284	17.5191	17.5481
	58	16.975	16.785	17.5354	17.4278	17.5185	17.5478
	62	16.9745	16.7849	17.5352	17.4276	17.5183	17.5476
	67	16.9737	16.784	17.5347	17.4262	17.5175	17.5465
	74	16.9731	16.7837	17.534	17.4262	17.5172	17.5462
	81	16.9726	16.783	17.5338	17.4248	17.5163	17.5457
	85	16.9722	16.7826	17.5335	17.4244	17.5156	17.545
	90	16.9718	16.782	17.5326	17.4232	17.515	17.5443
	101	16.9708	16.7813	17.5315	17.4221	17.5139	17.5432
	113	16.9699	16.7803	17.5308	17.4214	17.5127	17.5423
	121	16.9689	16.7798	17.5301	17.4203	17.5123	17.5418
	128	16.9687	16.7796	17.53	17.4179	17.5118	17.5413
	135	16.9681	16.779	17.5296	17.4188	17.5109	17.5405
	185	16.9671	16.7781	17.5284	17.4178	17.51	17.5395
	269	16.9661	16.7772	17.5277	17.4165	17.5088	17.5385
	412	16.965	16.7767	17.5269	17.4152	17.5078	17.5376
	517	16.9636	16.7749	17.5255	17.4132	17.5057	17.5359
	672	16.9614	16.7732	17.5235	17.4104	17.5031	17.5334

Table A.3. Instantaneous mass (W_i) of oven dried GFRP rebars while wetting at different RH (Cont'd).

		GFRP rebars immersed in water at 23 °C (100RH)			
	Days	S1	S2	S3	S4
W_b	0	20.4986	20.2820	20.3607	20.1794
W_i	1	20.5339	20.3110	20.3801	20.2394
	2	20.5310	20.3203	20.3867	20.2272
	4	20.5323	20.3423	20.3876	20.2315
	7	20.5490	20.3490	20.4014	20.2361
	9	20.5582	20.3550	20.4093	20.2515
	11	20.5686	20.3608	20.4162	20.2493
	14	20.5700	20.3724	20.4216	20.2525
	16	20.5855	20.3786	20.4323	20.2522
	18	20.5920	20.3892	20.4357	20.2541
	22	20.5943	20.3984	20.4495	20.2565
	25	20.6048	20.4050	20.4555	20.2601
	29	20.6137	20.4133	20.4579	20.2509
	32	20.6189	20.4149	20.4665	20.2509
	34	20.6219	20.4204	20.4695	20.2575
	38	20.6247	20.4276	20.4741	20.2593
	43	20.6301	20.4308	20.4726	20.2727
	49	20.6284	20.4353	20.4822	20.2685
	56	20.6385	20.4419	20.4842	20.2686
	60	20.6486	20.4517	20.4871	20.2736
	66	20.6485	20.4515	20.4950	20.2767
	74	20.6613	20.4657	20.5027	20.2801
	82	20.6721	20.4774	20.5072	20.2867
	94	20.6805	20.4809	20.5210	20.2894
	102	20.6863	20.4906	20.5208	20.2904
	109	20.6941	20.4914	20.5289	20.2939
	115	20.6968	20.4905	20.5344	20.2963
	119	20.6980	20.4950	20.5341	20.3001
	126	20.6956	20.5016	20.5361	20.3034
	176	20.7059	20.5100	20.5483	20.3223
	260	20.7206	20.5218	20.5545	20.3514
	395	20.7169	20.5249	20.5650	20.3769
	515	20.7369	20.5230	20.5723	20.4014
	612	20.7415	20.5249	20.5815	20.4126
	672	20.7406	20.5263	20.5846	20.4139
	730	20.7398	20.5285	20.5835	20.4138

S: Sample

Table A.4. Instantaneous mass (W_i) of GFRP rebars immersed at different temperatures.

		4 °C			23 °C			50 °C		
	Days	S1	S2	S3	S1	S2	S3	S1	S2	S3
W_b	0	19.7194	20.0399	20.1477	20.4986	20.2820	20.3607	20.2437	20.0989	20.8741
W_i	1	19.7265	20.0435	20.1547	20.5339	20.3110	20.3801	20.3108	20.2252	20.9774
	2	19.7343	20.0439	20.1579	20.5310	20.3203	20.3867	20.3546	20.2814	21.0075
	4	19.7446	20.0443	20.1676	20.5323	20.3423	20.3876	20.4259	20.3359	21.0628
	7	19.7543	20.0450	20.1700	20.5490	20.3490	20.4014	20.4718	20.3700	21.1098
	9	19.7603	20.0455	20.1712	20.5582	20.3550	20.4093	20.4908	20.3941	21.1384
	11	19.7636	20.0474	20.1719	20.5686	20.3608	20.4162	20.5094	20.4120	21.1635
	14	19.7639	20.0527	20.1728	20.5700	20.3724	20.4216	20.5300	20.4277	21.1835
	16	19.7646	20.0562	20.1729	20.5855	20.3786	20.4323	20.5311	20.4412	21.1978
	18	19.7648	20.0578	20.1746	20.5920	20.3892	20.4357	20.5395	20.4578	21.2074
	22	19.7680	20.0653	20.1800	20.5943	20.3984	20.4495	20.5565	20.4578	21.2117
	25	19.7691	20.0690	20.1830	20.6048	20.4050	20.4555	20.5572	20.4708	21.2201
	29	19.7711	20.0719	20.1837	20.6137	20.4133	20.4579	20.5730	20.4715	21.2257
	32	19.7717	20.0785	20.1852	20.6189	20.4149	20.4665	20.5683	20.4770	21.2274
	34	19.7717	20.0800	20.1858	20.6219	20.4204	20.4695	20.5675	20.4799	21.2327
	38	19.7731	20.0826	20.1883	20.6247	20.4276	20.4741	20.5734	20.4727	21.2328
	43	19.7762	20.0874	20.1962	20.6301	20.4308	20.4726	20.5697	20.4798	21.2380
	49	19.7778	20.0891	20.1995	20.6284	20.4353	20.4822	20.5807	20.4870	21.2168
	56	19.7791	20.0930	20.2035	20.6385	20.4419	20.4842	20.5743	20.4885	21.2259
	60	19.7788	20.0963	20.2035	20.6486	20.4517	20.4871	20.5689	20.4919	21.2286
	66	19.7792	20.0970	20.2042	20.6485	20.4515	20.4950	20.5674	20.4963	21.2330
	74	19.7786	20.1002	20.2049	20.6613	20.4657	20.5027	20.5643	20.4879	21.2426
	82	19.7798	20.1042	20.2086	20.6721	20.4774	20.5072	20.5737	20.4812	21.2446
	94	19.7815	20.1134	20.2160	20.6805	20.4809	20.5210	20.5871	20.4711	21.2418
	102	19.7825	20.1156	20.2167	20.6863	20.4906	20.5208	20.5888	20.4753	21.2521
	109	19.7847	20.1180	20.2162	20.6941	20.4914	20.5289	20.5897	20.4929	21.2506
	115	19.7901	20.1211	20.2192	20.6968	20.4905	20.5344	20.5942	20.5074	21.2603
	119	19.7914	20.1233	20.2211	20.6980	20.4950	20.5341	20.6084	20.5193	21.2695
	126	19.7918	20.1257	20.2213	20.6956	20.5016	20.5361	20.6550	20.5145	21.2627
	176	19.8002	20.1429	20.2308	20.7059	20.5100	20.5483	20.6887	20.5870	21.2812
	260	19.8029	20.1610	20.2528	20.7206	20.5218	20.5545	20.6900	20.6719	21.3155
	395	19.8202	20.1782	20.2679	20.7169	20.5249	20.5650	20.7001	20.6819	21.3260
	515	19.8267	20.1932	20.2710	20.7369	20.5230	20.5723	20.7001	20.6819	21.3260
	612	19.8414	20.1921	20.2814	20.7415	20.5249	20.5815			
	672	19.8424	20.1925	20.2879	20.7406	20.5263	20.5846			
	730	19.8454	20.1927	20.2907	20.7398	20.5285	20.5835			

S: Sample

APPENDIX B: COMPOSITE MANUFACTURING PROCESS

There are a wide variety of processes available to the composites manufacturer to produce cost efficient products. The specific manufacturing process is used to produce the specific composite product. For example, hand lay-up process is used to manufacture FRP sheets and fabrics, Pultrusion process produces pultruded composite materials, whereas filament winding method is used to develop hollow FRP pipes, tubes and poles etc. A short description of composite manufacturing methods is included here.

Pultrusion is a continuous process for manufacturing composites that have a cross-sectional shape. The technique is fully automated and is thus highly economical. It is similar to the extrusion process by which many metal sections are fabricated. Illustrated in Figure A1 (ACME 2006), the Pultrusion process is accomplished by pulling raw fibres through a resin bath and then through a heated die. As the resin-impregnated fibres pass through the die the polymer matrix hardens into the shape of the die, thus producing a structural component. The FRP component is pulled from the cured end. This process is continuous and has the advantage that FRP components of virtually any length can be fabricated. All fibres in a pultruded element are aligned along the length of the component, thus creating a unidirectional FRP.

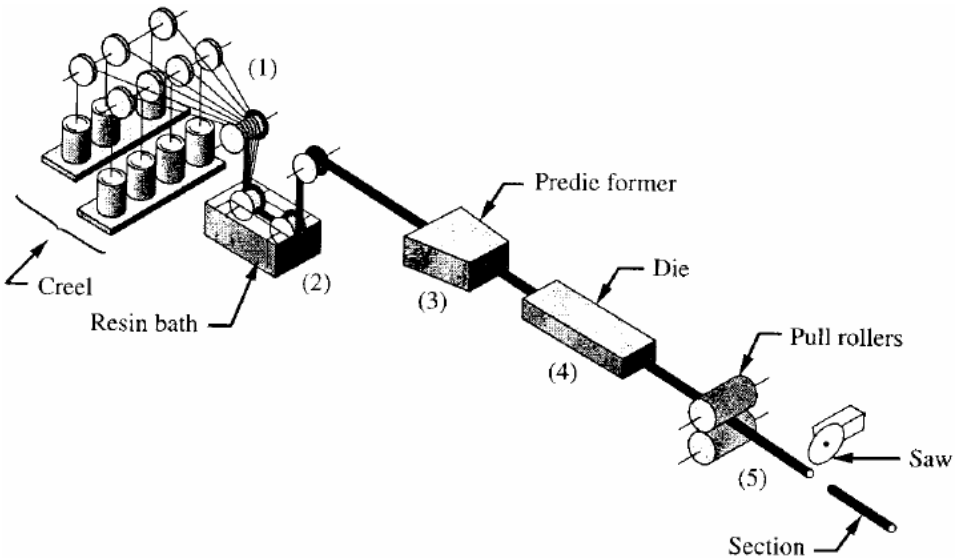

Figure A1. Schematic showing the Pultrusion manufacturing process.

Hand lay-up, sometimes referred to as Wet lay-up or contact moulding, is a manufacturing technique for FRP often used in structural rehabilitation applications, whereas FRP sheets or fabrics are bonded to the exterior of reinforced concrete, steel, aluminum, or timber members.

Resins are impregnated by hand into fibres which are in the form of woven, knitted, stitched or bonded fabrics. This is usually accomplished by rollers or brushes, with an increasing use of nip-roller type impregnators for forcing resin into the fabrics by means of rotating rollers and a bath of resin as shown in Figure A2 (Netcomposites 2005). Laminates are left to cure under standard atmospheric conditions. Epoxy, polyester, vinylester, phenolic can be used as resins, whereas any kind of fibres can be utilized in this method.

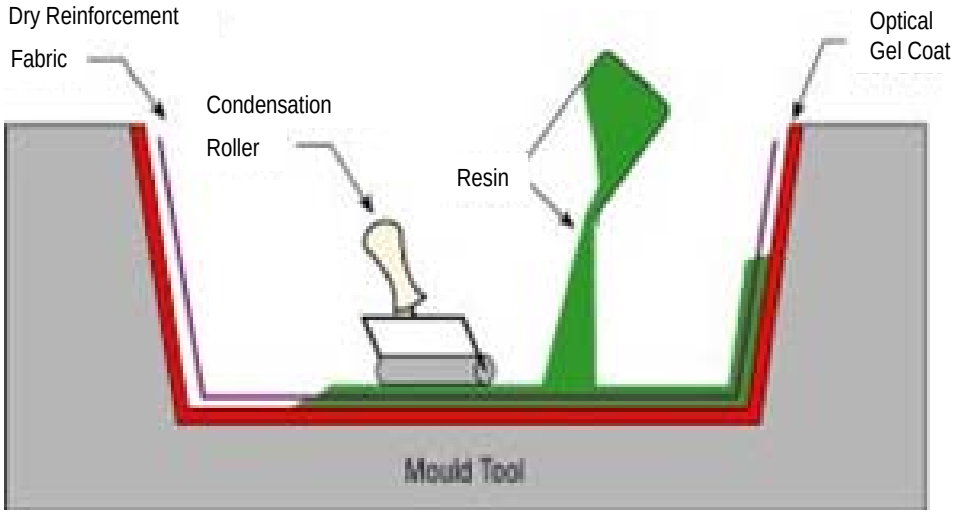

Figure A2. A schematic of a hand lay-up process.

Hand lay-up process has several advantages which include (i) widely used for many years, (ii) simple technology, (iii) low cost tooling (iv) wide choice of suppliers and material types and (v) higher fibre contents, and longer fibres than with spray lay-up. In order to be expert in this method, the following points have to considered: (i) expert technician, (ii) health and safety considerations of resins, (iii) resins used in this technique has to be less viscous and workable.

Filament winding has many innovative applications for FRP in structural engineering, such as stay-in-place formwork for concrete piles make use of hollow FRP poles, pipes, and tubes. These members are commonly produced using a manufacturing process called filament winding. In this automated process, illustrated in Figure A.3, raw fibres are drawn off spools, through a resin bath, and wound onto a rotating mandrel. The placement of the fibres on the mandrel is controlled by a computer, allowing for the fibres to be placed with extreme precision and with various desired orientations. By varying the fibre orientation, filament wound members can be created with a variety of mechanical properties tailored for specific applications.

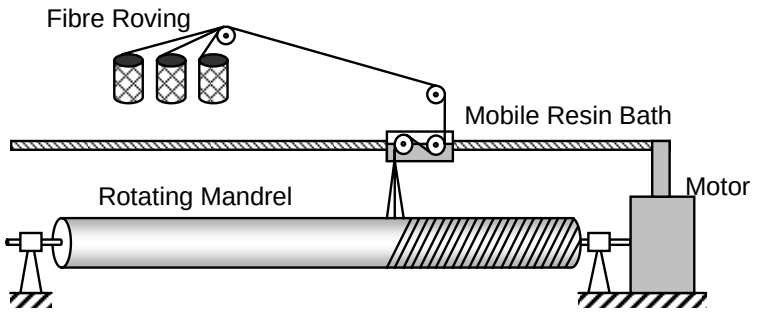

Figure A.3. A schematic of filament winding (ISIS 2003).